

Development of Molecular Probes and Nano-carrier Delivery System for Intracellular Sensing and Theranostic Applications

By

RAMYA A.N.

10CC16A39008

A thesis submitted to the
Academy of Scientific and Innovative Research
for the award of the degree of
DOCTOR OF PHILOSOPHY
in
SCIENCE

Under the supervision of
Dr. Kaustabh Kumar Maiti



**CSIR-National Institute for Interdisciplinary
Science and Technology (CSIR-NIIST),
Thiruvananthapuram – 695 019**



Academy of Scientific and Innovative Research
AcSIR Headquarters, CSIR-HRDC campus
Sector 19, Kamla Nehru Nagar,
Ghaziabad, Uttar Pradesh – 201 002, India

March 2021

Dedicated to

My Family



National Institute for Interdisciplinary Science and Technology (NIIST)
Council of Scientific and Industrial Research (CSIR)
Industrial estate P.O., Thiruvananthapuram- 695019
Kerala, India

Dr. Kaustabh Kumar Maiti
Principal Scientist
Chemical Sciences and Technology Division

Tel : 0471-2515475
e-mail: kkmaiti@niist.res.in
kkmaiti29@gmail.com




26-03-2021

CERTIFICATE

*This is to certify that the work incorporated in this Ph.D. thesis entitled, "Development of Molecular Probes and Nano-carrier Delivery System for Intracellular Sensing and Theranostic Applications", submitted by Ms. Ramya A.N. to the Academy of Scientific and Innovative Research (AcSIR) in partial fulfilment of the requirements for the award of the **Degree of Doctor of Philosophy in Sciences**, embodies original research work carried-out by the student. We further certify that this work has not been submitted to any other University or Institution in part or full for the award of any degree or diploma. Research materials obtained from other sources and used in this research work have been duly acknowledged in the thesis. Images, illustrations, figures, tables etc., used in the thesis from other sources, have also been duly cited and acknowledged.*

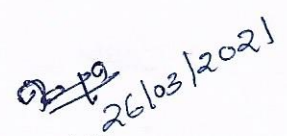

RAMYA A.N.


Dr. Kaustabh Kumar Maiti
(Thesis Supervisor)

STATEMENTS OF ACADEMIC INTEGRITY


I **Ramya A.N.**, a Ph.D. student of the Academy of Scientific and Innovative Research (AcSIR) with Registration No. 10CC16A39008 hereby undertake that, the thesis entitled **“Development of Molecular Probes and Nano-carrier Delivery System for Intracellular Sensing and Theranostic Applications”** has been prepared by me and that the document reports original work carried out by me and is free of any plagiarism in compliance with the UGC Regulations on *“Promotion of Academic Integrity and Prevention of Plagiarism in Higher Educational Institutions (2018)”* and the CSIR Guidelines for *“Ethics in Research and in Governance (2020)”*.

March 26, 2021
Thiruvananthapuram


Ramya A.N.

It is hereby certified that the work done by the student, under my supervision, is plagiarism-free in accordance with the UGC Regulations on *“Promotion of Academic Integrity and Prevention of Plagiarism in Higher Educational Institutions (2018)”* and the CSIR Guidelines for *“Ethics in Research and in Governance (2020)”*.

March 26, 2021
Thiruvananthapuram


Dr. Kaustabh Kumar Maiti


DECLARATION

I, **Ramya A.N.**, bearing AcSIR Registration No. 10CC16A39008 declare that my thesis entitled, "**Development of Molecular Probes and Nano-carrier Delivery System for Intracellular Sensing and Theranostic Applications**" is plagiarism free in accordance with the UGC Regulations on "*Promotion of Academic Integrity and Prevention of Plagiarism in Higher Educational Institutions (2018)*" and the CSIR Guidelines for "*Ethics in Research and in Governance (2020)*".

I would be solely held responsible if any plagiarised content in my thesis is detected, which is violative of the UGC regulations 2018.

March 26, 2021

Thiruvananthapuram


26/03/2021

Ramya A.N.

ACKNOWLEDGEMENTS

It is with great pleasure that I extend my deep sense of gratitude to Dr. Kaustabh Kumar Maiti, my thesis supervisor, for suggesting the research problem, for his valuable guidance, support, motivation and encouragement, leading to the successful completion of this work.

I would like to express my gratitude to Prof. Vijay Nair and Prof. M. V. George for being an illuminating source of inspiration.

I thank Dr. A. Ajayaghosh (present Director), Dr. Suresh Das (former Director) and Dr. Gangan Pratap (former Acting Director) of CSIR-National Institute for Interdisciplinary Science and Technology (CSIR-NIIST), Thiruvananthapuram, for providing the necessary facilities to carry out this work.

I also extend my sincere thanks to:

- ✓ *Dr. V. Karunakaran, Dr. C. H. Suresh and Dr. R. Luxmi Varma, present and former AcSIR co-ordinators.*
- ✓ *Dr. K.V. Radhakrishnan, Dr. Vijayakumar C. and Dr. Priya S., Doctoral Advisory Committee (DAC) members and the whole AcSIR faculty for the successful completion of the course work.*
- ✓ *Dr. P. Sujatha Devi, Dr. R. Luxmi Varma, Dr. K. R. Gopidas, present and former Head of the Division, Chemical Sciences and Technology Division (CSTD).*
- ✓ *Dr. A. Kumaran, Dr. L. Ravi Sankar, Dr. B. S. Sasidhar, Dr. Sunil Varughese, Dr. Jubi John and Dr. Shridevi. D, Scientists of Organic Chemistry Section, for their help and support extended to me.*

- ✓ *Mr. Kiran Mohan & Mr. Robert Philip for TEM analysis, Mrs. Saumini Matthew, Mr. Saran P., Mr. R. Gokul for NMR, Mrs. Viji S., Ms. Athira for mass spectral analyses, Mr. Harish Raj V. for SEM analysis, Mr. Gourab Das for AFM analysis.*
- ✓ *Dr. Manu M. Joseph and Dr. Adarsh N. for their timely suggestions and help.*
- ✓ *Dr. Nisha, Dr. S. Maniganda, Dr. Jyothi B Nair, Dr. Susan Alex, Dr. Vineeth Vijayan, Dr. Varsha Karunakaran, Dr. Vishnu Priya Murali, Dr. Sujai P.T., Dr. Saranya Giridharan, Ms. Arya J.S., Mr. Shamjith S, Mr. Madhukrishnan M, Ms. Vidyalekshmi M.S., Ms. Shamna K, Ms. Sreedevi P., Ms. Sreedevi D., Mr. Shihash Ahammed, Ms. Deepika S, Ms. Anjitha Ajith, Ms. Anusree and Ms. Anjitha U.M. for their love, friendship and support.*
- ✓ *Dr. Parvathy Rathnam, Dr. Dhanya SR, Dr. Sajin Francis, Ms. Ranjitha J., Mr. Vishnu K. Omanakuttan for their encouragement and support.*
- ✓ *Former and present members of CSTD and friends at CSIR-NIIST, for their help and support.*
- ✓ *All my teachers for their encouragement at different stages of my academic career.*
- ✓ *Council of Scientific and Industrial Research (CSIR) and Department of Science and Technology (DST) for Research fellowship.*

I am deeply and forever indebted to my parents and brother for their constant source of love, inspiration and blessings. Above all, I thank the Almighty for all the blessings showered upon me.

Ramya A.N.

TABLE OF CONTENTS

Certificate		i
Statements of Academic Integrity		ii
Declaration		iii
Acknowledgements		iv
Table of Contents		vi
List of Abbreviations		xi
Preface		xvii
Chapter 1	Molecular and Nanocarrier Probes for Sensing, Imaging and Therapeutic Applications in Cellular Biology	1-53
1.1	Abstract	1
1.2	Introduction	2
1.3	Optical imaging	3
1.3.1	Fluorescence imaging	4
1.3.1.1.	Fluorescent probes	5
1.3.1.2.	Role of fluorescent probes in biomedical applications	7
1.3.1.3.	Fluorescent probes for the sensing of multiple biological analytes	7
1.3.1.3.1.	Turn-on fluorescent probes	8
1.3.1.3.2.	Turn-off fluorescent probes	14
1.3.1.3.3.	Ratiometric fluorescent probes	18
1.3.2	Raman imaging	21
1.3.2.1.	Evaluation of SERS and recent developments	23
1.3.2.2	Enhancement factor and hotspot generation	23
1.3.2.3.	SERS substrates	25
1.3.2.4.	SERS nanoparticle tags	26
1.3.2.5.	SERS nanotags for diagnosis and imaging	27
1.4	Recent development of nano-theranostic systems for nanomedicine	33
1.4.1.	Nano carriers for targeted drug delivery	34
1.4.2	SERS based nano-carrier system for theranostic application	35
1.4.2.1.	Gold nanoparticle based nanocarrier systems	36

1.4.2.2.	Silver nanoparticle based nano carrier systems	38
1.4.2.3.	Mesoporous silica nanoparticle based nanocarrier systems	39
1.5	Objectives and methodologies for the present investigation	40
1.6	References	42
Chapter 2	SERS Nanoprobe Based on Tetraphenylethylene Raman Signatures for The Detection of Prostate Cancer Biomarker	55-89
2.1.	Abstract	55
2.2.	Introduction	56
2.3.	Results and discussion	61
2.3.1.	Synthesis and characterization of TPE analogues	61
2.3.2.	Photophysical properties of TPE analogues	62
2.3.3.	SERS analysis of the TPE derivative	63
2.3.4.	Construction of TPE-In-PSA SERS nanoprobe	65
2.3.5.	PSA protease detection and LOD calculation through SERS	68
2.3.6.	PSA expression and cytotoxicity study on cancer cell lines	69
2.3.7.	Recognition of human prostate cancer cells using SERS nanoprobe	70
2.3.8.	SERS imaging in living cells	71
2.4.	Conclusions	72
2.5.	Experimental section: synthesis	73
2.5.1.	General techniques	73
2.5.2.	Materials and methods	74
2.5.3.	Synthesis of TPE derivatives	74
2.5.3.1.	Synthesis of TPE-CHO	74
2.5.3.2.	Synthesis of indoline propylamine	75
2.5.3.3.	Synthesis of boc protected indoline propylamine	75
2.5.3.4.	Synthesis of indoline propyl	76
2.5.3.5.	Synthesis of lipoic acid succinimidyl ester	76
2.5.3.6.	Synthesis of TPE-In	77
2.5.3.7.	Synthesis of TPE-In-NH ₂ -Boc	78
2.5.3.8.	De-protection of Boc from TPE-In-NH ₂ -Boc	78
2.5.3.9.	Synthesis of TPE-In-L	79
2.5.3.10.	Synthesis of TPE-Q	80
2.5.3.11.	Synthesis of TPE-B	80

2.5.3.12.	Solid phase peptide synthesis of PSA peptide sequence	81
2.5.3.13.	Coupling reaction between TPE-In-Boc and PSA peptide sequence	81
2.5.4.	Synthesis of gold nanoparticles	82
2.5.6.	Western blot analysis	83
2.5.7.	Cytotoxicity assay	83
2.6	References	84
Chapter 3	Tetraphenylethylene based Molecular Probe for Endogenous H₂S Detection and its Therapeutic Potential in Alzheimer's Disease	91-125
3.1.	Abstract	91
3.2.	Introduction	92
3.3.	Results and discussion	98
3.3.1.	Synthetic framework for molecular fluorogens	98
3.3.2.	Photophysical evaluation and its molecular mechanism	99
3.3.3.	Investigation of TPE-NBD-D towards endogenous detection of H ₂ S in cellular and mice model level	106
3.3.4.	Assessment of TPE-NBD-D in Alzheimer disease: H ₂ S mediated de-agglomeration of A β protein	110
3.4.	Conclusions	115
3.5.	Materials and methods	115
3.5.1	General techniques	115
3.5.2.	Materials and methods	116
3.5.3.	Synthesis of molecular probes	117
3.5.3.1.	Synthesis of TPE-OH-2	117
3.5.3.2.	Synthesis of the sensor TPE-NBD-2	117
3.5.3.3.	Synthesis of the intermediate TPE-NBD-OH	118
3.5.3.4.	Synthesis of donor	119
3.5.3.5.	Synthesis of the molecular probe TPE-NBD-D	119
3.6.	References	120

Chapter 4	Gold-mesoporous Silica Nanotheranostic Platform for Targeted Chemotherapy with the Aid of Fluorescence and SERS Dual Detection Modality	127-169
4.1.	Abstract	127
4.2.	Introduction	128
4.3.	Results and discussion	133
4.3.1.	Preparation and characterization of TNEDS	133
4.3.2.	Stimuli responsive drug releases	137
4.3.3.	Western blot analysis and hemolysis assay	139
4.3.4.	SERS Imaging of live cells using Au@SiO ₂ -CS-FA	141
4.3.5.	Evaluation of cytotoxicity	144
4.3.6.	Investigation of cellular uptake pathways and intracellular Dox release by fluorescence modality	145
4.3.7.	Cellular internalization and Dox release by SERS imaging	147
4.3.8.	Evaluation of apoptotic events by SERS fingerprinting	149
4.3.9.	Investigation of cell death mechanism	150
4.3.10.	Therapeutic efficacy in murine models	152
4.4.	Conclusions	154
4.5.	Experimental section	155
4.5.1.	Materials	155
4.5.2.	Culture and maintenance of cell lines	155
4.5.3.	TEOS mediated synthesis of Au@SiO ₂ Nanoparticles	156
4.5.4.	Conjugation of folic acid with chitosan	156
4.5.5.	Synthesis of CS-FA coated Au@SiO ₂ nanoparticle	157
4.5.6.	Dox loading and redox and pH-responsive Dox release kinetics of Au@SiO ₂ -Dox-CS-FA NPs	157
4.5.7.	Cytotoxicity assays	158
4.5.8.	Western blot analysis and hemolysis assay	158
4.5.9.	Apoptotic assays	159
4.5.10.	Live cell Raman imaging	160
4.5.11.	Cellular internalization study	160
4.5.12.	Evaluation of Dox uptake and apoptosis using SERS	161
4.5.13.	Tumor reduction studies on ascites and solid tumor mice	162

4.5.13.1.	Tumor reduction on ascites tumor mice	162
4.5.13.2.	Tumor reduction on solid tumor mice syngraft	163
4.6.	References	163
	Abstract of the thesis	171
	List of publications	173
	List of conference presentations	175

List of Abbreviations

A375	Human malignant melanoma cells
A549	Adenocarcinomic human alveolar basal epithelial cells
Ac ₂ O	Acetic anhydride
ACQ	Aggregation caused quenching
AD	Alzheimer's disease
ADT	Anethole 1,2-dithiole-3-thione
AFM	Atomic force microscopy
AgNPs	Silver nanoparticles
AIE	Aggregation induced emission
AIEE	aggregation induced enhanced emission
AOAA	Aminooxyacetic acid
APTES	(3-Aminopropyl) triethoxysilane
ATCC	American type culture collection
AuNF	Gold nanoflower
AuNPs	Gold nanoparticles
Au@SiO ₂	AuNPs with silica layer
A β	Amyloid-beta
Bcl-2	B-cell-lymphoma-2-gene
Boc	Tert-butyloxycarbonyl
BSA	Bovine serum albumin
CAT	Cysteine aminotransferase
CBS	Cystathionine β -synthase
CCD	Charge coupled device
CDCl ₃	Deuterated chloroform
CH ₂ Cl ₂	Dichloromethane
CHCl ₃	Chloroform
CH ₃ OH	Methanol
CNTs	Carbon nanotubes
cm	Centimetre
CO	Carbon monoxide
CO ₂	Carbondioxide

CRS	Coherent Raman scattering
CSE	Cystathionine γ -lyase
CS-FA	Chitosan-folic acid
CT	Computed tomography
Cys	Cysteine
DATS	Diallyltrisulfide
DCC	N, N'-Dicyclohexylcarbodiimide
DCM	Dichloromethane
DIC	N,N'-Diisopropylcarbodiimide
DIPEA	N,N-Diisopropylethylamine
DLA	Daltons lymphoma ascites
DLC	Drug loading content
DLE	Drug loading efficiency
DLS	Dynamic light scattering
DMAP	4-Dimethylaminopyridine
DMEM	Dulbecco's modified Eagle's medium
DMF	Dimethylformamide
DMSO	Dimethyl sulfoxide
DOT	Diffuse optical tomography
Dox	Doxorubicin
DTNB	5,5'-dithiobis-(2-nitrobenzoic acid)
EAC	Ehrlich ascites carcinoma
EDC	1-Ethyl-3-(3-dimethylaminopropyl)carbodiimide
EF	Enhancement factor
EGFR	Epidermal growth factor receptor
ELISA	Enzyme-linked immunosorbent assay
EM	Electromagnetic
EPR	Enhanced permeation and retention
ER	Estrogen receptor
ESI-MS	Electrospray ionization mass spectrometry
ESIPT	excited state intramolecular proton transfer
Et ₂ O	Diethyl ether
FA	Folic acid

FAB	Fast atom bombardment
FBS	Fetal bovine serum
FDA	Food and drug administration
FITC	Fluorescein isothiocyanate
FR	Folate receptor
FRET	Fluorescence resonance energy transfer
FT-IR	Fourier-transform infrared spectroscopy
g	Gram
Gln	Glutamine
GMP	Guanosine 3',5'-cyclic monophosphate
GSH	Glutathione
¹ H	Proton
HCA	Hyper cluster analysis
hr	Hour
HBTU	(2-(1H-benzotriazol-1-yl)-1,1,3,3-tetramethyluronium hexafluorophosphate
HCl	Hydrochloric acid
HeLa	Cervical cancer
HEPES	4-(2-hydroxyethyl)-1-piperazineethanesulfonic acid
HepG2	Hepatocellular carcinoma cells
HER2	Human epidermal growth factor receptor-2
HEWL	Hen egg white lysosome
H ₂ O	Water
H ₂ O ₂	Hydrogen peroxide
HOBT	Hydroxybenzotriazole
HPLC	High performance liquid chromatography
HRMS	High resolution mass spectroscopy
H ₂ S	Hydrogen sulfide
HSA	Human serum albumin
Hz	Hertz
ICT	Internal charge transfer
ip	Intraperitoneal
i.t.	Intratumoral

ITO	Indium tin oxide
K ₂ CO ₃	Potassium carbonate
Leu	Leucine
LNCaP	Human prostate cancer
LOD	Limit of detection
LSPRs	Localized surface plasmon resonance
Lys	Lysine
m	Metre
M	Molar
4-MBA	4-mercaptobenzoic acid
MCF-7	Human breast cancer cells
mg	Milligram
mL	Millilitre
MgSO ₄	Magnesium sulphate
MHz	Mega hertz
min	Minutes
mm	Millimetre
mM	Millimolar
MMA	Methyl methacrylate
mmol	Millimol
MRI	Magnetic resonance imaging
MSNs	Mesoporous silica nanoparticles
3-MST	3-Mercaptopyruvate sulphur transferase
MTT	3-[4,5-dimethylthiazol-2yl]-2, 5 diphenyl tetrazolium
mW	Milliwatt
NaHS	Sodium hydrosulfide
NaOH	Sodium hydroxide
Na ₂ S	Sodium sulfide
Na ₂ SO ₄	Sodium sulphate
2-NAT	2-naphthalenethiol
NBD	4-chloro-7-nitrobenzofurazan
NCCS	National centre for cell science
NEM	N-Ethylmaleimide

NHS	N-hydroxysuccinimide
NIR	Near infrared
nm	Nanometre
NMR	Nuclear magnetic resonance
NO	Nitric oxide
NPs	Nanoparticles
OCT	Optical coherence tomography
ONOO ⁻	Peroxynitrile
OPD	o-phenylenediamine
OSCC	Cellosaurus cell line
PEG	poly ethylene glycol
PET	Positron emission tomography
PI	Photoacoustic Imaging
ppm	Parts per million
PSA	Prostate specific antigen
QDs	Quantum dots
RBCs	Red blood cells
RFP	Red fluorescent protein
RNA	Ribo nucleic acid
rpm	Revolutions per minute
r.t	Room temperature
SAM	S-adenosyl methionine
SDS-PAGE	Sodium dodecyl sulphate PAGE
SEM	Scanning electron microscope
Ser	Serine
SEHRS	Surface enhanced hyper Raman scattering
SERRS	Surface enhanced resonance Raman scattering
SERS	Surface enhanced Raman spectroscopy
SH-SY5Y	Neuroblastoma cells
SK-BR-3	Human breast cancer cell line
SKOV3	Ovarian cancer
SPIONs	Super paramagnetic iron oxide nanoparticles
SPPS	Solid phase peptide synthesis

SRS	Spontaneous Raman scattering
SVM	Support vector machine
SWCN	Single-wall carbon nanotubes
t	Triplet
T	Temperature
TBAB	Tetrabutylammonium bromide
TEA	Triethylamine
TEM	Transmission electron microscopy
TEOS	Tetraethylorthosilicate
TERS	Tip enhanced Raman scattering
TFA	Trifluoro acetic acid
THF	Tetrahydrofuran
TiCl ₄	Titanium tetrachloride
TLC	Thin layer chromatography
TNEDS	Targeted nano-envelop delivery system
TPE	Tetraphenylethylene
TUNEL	Terminal deoxynucleotidyltransferase (TdT) dUTP nick-end labeling
UPCNs	Up conversion nanoparticles
UV-Vis	Ultraviolet-visible
WRI	Wild field Raman imaging
Xe	Xenon
YFP	Yellow fluorescent protein
Zn	Zinc
μM	Micromolar
μm	Micrometre

PREFACE

The precise detection, diagnosis and the proper treatments for various diseases requires immediate attention. The search for new techniques in lieu of theranostic applications gains immense attention in recent times. Among various techniques, optical methods accomplish increased interest due to its high accuracy and sensitivity. Fluorescence and surface enhanced Raman scattering (SERS) are the two extensively employed optical methods for the in-depth analysis of the complex biological systems. In this regard, a variety of molecular probes and nanocarrier systems have been explored for biomedical applications. The first chapter deals with the versatile attempts to develop the probes, mainly based on fluorescence and SERS techniques, and also describes the variety of applications of such probes in biology and medicine.

In the second chapter, the design, synthesis and characterization of tetraphenylethylene (TPE) based SERS nanoprobe has been demonstrated for the detection of prostate cancer cells. All the derivatives exhibited predominantly aggregation induced emission (AIE) and aggregation caused quenching (ACQ) phenomenon and as a new insight all showed excellent SERS fingerprint with multiplex spectral pattern. The unique SERS nanoprobe TPE-In-PSA@Au has been developed in conjugation with target-specific PSA peptide (Cys-SerLys-Leu-Gln-OH) substrate aiming for the detection of PSA protein. TPE-In-PSA@Au possesses excellent SERS fingerprinting with solid multiplex signal pattern. The nanoprobe successfully recognizes PSA enzyme in SERS-based detection platform with a LOD of 0.5 ng which unfold a new avenue in prostate cancer diagnosis. Furthermore, TPE-In-PSA@Au nanoprobe was nicely recognized by PSA overexpressed LNCaP cells, which was visualized through SERS spectral analysis and SERS mapping.

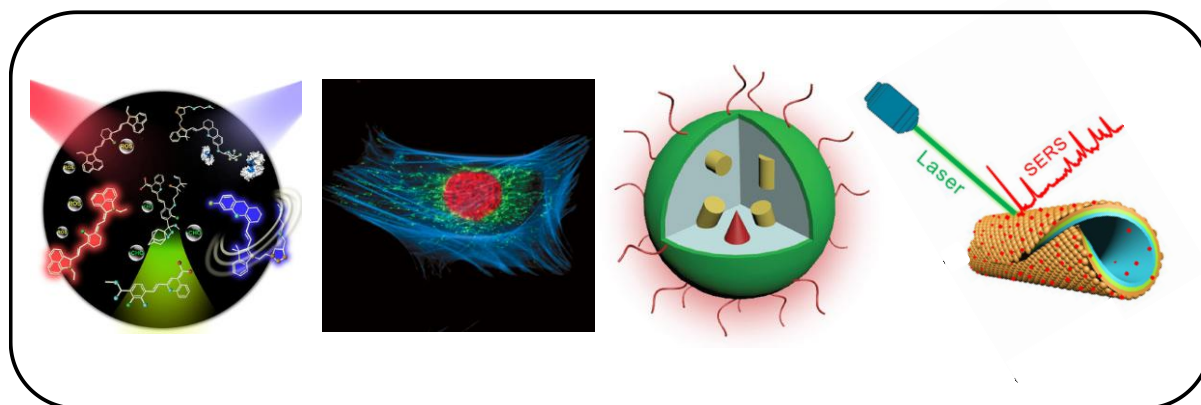
In the third chapter, a novel molecular probe comprised of TPE core as a fluorescent molecular framework has been elucidated for the detection of endogenous H₂S and synergistic delivery of H₂S in lieu of progressive therapy on Alzheimer's dementia. In this regard, two AIE active orthogonally substituted TPE based molecular probes TPE-NBD-D and TPE-NBD-2 were synthesized and characterized. Both the probes showed sensitivity and selectivity towards H₂S. In TPE-NBD-D, disulfide donor was used to generate H₂S in presence of bio thiols. Efficient H₂S sensing was reflected in both neuroblastoma cell lines and in mice models. The newly evolved molecular probe TPE-NBD-D enabled to act as H₂S donor and subsequently utilized for amyloid beta de-agglomeration (A β ₁₋₄₂ protein) to reduce the progression of AD. The toxic agglomerated A β ₁₋₄₂ turns to non-toxic de-agglomerated A β ₁₋₄₂ in presence of TPE-NBD-D.

Design and fabrication of a gold mesoporous silica hybrid nano envelop system for therapeutic applications stands the subject matter of Chapter 4. Silica coated gold nanoparticles were synthesized followed by chitosan-folic acid conjugate surface functionalization for precise loading of doxorubicin (Dox), resembled as Au@SiO₂-Dox-CS-FA. In diagnostic modality, the core Au@SiO₂ to be an effective SERS nanoprobe for Raman imaging to monitor the cellular uptake, release of the impregnated Dox, and dynamic visualization of biochemical changes at molecular level during apoptosis. Also, the probe demonstrated excellent in vitro FR-targeted cytotoxicity and also presented to be an appalling biocompatible targeted nanocarrier delivery construct. Finally, the TNEDS was explored in mouse models that clearly showed greater therapeutic efficiency superior to the clinically used Dox and Lipodox.

References

1. **A. N. Ramya**, M. M. Joseph, J. B. Nair, V. Karunakaran, N. Narayanan, K. K. Maiti, New insight of tetraphenylethylene-based Raman signatures for targeted SERS nanoprobe construction toward prostate cancer cell detection, *ACS Appl. Mater. Interfaces* **2016**, *8*, 10220–10225.
2. **A. N. Ramya**, M. M. Joseph, S. Maniganda, V. Karunakaran, T. T. Sreelekha, K. K. Maiti, Emergence of Gold-Mesoporous Silica Hybrid Nano-Theranostic: Dox-Encoded, Folate Targeted Chemotherapy with Modulation of SERS Fingerprinting for Apoptosis Toward Tumor Eradication. *Small*, **2017**, *13*, 1700819.
3. **A. N. Ramya**, Manu M. Joseph, Varsha Karunakaran, Shihab Ahammed, Vishnu Priya Murali and Kaustabh K. Maiti, Molecular Luminophore Structured with Orthogonally Substituted Tetraphenylethylene (TPE) Enabling Endogenous Detection and Signaling Role of Hydrogen Sulfide in Alzheimer's disease, **2021**, (Under preparation).

Molecular and Nanocarrier Probes for Sensing, Imaging and Therapeutic Applications in Cellular Biology



1.1. Abstract:

An ultrafast, sensitive and quantitative detection technique for diagnosis and therapy of prevalent disorders is desirable to achieve for improved therapeutic outcomes in biomedicine. In this scenario, the development of molecular probes and functional nanomaterials with improved sensing capabilities together with high therapeutic potential is a hot topic for researchers in current scientific community. Among the numerous detection techniques, optical methods based on fluorescence and surface enhanced Raman spectroscopy (SERS) enable inclusive and detailed understanding of cellular processes in biological systems due to their excellent sensitivity and specificity. So, design and synthesis of small molecular probes and nanomaterials with precise detection and therapeutic ability has emerged as a significant approach in recent times, in order to meet these requirements. The present chapter gives an insight in to the

current progresses in fluorescent probes and SERS nanotags for diagnostic and therapeutic applications in biomedical research.

1.2. Introduction

The advancement of novel optical techniques has introduced new opportunities for monitoring various biological targets and the associated events in intracellular milieu. Among the various diagnostic tools, optical techniques attain increased interest due to their non-invasiveness, sensitivity and accuracy¹. Fluorescence imaging is one of the commonly used optical imaging technique for the diagnosis of various diseases, due to its high spatial and temporal resolution. The development of novel organic dye molecules as fluorescent agents has significant advantage in the field of disease diagnosis and therapy². Apart from the fluorescence techniques, SERS has evolved recently, with great potential in diagnostic applications^{3,4}, mainly identifying infected cells, tissues, and many bio-analytes, which ensures the accurate investigation by analysing the spectral fingerprinting pattern. SERS technique is considered as an active competitor for fluorescence-based detection due to the advantages including high sensitivity, multiplexing capability and the ability to capture minute chemical modification in many biological species at molecular level. Design and synthesis of SERS active metal substrate based nano system and novel Raman reporter molecules enabled the immense consumption of this technique in biomedical applications⁵.

In addition to diagnostics, nanotechnology has been extensively studied and exploited for cancer treatment as nanoparticles based nano carrier systems for drug delivery applications⁶. The term “Theranostics” coined in biomedicine, which combine diagnosis and therapy in a single architecture. Theranostic agents in the form

of molecular or nanoconstructs precisely identify and enable to exert therapy such as cancers in a targeted fashion. Apart from cancer, Alzheimer's disease (AD)^{7,8} is likewise another cause of death in word wide, which is a type of dementia that affects thinking, memory and behaviour. Since the accurate detection, diagnosis and the proper treatments for various diseases requires immediate attention. The search for new agents for theranostic applications gains immense attention in recent times. The present chapter deals with the versatile attempts to develops the probes, mainly based on fluorescence and SERS techniques. This section also describes the variety of applications of such probes in biology and medicine.

1.3. Optical imaging

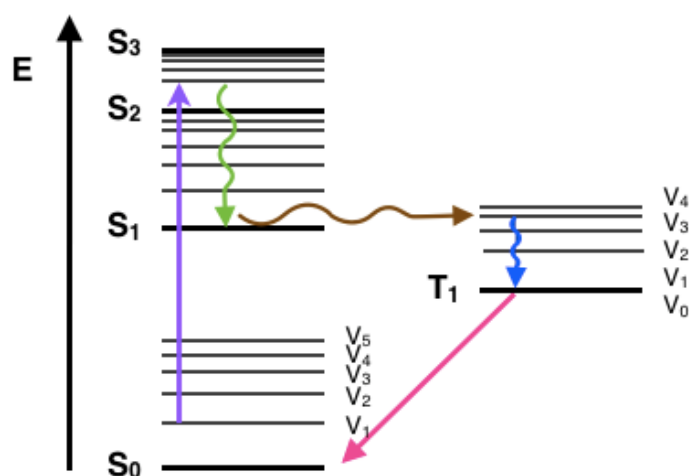
Early stage recognition and precise diagnosis are crucial for the real treatment and prevention of cancer, dementia and other non-communicable diseases. Biomedical imaging methods are extensively useful in each stages of disease management. In the past decades, a number of techniques have been emerged for diagnosis includes X-ray computed tomography (CT), magnetic resonance imaging (MRI) and positron emission tomography (PET). All these techniques provide good performance in understanding the pathological dysfunction, due to its good penetration depth. Still, most of these methods suffered from good imaging sensitivity, low spatial resolution and whole area analysis etc. So, compared with these imaging techniques, optical imaging plays a major role in biomedical and clinical diagnosis, owing to its extensive spatial resolution, high sensitivity etc.

Optical imaging can provide a new and versatile platform for non-invasive and in-vivo molecular imaging of cells, tissues, organs and molecules which gives the

information to quick and precise diagnosis. It involves the application of light as an imaging source to generate molecular images for biomedical application. Moreover, molecular fingerprints derived from the optical images gives favourable contributions to reveal the extent of diagnosis. Cells or organs absorb and scatter light, therefore, optical imaging can quantify metabolic changes that are early markers of abnormal functioning of organs and tissues. Different types of optical imaging techniques available for the use in medicinal purposes are Photoacoustic Imaging (PI), endoscopy, Optical Coherence Tomography (OCT), Diffuse Optical Tomography (DOT), Raman spectroscopy, Fluorescence imaging etc. Among these modalities fluorescence imaging and Raman imaging stands as two efficient techniques that enable real-time visualization of molecular events in the cellular environment with high sensitivity and resolution.

1.3.1. Fluorescence imaging

Fluorescence imaging is a non-invasive imaging method to describe the spatial scattering of substances that emit fluorescence which can help to visualize biological processes in a living organism. Fluorescence is a physical phenomenon related to



Scheme 1.1. Representation of the fluorescence phenomenon by Jablonski diagram.

luminescent processes in which a molecule or material absorbs light and excited in to higher electronic level. The molecule then relaxes by reemitting the photon from electronically excited state after a given time (**Scheme 1.1.**). By exploiting the features of fluorescence, various techniques have been developed for the analysis and visualization of biological processes in organelles, sub-organelles and cells.

1.3.1.1. Fluorescent probes

Molecules that display fluorescent properties are generally called fluorescent probes or fluorophores or dyes. Due to their versatility, sensitivity and quantitative capabilities, it has many applications in biomedical field. Fluorescent probes can be conjugated to certain targeting ligand and act as a marker for cellular diagnosis.

Mainly, the fluorophores can be classified in to three categories such as small molecule fluorophores, genetically encoded fluorophores and fluorescent nanocrystals. Small molecule fluorophores having low molecular weight are more attracted towards modern science due to smaller in size, bright, hydrophilic nature etc. Most commonly available core structure for small molecular fluorophores are BODIPY, rhodamine, cyanine, tetraphenylethylene (TPE), fluorescein etc. (**Figure 1.1A**). Among various small molecular probes, TPE is the most commonly used chromophore showing aggregation properties and there for it has many applications in sensing and detection of different bio-analytes. Due to its free intramolecular rotation, it is non-emissive in solutions, but emits extensively in aggregated or in the solid state. Owing to its aggregation properties, it has been utilized for the development of chemo-sensors, biological sensors, solar cell light emitting materials etc^{9,10}.

Genetically encoded fluorescent proteins are found in animals. Endogenous proteins include GFP (**Figure 1.1B**), yellow fluorescent protein (YFP), and red fluorescent protein (RFP) are some of the examples for genetically encoded fluorescent proteins. Fabrication of nanocrystals is currently a developing field in nanotechnology and cellular diagnosis. Different nanocrystals have been reported (**Figure 1.1C**) with unique optical properties, in which quantum dots (QDs) and up conversion nanoparticles (UPCNs) are having more advantages over other nano systems. QDs in particular, having broad absorption and distinct emission with high brightness, so target specific quantum dots are important in biomedical field.

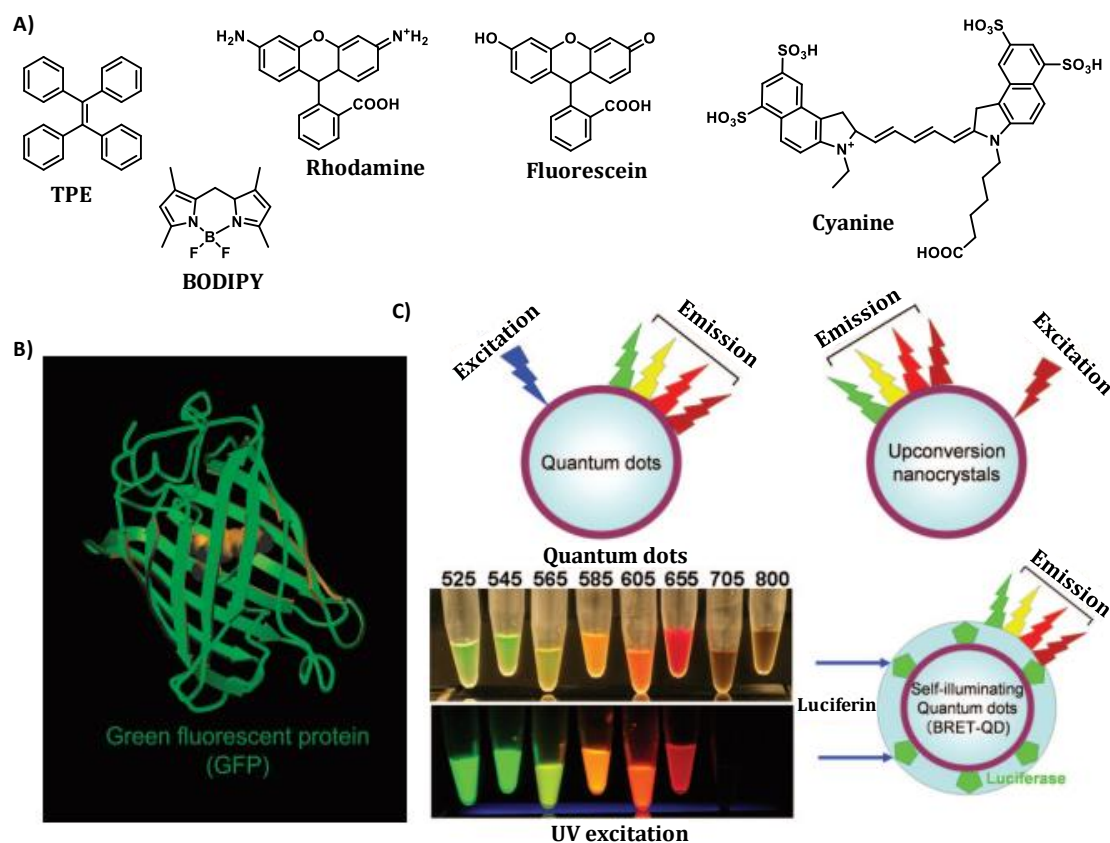


Figure 1.1. A) Small molecule probes with representative cores, B) structure of the green fluorescent protein, C) schematic illustration and emission profiles of nanocrystals. Figures adapted from ref.9&10.

Another category of nanocrystals are up conversion nanocrystals, which can absorb shorter wavelength and emit light at a longer wavelength. These types of nanocrystals are important because of low auto fluorescence and high tissue penetration. Main concern of this type of nanomaterial systems are their inherent toxicity. Size of nanocrystals larger than the renal excretion limit (<6 nm in diameter) showing delayed clearance and are mostly excreted through kidney and liver without any proper metabolism. Targeted nano-systems are developed by conjugating with targeting moieties, which is powerful tool for the treatment of cancer because of the site specific delivery. So major challenge in nanoparticle based targeted systems are to make it as a non-toxic targeted delivery nano-system.

1.3.1.2. Role of fluorescent probes in biomedical applications

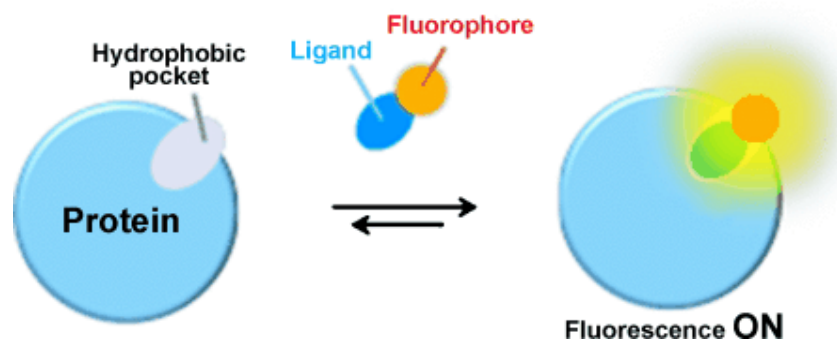
Applications of fluorescent probes in biomedical imaging are promising for analysing molecular events from single live cells to whole animals with high sensitivity and specificity. Targeted molecular probes containing three parts, a signaling part, targeting moiety and a carrier. When the signalling molecules are small in comparison with larger nanocrystals, are more important because of its easy clearance, brightness and easy internalization. So, these types of molecular probe containing optical imaging techniques possessed practical importance in medical diagnosis than other techniques like MRI, CT, radioscope imaging etc. In general, two approaches are available for improving the sensitivity and specificity of the molecular probes are: 1) maximising the target-specific signal, and 2) minimizing the background signal. So the molecular probes having these properties used in optical imaging having more attention towards cellular diagnosis.

1.3.1.3. Fluorescent probes for the sensing of multiple biological analytes

In recent decades, there has been a notable evaluation persisted in the use of small molecular fluorescent probes for the detection of multiple analytes in cellular biology. They hold an attractive potential in the optical imaging field because of their high chemical stability, low molecular weight and excellent penetration capability. Fluorescent probe design has focused on the basis of different rationale named as internal charge transfer (ICT), aggregation induced emission (AIE), aggregation caused quenching (ACQ), Forster resonance energy transfer (FRET), excimer/excimer formation, excited state intramolecular proton transfer (ESIPT) etc. Depending on the mode of fluorescent change during the signaling process, fluorescent probes can be classified into turn-on, turn-off and ratio-metric probes.

1.3.1.3.1. Turn-on fluorescent probes

Development of turn-on fluorescent probes working through chemical reactions activated by analytes has been emerged as a wide area in optical sensing owing to their high sensitivity and selectivity. General schematic representation of turn-on fluorescent probe using an environment sensitive response¹¹ is depicted in **scheme 1.2**.



Scheme 1.2. Turn-on fluorescence occurred by binding a hydrophobic ligand with target protein. Figure is adapted from ref. 11.

Nitric oxide (NO), one of the major signalling molecule plays important role in various biological processes. Lippard *et.al.* synthesized a number metal based small molecular turn-on sensors for the direct and specific detection of NO. They have utilized Co(II), Fe(II), Ru(II), Rh(II), and Cu(II) complexes as turn-on fluorescent probes. Metal based sensors are a promising candidate for the visualization of NO inside the bio organism¹².

In another report, the authors utilized a turn-on fluorescent probe based on coumarin core, **FP-NO** for the detection of NO in biological systems¹³. This probe was synthesized by re-structuring the core part coumarin with a recognition unit, thiosemicarbazide moiety (**Figure 1.2A**).

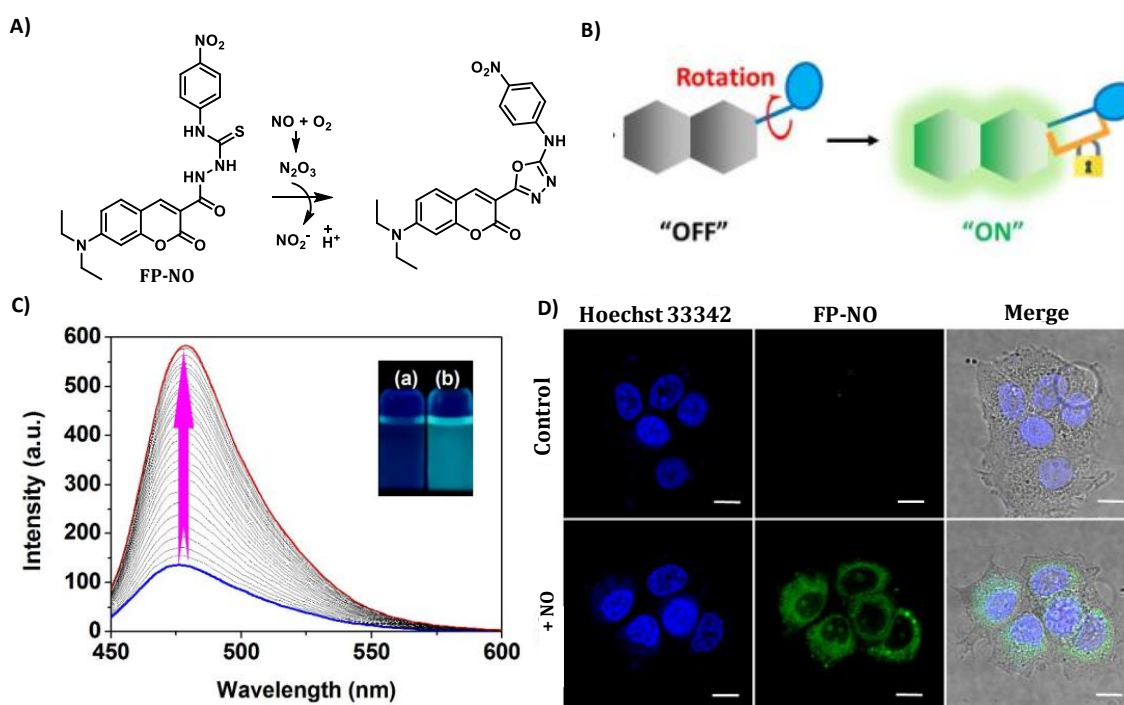


Figure 1.2. A) Structural illustration of the sensing mechanism of FP-NO in presence of NO, B) schematic representation of "OFF" "ON" strategy in coumarin probe based on rotation, C) emission spectra of FP-NO with varying concentration of NO (0-20 μM), D) fluorescence images of MCF-7 cells after treatment with probe and NO. Figure is adapted from ref. 13.

Initially, **FP-NO** was non-emissive due to the free rotation (**Figure 1.2B**) but in the presence of NO, probe become fluorescent by restricting the free rotation (**Figure 1.2C**). A rapid enhancement in fluorescence is evident from **figure 1.2D**, when human breast cancer (MCF-7) cells after treatment with probe and NO.

A dual emission NO detection probe based on pyrene, **PyDA-NP** was reported by Ali and co-workers in 2018. The probe exhibited aggregation induced enhanced emission (AIEE) in presence of water, which further reacts with trinitrophenol leads to the fluorescence quenching. Furthermore, the probe selectively detect NO by ICT mechanism¹⁴ (**Figure 1.3.**). In another report, the authors develop a simple turn-on fluorescent probe based on 1,2,3,4-oxatriazole ring for the detection of NO based on PET. Initially, the probe was non-fluorescent due to PET and in presence of NO in aerated water, PET was blocked and showed enhanced emission¹⁵.

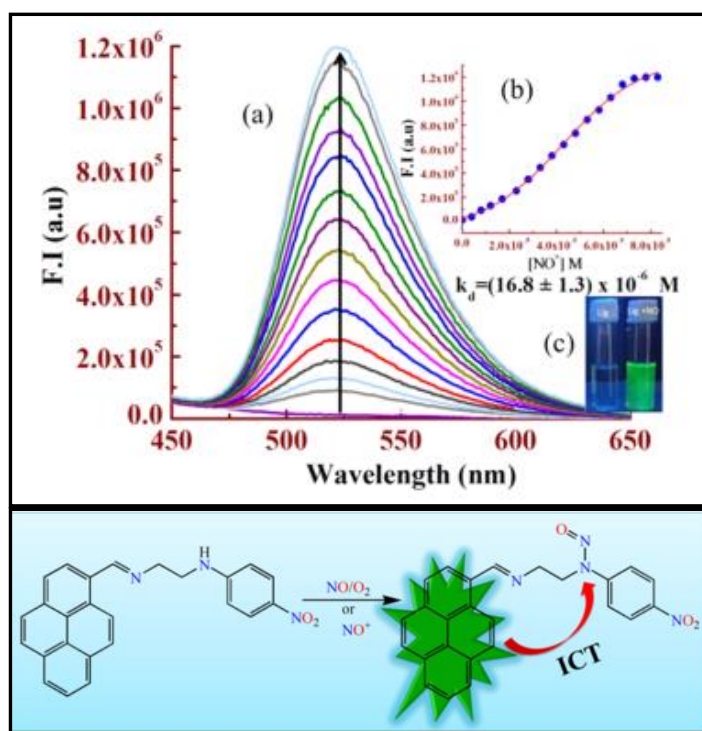


Figure 1.3. Schematic representation showing the NO sensing using the pyrene probe, **PyDA-NP**. Figure is adapted from ref.15.

Hydrogen sulphide (H_2S) is another signalling molecule along with NO and carbon monoxide (CO), which plays significant role in patho-physiological functions in living systems. Small molecular fluorescent probes-based detection methods have recently emerged for the sensing of H_2S in biological systems. Yi and co-workers reported a near infra-red (NIR) fluorescence-based cyanine probe for the detection and visualization of H_2S level in colorectal cancer (**Figure 1.4A**). The probe showed high selectivity, fast response, good water solubility and low toxicity towards biological systems. So, this probe could serve as an efficient tool for the non-invasive *in vivo* imaging of H_2S in living mice¹⁶ (**Figure 1.4B**).

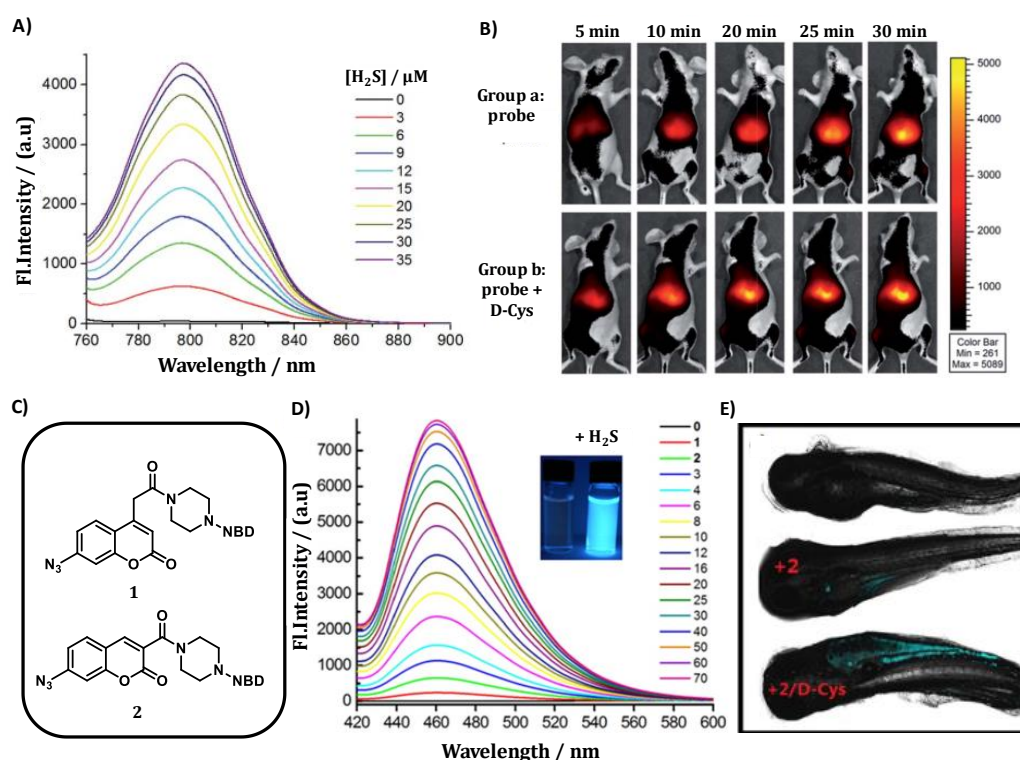


Figure 1.4. A) Fluorescence spectra of cyanine probe (10 μM) with different concentration of H_2S , B) Endogenous visualization of H_2S in living mice after incubation with probe and D-Cys as H_2S donor, C) structures of coumarin based probes 1 & 2, D) Emission spectra of highly sensitive probe 2 (1 μM) with different concentration of H_2S , E) fluorescent images of zebrafish, pretreated with probe 2 and D-Cys. Figure A is adapted from ref.16 & B is from ref.17.

In another report, a set of dual fluorescent probes (**Figure 1.4C**) were synthesized for the detection and visualization of H₂S in cells and zebrafish. Reaction mechanism of the probes include both FRET and ICT. The detection limit for both the probes were less than 30 nM, reveals the excellent sensitivity of the probes towards H₂S (**Figure 1.4D**). So, the authors have successfully utilized probe 2 for the detection and imaging of H₂S in zebrafish model¹⁷ (**Figure 1.4E**).

Chun *et al.* reported a dual response probe for detecting the imbalance of H₂S and viscosity in mitochondria. Probe consist of a dimethylaniline and pyridine moiety, so the initial fluorescence has been quenched due to the free intramolecular rotation. By increasing the viscosity, the rotation is restricted and fluorescence is turn-on in the red region. On the other hand, in presence of H₂S, a fluorescence turn-on is occurring due to the presence of ICT¹⁸ (**Figure 1.5A**).

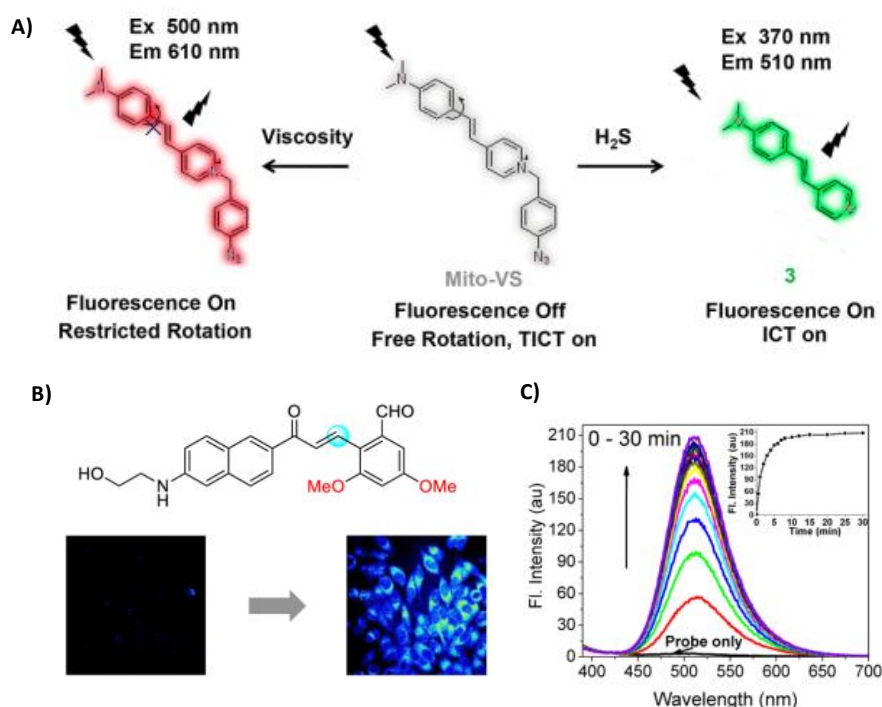


Figure 1.5. A) Sensing mechanism of the probe Mito-VS, B) structure and fluorescence images of HeLa cells before and after incubation with H₂S, C) emission spectra of the probe with varying concentration of H₂S. Figure A is adapted from ref.18 and B& is adapted from ref.19.

In another study, a selective, rapid and biocompatible two photon turn-on fluorescent probe has been developed for the detection of H₂S in living cells (**Figure 1.5B**). The probe was non-fluorescent because of the conjugated aromatic aldehyde system, but in presence of H₂S, formyl group and enone carbon would generate a acedan moiety which is highly fluorescent¹⁹ (**Figure 1.5C**).

In addition to the sensing of NO and H₂S, a number of molecular turn-on probes are available for different sensing applications in cellular biology. Li *et al.* described a series of three small molecular turn-on fluorescent probes (**Figure 1.6A**) for the detection of PDE δ protein in living cells and tissues. PDE δ is the δ subunit of rod-specific Guanosine 3',5'-cyclic monophosphate (GMP) phosphodiesterase. All the three probes showed good fluorescence turn-on in the presence of PDE δ , so they utilized the probes for the imaging of PDE δ protein in the living cell lines: Capan-1 cell line and KRAS dependent MIA PaCa-2 cell line (**Figure 1.6B**). In comparison with other immuno-fluorescent assays or protein based techniques, these probes are more specific towards the detection of PDE δ protein due to its rapid and convenient turn-on mechanism²⁰.

In another study, a thiazole- coumarin based fluorescent probe has been developed for the imaging of cellular DNA. The non-fluorescent probe become emissive after the intercalation of DNA with the probe²¹. Li and co-workers demonstrated a series of small molecular turn-on fluorescent probes for the detection of B-cell-lymphoma-2-gene (Bcl-2) family proteins. Proteins in the Bcl-2 family plays a major role in regulating apoptosis²². The overexpression of estrogen receptor (ER) α is an important biomarker for diagnosis and therapy of breast cancer. In one of the literature study the authors reported a turn-on fluorescent probe for the specific

detection of ER in breast cancer. Their probe contains three parts: emissive fluorophore, fluorescein isothiocyanate (FITC), ER α targeting ligand and a nitroaromatic group for hypoxic response. Due to the presence of nitroaromatic group, the probe was non-fluorescent in normoxic condition but shows high fluorescence after reaching a hypoxic condition²³.

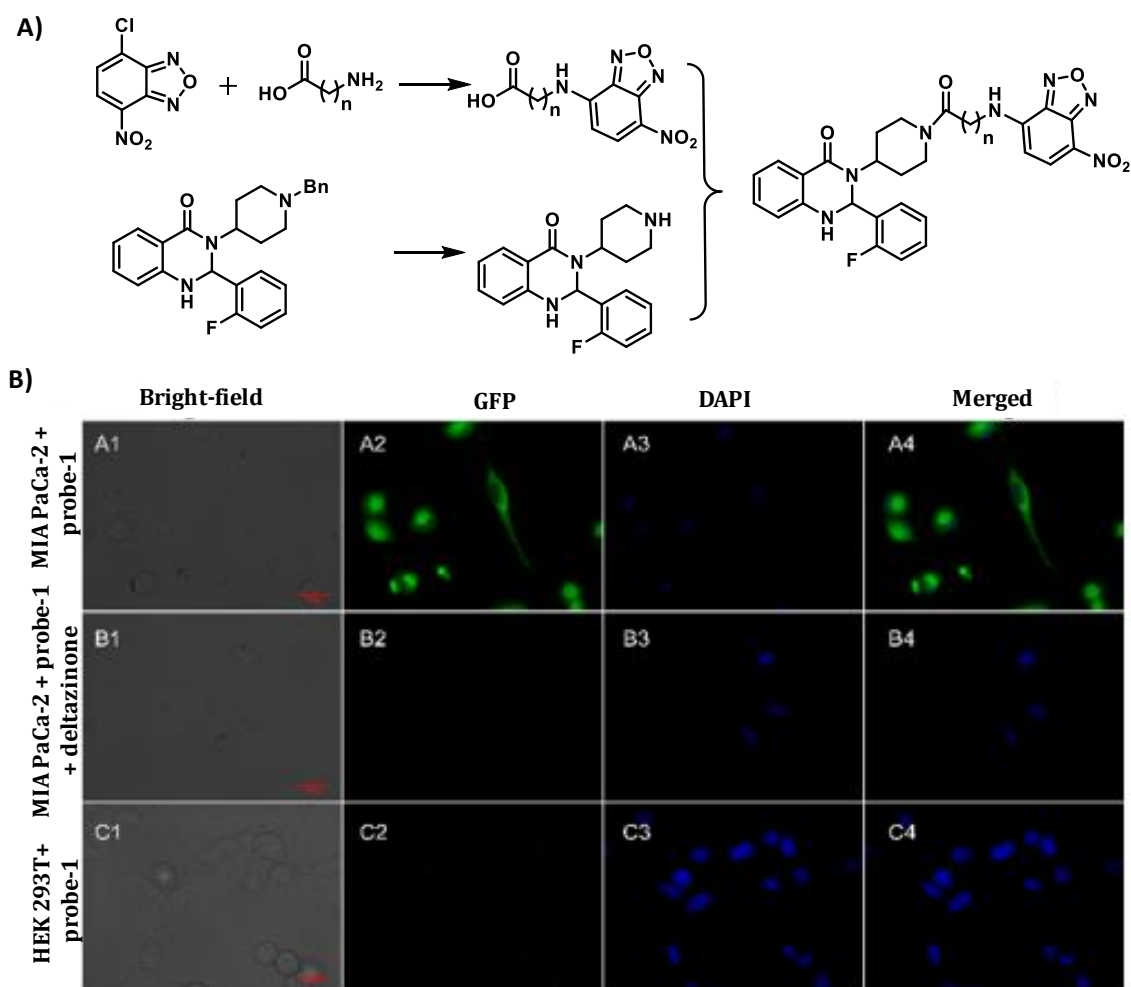


Figure 1.6. A) Synthetic route for small molecular fluorescent probes, B) Fluorescence images of MIA PaCa-2 and HEK 293 cell lines incubated with probe 1 (5 μ M). Figure adapted from ref.20.

Apart from the above mentioned examples, a number of turn-on fluorescent probes has been developed for different sensing applications such as detection of

nitramine and nitro aromatic explosives, detection of Fe^{3+} in water, imaging hERG potassium channel etc^{24,25,26}.

1.3.1.3.2. Turn-off fluorescent probes

These are the probes, which shows maximum intensity in the free state but exhibit a decline in fluorescence upon recognition with target analytes. A large number of turn-off fluorescent probes are available till now for different biological and molecular recognition applications. Kim and co-workers reported a turn-off fluorescent probe based on *N*-methyl-4-pyridiniumvinylcarbazole for the detection of CO in solution. Initially, the probe was highly fluorescent but in presence of CO the fluorescence gets quenched thereby enable the on-site detection of CO. This probe could also determine the CO level in animal blood²⁷ (**Figure 1.7A**).

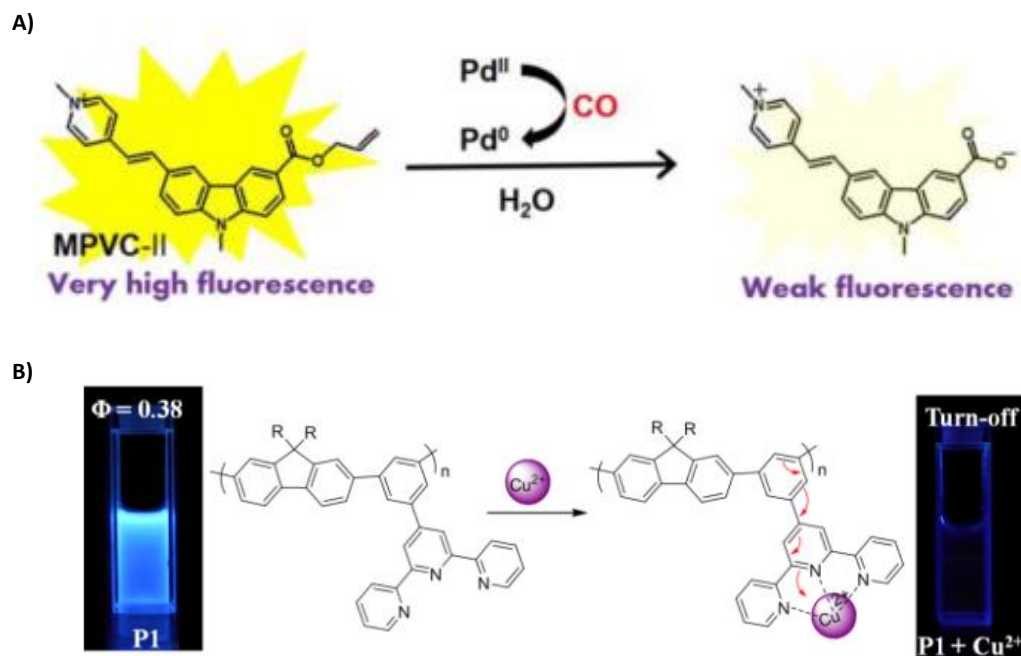


Figure 1.7. A) Pictorial representation of fluorescent off on mechanism towards CO, B) Schematic representation showing the turn-off fluorescent probe for before and after incubation with Cu^{2+} . Figure A is adapted from ref.27 and B from ref.28.

In another work, the authors demonstrated a terpyridyl appended poly(metaphenylene-alt-fluorene) π -conjugated fluorescent polymers for the detection of Cu^{2+} . The probe has blue emission and showed remarkable selectivity and sensitivity towards Cu^{2+} as evident from the turn-off fluorescence (**Figure 1.7B**) in comparison with other metal ions. Probe showed a low limit of detection (LOD) towards Cu^{2+} and found to be 8.4-9.2 ppb. This work reveals that, simple, selective and highly sensitive fluorescent platform for further application in metal ion sensing and other biological analytes detection²⁸. Aliaga *et.al.* described a set of coumarin based turn-off fluorescent probes (**Figure 1.8A**) for the detection of both copper (II) and iron (III) ions and its application in bio imaging.

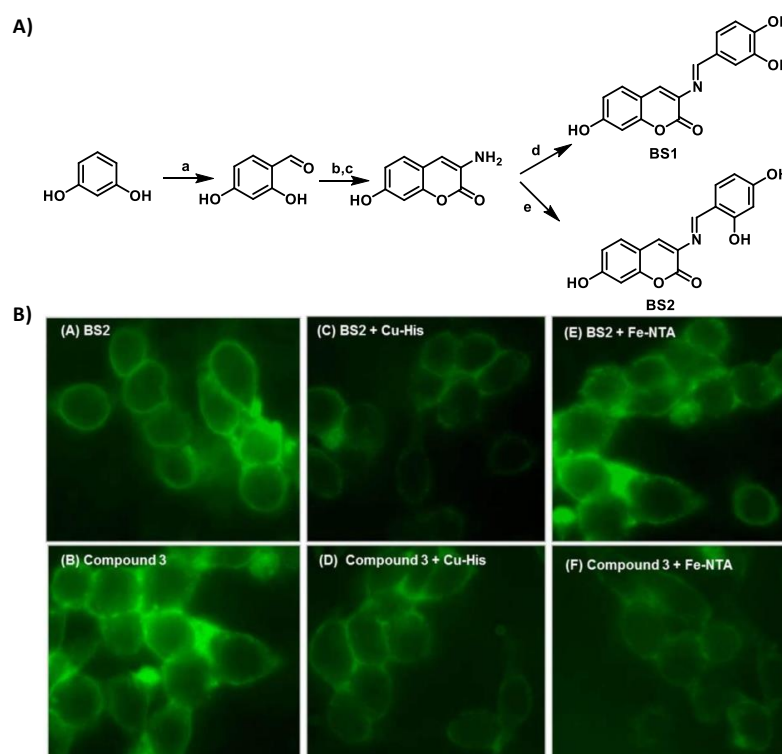


Figure 1.8. A) Synthetic route adopted for the synthesis of probes BS1 & BS2, where, (a) POCl_3 , DMF, acetonitrile, 0–5 °C, 2 h; (b) acetylglycine, acetic anhydride, anhydrous sodium acetate, reflux 4 h; (c) 2:1 HCl/ H_2O reflux, 2 h; (d) 3,4-dihydroxybenzaldehyde; (e) 2,4-dihydroxybenzaldehyde, EtOH, reflux, 4 h B) fluorescent images of SHSY5Y cells treated with probe BS2 and Cu-His as copper generator. Figure adapted from ref.29.

In this study, they have synthesized two coumarin probes and studied their fluorescent sensitivity towards copper (II) and iron (III) ions. Results revealed that both the probes showed excellent sensitivity and selectivity towards these two ions in comparison with other ions. They have checked the applicability of both the probes in living system for the visualization of copper (II) and iron (III) ions²⁹ (**Figure 1.8B**).

In another report, copper (II) was detected using a turn-off fluorescent sensor based on gold nanoclusters. In this study, the fluorescent sensor was synthesized using a lysosome stabilized gold nanocluster, whereas lysosome act as both reducing agent and stabilizing agent (**Figure 1.9A**). This probe showed a particle size of 2.5 ± 0.3 nm and exhibited strong fluorescence in the NIR region. After reacting with different concentration of Cu^{2+} , the fluorescence intensity of the sensor decreased linearly with a correlation coefficient of 0.9976 (**Figure 1.9B**). The probe showed a LOD of 9.00×10^{-9} mol dm^{-3} and displayed excellent selectivity towards copper (II) ions in comparison with other metal ions³⁰.

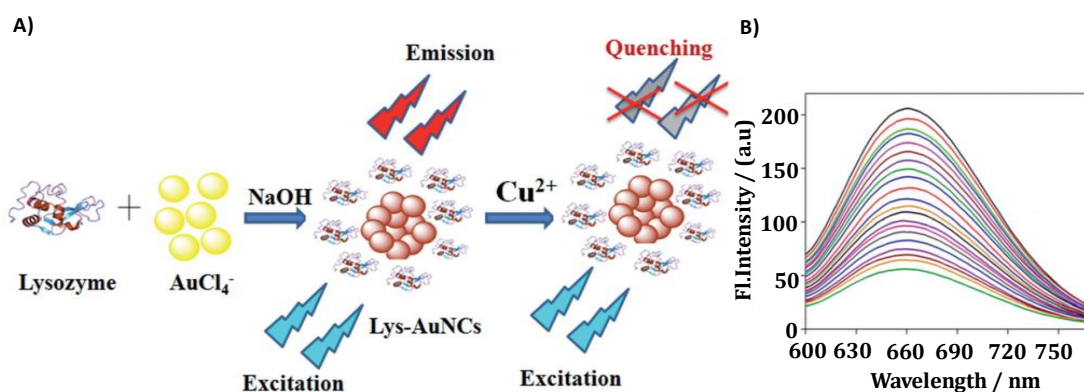


Figure 1.9. A) Schematic representation illustrating the formation of sensor, B) emission intensity of the sensor after reacting with different concentration of Cu^{2+} . Figure is adapted from ref.30.

In another study, a N-doped carbon dot-based turn-off fluorescent sensor was constructed for the detection of ferric ions in water. They have used *Prunus avium*

fruit extract for the green synthesis of sensor and displayed with a size of 7 nm. The sensor showed a bright blue fluorescence at 411 nm upon excitation at 310 nm with a quantum yield of 13% against quinine sulfate as a reference fluorophore. The synthesized probe was used for the selective detection of Fe^{3+} in water through fluorescence spectroscopy. Sensor showed low toxicity and good biocompatibility towards MDA-MB-231 cells and therefore used as a staining probe for bio imaging of the cells³¹.

Manoj and co-workers reported a BODIPY based dual functional turn-off fluorescent probe for the detection of H_2S as well as the visualization of H_2S induced apoptosis (**Figure 1.10A**). The probe exhibited a turn-off fluorescence behaviour towards H_2S , is due to PET from the nitrogen atom to the BODIPY moiety (**Figure 1.10B**). Sensor showed selectivity to H_2S and used for monitoring the H_2S induced cellular apoptosis³².

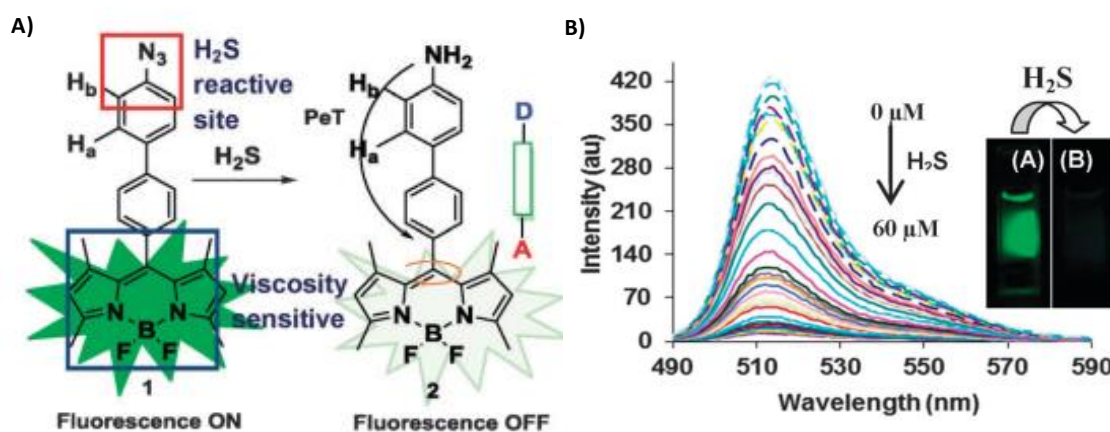


Figure 1.10. A) Design strategy adopted for the synthesis of BODIPY probe, B) fluorescence response of probe towards different concentration of H_2S . Figure adapted from ref.32.

1.3.1.3.3. Ratiometric fluorescent probes

In ratiometric fluorescence, intensities of two or more emission spectra are measured to detect the analytes by monitoring the ratiometric changes in

fluorescence. A ratiometric fluorescent probe is specifically sensitive towards environmental factors like ion concentration, polarity, pH, viscosity etc. Number of strategies like ICT, FRET, ESIPT etc. have been studied in the perspective of ratiometric fluorescence sensing³³.

Qian and co-workers demonstrated a ratiometric fluorescent probe based on coumarin for the detection of endogenous protein vicinal dithiols in cells. Protein vicinal dithiols plays an important role in cellular homeostasis and signaling of cells. Their target probe containing a coumarin and naphthalimide moiety (**Figure 1.11A**) for ratiometric fluorescence response and an arsenic part for the effective binding with vicinal dithiols³⁴ (**Figure 1.11B**).

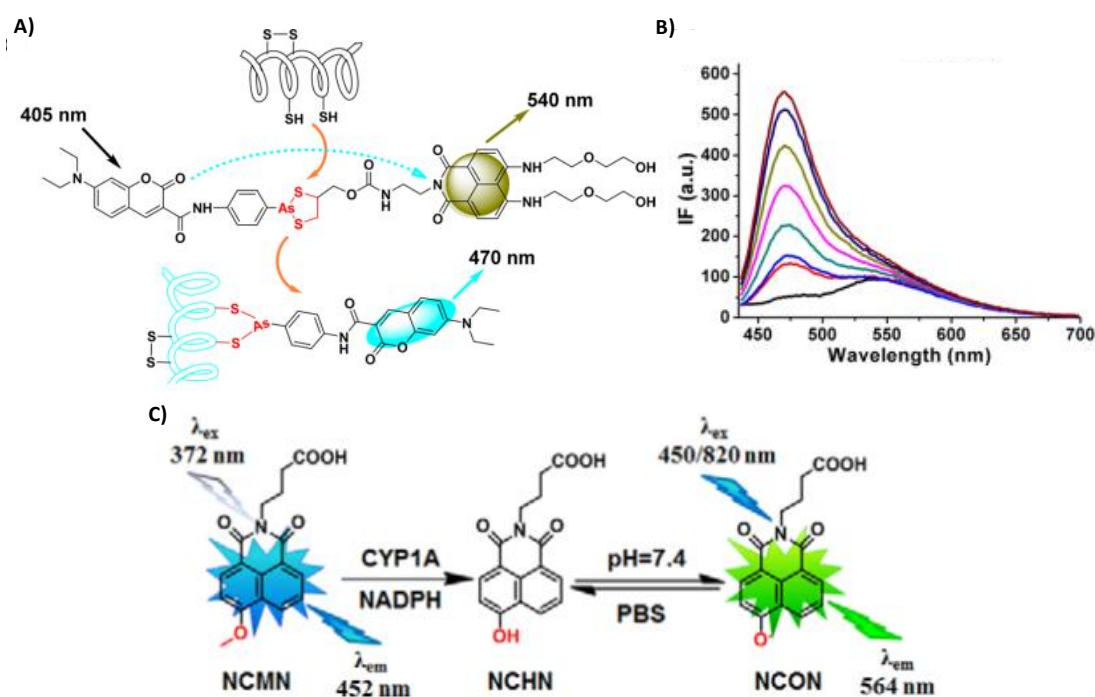


Figure 1.11. A) Chemical structure and ratiometric response of probe towards protein vicinal dithiols, B) naphthalimide probe and its response to CYP1A, C) schematic representation for the detection of NADPH using naphthalimide based probe. Figure A&B is adapted from ref. 34 and C is adapted from ref. 35.

In another report, a ratiometric two photon fluorescent probe was established for the detection and imaging of cytochrome P450 1A (CYP1A). CYP1A is a phase I drug metabolizing enzyme plays a significant role in metabolic activation. They have chosen 1,8 naphthalimide as the fluorophore because of its two-photon absorption properties (**Figure 1.11C**). Their probe displayed significant selectivity, sensitivity and ratiometric response towards CYP1A. Also, they have successfully utilized this probe for two photon imaging of CYP1A in living systems³⁵.

Iyer *et.al.* reported a series of polarity sensitive imidazole based ratiometric probes for the detection of methanol in biodiesel. All dyes exhibited a ratiometric fluorescent behaviour towards methanol is because of the intermolecular hydrogen bonding between methanol and aldehyde. For further application they have utilized these probes to check the methanol content in biodiesel using paper strips³⁶. In another work, a peroxynitrite (ONOO^-) detection has been carried out using a mitochondrion targetable ratiometric fluorescent probe. ONOO^- is a kind of reactive oxygen species and overproduction may lead to pathogenesis of many diseases. In the present study, the ratiometric response of the probe towards ONOO^- is based on FRET phenomenon. The probe applied for the detection of ONOO^- in cellular level and in mouse model (**Figure 1.12A**)³⁷. Tan and co-workers described a two-photon fluorescent sensor for the ratiometric imaging of cells and tissues. The sensor used for this study is based on a naphthalimide moiety directly connected through a rhodamine derivative (**Figure 1.12B**). Ratiometric mechanism of the probe (**Figure 1.12C**) was explained by a newly emerged strategy called through-bond energy transfer (TBET). This novel probe was then applied for the imaging of cells and

tissues. So, their ratiometric sensor provide an effective tool for analysing the biological processes³⁸.

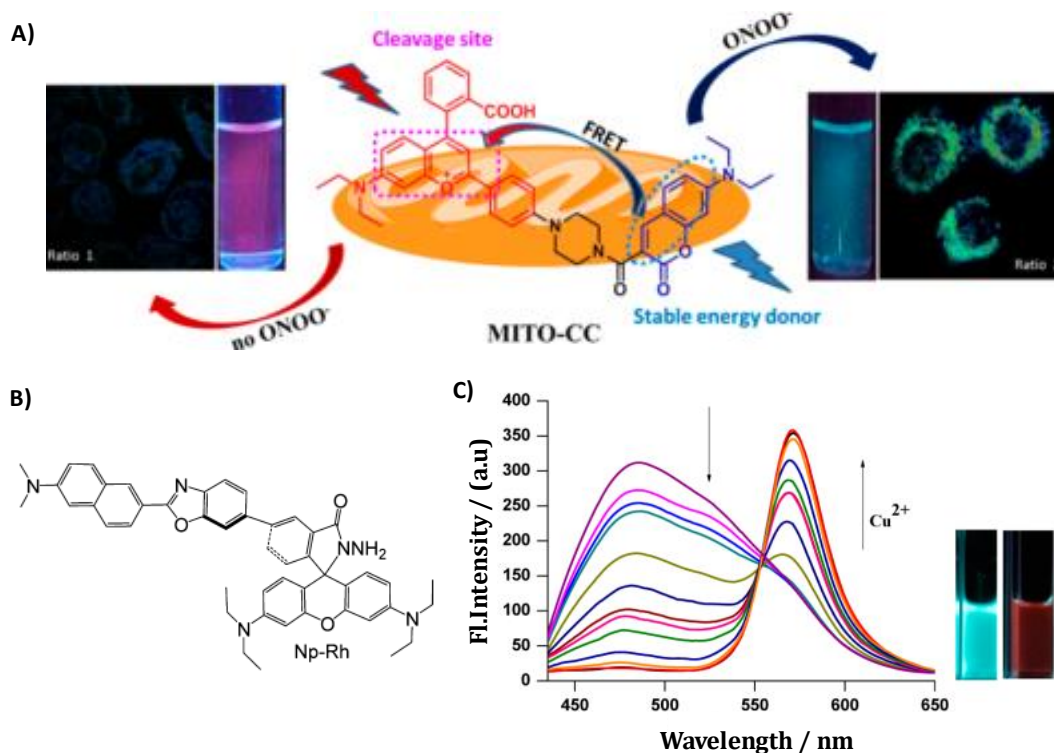


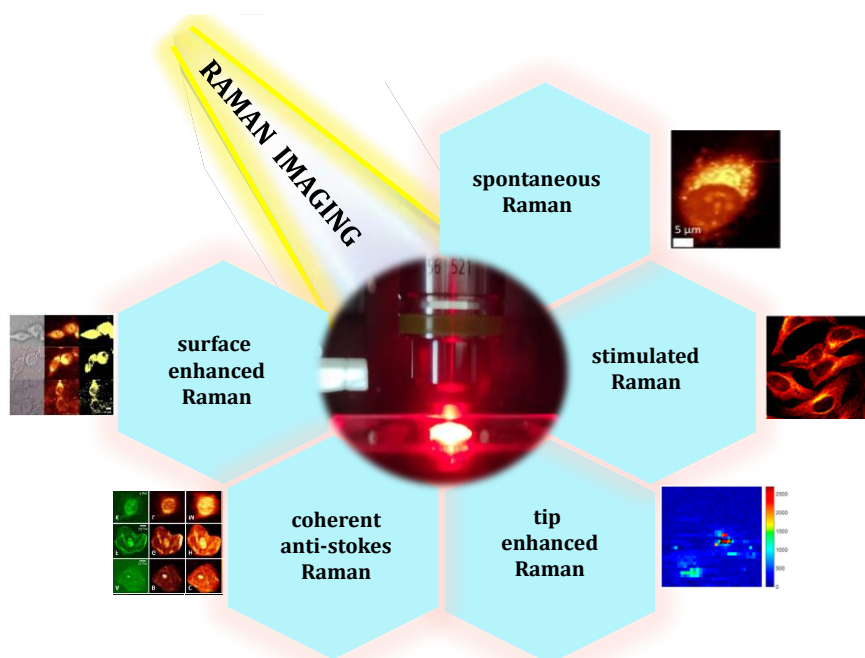
Figure 1.12. A) Structure and working mechanism of the probe in presence of ONOO⁻; B) **Np-Rh** probe for the ratiometric imaging of cells and tissues, C) ratiometric response of the probe in presence of Cu²⁺. Figure A is adapted from ref. 37 and B&C adapted from ref.38.

1.3.2. Raman imaging

Outcomes from each imaging modality has its own distinctive advantages and inherent disadvantages in terms of spatial resolution, selectivity, accuracy and specificity. Since last decade, advanced techniques of Raman scattering extensively practiced in the area of molecular diagnostics, due to its high signal to noise ratio, excellent sensitivity and respectable multiplexing capability which enable to detect ultra-low analytes concentration^{39,3}. Raman imaging is a potent method to generate in depth chemical images based on sample's Raman spectrum. Thus, in cancer diagnosis, it is used to determine the alteration of molecular fingerprints in a cellular

system which underwent disease transformation. So, it is well explored that Raman imaging is an appropriate tool for cancer diagnosis with higher sensitivity and specificity compared with other imaging techniques⁴⁰.

In accordance with the recent studies, Raman spectroscopy is well explored as a highly sensitive analytical and imaging technique in biomedical research, mainly for various disease diagnosis including cancer. In comparison with other imaging modalities, Raman spectroscopy facilitate numerous assistances owing to its low background signal, immense spatial resolution, high chemical specificity, multiplexing capability, excellent photo stability and non-invasive detection capability. There are a number of Raman scattering techniques (**Scheme 1.3.**) are available for theranostic applications: which includes spontaneous Raman scattering (SRS), coherent Raman scattering (CRS), SERS, tip enhanced Raman scattering (TERS), surface enhanced



Scheme 1.3. Schematic representation illustrating different techniques in Raman spectroscopy for imaging.

resonance Raman scattering (SERRS), wild field Raman imaging (WRI), surface enhanced hyper Raman scattering (SEHRS). However, spontaneous Raman is very weak due to small Raman cross section⁴¹ which requires long acquisition time for imaging and diagnosis. So, in recent years, Raman spectroscopy has evolved as a promising technique in biological and medical field, out of which SERS emerged as a new avenue in imaging and cancer diagnosis due to its excellent specificity, selectivity, multiplexing capability etc.

1.3.2.1. Evaluation of SERS and recent developments

SERS is an advanced form of conventional Raman spectroscopy in which incremental enhancement of signal intensity reflected by several orders in the vicinity of nano roughened metal surface. Fleischmann⁴² and co-workers observed the first SERS enhancement of pyridine molecules adsorbed over coarsened silver electrode. This surface enhancement phenomenon was later explained partially by Duyne⁴³ and Creighton⁴⁴. The enormous enhancement was generated by strong light-induced electric field at specific positions in metallic nanostructure called hot spots. Exponential growth of nanotechnology together with emergence of various SERS active substrates improved the sensitivity of the technique assuring to detect single molecular level. The enhanced specificity, high sensitivity and ease of sample preparation makes SERS prior over other technique in biomedical application. Apart from other biomedical technique SERS is capable of producing images using specific mapping of Raman spectral data without any photo bleaching³.

1.3.2.2. Enhancement factor and Hotspot generation

Enhancement factor (EF), is one of the significant term used for explaining the efficiency of SERS effect. There are many documented methods for calculating SERS-EF based on varying degree of complexity, such as with modest calculations of the

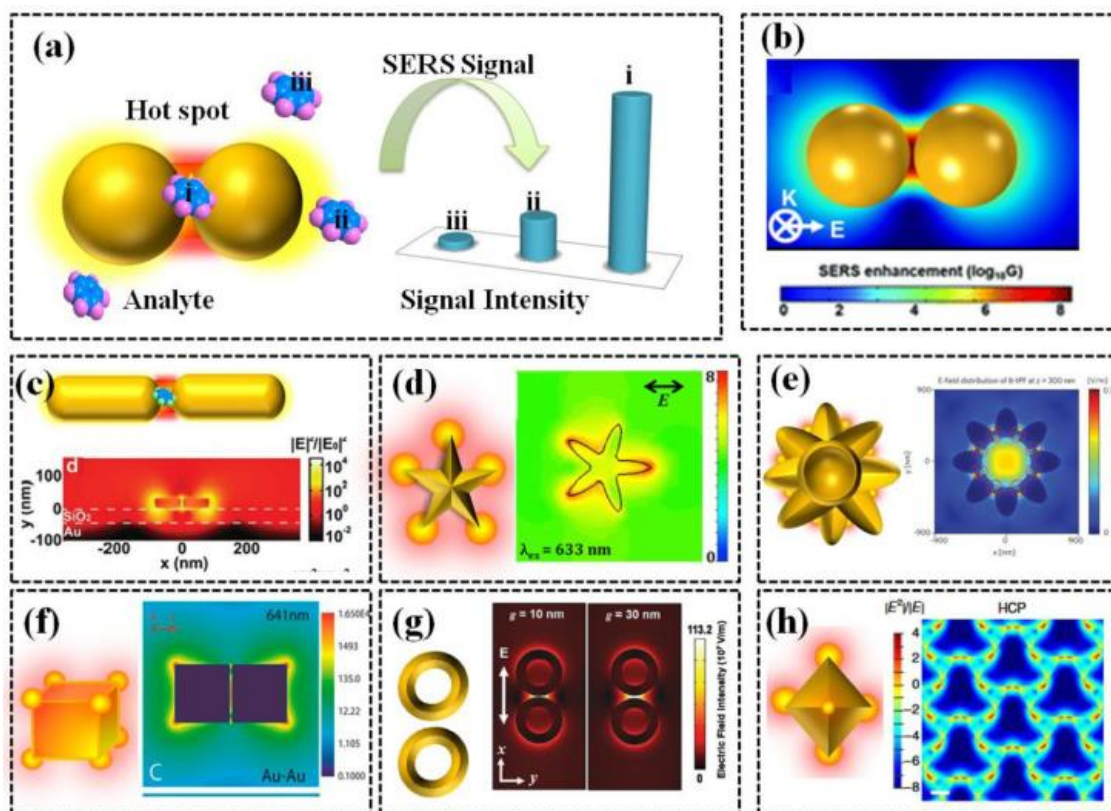
Raman intensity change with nanoparticles (NPs) to several complex procedures calculating minute details such as surface area of NPs, number of analytes per NPs, and much more. Inaccurate measurement of EF will not present information regarding the reproducibility of the substrate, molecule-metal interaction, analytes specificity etc. Hence, a properly co-ordinated approach considering precise and minute details with accuracy is highly appreciated. In general, SERS-EF is a culmination of the increased Raman intensity due to electromagnetic (EM) and chemical enhancement mechanism. On an average, the observed maximum EFs in SERS are in the order of $10^7 - 10^{10}$ in most cases and can go up to 10^{12} in rare conditions wherein the EM enhancements may contribute up to $\sim 10^{10}$ and the rest will be filled by chemical enhancement⁴⁵. A simple and honest approach for the averaged SERS-EF calculation may be illustrated as follows:

$$EF = \left(I_{SERS} / N_{\text{surface}} \right) / \left(I_{RFM} / N_{\text{bulk}} \right)$$

where, I_{SERS} and I_{RFM} – Raman signal intensities from SERS and free molecule,

N_{surface} and N_{bulk} - The number of molecules on the NP surface and bulk

The creation of localized plasmonic fields on the photoactive molecule present on the surface of metal structures by excitation with laser is referred to as hotspots. The incremental increase in the Raman signal is directly related to field intensity and molecular binding on close proximity of hot spot, which allows the fabrication of molecular probes with promising properties. Hotspots can be generated by the assembly of NPs such as spheres, rods, cubes, bars etc. and also by creating inter and intra nano-gap^{46,47} (**Scheme 1.4**) by purposefully tuning NPs.

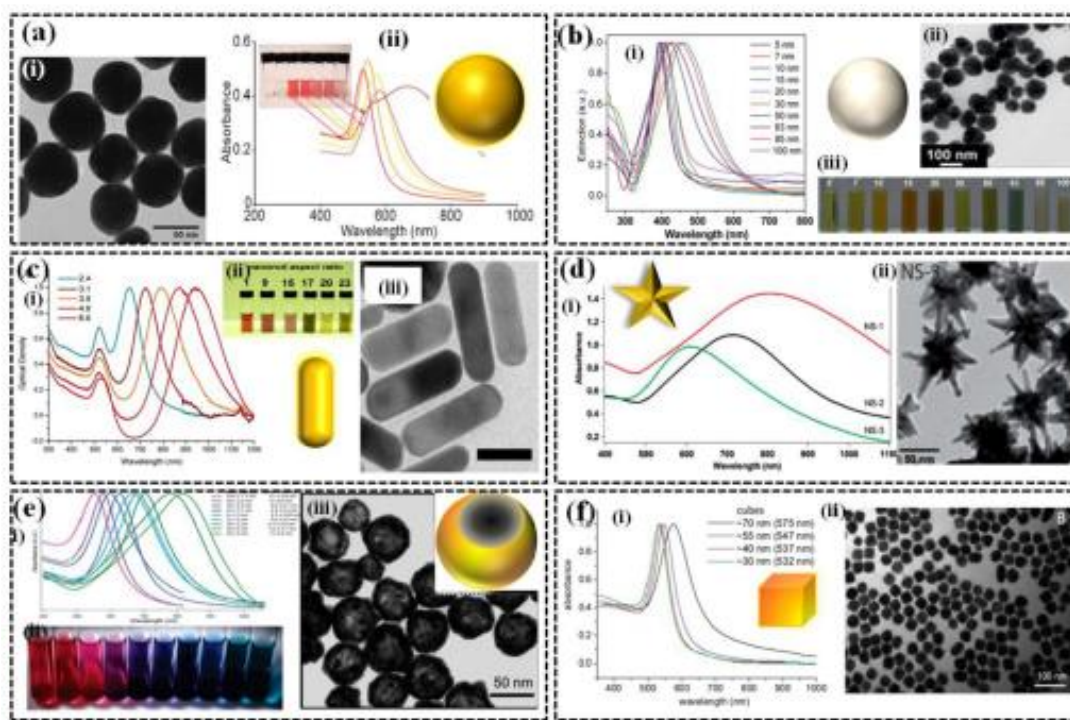


Scheme 1.4. Schematic representation of hot spot in between two NPs and corresponding SERS intensity.

1.3.2.3. SERS substrates

SERS substrates are molecules which enhances the weak Raman signal to several orders of magnitude. Commercially available SERS substrates are based on silver, gold and copper surfaces. The localized surface plasmon resonance (LSPRs) of these entire metal NPs span visible to NIR wavelength range, making them convenient for Raman measurements. Typically, SERS substrates are mainly classified in to three categories: 1) colloidal metal nanoparticle solution, 2) colloidal solution immobilized in solid substrates and 3) nanolithography and template-based substrates⁴⁸. Gold nanoparticles (AuNPs) are mostly exploited as SERS substrates to amplify the Raman signatures of the analytes which would otherwise remain undetectable owing to their lower Raman cross-sections. Researchers are striving to design new plasmonic materials and also to optimize the structure and configuration of existing SERS

substrates to maximize the enhancement efficiency. Concurrently, a wide array of SERS substrates were fabricated like gold and silver nanospheres (**Scheme 1.5.**)



Scheme 1.5. Common types of SERS substrates used in Raman spectroscopy

1.3.2.4. SERS nanoparticle tags

SERS nanotags, a nano construct widely used for the precise detection of biomolecules. Typically, SERS nanotag contains a substrate to enhance the Raman signal, Raman reporter molecule for identification and a targeting motif for specific biomolecular detection⁴⁹ (**Figure 1.13.**). Molecular fluorophores and dyes are commonly used Raman reporter molecules. These SERS nanotags provide unique optical properties in SERS analysis in comparison with other fluorescent techniques due to multiplexing analysis for target specific detection, single laser excitation wavelength, high photostability and quantification using the SERS fingerprint.

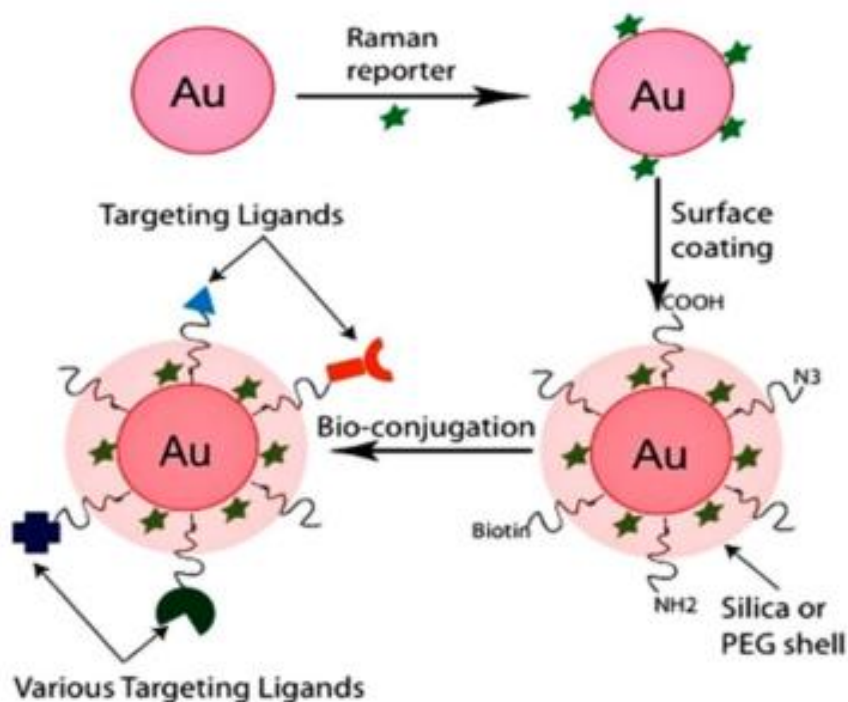


Figure 1.13. Schematic representation of SERS nanotags: consists of a Reporter molecule attached Au substrate, a PEG layer for stabilization and a target. Figure adapted from ref.49.

1.3.2.5. SERS nanotags for diagnosis and imaging

The high specificity, minimal sample volume and integration of advanced technologies improved the enormous applications of SERS in the qualitative and quantitative detection of a wide array of diseases. Most biomolecules are Raman active to provide distinctive fingerprint signals according to their occurrence and abundance. The minute changes due to a disease condition will be reflected in its characteristic Raman peak from biomolecules, organelles, cells or tissues and can be analysed and distinguished. An ultrafast, sensitive and quantitative diagnosis for the early detection of serious disorders is desirable for achieving improved therapeutic outcomes. Tracing of molecular events demands detection of very low quantities of biomolecules which makes diagnosis a challenging process⁴⁹.

SERS imaging, which combines Raman scattering with optical imaging techniques, is a promising method which can unravel the spatial distribution of a particular type of analyte in a heterogeneous environment. The basic principle of SERS imaging is the separation of the Raman scattered photons corresponding to the characteristic signal from the SERS spectrum of a particular analyte to obtain the spatial distribution of the analyte.

A potentially valid methodology for the selective and sensitive monitoring of intracellular H_2S was developed⁵⁰ by functionalization of AuNPs with 4-acetamidobenzenesulfonyl azide (4-AA) (**Figure 1.14A**). In the presence of H_2S , the azide groups present in 4-AA gets converted into amino groups which cause spectral

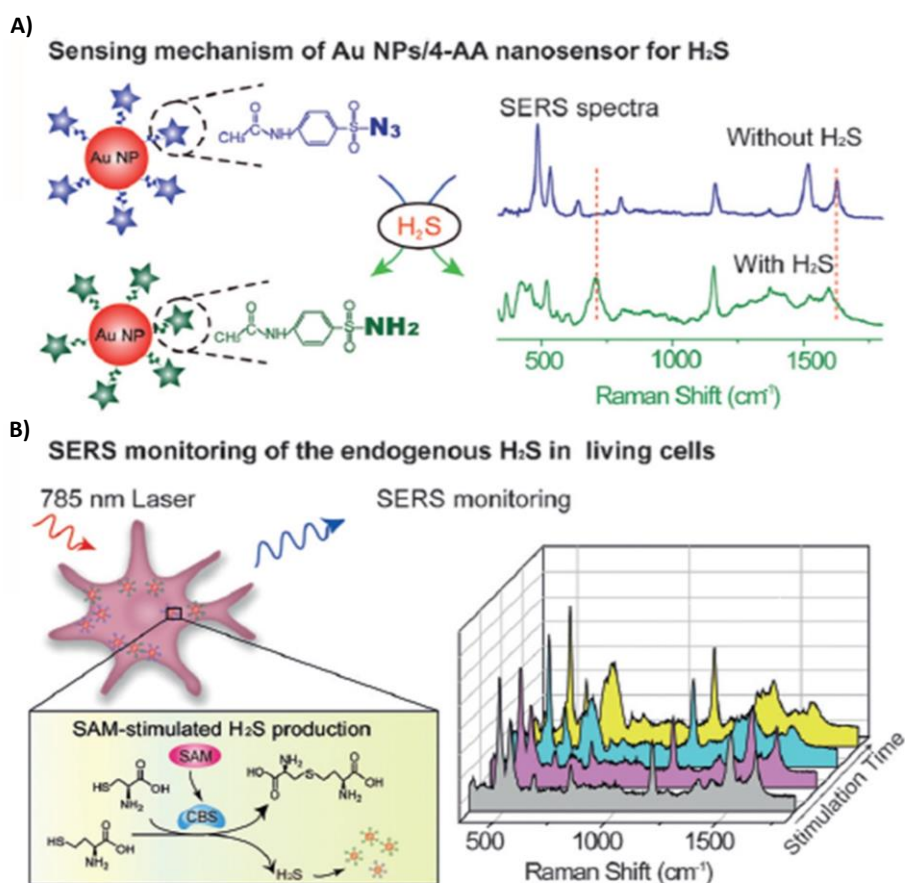


Figure 1.14. A) Schematic representation of SERS nanotag for the detection of H_2S , B) sensing of H_2S inside the living cells using the nano sensor. Figure is adapted from ref. 50.

changes in the SERS spectrum, thereby facilitating the rapid and accurate sensing of H₂S (**Figure 1.14B**). The authors further demonstrated the suitability of their nanoprobe in the real-time detection of H₂S generated under S-adenosyl methionine (SAM) stimulation in glioma cells which supported the activating effect of SAM on the production of H₂S by the cystathionine b-synthase dependent pathway.

Li and co-workers reported a SERS nano sensor for the detection of NO and ONOO⁻ in living cells. Their nanotag contains AuNPs as SERS substrate and a novel Raman reporter molecule 3,4-diaminophenylboronic acid pinacol ester for sensing.

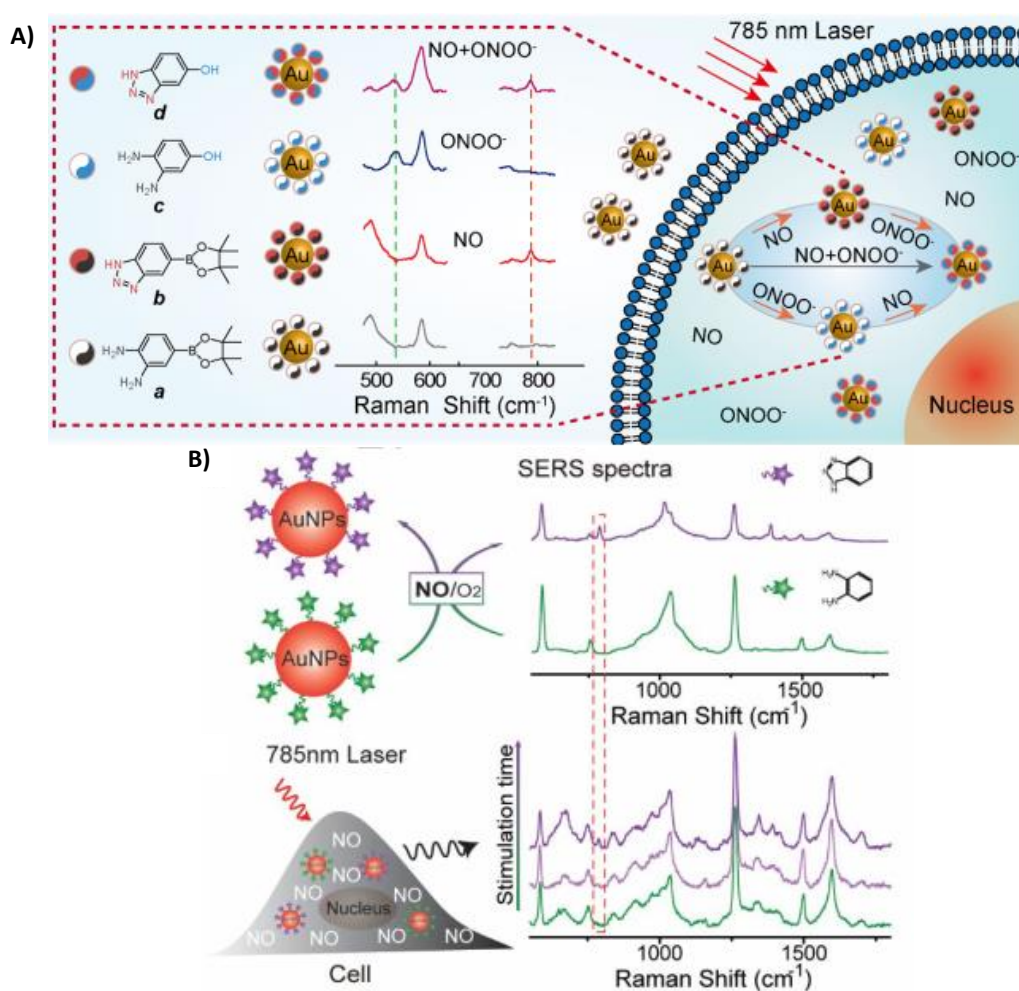


Figure 1.15. A) Pictorial illustration of SERS nano sensor for the detection of NO and ONOO⁻ in cellular level using SERS technique, B) schematic representation of SERS nanoprobe for the endogenous sensing of NO through SERS. Figure A is adapted from ref. 51 and B is adapted from ref. 52.

The simultaneous detection of both the analytes was achieved by the nano sensor using 785 nm laser. Results showed a shift in fingerprints of the Raman reporter after detection with NO and ONOO⁻. Nano sensor displayed excellent specificity, SERS sensitivity and selectivity towards these analytes and further used for the intracellular detection (**Figure 1.15A**)⁵¹. In another report, authors established a SERS nanoprobe for the endogenous detection of NO in living cells. In this study they have utilized a o-phenylenediamine (OPD)-modified AuNPs for achieving the low-level detection. In presence of NO, the diamine part in OPD molecule become transferred to triazole moiety, resulting a SERS change in the SERS nanoprobe (**Figure 1.15B**)⁵².

A palladacycle based SERS probe was reported for carbon monoxide detection in HeLa and human liver cells⁵³. The sensing strategy involves the carbonylation of AuNPs bound palladacycle reporters which in turn causes the removal of the palladium constituent thereby resulting in a carboxylic acid group producing distinct SERS spectral signatures (**Figure 1.16.**). The presence of carbon monoxide-releasing molecules under *in vitro* conditions was effectively detected using this approach.

In single plex detection of biologically relevant analytes, Raman reporter molecule is used to label the reference biomolecule and there by allows the sensing of molecule from SERS fingerprint of Raman reporter molecule. Chang *et al.* reported triphenylmethine dyes as novel candidates for SERS analysis and imaging. Triphenylmethine were recognized for sensitive biological detection as the signal intensities were superior to commercially available crystal violet dye⁵⁴. The same group has developed another two SERS-tags by using triphenylmethane and lipoic acid derivatives of cyanine dyes for multiplexed detection of cancerous cells.

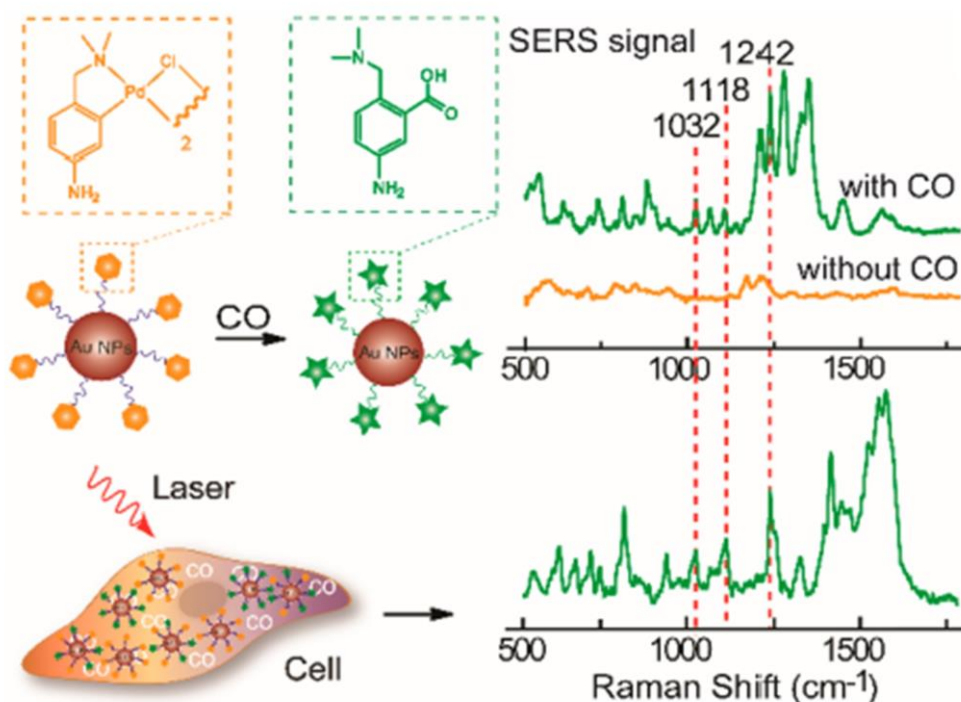


Figure 1.16. SERS based CO sensing using palladacycle based nanotag. Figure is adapted from ref. 53.

These tags were coated with PEG for enhancing the biocompatibility and further were conjugated with anti- Epidermal growth factor receptor (EGFR) and anti- Human epidermal growth factor receptor-2 (HER2) antibodies which selectively detected cellosaurus cell line (OSCC) and human breast cancer cell line (SK-BR-3) cells respectively using SERS imaging⁵⁵.

The systematic use of two Raman reporters, 5,5'-dithiobis-(2-nitrobenzoic acid (DTNB) and 4-mercaptobenzoic acid (4-MBA), Wu *et al.* demonstrated the simultaneous detection of p21 (cyclin-dependent kinase inhibitor) and p53 (tumor suppressor) proteins⁵⁶ (**Figure 1.17.**). The NR functionalized with reporter molecules and target specific antibodies were utilized for the quantification and identification of p53 and p21 which could be useful in early cancer predictions. Later, the same work was extended with a SERS based immunoassay constructed using a 3D

barcode chip for the high-throughput multiplex analysis of protein biomarkers⁵⁷. In this approach, multiple proteins from diverse specimens were segregated by a microfluidic device which is built with specific antibody patterns, so that it may facilitate the composition of a 2D hybridization array in the presence of target analytes. This novel strategy was exploited for the multiplex analysis of human IgG, mouse IgG, and rabbit IgG by utilizing the distinct Raman signals of 4-MBA, DTNB, and 2-naphthalenethiol (2-NAT) respectively.

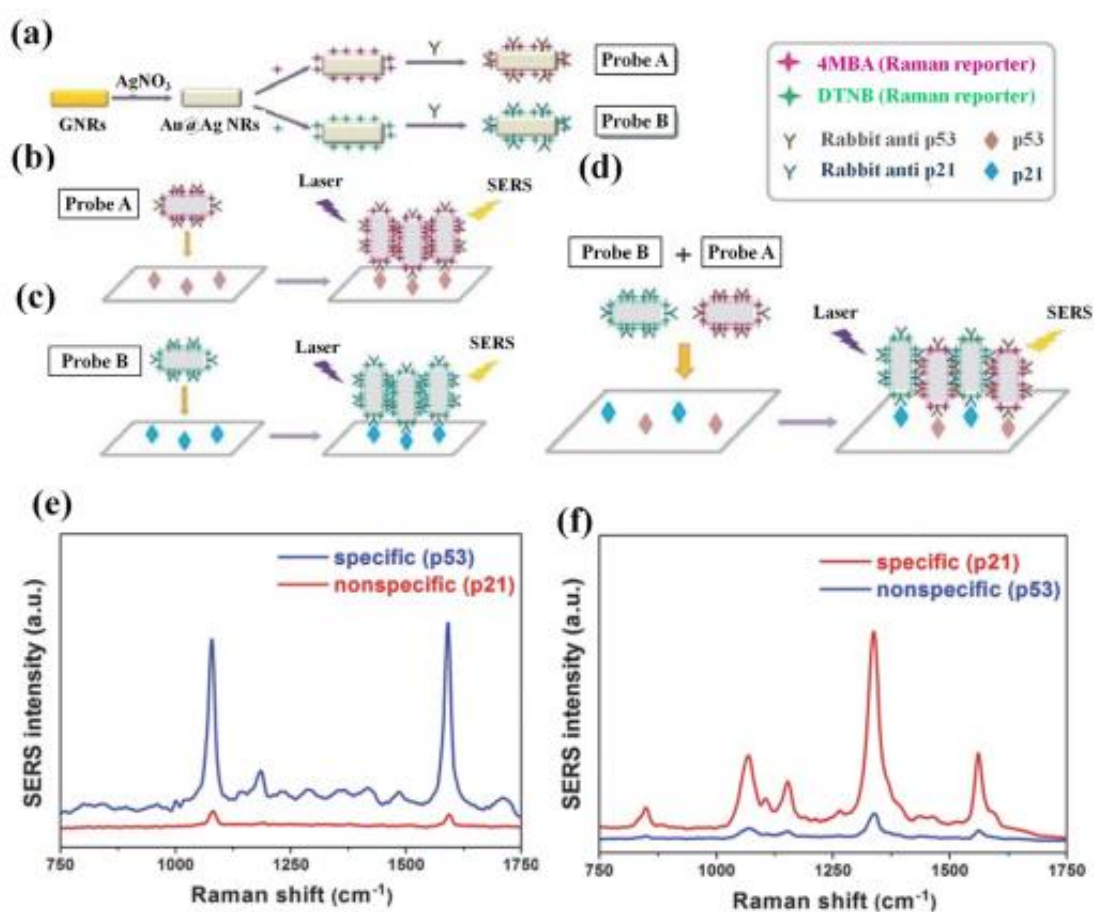


Figure 1.17. Scheme describing the fabrication of SERS probes constructed using Au@AgNRs functionalized with 4MBA and DTNB. Figure is adapted from ref. 56.

1.4. Recent development of nano-theranostic systems for nanomedicine

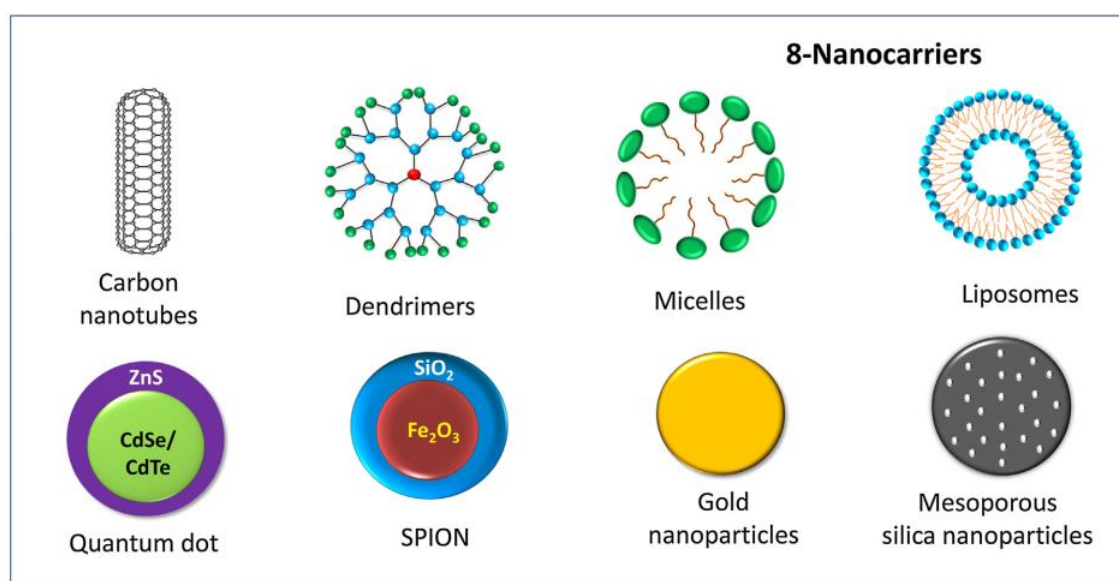
Nano-theranostic is emerging as a promising therapeutic paradigm in the development of nanomedicine which combines specific targeted therapy based on distinct diagnostic monitoring. Many direct and indirect methods were developed to study the molecular changes taking place inside the cells during therapy. Chemotherapy, photodynamic therapy (PDT), photo thermal therapy (PTT) and radiation therapy, surgery are among the most widely employed cancer treatment options⁵⁸. All these therapies cause damages to normal cells or tissues during the time of drug administration or light eradication. So, nanotechnology offers to target chemotherapies towards specific cancer cells, thereby reduce the damage near normal cells. Nanotechnology has been well explored for the therapy of diseases due to its excellent sensitivity, selectivity and specificity.

The term chemotherapy in a broad sense is used to refer the treatment using a drug or combination of drugs. Chemotherapeutic drugs can be synthetic or natural and are a powerful weapon to stop or decelerate the growth of cancer cells. Commonly used anticancer drugs kill cancer cells mainly by interacting with DNA and in general, they can be classified as either reactive or interactive. In the former case, pharmacological activity relies on the reaction between the drug and a target molecule, so the hybrid adducts hinder the cellular progression which leads to cell death. However, the interactive drugs interfere with cellular pathway which relies on lock and key recognition process. Cancer cell-drug interactions leads to a significant number of possible cellular responses like apoptosis and acquired drug immunity⁵⁹.

The limitations of conventional chemotherapy were overcome using the introduction of targeted drug delivery systems.

1.4.1. Nano carriers for targeted drug delivery

In order to overcome the adverse side effects of chemotherapeutic agents used, targeted delivery of drugs with the aid of NPs based drug carrier systems was employed. These types of systems offer localized, efficient, targeted drug transportation and drastically reducing the potential side effects. Drugs can be placed either on the surface or interior of NPs via either non-covalent or covalent bonds, depending on the assess ability of functional groups of the drugs and the nanocarrier.



Scheme 1.6. Different types of nano carriers in targeted drug delivery system.

NPs are taken up at the tumor site by endocytosis, and the release of the drug inside the cancer cell can follow by different mechanisms, including pH change, heat, redox reaction, and enzymatic or protein actions⁶⁰. Particles with size between 1-100 nm is called nanoparticles. Most commonly used eight nano carriers are carbon nanotubes (CNTs), dendrimers, micelles, liposomes, QDs, super paramagnetic iron oxide

nanoparticles (SPIONs), AuNPs and meso-porous silica nanoparticles (MSNs) **(Scheme 1.6)**.

1.4.2. SERS based nano-carrier system for theranostic application

The fingerprint information in Raman spectra could be utilized for the better understanding of the time-resolved biochemical changes in cells towards different treatments. Raman spectroscopy was purposefully explored to detect molecular changes in response to different treatments on the cells, causing specific time dependent biochemical changes associated with the process of cell death as well as cellular changes at different time points in the cell cycle. So due to the unique characteristics of high sensitivity, accurate Raman fingerprinting, and rapid detection capability without complicated sample preparation, SERS was employed as effective tools to detect DNA, small biomolecules, and proteins⁶¹.

In SERS, the drug molecule is adsorbed to NPs and these structures support SPRs, which may cause an enormous increase of the near-field excitation intensity at the vicinity of the adsorbed molecule. In addition, NP-drug interaction leads to the quenching of fluorescence through non-radiative relaxation via the NPs surface, so the Raman fingerprint intensity of the molecule is increased by chemical enhancement. In this section, SERS aided nano-carriers has been described for effective delivery of chemotherapeutic agents. Most commonly used nano carrier systems is based on AuNPs, AgNPs and MSNs.

1.4.2.1. Gold nanoparticle based nanocarrier systems

The wide spread use of AuNPs in drug delivery systems is due to its unique physical, chemical and mechanical properties ideal to make it right vehicle for drug delivery. In 2010, El-Said *et al.* reported a procedure with gold nanoflower (AuNF) array on an indium tin oxide (ITO) substrate to study the fate of cancer cells upon administration of chemotherapeutic drugs by SERS analysis (**Figure 1.18A**). This approach was effective enough for the ultra-low level detection of the chemotherapeutics like hydroxyurea, 5- fluorouracil, and cyclophosphamide on hepatocellular carcinoma cells (HepG2) due to the high sensitivity of AuNF substrates⁶²(**Figure 1.18B**).

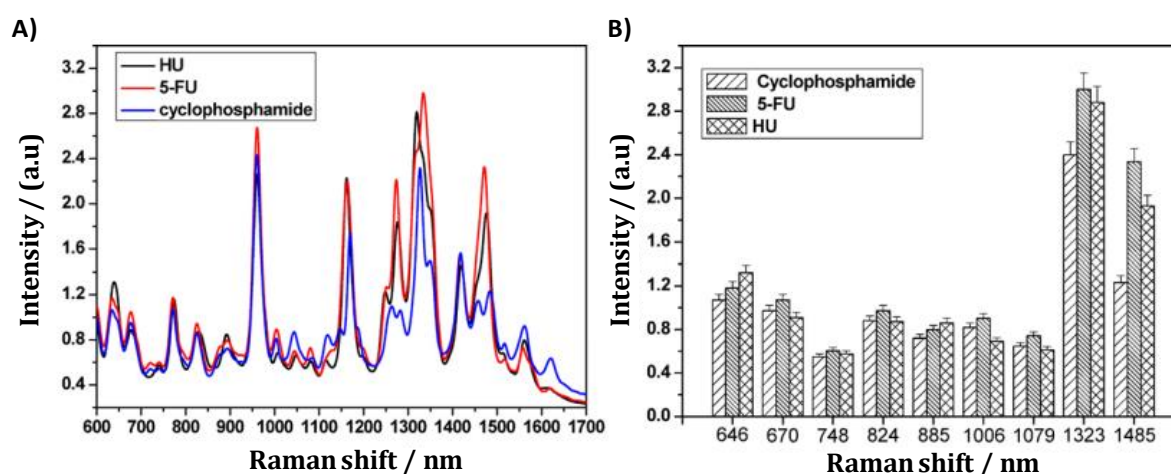


Figure 1.18. A) SERS spectra obtained from HepG2 cells after treatment with hydroxyurea, 5- fluorouracil, and cyclophosphamide, B) changes obtained by Raman peak of cells after treatment with drug molecules. Figure is adapted from ref.62.

Later on, the same group developed an excellent approach, plasmonic-tuneable Raman/fluorescence imaging spectroscopy for tracking the intracellular release of doxorubicin (Dox) from AuNPs in real-time manner (**Figure 1.19A**). They illustrated the ability of AuNPs in tuning Raman and fluorescence intensities of Dox molecules in order to enable a selective switch ON and OFF mechanism. This technique could be

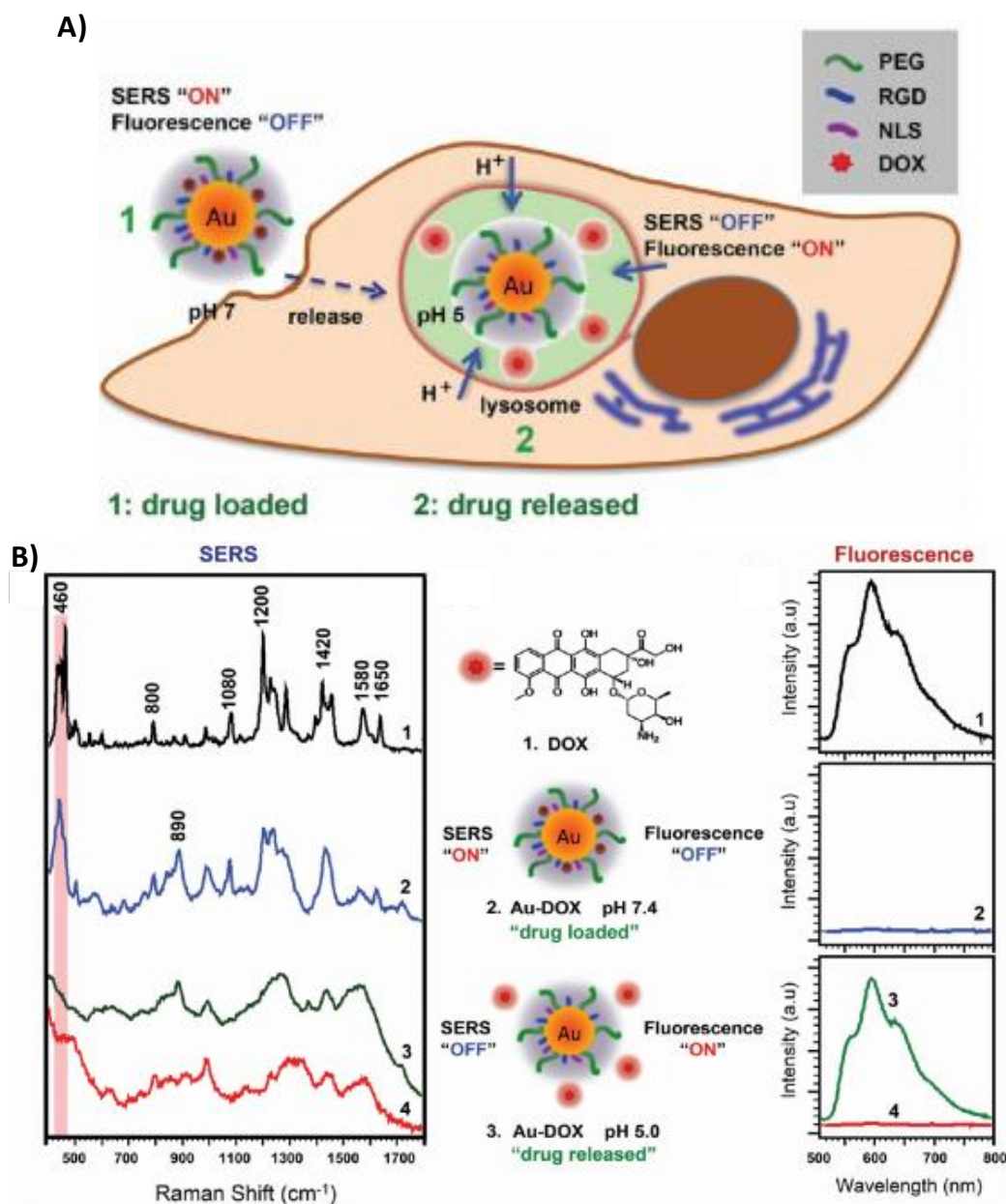


Figure 1.19. A) Pictorial representation of Dox release from the carrier system by SERS and fluorescence, B) SERS spectra and fluorescence spectra of released Dox from the construct and the chemical structure and representation of the delivery system. Figure is adapted from ref. 61.

more engineered as a practical tool for illustrating the cellular response to drug action⁶¹ (**Figure 1.19B**). In a recent report, non-invasive monitoring of drug release from the nanocages was demonstrated using SERS. Here, the authors demonstrated a gold nanocage based nanocarrier system for the release of Dox with external trigger such as light or ultrasound. The usage of biocompatible phase change material, called

1-tetradecanol, act as a gate keeper to manage the release of Dox in response to an external stimulus. This simple yet powerful technique endeavoured with the ability for the real-time noninvasive monitoring of drug release kinetics⁶³.

1.4.2.2. Silver nanoparticle based nano carrier systems

Among different plasmonic NPs, silver nanoparticles (AgNPs) are attaining substantial interest due to their good physicochemical qualities such as optical and magnetic polarizability, antimicrobial behaviour, catalysis, electrical conductivity, and are revealed to be a good SERS substrate. Srinivasan and co-workers reported a

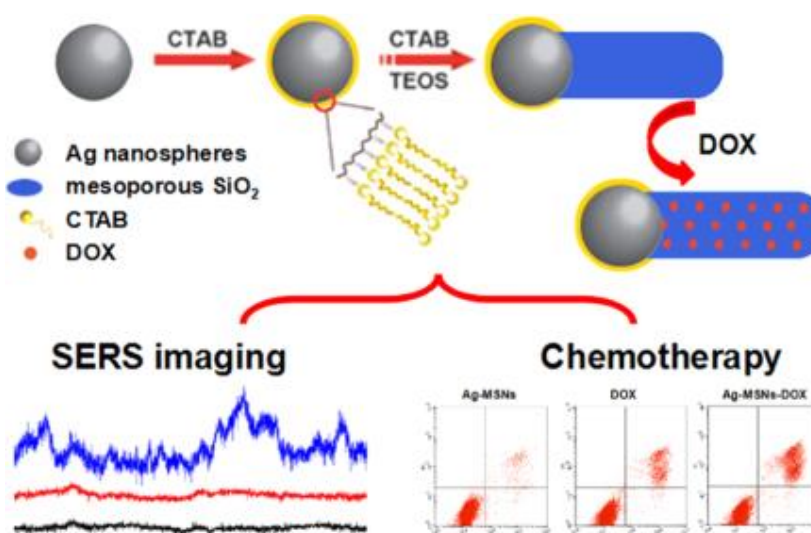


Figure 1.20. Schematic representation showing the synthesis of janus-mesoporous silica nanocomposite and their therapy monitored by SERS and fluorescence. Figure is adapted from ref. 65.

multifunctional anti-cancer prodrug system based on AgNPs wherein the NPs were conjugated with folic acid (FA) as a targeting moiety and Dox as the drug candidate. The multifunctional NPs internalised and released the drug which was monitored through SERS and fluorescence bi-modal spectroscopy⁶⁴. In another report, Janus silver-mesoporous SiO₂ NPs with excellent SPR and mesoporous properties were

synthesized for simultaneous SERS imaging and pH-responsive drug release. Ag-MSN nanocarriers were found to be an efficient drug delivery system, which was favourable for endocytosis, pH-responsive drug release, and simultaneous SERS imaging (**Figure 1.20**). More importantly, Dox-loaded **Ag-MSNs** selectively inhibited cancer cell growth, rather than normal cells⁶⁵.

1.4.2.3. Mesoporous silica nanoparticle based nanocarrier systems

Mesoporous SiO₂ nanoparticle based drug carrier systems attracted greater attention in the recent decade. A pH-controllable drug carrier based on MSNs and chitosan/poly (methacrylic acid) was fabricated, which can be used as SERS guided drug carriers⁶⁶. Similarly, Au nanocage-SiO₂ nano rattle, assembled with galvanic replacement and surface-protected etching, served as an efficient carrier of Dox (**Figure 1.21A**) in which the cellular internalization and drug release in MCF-7 cells was synergistically monitored using SERS mapping and spectral analysis⁶⁷. In an interesting study, telomerase was used as a trigger for stimuli-responsive drug release in an MSNs wherein the metal core serves as SERS substrate. The above mentioned SERS active nanocarrier not only improved the therapeutic efficacy, but also facilitated the investigation of Raman enabled drug metabolism⁵⁹. Zong *et al.* reported an efficient NP system containing Raman molecule tagged Au@Ag nanorod as the core which serves as SERS substrate and mesoporous SiO₂ layer which promotes the loading of DOX (**Figure 1.21B**). The authors examined the cellular uptake and drug release with both fluorescence and SERS. Moreover, the SERS based Dox mapping was found to be more effective than the fluorescence-based investigations⁶⁸.

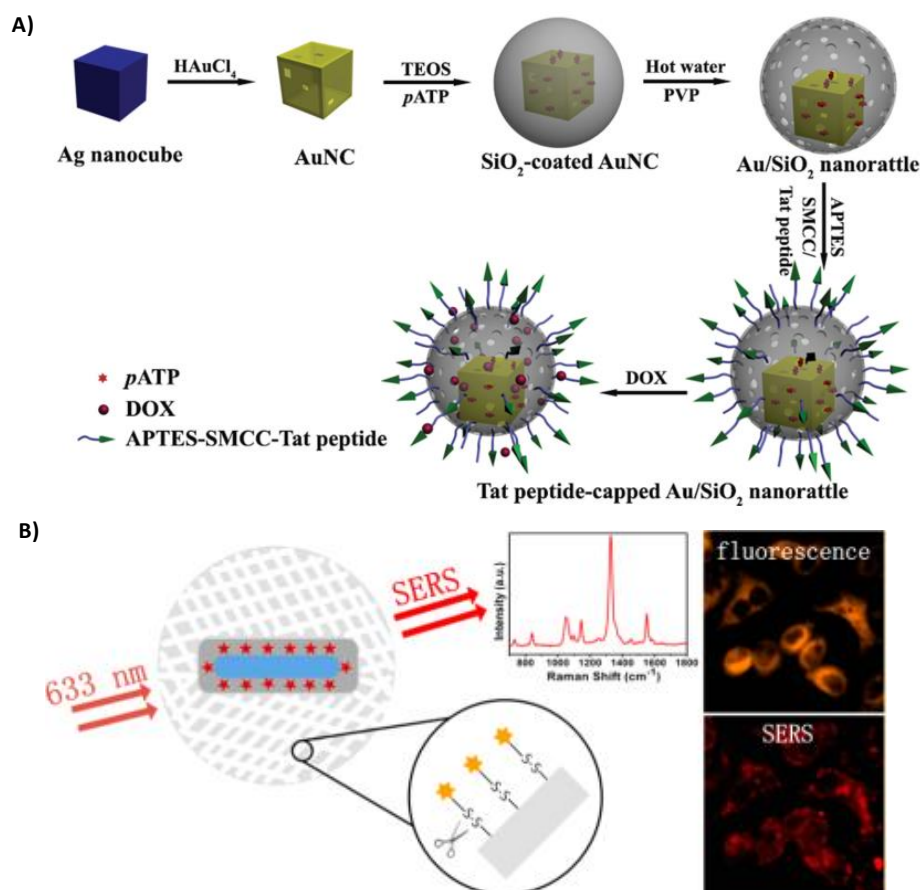


Figure 1.21. A) Representation of double-walled Au/SiO₂ nanorattles for therapeutic applications, B) schematic representation of disulphide based nanocarrier for therapy. Figure A is adapted from ref. 67 and B is adapted from ref. 68.

1.5. Objectives and methodologies for the present investigation

The development of molecular probes and functional nanomaterials with improved sensing capabilities together with high therapeutic effects is a hot topic for biomedical scientific community. In this regard, the present thesis describes the design, synthesis and fabrication of small molecule based optical probes and nanoparticle-based nano-carrier systems for diagnostic and therapeutic applications in cancer and Alzheimer's diseases. Small molecular fluorescent probes have been synthesized and investigated their optical properties and applied for various sensing, imaging and therapeutic applications. In addition, SERS guided nanoparticle based targeted drug delivery system has been developed for therapeutic applications of

various cancers. Cross discipline co-operation will be essential in the design, synthesis, fabrication and implementation of future small molecular probes and nano technological analytical platforms capable for the direct analysis, observation and manipulation of molecular signatures of disease.

In the present thesis, first objective was the design, synthesis and characterization of TPE based SERS nanoprobe for the detection of prostate cancer cells. The unique SERS nanoprobe TPE-InPSA@Au has been developed in conjugation with target-specific PSA peptide (Cys-SerLys-LeuGln-OH) substrate aiming for the detection of PSA protein. **TPE-In-PSA@Au** possess excellent SERS fingerprinting with solid multiplex signal pattern. The nanoprobe successfully recognizes PSA enzyme in SERS-based detection platform with a LOD of 0.5 ng which unfold a new avenue in prostate cancer diagnosis. Moreover, the nanoprobe was nicely documented by PSA overexpressed human prostate cancer (LNCaP) cells, which was imaged through SERS spectral analysis and mapping.

The next objective was to design a novel molecular probe comprised of TPE core as a fluorescent molecular framework for the detection of endogenous H₂S and synergistic delivery of H₂S in lieu of progressive therapy on Alzheimer's dementia. In this regard, two AIE active orthogonally substituted TPE based molecular **probes** **TPE-NBD-D** and **TPE-NBD-2** were synthesized and characterized. Preliminary studies revealed that both the probes exhibit sensitivity and selectivity towards H₂S. In TPE-NBD-D, disulfide donor was used to generate H₂S in presence of cellular bio thiols. Efficient H₂S sensing was reflected in both neuroblastoma cell lines and in mice models. Molecular probe TPE-NBD-D was further utilized for amyloid beta (A β) deagglomeration (A β ₁₋₄₂ protein).

Design and fabrication of a gold core mesoporous silica hybrid nano envelop system for therapeutic applications was the objective of last chapter. A silica coated gold nanoparticles (Au@SiO_2) were synthesized followed by the surface functionalization with chitosan–folic acid (CS-FA) conjugate for precise loading of Dox, resembled as **Au@SiO₂-Dox-CS-FA**. In diagnostic modality, the core Au@SiO_2 to be an effective SERS nanoprobe for Raman imaging to monitor the cellular uptake, release of the impregnated Dox, and dynamic visualization of biochemical changes at molecular level during apoptosis. Also, the probe demonstrated excellent *in vitro* folate receptor (FR)-targeted cytotoxicity and also presented to be an appalling biocompatible targeted nanocarrier delivery construct. Finally, the targeted nano-envelop drug delivery system (**TNEDS**) was explored in mouse models that clearly showed greater therapeutic efficiency superior to the clinically used Dox and Lipodox.

1.6. References

- (1) Stender, A. S.; Marchuk, K.; Liu, C.; Sander, S.; Meyer, M. W.; Smith, E. A.; Neupane, B.; Wang, G.; Li, J.; Cheng, J.; Huang, B.; Fang, N. Single Cell Optical Imaging and Spectroscopy. *Chem. Rev.* **2013**, *113*, 2469–2527.
- (2) Jun, J. V.; Petersson, E. J.; Chenoweth, D. M. Rational Design and Facile Synthesis of a Highly Tunable Quinoline-Based Fluorescent Small-Molecule Scaffold for Live Cell Imaging. *J. Am. Chem. Soc.* **2018**, *140* (30), 9486–9493. <https://doi.org/10.1021/jacs.8b03738>.
- (3) Joseph, M. M.; Narayanan, N.; Nair, J. B.; Karunakaran, V.; Ramya, A. N.; Sujai, P. T.; Saranya, G.; Arya, J. S.; Vijayan, V. M.; Kumar, K. Exploring the Margins of SERS in Practical Domain : An Emerging Diagnostic Modality for Modern Biomedical

-
- Applications. *Biomaterials* **2018**, *181*, 140–181.
<https://doi.org/10.1016/j.biomaterials.2018.07.045>.
- (4) Langer, J.; de Aberasturi, D. J.; Aizpurua, J.; Alvarez-Puebla, R. A.; Auguie, B.; Baumberg, J. J.; Bazan, G. C.; Bell, S. E. J.; Boisen, A.; Brolo, A. G.; Choo, J.; Cialla-May, D.; Deckert, V.; Fabris, L.; Faulds, K.; Javier García de Abajo, F.; Goodacre, R.; Graham, D.; Haes, A. J.; Haynes, C. L.; Huck, C.; Itoh, T.; Käll, M.; Kneipp, J.; Kotov, N. A.; Kuang, H.; Le Ru, E. C.; Lee, H. K.; Li, J. F.; Ling, X. Y.; Maier, S. A.; Mayerhöfer, T.; Moskovits, M.; Murakoshi, K.; Nam, J. M.; Nie, S.; Ozaki, Y.; Pastoriza-Santos, I.; Perez-Juste, J.; Popp, J.; Pucci, A.; Reich, S.; Ren, B.; Schatz, G. C.; Shegai, T.; Schlücker, S.; Tay, L. L.; George Thomas, K.; Tian, Z. Q.; van Duyne, R. P.; Vo-Dinh, T.; Wang, Y.; Willets, K. A.; Xu, C.; Xu, H.; Xu, Y.; Yamamoto, Y. S.; Zhao, B.; Liz-Marzán, L. M. Present and Future of Surface-Enhanced Raman Scattering. *ACS Nano* **2020**, *14* (1), 28–117.
<https://doi.org/10.1021/acsnano.9b04224>.
- (5) Samanta, A.; Maiti, K. K.; Soh, K. S.; Liao, X.; Vendrell, M.; Dinish, U. S.; Yun, S. W.; Bhuvaneshwari, R.; Kim, H.; Rautela, S.; Chung, J.; Olivo, M.; Chang, Y. T. Ultrasensitive Near-Infrared Raman Reporters for SERS-Based in Vivo Cancer Detection. *Angew. Chemie - Int. Ed.* **2011**, *50* (27), 6089–6092.
<https://doi.org/10.1002/anie.201007841>.
- (6) Yang, Q.; Li, L.; Sun, W.; Zhou, Z.; Huang, Y. Dual Stimuli-Responsive Hybrid Polymeric Nanoparticles Self-Assembled from POSS-Based Starlike Copolymer-Drug Conjugates for Efficient Intracellular Delivery of Hydrophobic Drugs. *ACS Appl. Mater. Interfaces* **2016**, *8* (21), 13251–13261.
<https://doi.org/10.1021/acsmi.6b02403>.

- (7) Cheng, X. J.; Gu, J. X.; Pang, Y. P.; Liu, J.; Xu, T.; Li, X. R.; Hua, Y. Z.; Newell, K. A.; Huang, X. F.; Yu, Y.; Liu, Y. Tacrine-Hydrogen Sulfide Donor Hybrid Ameliorates Cognitive Impairment in the Aluminum Chloride Mouse Model of Alzheimer's Disease. *ACS Chem. Neurosci.* **2019**, *10* (8), 3500–3509. <https://doi.org/10.1021/acchemneuro.9b00120>.
- (8) Ma, Y.; Ye, Z.; Zhang, C.; Wang, X.; Li, H. W.; Wong, M. S.; Luo, H. Bin; Xiao, L. Deep Red Blinking Fluorophore for Nanoscopic Imaging and Inhibition of β -Amyloid Peptide Fibrillation. *ACS Nano* **2020**, *14* (9), 11341–11351. <https://doi.org/10.1021/acsnano.0c03400>.
- (9) Jana, D.; Boxi, S.; Parui, P. P.; Ghorai, B. K. Biomolecular Chemistry Vinyl – Tetraphenylethylene Conjugated Systems: *Org. Biomol. Chem.* **2015**, *13*, 10663–10674. <https://doi.org/10.1039/c5ob01564b>.
- (10) Jayaram, D. T.; Ramos-Romero, S.; Shankar, B. H.; Garrido, C.; Rubio, N.; Sanchez-cid, L.; Borros, S.; Blanco, J.; Ramaiah, D. In Vitro and in Vivo Demonstration of Photodynamic Activity and Cytoplasm Imaging through TPE Nanoparticles. *ACS Chem. Biol.* **2016**, *11*, 104–112. <https://doi.org/10.1021/acscchembio.5b00537>.
- (11) Zhuang, Y.; Chiang, P.; Wang, C.; Tan, K. Angewandte Environment-Sensitive Fluorescent Turn-On Probes Targeting Hydrophobic Ligand-Binding Domains for Selective Protein Detection **. *Angew. Chemie* **2013**, *52*, 1–6. <https://doi.org/10.1002/anie.201302884>.
- (12) Lim, M. I. H. E. E.; Lippard, S. J. Metal-Based Turn-On Fluorescent Probes for Sensing Nitric Oxide. *Acc.Chem.Res.* **2007**, *40*, 41–51.
- (13) Han, Q.; Liu, J.; Meng, Q.; Wang, Y.; Han, Q.; Liu, J.; Meng, Q.; Wang, Y.; Feng, H.;

- Zhang, Z. Turn-on Fluorescence Probe for Nitric Oxide Detection and Bioimaging in Live Cells and Zebrafish Turn-on Fluorescence Probe for Nitric Oxide Detection and Bioimaging in Live Cells and Zebrafish. *ACS Sensors* **2019**, *4*, 309–316. <https://doi.org/10.1021/acssensors.8b00776>.
- (14) Saleh, A.; Islam, M.; Sasmal, M.; Maiti, D.; Dutta, A.; Show, B.; Ali, M. Design of a Pyrene Scaffold Multifunctional Material: Real-Time Turn-On Chemosensor for Nitric Oxide, AIEE Behavior, and Detection of TNP Explosive. *ACS Omega* **2018**, *3*, 10306–10316. <https://doi.org/10.1021/acsomega.8b01294>.
- (15) Saleh, A.; Islam, M.; Bhowmick, R.; Garain, B. C.; Katarkar, A.; Ali, M. Formation from Acylhydrazide : A Kinetic Study Nitric Oxide Sensing through 1 , 2 , 3 , 4-Oxatriazole Formation from Acylhydrazide : A Kinetic Study. *J. Org. Chem.* **2018**, *83*, 13287–13295. <https://doi.org/10.1021/acs.joc.8b02110>.
- (16) Article, E.; Zhang, K.; Zhang, J.; Xi, Z.; Li, L.; Gu, X. A New H₂S-Specific near-Infrared Fluorescence- Enhanced Probe That Can Visualize the H₂S Level in Colorectal Cancer Cells in Mice. *Chem. Sci.* **2017**, *00*, 1–6. <https://doi.org/10.1039/C6SC05646F>.
- (17) Wei, C.; Wang, R.; Zhang, C.; Xu, G.; Li, Y.; Zhang, Q. Dual-Reactable Fluorescent Probes for Highly Selective and Sensitive Detection of Biological H₂S. **2016**, *300071*, 1376–1381. <https://doi.org/10.1002/asia.201600262>.
- (18) Li, S.; Li, Y.; Liu, H.; Zhou, D.; Jiang, W.; Ou-yang, J.; Li, C. A Dual-Response Fluorescent Probe for the Detection of Viscosity and H₂S and Its Application in Studying Their Cross-Talk In Fluorescence in Mitochondria. *Anal. Chem.* **2018**. <https://doi.org/10.1021/acs.analchem.8b02068>.

- (19) Singha, S.; Kim, D.; Moon, H.; Wang, T.; Kim, K. H.; Shin, Y. H.; Jung, J.; Seo, E.; Lee, S.; Ahn, K. H. Toward a Selective, Sensitive, Fast-Responsive, and Biocompatible Two-Photon Probe for Hydrogen Sul Fi de in Live Cells. *Anal. Chem.* **2015**, *87*, 1158–1195. <https://doi.org/10.1021/ac503806w>.
- (20) Dong, G.; Chen, L.; Zhang, J.; Liu, T.; Du, L.; Sheng, C.; Li, M. Discovery of Turn-On Fluorescent Probes for Detecting PDE δ Protein in Living Cells and Tumor Slices. *Anal. Chem.* **2020**, *92*, 9516–9522. <https://doi.org/10.1021/acs.analchem.0c00335>.
- (21) Ganguly, S.; Ghosh, D.; Narayanaswamy, N.; Govindaraju, T.; Id, G. B. Dual DNA Binding Mode of a Turn-on Red Fluorescent Probe Thiazole Coumarin. *PLoS One* **2020**, 1–11. <https://doi.org/10.1371/journal.pone.0239145>.
- (22) Liu, T.; Dong, G.; Xu, F.; Han, B.; Fang, H.; Huang, Y.; Zhou, Y.; Du, L.; Li, M. Discovery of Turn-On Fluorescent Probes for Detecting Bcl - 2 Protein. *Anal. Chem.* **2019**, *91*, 5722–5728. <https://doi.org/10.1021/acs.analchem.8b05853>.
- (23) Meng, Q.; Xie, B.; Ma, X.; Hu, Z.; Zhou, F.; Zhou, H.; Dong, C. Rational Design of ER a Targeting Hypoxia Turn-on Fluorescent Probes with Antiproliferative Activity for Breast Cancer †. *Chem. Commun.* **2020**, *56*, 10493–10496. <https://doi.org/10.1039/c9cc09754f>.
- (24) Mosca, L.; Behzad, S. K.; Anzenbacher, P. Small-Molecule Turn-On Fluorescent Probes for RDX. *J. Am. Chem. Soc.* **2015**, *137*, 7967–7969. <https://doi.org/10.1021/jacs.5b04643>.
- (25) Li, H.; Liu, Z.; Jia, R. “ Turn-on ” Fluorescent Probes Based on Rhodamine B / Amino Acid Derivatives for Detection of Fe 3 + in Water. *Spectrochim. Acta Part*

- A Mol. Biomol. Spectrosc.* **2021**, *247*, 119095.
<https://doi.org/10.1016/j.saa.2020.119095>.
- (26) Xiaomeng Zhanga, Tingting Liu a, Beilei Wanga, Yuqi Gaoa, Pan Liua, Minyong Lia, L. D. Astemizole-Based Turn-on Fluorescent Probes for Imaging HERG Potassium Channel. *Medchemcomm* **2019**, *10*, 513–516.
<https://doi.org/10.1039/C8MD00562A>.
- (27) Shi, G.; Yoon, T.; Cha, S.; Kim, S.; Yousuf, M.; Ahmed, N.; Kim, D.; Kang, H.; Kim, K. S. Turn-on and Turn-off Fluorescent Probes for Carbon Monoxide Detection and Blood Carboxyhemoglobin Determination. *ACS Sensors* **2018**, *3*, 1102–1108. <https://doi.org/10.1021/acssensors.8b00083>.
- (28) Sil, A.; Islam, S. N.; Patra, S. K. Terpyridyl Appended Poly(Metaphenylene-Alt-Fluorene) π -Conjugated Fluorescent Polymers: Highly Selective and Sensitive Turn off Probes for the Detection of Cu²⁺. *Sensors Actuators B. Chem.* **2017**, *254*, 618–628. <https://doi.org/10.1016/j.snb.2017.07.067>.
- (29) Nú, M. T. Coumarin-Based Fluorescent Probes for Dual Recognition of Copper(II) and Iron(III) Ions and Their Application in Bio-Imaging. *Sensors* **2014**, *14*, 1358–1371. <https://doi.org/10.3390/s140101358>.
- (30) Shanmugaraj, K.; Ilanchelian, M. A “Turn-off” Fluorescent Sensor for the Selective and Sensitive Detection of Copper(II) Ions Using Lysozyme Stabilized Gold Nanoclusters. *RSC Adv.* **2016**, *6*, 54518–54524.
<https://doi.org/10.1039/c6ra08325k>.
- (31) Nesakumar, T.; Immanuel, J.; Atchudan, R.; Shim, J.; Kalimuthu, S.; Ahn, B.; Rok, Y. Turn-off Fluorescence Sensor for the Detection of Ferric Ion in Water Using

- Green Synthesized N-Doped Carbon Dots and Its Bio-Imaging. *J. Photochem. Photobiol. B Biol.* **2016**, *158*, 235–242.
<https://doi.org/10.1016/j.jphotobiol.2016.03.010>.
- (32) Gupta, N.; Reja, I.; Bhalla, V.; Gupta, M. A Bodipy Based Dual Functional Probe for the Detection of Hydrogen Sulfide and H₂S Induced Apoptosis in Cellular Systems †. *Chem. Commun.* **2015**, *51* (515), 10875–10878.
<https://doi.org/10.1039/C5CC02984H>.
- (33) Lee, M. H.; Kim, J. S.; Sessler, J. L. Chem Soc Rev Probes for Cations, Anions, and Biomolecules. *Chem. Soc. Rev.* **2014**, *44* (4185–4191).
<https://doi.org/10.1039/C4CS00280F>.
- (34) Huang, C.; Jia, T.; Tang, M.; Yin, Q.; Zhu, W.; Zhang, C.; Yang, Y.; Jia, N.; Xu, Y.; Qian, X. Selective and Ratiometric Fluorescent Trapping and Quantification of Protein Vicinal Dithiols and in Situ Dynamic Tracing in Living Cells. *J. Am. Chem. Soc.* **2014**, *136*, 14237–14244.
- (35) Dai, Z.; Ge, G.; Feng, L.; Ning, J.; Hu, L.; Jin, Q.; Wang, D.; Lv, X.; Dou, T.; Cui, J.; Yang, L. A Highly Selective Ratiometric Two-Photon Fluorescent Probe For. *J. Am. Chem. Soc.* **2015**, *137*, 14488–14495.
<https://doi.org/10.1021/jacs.5b09854>.
- (36) Sathish Sawminathan and Sathiyarayanan Kulathu Iyer. A New Imidazole Based Phenanthridine Probe for Ratiometric Fluorescent Monitoring of Methanol in Biodiesel. *New J. Chem.* **2021**, doi.org/10.1039/D0NJ06252A.
<https://doi.org/10.1039/D0NJ06252A>.
- (37) Cheng, D.; Pan, Y.; Wang, L.; Zeng, Z.; Yuan, L.; Zhang, X.; Chang, Y. Selective

- Visualization of the Endogenous Peroxynitrite in an In Fl Amed Mouse Model by a Mitochondria-Targetable Two-Photon Ratiometric Fluorescent Probe. *J. Am. Chem. Soc.* **2017**, *139*, 285–292. <https://doi.org/10.1021/jacs.6b10508>.
- (38) Zhou, L.; Zhang, X.; Wang, Q.; Lv, Y.; Mao, G.; Luo, A.; Wu, Y.; Wu, Y.; Zhang, J.; Tan, W. Molecular Engineering of a TBET-Based Two-Photon Fluorescent Probe for Ratiometric Imaging of Living Cells and Tissues. *J. Am. Chem. Soc.* **2014**, *136*, 9838–9841.
- (39) Langer, J.; Aberasturi, D. J. De; Aizpurua, J.; Alvarez-puebla, R. A.; Auguie, B.; Baumberg, J. J.; Bazan, G. C.; Bell, S. E. J.; Boisen, A.; Alexandre, B. G.; Liz-Marzán, M. L. Present and Future of Surface-Enhanced Raman Scattering. *ACS Nano* **2020**, *14*, 28–117. <https://doi.org/10.1021/acsnano.9b04224>.
- (40) Cui, S.; Zhang, S.; Yue, S. Raman Spectroscopy and Imaging for Cancer Diagnosis. *J. Healthc. Eng. using* **2018**, *2018*, 1–11.
- (41) Austin, L. A.; Osseiran, S.; Evens, C. L. Raman Technologies in Cancer Diagnostics. *Analyst* **2016**, *141*, 476–503. <https://doi.org/10.1039/c5an01786f>.
- (42) Fleischmann, M.; Hendra, P. J.; McQuillan, A. J. Raman Spectra of Pyridine Adsorbed at a Silver Electrode. *Chem. Phys. Lett.* **1974**, *26* (2), 163–166. [https://doi.org/10.1016/0009-2614\(74\)85388-1](https://doi.org/10.1016/0009-2614(74)85388-1).
- (43) Jeanmaire, D. L.; Duynes, R. P. VAN. Surface Raman Spectroelectrochemistry Part1. Heterocyclic. *J. Electroanal Chem.* **1977**, *84*, 1–20.
- (44) Albrecht, M. G.; Creighton, J. A. Anomalous Intense Raman Spectra of Pyridine

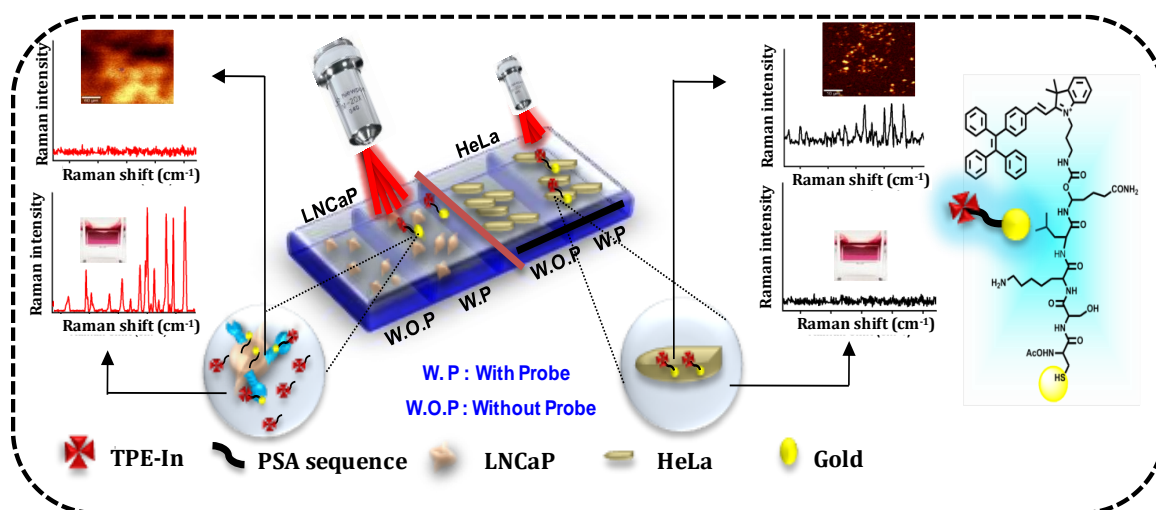
- at a Silver Electrode. *J. Am. Chem. Soc.* **1977**, *99* (15), 5215–5217.
<https://doi.org/10.1021/ja00457a071>.
- (45) Ashton, L.; Hollywood, K. A.; Goodacre, R. Making Colourful Sense of Raman Images of Single Cells. *Analyst* **2015**, *140* (6), 1852–1858.
<https://doi.org/10.1039/c4an02298j>.
- (46) Ding, S. Y.; You, E. M.; Tian, Z. Q.; Moskovits, M. Electromagnetic Theories of Surface-Enhanced Raman Spectroscopy. *Chem. Soc. Rev.* **2017**, *46* (13), 4042–4076. <https://doi.org/10.1039/c7cs00238f>.
- (47) Wang, D.; Zhu, W.; Chu, Y.; Crozier, K. B. High Directivity Optical Antenna Substrates for Surface Enhanced Raman Scattering. *Adv. Mater.* **2012**, *24* (32), 4376–4380. <https://doi.org/10.1002/adma.201201625>.
- (48) Mosier-Boss, P. A. Review of SERS Substrates for Chemical Sensing. *Nanomaterials* **2017**, *7* (6). <https://doi.org/10.3390/nano7060142>.
- (49) Zhang, W.; Jiang, L.; Piper, J. A.; Wang, Y. SERS Nanotags and Their Applications in Biosensing and Bioimaging. *J. Anal. Test.* **2018**, *2* (1), 26–44.
<https://doi.org/10.1007/s41664-018-0053-9>.
- (50) Li, D. W.; Qu, L. L.; Hu, K.; Long, Y. T.; Tian, H. Monitoring of Endogenous Hydrogen Sulfide in Living Cells Using Surface-Enhanced Raman Scattering. *Angew. Chemie - Int. Ed.* **2015**, *54* (43), 12758–12761.
<https://doi.org/10.1002/anie.201505025>.
- (51) Chen, H. Y.; Kouadio Fodjo, E.; Jiang, L.; Chang, S.; Li, J. Bin; Zhan, D. S.; Gu, H. X.; Li, D. W. Simultaneous Detection of Intracellular Nitric Oxide and Peroxynitrite

- by a Surface-Enhanced Raman Scattering Nanosensor with Dual Reactivity. *ACS Sensors* **2019**, *4* (12), 3234–3239. <https://doi.org/10.1021/acssensors.9b01740>.
- (52) Cui, J.; Hu, K.; Sun, J. J.; Qu, L. L.; Li, D. W. SERS Nanoprobes for the Monitoring of Endogenous Nitric Oxide in Living Cells. *Biosens. Bioelectron.* **2016**, *85*, 324–330. <https://doi.org/10.1016/j.bios.2016.04.094>.
- (53) Cao, Y.; Li, D. W.; Zhao, L. J.; Liu, X. Y.; Cao, X. M.; Long, Y. T. Highly Selective Detection of Carbon Monoxide in Living Cells by Palladacycle Carbonylation-Based Surface Enhanced Raman Spectroscopy Nanosensors. *Anal. Chem.* **2015**, *87* (19), 9696–9701. <https://doi.org/10.1021/acs.analchem.5b01793>.
- (54) Cho, S. J.; Ahn, Y. H.; Maiti, K. K.; Dinish, U. S.; Fu, C. Y.; Thoniyot, P.; Olivo, M.; Chang, Y. T. Combinatorial Synthesis of a Triphenylmethine Library and Their Application in the Development of Surface Enhanced Raman Scattering (SERS) Probes. *Chem. Commun.* **2010**, *46* (5), 722–724. <https://doi.org/10.1039/b921550f>.
- (55) Maiti, K. K.; Samanta, A.; Vendrell, M.; Soh, K.; Olivo, M.; Chang, Y.-T. Multiplex Cancer Cell Detection by SERS Nanotags with Cyanine and Triphenylmethine Raman Reporters. *Chem. Commun* **2011**, *47*, 3514–3516. <https://doi.org/10.1039/c0cc05265e>.
- (56) Wu, L.; Wang, Z.; Zong, S.; Chen, H.; Wang, C.; Xu, S.; Cui, Y. Simultaneous Evaluation of P53 and P21 Expression Level for Early Cancer Diagnosis Using SERS Technique. *Analyst* **2013**, *138* (12), 3450–3456. <https://doi.org/10.1039/c3an00181d>.

- (57) Wu, L.; Wang, Z.; Fan, K.; Zong, S.; Cui, Y. A SERS-Assisted 3D Barcode Chip for High-Throughput Biosensing. *Small* **2015**, *11* (23), 2798–2806. <https://doi.org/10.1002/sml.201403474>.
- (58) Ilkhani, H.; Hughes, T.; Li, J.; Jian, C.; Hepel, M. Nanostructured SERS-Electrochemical Biosensors for Testing of Anticancer Drug Interactions with DNA. *Biosens. Bioelectron.* **2016**, 10.1016/j.bios.2016.01.068. <https://doi.org/10.1016/j.bios.2016.01.068>.
- (59) Zong, S.; Wang, Z.; Chen, H.; Zhu, D.; Chen, P.; Cui, Y. Telomerase Triggered Drug Release Using a SERS Traceable Nanocarrier. *IEEE Trans. Nanobioscience* **2014**, *13* (1), 55–60.
- (60) Iversen, T. G.; Skotland, T.; Sandvig, K. Endocytosis and Intracellular Transport of Nanoparticles: Present Knowledge and Need for Future Studies. *Nano Today* **2011**, *6* (2), 176–185. <https://doi.org/10.1016/j.nantod.2011.02.003>.
- (61) Kang, B.; Afifi, M. M.; Austin, L. A.; El-Sayed, M. A. Exploiting the Nanoparticle Plasmon Effect: Observing Drug Delivery Dynamics in Single Cells via Raman/Fluorescence Imaging Spectroscopy. *ACS Nano* **2013**, *7* (8), 7420–7427. <https://doi.org/10.1021/nn403351z>.
- (62) El-Said, W. A.; Kim, T. H.; Kim, H.; Choi, J. W. Detection of Effect of Chemotherapeutic Agents to Cancer Cells on Gold Nanoflower Patterned Substrate Using Surface-Enhanced Raman Scattering and Cyclic Voltammetry. *Biosens. Bioelectron.* **2010**, *26* (4), 1486–1492. <https://doi.org/10.1016/j.bios.2010.07.089>.
- (63) Tian, L.; Gandra, N.; Singamaneni, S. Monitoring Controlled Release of Payload

- from Gold Nanocages Using Surface Enhanced Raman Scattering. *ACS Nano* **2013**, *7* (5), 4252–4260. <https://doi.org/10.1021/nn400728t>.
- (64) Srinivasan, S.; Bhardwaj, V.; Ms, A. N.; Carolina, S. Multifunctional Surface-Enhanced Raman Spectroscopy-Detectable Silver Nanoparticles for Combined Photodynamic Therapy and PH-Triggered Chemotherapy. *J. Biomed. Nanotechnol.* **2016**, *12*, 2202–2219. <https://doi.org/10.1166/jbn.2016.2312>.
- (65) Shao, D.; Zhang, X.; Liu, W.; Zhang, F.; Zheng, X.; Qiao, P.; Li, J.; Dong, W. F.; Chen, L. Janus Silver-Mesoporous Silica Nanocarriers for SERS Traceable and PH-Sensitive Drug Delivery in Cancer Therapy. *ACS Appl. Mater. Interfaces* **2016**, *8* (7), 4303–4308. <https://doi.org/10.1021/acsami.5b11310>.
- (66) Fang, W.; Wang, Z.; Zong, S.; Chen, H.; Zhu, D.; Zhong, Y.; Cui, Y. PH-Controllable Drug Carrier with SERS Activity for Targeting Cancer Cells. *Biosens. Bioelectron.* **2014**, *57*, 10–15. <https://doi.org/10.1016/j.bios.2014.01.042>.
- (67) Hu, F.; Zhang, Y.; Chen, G.; Li, C.; Wang, Q. Double-Walled Au Nanocage/SiO₂ Nanorattles: Integrating SERS Imaging, Drug Delivery and Photothermal Therapy. *Small* **2015**, *11* (8), 985–993. <https://doi.org/10.1002/sml.201401360>.
- (68) Zong, S.; Wang, Z.; Chen, H.; Yang, J.; Cui, Y. Surface Enhanced Raman Scattering Traceable and Glutathione Responsive Nanocarrier for the Intracellular Drug Delivery. *Anal. Chem.* **2013**, *85* (4), 2223–2230. <https://doi.org/10.1021/ac303028v>.

SERS Nanoprobe Based on Tetraphenylethylene Raman Signatures for the Detection of Prostate Cancer Biomarker



2.1. Abstract:

A new class of Raman signatures has been designed and synthesized based on TPE appended organic fluorogens and unfold their unique Raman fingerprints by SERS upon adsorption on nanoroughened gold surface. Five TPE analogues were synthesized with a series of electron donors such as (1) indoline with propyl (**TPE-In**), (2) indoline with lipoic acid (**TPE-In-L**), (3) indoline with Boc-protected propyl amine (**TPE-In-Boc**), (4) benzothiazole (**TPE-B**), and (5) quinaldine (**TPE-Q**). All the derivatives of TPE showed their prevalent AIE and ACQ phenomena. Interestingly, all the TPE derivatives displayed good multiplexing Raman peaks, out of which **TPE-In-Boc** showed a substantial enhancement in signal intensity in the fingerprint region. An efficient SERS nanoprobe has been fabricated with AuNPs as SERS substrate where **TPE-In** integrated

as the Raman reporter, which was further conjugated with a specific peptide substrate, cysteine-serine-lysine-leucine-glutamine (Cys-Ser-Lys-Leu-Gln-OH), well-known for the detection of PSA. The chosen nanoprobe **TPE-In-PSA@Au** represented as SERS “ON/OFF” probe in the surface of PSA protease, which clearly recognizes PSA appearance with a LOD of 0.5 ng in SERS platform. Furthermore, **TPE-In-PSA@Au** nanoprobe was efficiently recognized the overexpressed PSA in LNCaP cells, which can be imagined through SERS spectral analysis and mapping.

2.2. Introduction

The diversified chemical structure of organic fluorescent molecules modulating fundamental photophysical properties have continuously evolved over the past several years, imparting a huge impact on biomedical research with special emphasis on bioimaging.^{1,2} One such unique photophysical phenomenon of organic fluorogen is known as AIE, which was first reported in 2001 for silole molecules.^{3,4,5} On the contrary, an opposite mechanism called ACQ, occurred due to the formation of excimers and exciplexes upon collision between the aromatic molecules in the excited and ground states, which is mainly through FRET, ICT, or both. A well-known example for an AIE fluorogen is TPE, in which the olefin stator is surrounded by phenyl rotors that are non-emissive in a molecularly dissolved state and are emissive by aggregate formation⁶ and also exhibit ACQ effect by modifying the molecular structure. Due to AIE and ACQ effects, TPE analogues found surplus applications in sensing and detection of various metal cations^{7,8,9} (**Figure 2.1A**) and anions¹⁰, biological applications such as cell imaging,^{11,12} detection of mitochondrial H₂O₂ in living cells¹³, and targeted intracellular thiol imaging.¹⁴ In one such report, Ramaiah et.al described a TPE nanoparticles which exhibit AIE property for therapeutic applications¹². Their

nanoparticle showed excellent singlet oxygen generation ability, rapid cellular uptake and high localization in the cytoplasmic area. So this TPE self-assembly demonstrated good photodynamic effect on human prostate animal model (**Figure 2.1B**).

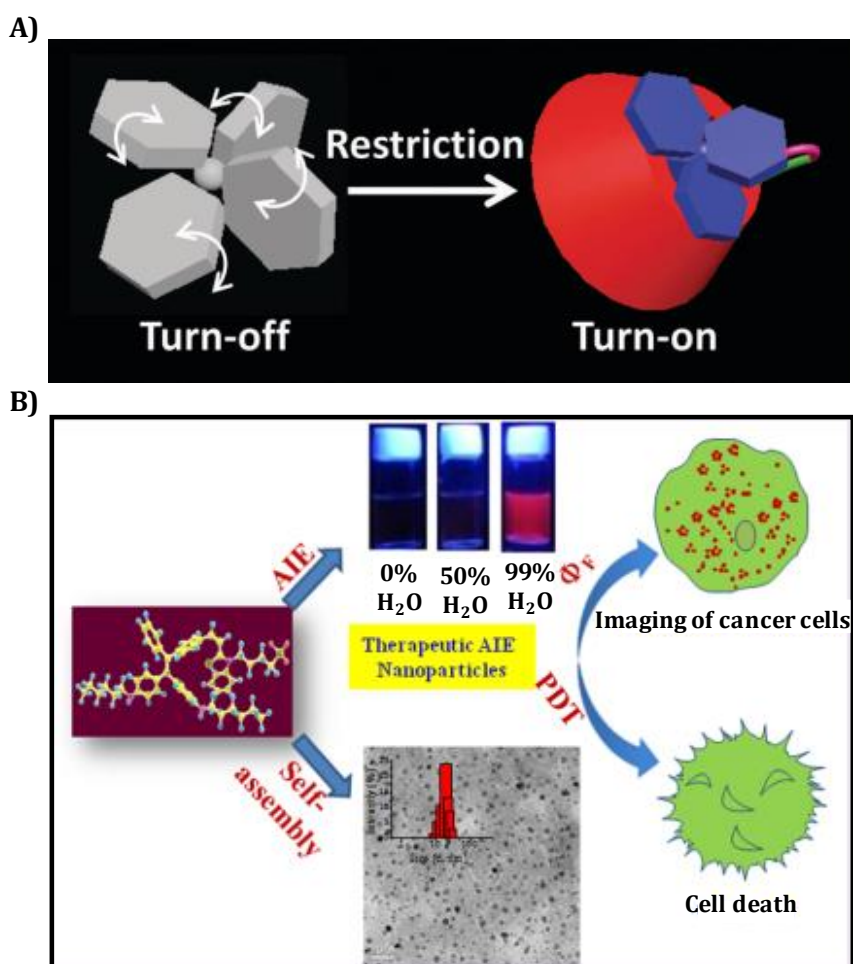


Figure 2.1. A) Schematic illustration of fluorescent enhancement of TPE in presence of water: acetonitrile solvent system, B) Representation showing the turn on fluorescence after restricting the rotation of TPE. Figure is adapted from ref.12.

In the present decade, SERS has evolved with great potential in diagnostic applications^{15,16}, mainly diagnosing infected cells, tissues, and many bioanalytes, which assures the accurate investigation by fingerprinting of spectral cytopathology and spectral histopathology. SERS is an advanced form of conventional Raman spectroscopy in which incremental enhancement of signal intensity reflected by several orders in the vicinity of nano-roughened metal surface. Exponential growth of

nanotechnology together with emergence of various SERS active substrates improved the sensitivity of this technique assuring to detect single molecular level. The enhanced specificity, high sensitivity and ease of sample preparation makes SERS prior over other technique in biomedical application. Apart from other modalities, SERS is capable of producing images using specific mapping of Raman spectral data without any photo bleaching. In this context, the recent advances of SERS in cancer diagnosis and imaging has been explored.¹⁷ SERS technique aroused as an active future competitor against fluorescence-based detection and imaging which has several advantages including extremely high sensitivity, multiplexing ability and captured minute chemical modification in many biological species at molecular level.^{18,19} In recent studies SERS technique successfully utilize on cancer diagnosis as an alternative detection tool emphasizing a great potential over conventional cytopathology.^{20,21} In this regard, early stage diagnosis of prostate cancer has a huge impact as it is the second most leading cancer-related death among male population.²² PSA, belonging to the human kallikrein family, has been recognized as a tumor marker for the detection of early stage prostate cancer. In general, PSA concentration for a normal man ranges from 0 to 4 ng/mL, but it rises significantly in patients with prostate cancer.²³ Generally, most of the PSA biomarker detection strategies are carried out using an enzyme-linked immunosorbent assay (ELISA), HPLC and electrochemical immunosensors using single-wall carbon nanotubes (SWCN). In a recent report, Chen and co-workers reported a gold nanoparticle-based probe for sensing ultra-low level of PSA through fluorescence spectroscopy.²⁴ Their newly described fluorescent probe accounts a low limit of detection of 0.032 pg/mL level in PSA in patient serum (**Figure 2.2A**). Recently, SERS also emerged as an important investigative tool for the sensitive detection of prostate cancer. In a report authors

demonstrated a label free SERS analysis to discriminate prostate cancer patients from normal persons by measuring SERS spectra (**Figure 2.2B**) of serum from patients and normal persons using silver colloids.²⁵ So SERS technique associating with support vector machine (SVM) algorithms have great potential to screen prostate cancer blood samples from normal samples. In another report SERS technique has been used for the diagnosis of prostate cancer by measuring the urine samples using AuNPs as the substrate.²⁶

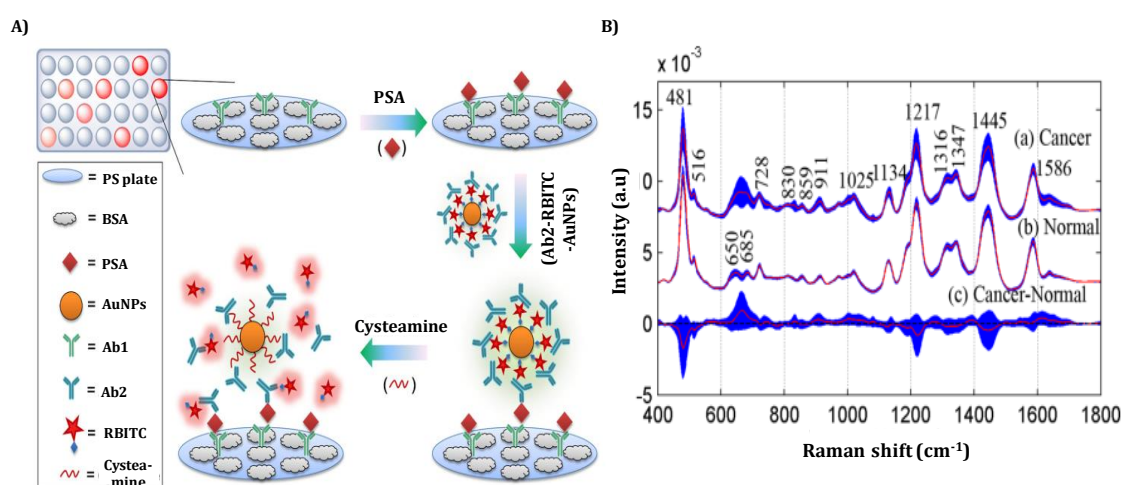
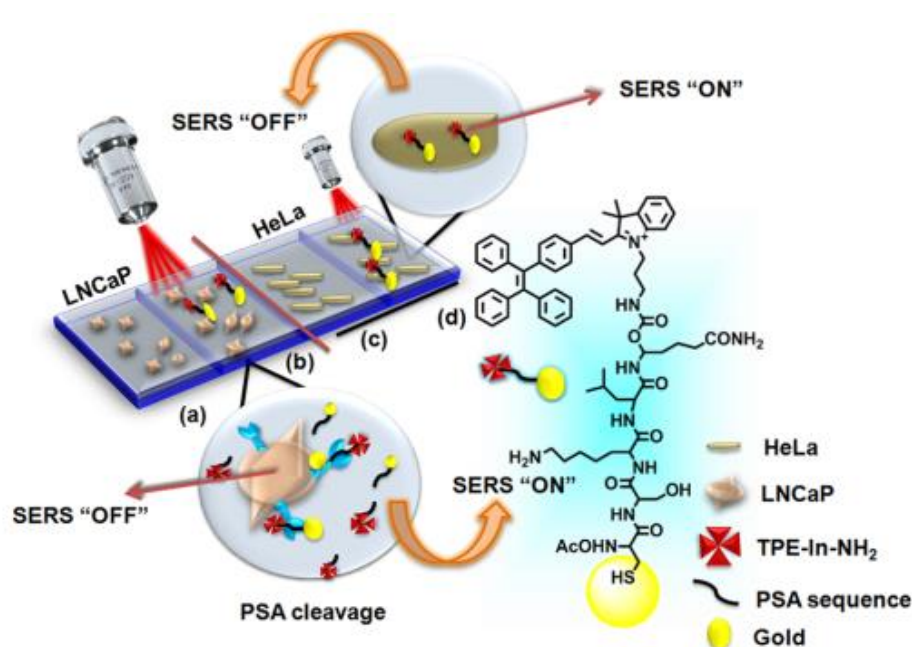


Figure 2.2. A) Representation of fluorescence-activatable probe for PSA detection, B) SERS spectra measured from serum of prostate cancer and normal persons. Figure A is adapted from ref. 24 and B is adapted from ref. 25.

Herein, a series of TPE-appended fluorogens has been synthesized, investigated their AIE and ACQ properties in dimethyl sulfoxide (DMSO)-water (H_2O) solvent mixture and consequently revealed their SERS activity as a new insight when adsorbed on colloidal AuNPs. Though TPE derivatives are well exploited for their unique fluorescence properties, no pertinent literature reports demonstrating their use as Raman signatures are available. Because the TPE derivatives are well-known for their aggregation due to restricted molecular rotation, it may enhance the Raman signal intensity due to molecular orientation on nanoparticle surface by generating

good number of hotspots and produce enhanced electromagnetic field.²⁷ Moreover, TPE derivatives show excellent shelf life, high photo stability, and synthetic ease when compared to the reported Raman signature molecules. So, we attempted to utilize TPE as Raman reporter to construct SERS nanotags for the sensitive detection of PSA. TPE-derivatives transformed as a potential Raman reporter which enable to produce multiplexing signal pattern. Further the promising SERS nanoprobe, TPE-InPSA@Au utilized successfully to diagnosis PSA expression on cancer cells after coupling with PSA specific peptide substrate, **Cys-Ser-Lys-Leu-Gln-OH (Scheme 2.1)**.

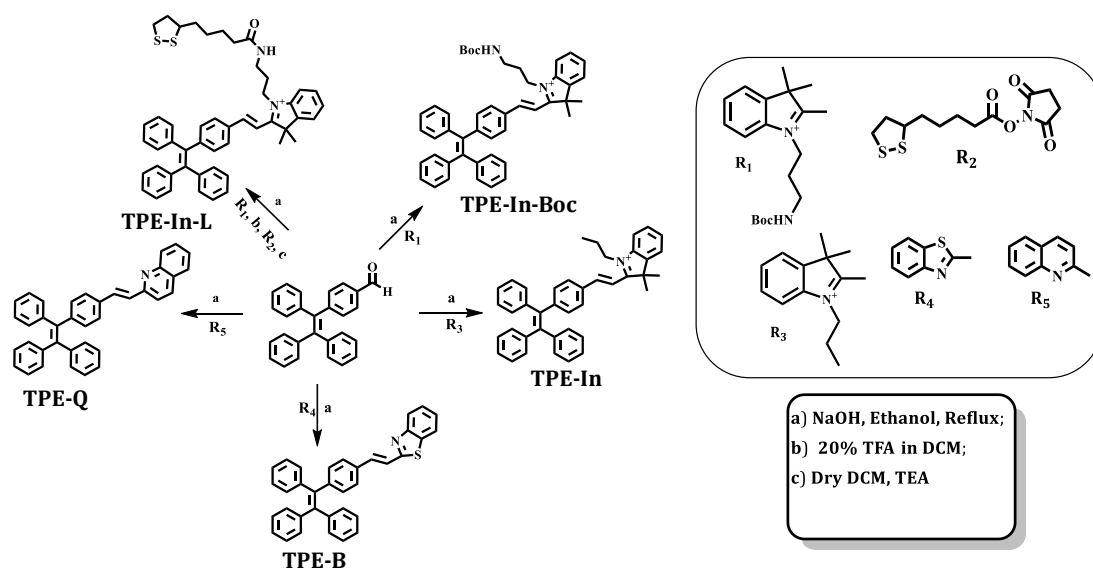


Scheme 2.1: Thematic Representation of PSA Recognition by **TPE-In-PSA@Au** Nanoprobe through SERS, (a) & (b) represents the LNCaP cells without and with probes, (c) & (d) represents HeLa cells without and with probes.

2.3 Results and discussion

2.3.1. Synthesis and characterization of TPE analogues

The key synthetic intermediate, aldehyde functionalized tetraphenylethylene (**TPE-CHO**) was synthesized by palladium catalyzed Suzuki reaction between bromotriphenylethylene and 4-formylphenylboronic acid in a mixture of toluene, tetrabutylammonium bromide (TBAB), and 2 M aqueous potassium carbonate (K_2CO_3). A series of five novel TPE analogues were synthesized *via* aldol type condensation between **TPE-CHO** and different aromatic moieties like indoline with lipoic acid, indoline with Boc protected propylamine, indoline with propyl, benzothiazole and quinaldine, represented as **TPE-In-L**, **TPE-In-Boc**, **TPE-In**, **TPE-B** and **TPE-Q**, respectively (**Scheme 2.2.**). The products and intermediates formed were isolated, purified through column chromatography and were characterized on the basis of spectral and analytical evidence.



Scheme 2.2. Synthetic route to TPE derivatives.

2.3.2. Photophysical properties of TPE analogues

To evaluate the photophysical properties of newly synthesized TPE analogues, recorded the absorption spectra in DMSO as solvent where **TPE-Q** and **TPE-B** showed absorption maxima at 376 and 371 nm (**Figure 2.3 A&C**) and were yellow in color. whereas **TPE-In**, **TPE-In-L**, and **TPE-In-Boc** showed absorption at 445, 449, and 446 nm (**Figure 2.4 A, C&E**) and were red in color. Because TPE molecules are well-known for aggregation studies we have evaluated their aggregation properties in DMSO–H₂O system. Upon increasing the water (f_w) proportion, **TPE-B** and **TPE-Q** showed AIE effect (**Figure 2.3 B&D**), whereas the fluorescent quenching, ACQ was observed in **TPE-In**, **TPE-In-L**, and **TPE-In-Boc** (**Figure 2.4 B, D&F**) under similar conditions, which is probably due to the intermolecular FRET.²⁸

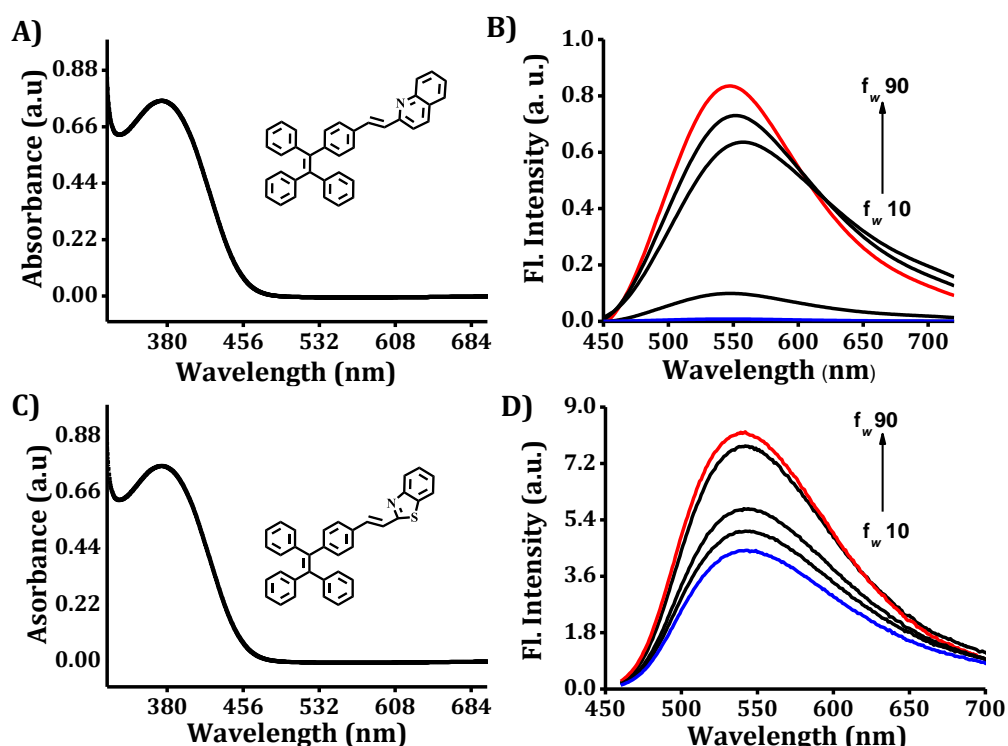


Figure 2.3. Representative A) absorption and B) fluorescence spectra of the **TPE-Q** derivative, C) absorption and D) fluorescence spectra of the **TPE-B** derivative respectively.

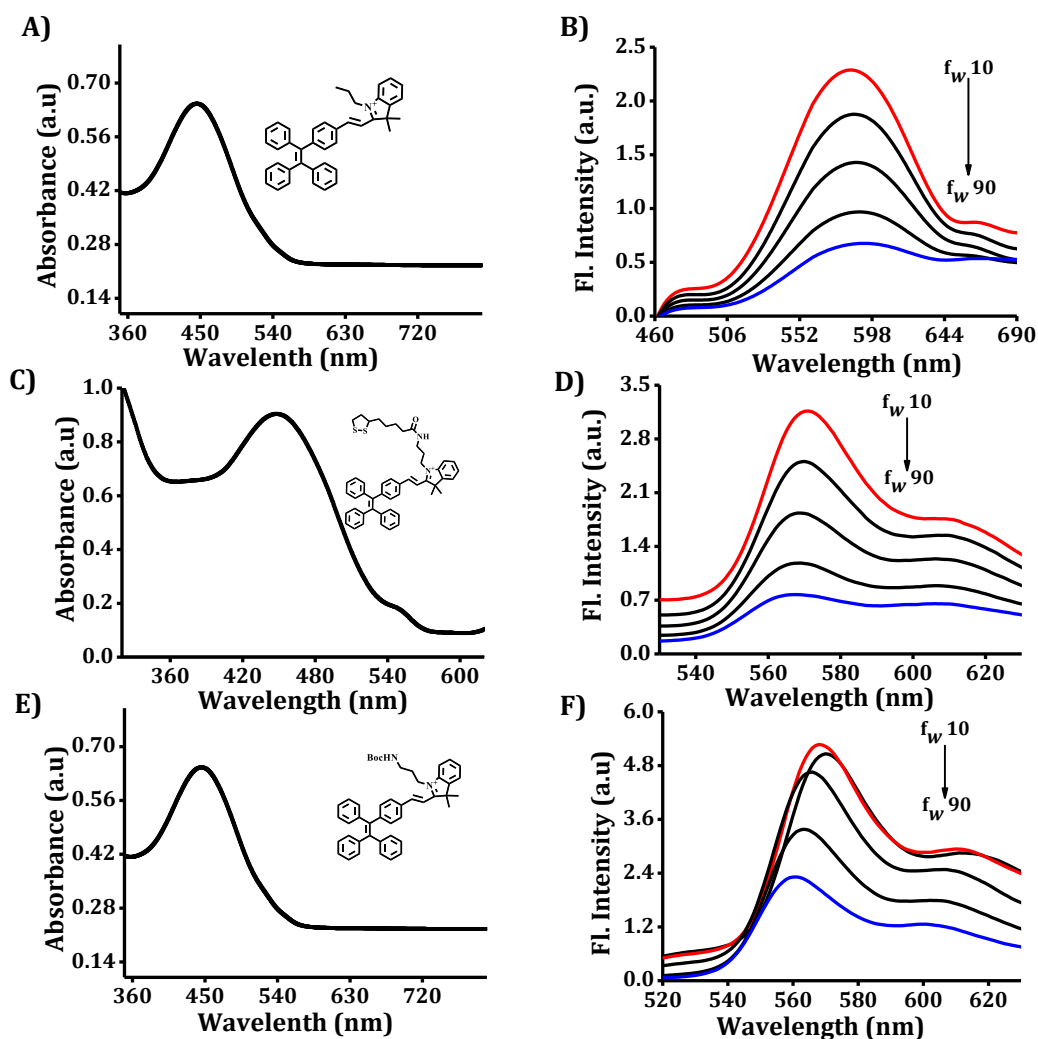


Figure 2.4. Representative A) absorption and B) fluorescence spectra of the **TPE-In** derivative, C) absorption and D) fluorescence spectra of the **TPE-In-L** derivative, E) absorption and F) fluorescence spectra of the **TPE-In-Boc** derivative respectively.

2.3.3. SERS analysis of the TPE derivative

Further, the SERS fingerprint pattern were investigated for all the five TPE derivatives under a particular solvent concentration other than their AIE and ACQ properties. SERS experiments have been carried out by incubating the TPE analogues as Raman reporter with citrate stabilized spherical Au NPs (40 nm) as a SERS substrate and SERS spectra was measured under a WI-Tec Raman microscope with a wavelength of 633 nm laser excitation and 20 X objective. Initially, the AuNPs was characterized using UV-Vis absorption spectroscopy and Transmission Electron

Microscopy (TEM). **Figure 2.5A** shows the absorption spectrum of AuNPs and the corresponding TEM image is shown in **figure 2.5B**.

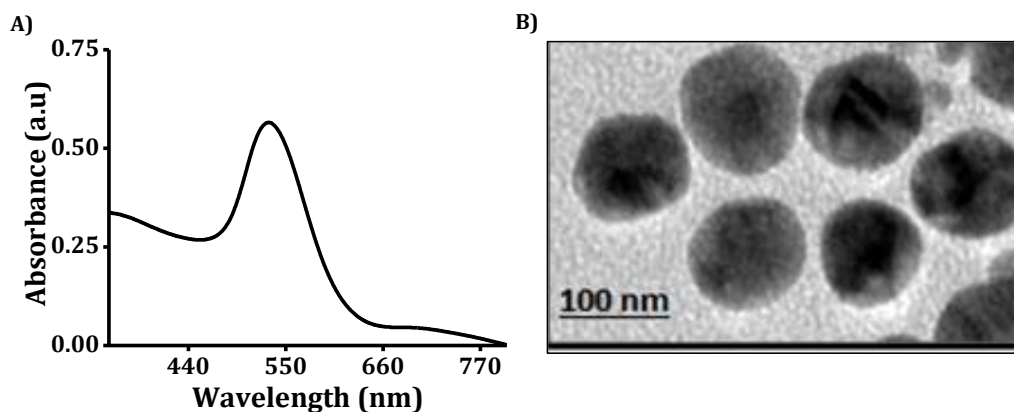


Figure 2.5. Representative A) absorption spectrum and B) TEM images of AuNPs.

SERS experiments were carried out after incubating TPE derivatives with citrate stabilized AuNPs as SERS substrates by 1: 9 ratios. All the TPE derivatives exhibit signature Raman peaks at 687, 800–930, and 1000–2000 cm^{-1} corresponding to C–C in plane bending, aliphatic chain vibrations and aromatic ring vibrations, respectively (**Figure 2.6**).²⁹ Significant Raman fingerprints are obtained for the derivative, **TPE-In-L**. This noticeable enhancement of Raman signal in SERS platform depends on variable factors, for example, particular molecular orientation on nanoparticle surface, which can generate a good number of hotspots and produce enhanced electromagnetic field, leading to signal enhancement.²⁷ The tentative SERS peak assignments from the spectra is shown in **table 2.1**.

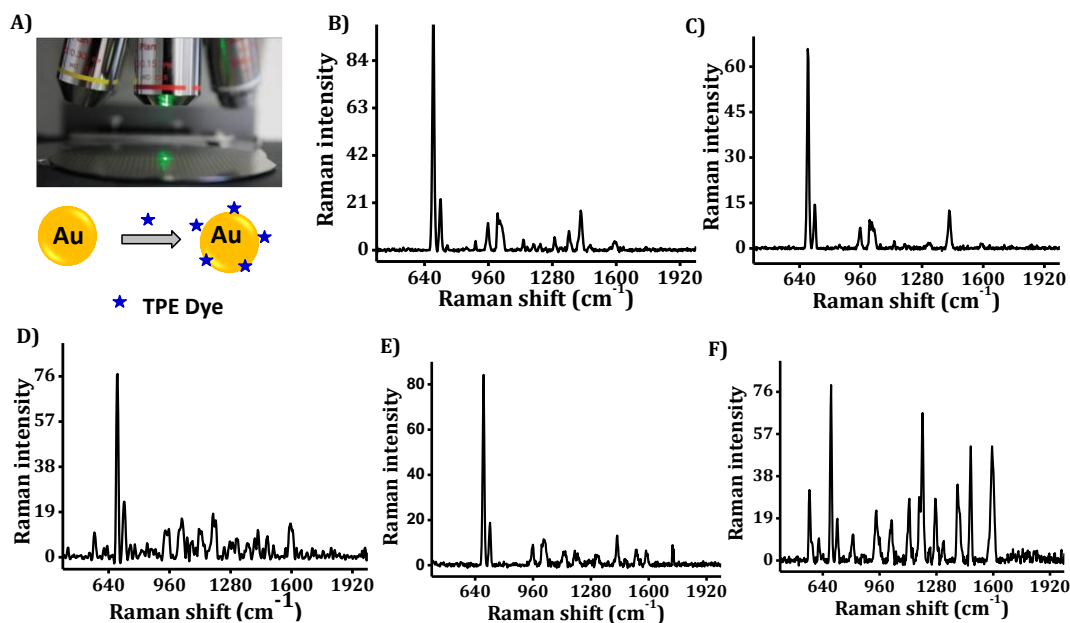


Figure 2.6. A) SERS spectral analysis, SERS spectra of TPE derivatives after incubating with citrate stabilized gold nanoparticles as substrate by 9:1 ratio; (B) **TPE-Q**, (C) **TPE-B**, (D) **TPE-In**, (E) **TPE-In-Boc**, and (F) **TPE-In-L**.

Table 2.1: SERS peak assignments from **TPE-In-L**.

Peak (cm ⁻¹)	Assignment
562	In plane and out of plane ring deformations (ring in benzene derivatives)
600-930	C-C aliphatic chain vibrations
1000-2000	Aromatic ring vibrations

2.3.4. Construction of TPE-In-PSA SERS nanoprobe

The best Raman signature **TPE-In-Boc** has been chosen for further construction of SERS nanoprobe aiming to detect PSA, cancer protein by SERS spectral analysis. For the construction of designated synthetic counterpart **TPE-In-PSA**, the corresponding Boc protected analogue (**TPE-In-Boc**) was conjugated to PSA recognizing peptide substrate, **Cys-SerLys-Leu-Gln-OH**. The peptide sequence was

synthesized by adopting the well-known solid phase peptide synthesis (SPPS) (Figure 2.7.).

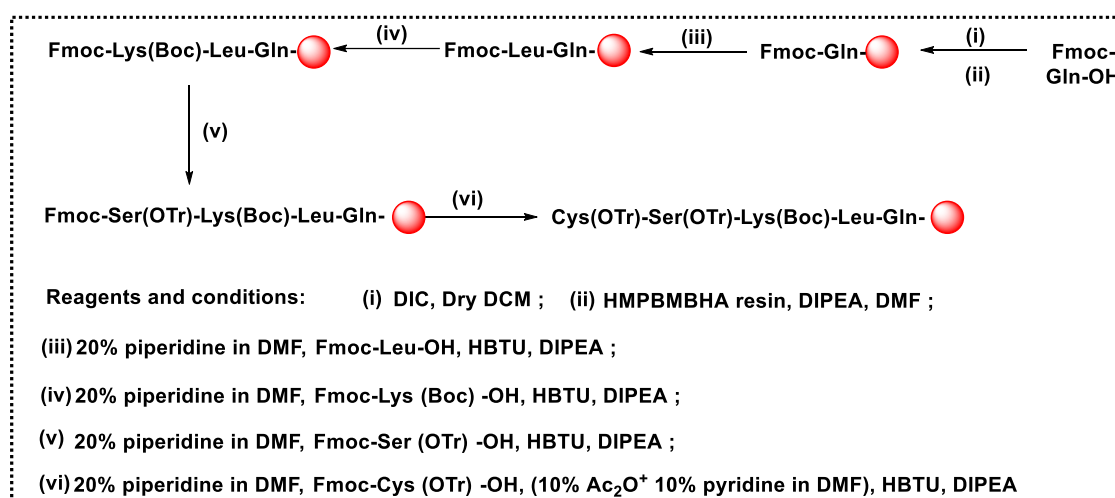


Figure 2.7. A) SPPS adopted for the synthesis of PSA peptide sequence, **Cys-Ser-Lys-Leu-Gln-OH**.

Subsequently, the synthesized peptide sequence was coupled with Boc deprotected free amino terminal of **TPE-In** in the presence of 1-Ethyl-3-(3-dimethylaminopropyl) carbodiimide (EDC) using Hydroxybenzotriazole (HOBt) as coupling agent and characterized by proton nuclear magnetic resonance (¹H NMR) and mass spectral analysis. Trityl group of Cys residue from **TPE-In-PSA** counterpart underwent deprotection by 20% trifluoroacetic acid (TFA) in dichloromethane (DCM) which resulted free thiol functionality. The free thiol moiety undergoes chemisorption on AuNPs surface resulting in a formation of the targeted nanoprobe, **TPE-In-PSA@Au**. Nanoprobe then characterized using UV-Vis absorption spectroscopy and TEM analysis. A shift in the absorption maxima is observed from the absorption spectrum is due to the incorporation of peptide bearing TPE on to the surface of AuNPs (Figure 2.8).

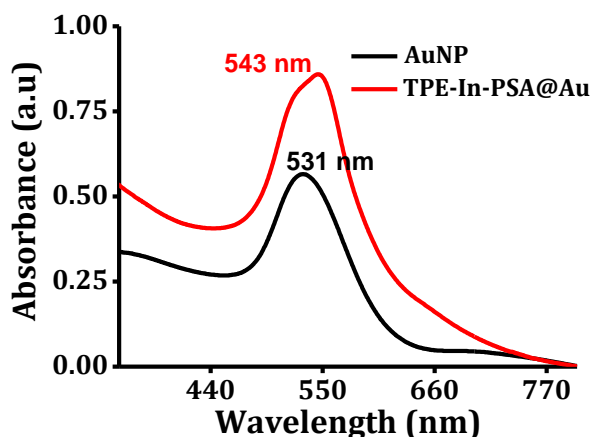


Figure 2.8. Representative absorption spectra of the **TPE-In-PSA** Nanoprobe showing the changes before and after the incorporation of AuNPs.

The fluorescent property of **TPE-In-PSA** has been monitored upon incubation with different percentage of colloidal AuNPs which exhibited ACQ effect similar to **TPE-In-Boc**, but the strong quenching efficiency was observed because of internal charge transfer between the AuNPs and the TPE moiety. These two reversal effects i.e. fluorescence quenching and SERS signal enhancement envisaged at 90% of colloidal AuNPs solution.

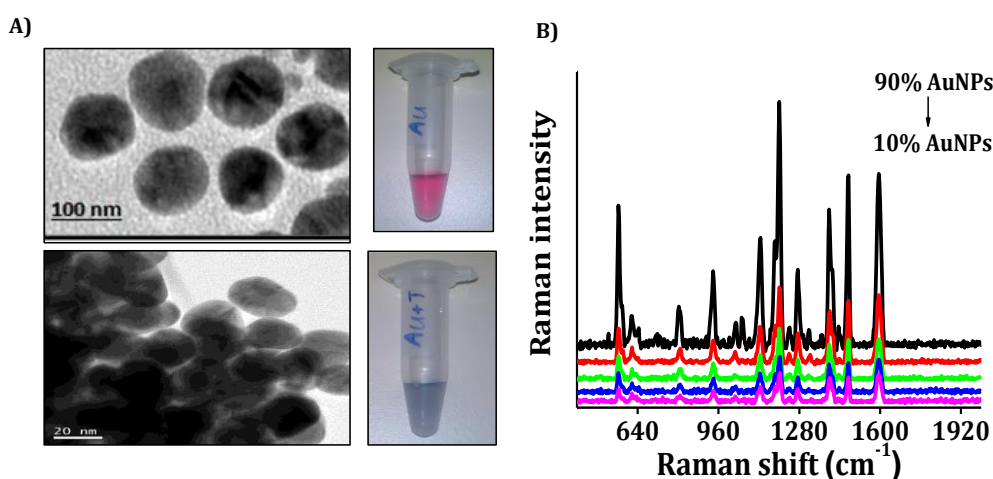


Figure 2.9. A) TEM images of (top) gold nanoparticle alone and (bottom) **TPE-In-PSA@Au** nanoprobe and corresponding visual color changes. B) SERS spectra of **TPE-In-PSA@Au** nanoprobe by varying the percentage of gold concentration.

The maximum SERS signal enhancement occurred at 90% of colloidal AuNPs which is further reflected in a visible colour change from red to blue attributed to the formation of **TPE-In-PSA** and AuNP aggregates (**Figure 2.9A&B**). Subsequently, more hotspots are generated which significantly enhances the SERS intensity.

2.3.5. PSA Protease detection and LOD calculation through SERS

For the detection of PSA protein, the initial study was performed by incubating PSA protease in PSA buffer within **TPE-In-PSA@Au** nanoprobe at 37 °C.³⁰ During incubation with PSA protease the target specific peptide sequence from **TPE-In-PSA** was cleaved and **TPE-In** detached from AuNPs, and subsequently, gradual decrease in SERS signal intensity was observed. Interestingly, with time the SERS intensity of the nanoprobe was minimized and completely lost after 210 min (**Figure 2.10A**).

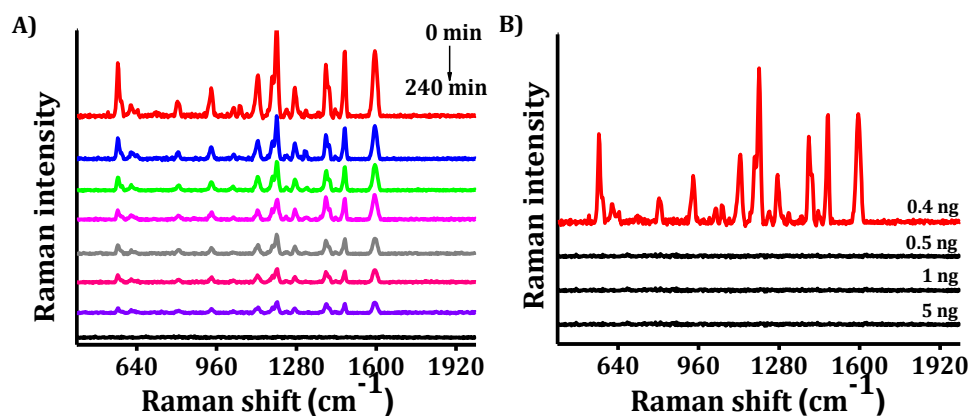


Figure 2.10. A) Time-dependent changes in SERS spectra of **TPE-In-PSA@Au** nanoprobe after the incubation of 0.5 ng of the PSA protease in PSA buffer solution at 37 °C recorded at each 30 min. B) SERS spectra showing the limit of detection by varying the concentration of PSA protease.

LOD was evaluated of the probe through SERS spectra by changing the concentration of the PSA protease (5, 1, 0.5, and 0.4 ng). **Figure 2.10B** represents the SERS spectra showing the limit of detection by varying the concentration of PSA enzyme which is

responsible for the effective cleavage of the peptide sequence at 210 min. The LOD of our probe was found to be 0.5 ng of PSA protease, which could effectively cleave the peptide sequence.

2.3.6. PSA expression and cytotoxicity study on cancer cell lines

PSA expression varies between cancer types and hence PSA expression was investigated on LNCaP and cervical cancer (HeLa) cells by western blot analysis using PSA antibodies. Quantitative evaluation of the bands was performed after normalizing with that of β -actin which indicated significantly high expression of PSA on LNCaP than HeLa cells (**Figure 2.11A**). In this context, LNCaP could be used as positive and HeLa as negative control for the PSA expression studies. The results obtained was correlated with other similar studies reported in the literature.³¹ Evaluation of the cytotoxicity of **TPE-In-PSA@Au** nanoprobe was performed on both the cell lines by 3-[4,5-dimethylthiazol-2yl]-2, 5 diphenyl tetrazolium (MTT) assay against a wide dose range (0.005 mM to 1 mM) for 4, 8, and 12 hr including doxorubicin (1 μ M) as positive control. It was observed that the nanoprobe was largely nontoxic to both the cell lines for all doses and time periods (**Figure 2.11B&C**), whereas the positive control Dox demonstrated its cytotoxicity. The nontoxic behavior of nanoprobe will enable detailed biological assays in all contexts. Further the SERS based assay was carried out for the detection of PSA expression on LNCaP and HeLa cells.

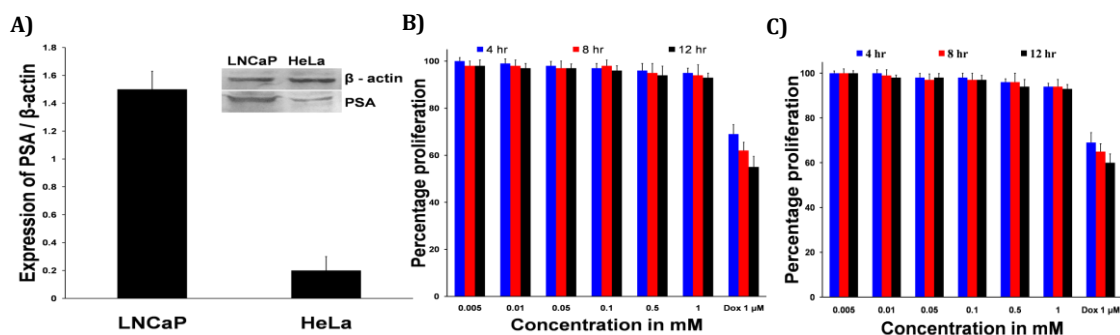


Figure 2.11. A) Protein level expression analysis of PSA on LNCaP and HeLa cell lines by Western blot, the bands normalized to β -actin and quantified using ImageJ software, Cytotoxicity profiles of **TPE-PSA@Au** using MTT assay on (B) LNCaP and (C) HeLa cell line.

2.3.7. Recognition of human prostate cancer cells using SERS nanoprobe

LNCaP cells were cultured in four-well chamber slide and 200 μ L (9:1, Au/**TPE-In-PSA**) of **TPE-In-PSA@Au** nanoprobe were added to the wells separately and was incubated at 37 °C. SERS spectra were recorded after 30 min onward and continued up to 4 hr. Due to the overexpression of PSA on LNCaP cell surfaces, PSA peptide bearing AuNPs was cleaved from **TPE-In-PSA@Au** and AuNPs was internalized without TPE analogue, so that **TPE-In** part is remained in the culture medium. Therefore, the SERS intensity of the **TPE-In** part in the culture medium was decreased gradually with time and completely lost at around 4 hr which resembled to the detection of PSA with concentration dependent manner. To confirm the above-mentioned facts, the SERS spectra inside the cells after 4 hr was monitored but no characteristic spectra were obtained (**Figure 2.12**). Complete absence of SERS spectra inside the cell confirmed the fact that highly expressed PSA enzyme effectively cleaved off the Raman reporter bearing PSA peptide sequence from the nanoprobe. A similar study has been carried out using PSA negative HeLa cells and monitored the SERS intensity from both culture medium and within the cells. In contrary to LNCaP cells, a complete absence of SERS spectra in the culture medium even after 4 hr accompanied by significant SERS intensity was observed inside the cells. The absence of PSA enzyme in HeLa cell enabled the entry of the nanoprobe inside the cell.

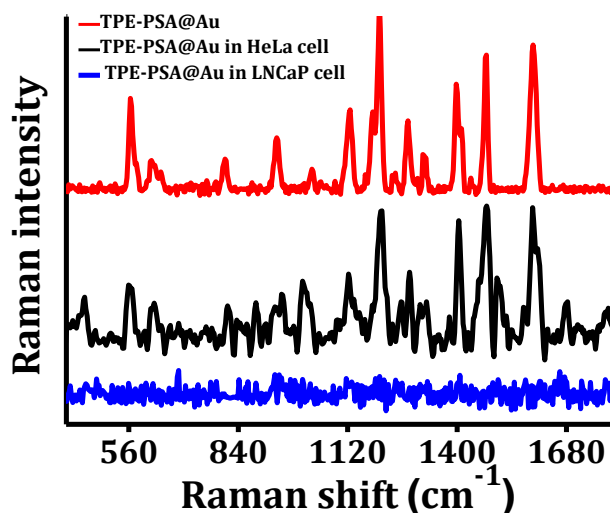


Figure 2.12. SERS spectra analysis of probe incubated on HeLa and LNCaP cells, the spectra were collected after 4 hr washing with PBS solution.

2.3.8 SERS imaging in living cells

After checking the SERS spectra inside the cells, SERS mapping of two cells was performed by confocal Raman microscopy using 0.5 as integration time, 150×150 as points per line and $50 \times 50 \mu\text{m}$ mapping area along X and Y directions. In **figure 1.13**, panels **A, B & C** showed the bright field, Raman images and corresponding single spectra of LNCaP cells respectively, and panels **D, E & F** showed the corresponding bright field, Raman images, and single spectra of HeLa cells. The histogram images^{32,33} in **Figure 1.13G,H** shows the statistical representation of the most intense peak coming from the Raman reporter (I1600/I1100) chemisorbed on AuNPs. From the Raman images and histogram images it is clear that **TPE-In-PSA@Au** nanoprobe is entered only into HeLa cells but not in to LNCaP cells, in which effective cleavage is occurred from the cell surface and **TPE-In-PSA** part failed to enter in to the cells.

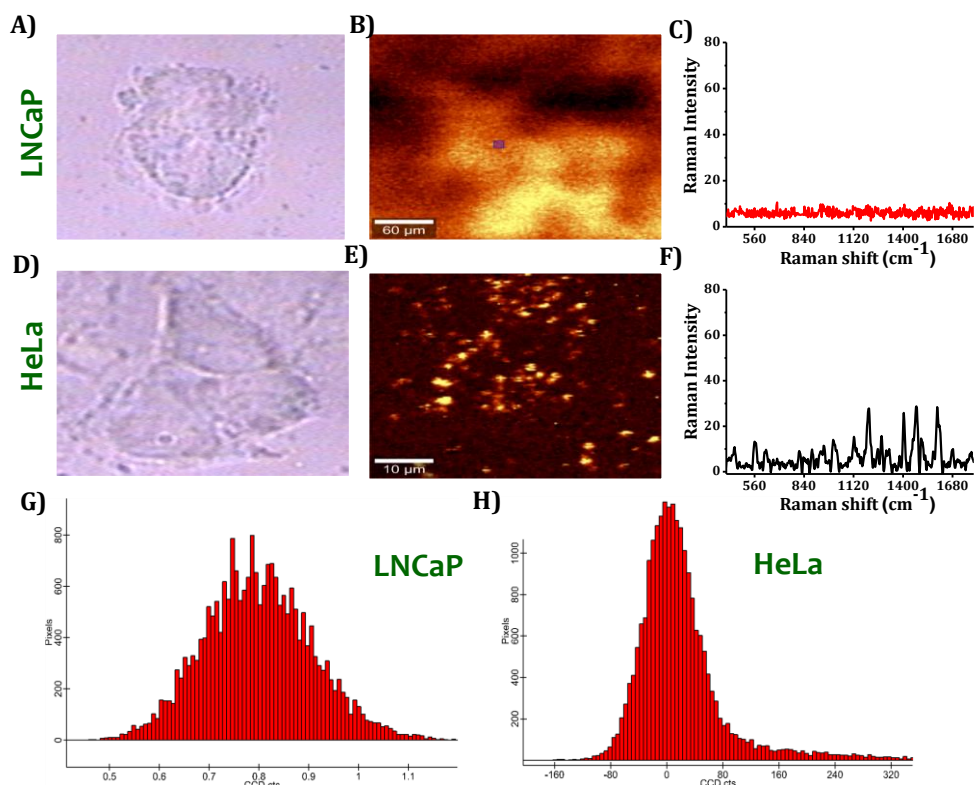


Figure 2.13. Raman imaging of cells with nanoprobe. Bright field image (A) Raman image (B) and single spectrum (C) of LNCaP and Bright field image (D) Raman image (E) and single spectrum (F) of HeLa cells. Histogram representation of the most intense peak coming from the Raman reporter (I1600/I1100) with the gold nanoparticles in (G) LNCaP cells and (H) HeLa cells.

2.4 Conclusions

In summary, a series of five diversified TPE analogues were synthesized and evaluated their predominantly AIE and ACQ phenomenon with excellent SERS fingerprint and multiplex signal pattern. The unique SERS nanoprobe **TPE-In-PSA@Au** has been developed in conjugation with target-specific PSA peptide substrate aiming for the detection of PSA protein. The nanoprobe successfully recognizes PSA enzyme in SERS-based detection platform with a LOD of 0.5 ng which unfold a new avenue in prostate cancer diagnosis. Moreover, **TPE-In-PSA@Au** was nicely predictable by PSA overexpressed LNCaP cells, which was imagined through SERS spectral analysis and SERS mapping. For the first time, a SERS nanoprobe has

been explored that recognizes PSA overexpression on cancer cells using a novel TPE analogue as Raman reporter.

2.5. Materials and methods

2.5.1. General techniques

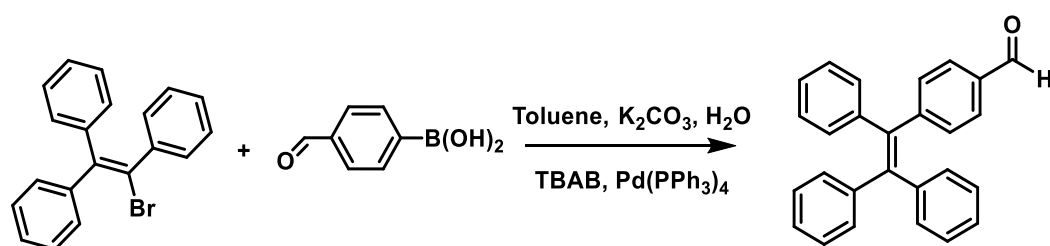
Column chromatography was done on 100–200 mesh Merck 60 silica gel. NMR spectra were noted on Bruker Advance 500 NMR spectrometer, and chemical shifts are showed in parts per million (ppm). The mass spectra were noted on Thermo Scientific Ex-Active Electrospray ionization mass spectrometry (ESI-MS) spectrophotometer. Absorption spectrum of the TPE derivatives was measured on a Shimadzu (UV-2450) UV–vis–NIR spectrophotometer. The emission and excitation spectrum of TPE compounds was recorded on a Spex-Fluorolog FL22 spectrofluorimeter equipped with a double grating 0.22 m Spex 1680 monochromator and a 450 W Xenon (Xe) lamp as the excitation source and a Hamamatsu R928P photomultiplier tube detector. SERS measurements were carried out in a WI-Tec Raman microscope (WI-Tec, Inc., Germany, alpha 300R) with a laser beam directed to the sample through 20X objective with 600 g/mm grating and a Peltier cooled charge-coupled device (CCD) detector. Samples were excited with a 633 nm excitation wavelength laser with 7 mW powers and Stokes shifted Raman spectra were collected in the range of 400–3000 cm^{-1} with 1 cm^{-1} resolution and an integration time of 0.5 and 20 accumulations. Prior to every measurement, a calibration with a silicon standard (Raman peak centered at 520 cm^{-1}) was performed. WI-Tec Project plus (v 2.1) software package was used for data evaluation.

2.5.2. Materials and methods

All reagents were purchased from sigma Aldrich, Merck, and Specrochem. The human cancer cell lines LNCaP and HeLa were obtained from American Type Culture Collection (ATCC, Manassass, VA). Cells are maintained in Dulbecco's Modified Eagle's medium (DMEM) with 10% fetal bovine serum (FBS) and under an atmosphere of 5% carbon dioxide (CO₂) at 37 °C in an incubator.

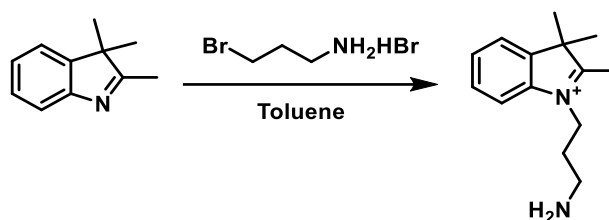
2.5.3 Synthesis of TPE derivatives

2.5.3.1. Synthesis of TPE-CHO



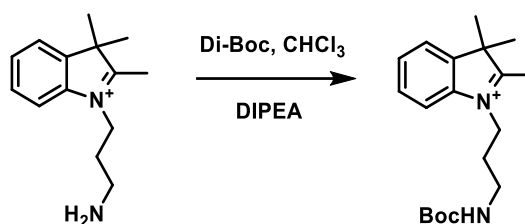
4-formylphenylboronic acid (2.25 g, 15 mmol) and Bromotriphenylethylene (3.35 g, 10 mmol) were dissolved in the mixture of TBAB (0.32 g, 1.0 mmol), toluene (60 mL), and 2 M K₂CO₃ aqueous solution (18 mL). The composition was stirred at room temperature (rt) for 0.5 hr under argon gas. Pd(PPh₃)₄ (0.010 g, 8.70×10⁻³ mmol) was added in to it and heated to 90 °C for 24 hr. Then the mixture was extracted with H₂O and ethyl acetate. After removing the solvent, the residue was chromatographed on a silica gel column with *n*-hexane/ CH₂Cl₂. ¹HNMR (500 MHz, CDCl₃) δ ppm: 9.898 (s, 1H), 7.604-7.620(d, 2H, J=8Hz), 7.182-7.199 (d, 2H, J=8.5Hz), 7.110-7.130 (m, 9H), 6.996-7.034 (m, 6H). HRMS: m/z (C₂₇H₂₀O) calcd: 360.45, found: 361.15 [M+H].

2.5.3.2. Synthesis of indoline propylamine



3-bromopropylamine hydrobromide was added in a seal tube containing 2, 3, 3-trimethyl-3H-indolium under N₂ atmosphere, and was gently heated up to 110 °C in an oil bath. The mixture was kept at 120 °C for 10 hr with stirring. After the reaction was completed, the mixture was cooled down to r.t to form a solid cake that was washed with diethyl ether (Et₂O) and a chloroform (CHCl₃)-Et₂O solution. The resulting solid was then dried under high vacuum to obtain it as a solid.¹HNMR (500 MHz, CDCl₃) δ 7.99-7.66(m, 1H) ,7.26- 7.24(m, 1H), 7.18-7.14 (m, 2H), 3.71(s, 1H), 3.53-3.47(m, 2H), 3.23-3.20(m, 2H), 2.51-2.43(m, 2H), 1.54(s, 6H), 1.25(s, 3H); HRMS: (FAB), m/z (C₁₄H₂₁N₂⁺) calcd: 217.3299, found: 217.3222.

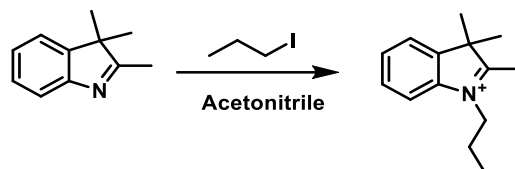
2.5.3.3. Synthesis of boc protected indoline propylamine



1-(3-aminopropyl) – 2, 3, 3- tri-methyl indolium and di-tert-butyl dicarbonate were added to a mixture of dry CHCl₃ and diisopropylethylamine (DIPEA). The reaction mixture was gently heated to reflux temperature and stirred for 4hr. Afterwards, the organic layer was extracted with Et₂O, dried and purified by column using DCM and methanol yielded the product as a brown liquid.¹HNMR (500 MHz, CDCl₃): δ 7.12 -7.07(m, 2H), 6.76 (d, 1H, J=7.5 Hz), 6.52(d, 1H), 4.62(s, 1H), 3.85(d, 2H,

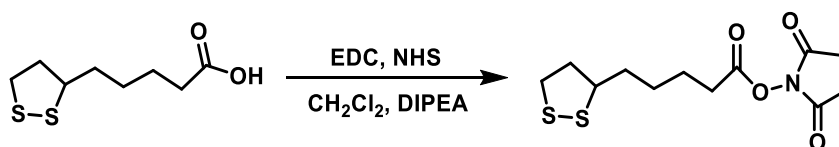
$J=10$ Hz), 3.27(d, 2H, $J=5$ Hz), 1.57(s, 9H), 1.42(s, 6H), 1.32(s, 3H); HR-MS: (FAB), m/z ($C_{19}H_{29}N_2O_2^+$) calcd: 317.4458, found: 317.4410.

2.5.3.4. Synthesis of indoline propyl



To a solution of 2, 3, 3-trimethyl-3H-indole in acetonitrile, 1-iodopropane was added, and refluxed with continuous stirring for 15 hr. The mixture was recrystallized in acetone to obtain the product as a white solid. 1H NMR (500 MHz, $CDCl_3$) δ 7.67(t, 1H, $J=5$ Hz), 7.59(t, 3H, $J=5.5$ Hz), 4.70 (t, 2H, $J=7.5$ Hz), 3.14(s, 3H), 2.06-2.01(m, 2H), 1.67(s, 6H), 1.62(s, 3H), 1.10(t, 3H, $J=7.5$ Hz) HR-MS: (FAB), m/z ($C_{14}H_{20}N^+$) calcd: 202.3153, found: 202.3121.

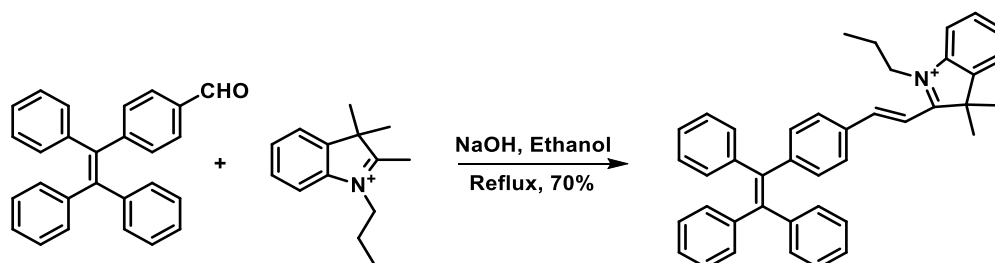
2.5.3.5. Synthesis of lipoic acid succinimidyl ester



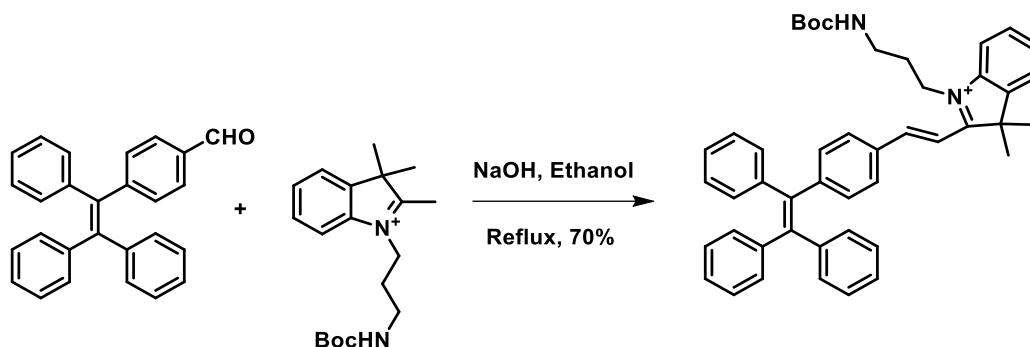
To a solution of EDC in DCM, DIPEA was added and stirred for 10 min. N-Hydroxysuccinimide (NHS) was added followed by DL-Lipoic acid. The reaction mixture was stirred in an ice bath for half an hr and then slowly continued in r. t for 12 hr. The reaction product was washed with hydrochloric acid (HCl) and H_2O , dried and purified by silica gel column using ethyl acetate and hexane. 1H NMR (500 MHz, $CDCl_3$) δ ppm: 3.557-3.612 (m, 2H), 3.178-3.212 (m, 1H), 3.097-3.133 (m, 2H), 2.617-

2.647 (m, 2H), 2.442-2.5.0 (m, 2H), 1.897-1.964 (m, 2H), 1.750-1.824 (m, 2H), 1.665-1.720 (m, 2H), 1.571-1.624 (m, 2H).

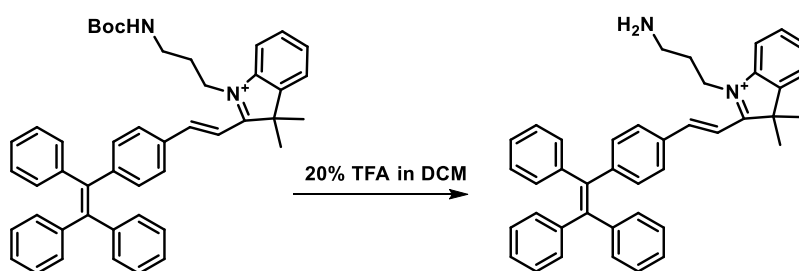
2.5.3.6. Synthesis of TPE-In



A mixture of TPE-CHO (0.20 g, 0.66 mmol), Indoline-propyl (0.24 g, 0.66 mmol) and sodium hydroxide (NaOH) (0.01 g, 0.27 mmol) in ethanol (20 mL) were refluxed for 6 hr under argon. After cooling to r.t, the residue was extracted using DCM and H₂O. The residue was subjected to column chromatography with CH₂Cl₂/CH₃OH as eluent. Compound was obtained as red solid.¹HNMR (500 MHz, CDCl₃)δ ppm: 8.033-8.066 (d, 1H, J=16.5), 7.861-7.878 (d, 2H, J=8.5Hz), 7.758-7.791(d, 1H, J=16.5Hz), 7.584-7.628 (m, 6H), 7.542-7.576 (m, 3H), 7.215-7.232(d, 3H, J=8.5Hz), 7.159-7.170 (t, 2H), 6.994-7.111 (m, 2H), 6.728-6.758 (t, 1H), 6.523-6.539 (d, 1H, 8Hz), 3.442-3.471 (t, 2H), 1.836 (s, 6H), 1.329 (s, 3H), 2.017-2.061 (m, 2H).¹³C NMR (500 MHz, CDCl₃)δ ppm: 188.49, 174.56, 143.69, 142.74, 140.56, 132.76, 131.34, 128.98, 128.01, 126.99, 100.00, 96.13, 70.29, 65.19, 63.39, 53.43, 51.81, 48.95, 45.38, 34.17, 31.51, 29.63, 28.40, 27.31, 24.92, 22.70, 14.13. HRMS:m/z (C₄₁H₃₈ N⁺) calcd: 544.75, found: 544.29.

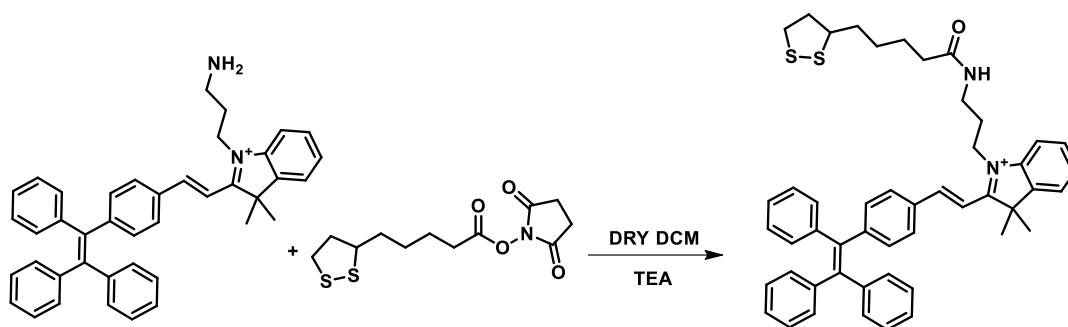
2.5.3.7. Synthesis of TPE-In-NH₂-Boc

A mixture of TPE-CHO (0.20 g, 0.66 mmol), Indoline-Boc (0.24 g, 0.66 mmol) and NaOH (0.01 g, 0.27 mmol) in ethanol (20 mL) were refluxed for 6.0 hours under argon. The residue was purified by column chromatography with CH₂Cl₂/CH₃OH as eluant. Compound was obtained as red solid.¹HNMR (500 MHz, CDCl₃) δ ppm: 7.982-8.014 (d, 1H, J=16Hz), 7.831-7.863 (d, 1H, J=16Hz), 7.735-7.751 (d, 1H, J=8Hz), 7.654-7.669 (d, 1H, J=7.5Hz), 7.510-7.621 (m, 2H), 7.183-7.199 (d, 8H, J=8Hz), 7.122-7.052 (m, 6H), 6.999-7.024 (m, 3H), 4.930-4.944 (t, 2H), 4.689 (s, 1H), 3.311-3.485 (t, 2H), 1.782 (s, 6H), 1.405-1.428 (t, 2H), 1.326 (s, 9H).¹³C NMR (500 MHz, CDCl₃) δ ppm: 191.97, 181.40, 151.12, 143.06, 140.53, 132.71, 131.76, 131.29, 130.48, 129.91, 129.17, 128.00, 127.29, 122.44, 115.16, 111.87, 53.44, 45.04, 34.18, 31.64, 29.47, 28.36, 24.92, 14.13. HRMS: m/z (C₄₆H₄₇ N₂O₂⁺) calcd: 659.88, found: 659.36.

2.5.3.8. De-protection of Boc from TPE-In-NH₂-Boc

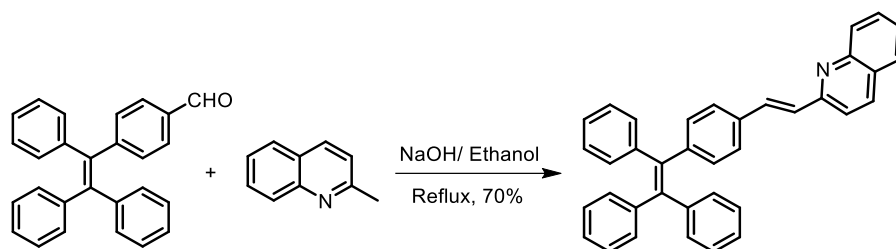
The Boc protected TPE-In-Boc compound is dissolved in dry DCM. Add around 5 ml of 20% TFA in DCM and stirred for 2 hr and checked the TLC to make sure that the compound is deprotected. Also the deprotection was confirmed by Mass. HRMS: m/z calcd: 559.88, found: 559.36.

2.5.3.9. Synthesis of TPE-In-L



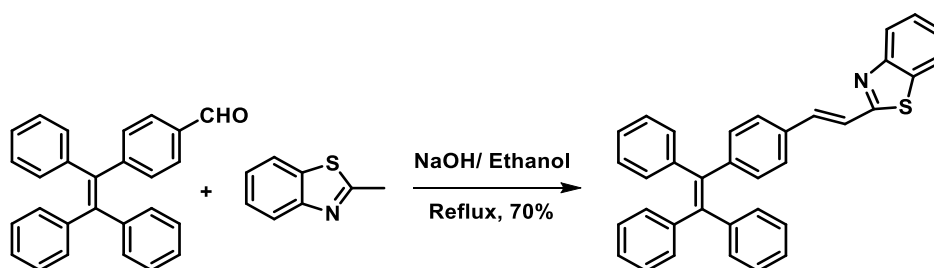
TPE-In-NH₂ (0.063g, 1 mmol), Triethylamine (TEA) (0.2ml, 0.56 mmol) are stirred for 10 min, after that add lipoic acid succinimidyl ester (0.119 g, 0.39 mmol) in to it and continue stirring overnight. The residue was subjected to column chromatography with CH₂Cl₂/CH₃OH as eluant. Compound was obtained as red solid.¹HNMR (500 MHz, CDCl₃) δ ppm: 8.352 (s, 1H), 7.981-8.013 (d, 1H, J=16Hz), 7.794-7.821 (t, 1H), 7.593-7.621 (t, 1H), 7.540-7.569 (m, 6H), 7.501-7.516 (d, 8H, J=7.5Hz), 7.109-7.206 (d, 1H, J=8Hz), 7.001-7.161 (m, 6H), 6.616-6.33 (d, 1H, J=8.5Hz), 3.644-3.669 (m, 2H), 3.545-3.482 (m, 2H), 3.372-3.346 (m, 3H), 3.153-3.131 (m, 2H), 2.647-2.276 (m, 2H), 1.783 (s, 6H), 0.676-1.569 (m, 2H). ¹³C-NMR (500MHz, CDCl₃) δ ppm: 172.98, 150.83, 143.02, 139.30, 132.57, 131.33, 129.87, 127.93, 127.70, 124.01, 114.07, 56.51, 52.34, 40.24, 38.4635.91, 34.51, 31.63, 29.62, 27.04, 25.42, 22.70, 14.13. HRMS:m/z (C₄₉H₅₁N₂OS₂⁺) calcd: 748.08, found: 747.34 [M-1].

2.5.3.10. Synthesis of TPE-Q



A mixture of TPE-CHO (0.20 g, 0.66 mmol), Quinaldine (0.24 g, 0.66 mmol) and NaOH (0.01 g, 0.27 mmol) in ethanol (20 mL) were refluxed for 6 hr under argon. Column chromatography was done with CH₂Cl₂/CH₃OH as eluant. Compound was obtained as yellow solid. ¹HNMR (500 MHz, CDCl₃) δ ppm: 8.022-8.039 (d, 1H, J=8.5Hz), 7.750-7.766 (d, 2H, 8Hz), 7.655-7.688 (m, 2H), 7.455-7.484 (t, 6H), 7.264-7.81 (d, 6H, J=8.5), 7.090-7.116 (m, 6H), 7.023-7.058 (m, 4H). ¹³C NMR (500 MHz, CDCl₃) δ ppm: 188.81, 146.38, 145.02, 143.39, 142.61, 141.37, 140.28, 134.13, 132.84, 131.85, 131.35, 128.71, 127.80, 126.67, 125.09, 125.03. HRMS:m/z (C₃₇H₂₇N) calcd: 485.62, found: 486.22[M+1].

2.5.3.11. Synthesis of TPE-B



A mixture of TPE-CHO (0.20 g, 0.66 mmol), Benzothiazole (0.24 g, 0.66 mmol) and NaOH (0.01 g, 0.27 mmol) in ethanol (20 mL) were refluxed for 6 hr under argon. The residue was subjected to column chromatography with CH₂Cl₂/CH₃OH as eluant. Compound was obtained as yellow solid. ¹HNMR (500 MHz, CDCl₃) δ ppm: 7.585-7.617 (d, 1H, J=16Hz), 7.390-7.423 (d, 1H, J=16.5), 7.317-7.333 (d, 2H, 8Hz), 7.267-7.283 (d,

8H, J=8Hz), 7.205-7.283 (m, 6H), 7.089-7.115 (5H, m), 6.923-6.955 (d, 1H, J=16Hz), 6.601-6.634 (d, 1H, 16.5Hz). ¹³C NMR (500 MHz, CDCl₃) δ ppm: 198.40, 188.74, 146.45, 146.37, 143.50, 143.25, 142.88, 141.38, 140.13, 132.33, 127.83, 126.67, 122.36, 121.38. HRMS:m/z (C₃₅H₂₅NS) calcd: 491.64, found: 492.17[M+1].

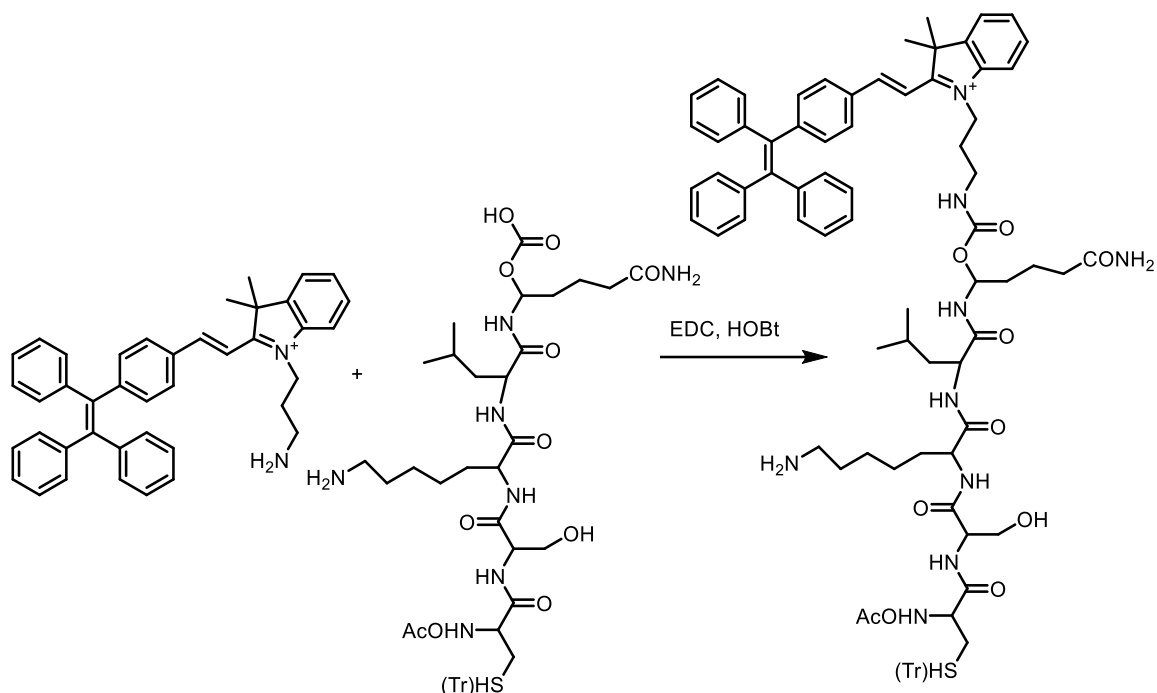
2.5.3.12. Solid Phase Peptide Synthesis of PSA peptide sequence

First amino acid Glutamine was charged to HMPB-MBHA resin using N,N'-Diisopropylcarbodiimide (DIC), Dry DCM, DIPEA and Dimethylformamide (DMF). After that deprotection of Fmoc group with 20% piperidine in DMF yielded amine functionalised glutamine bearing resin, which was coupled to the second amino acid leucine in a condition of (2-(1H-benzotriazol-1-yl)-1,1,3,3-tetramethyluronium hexafluorophosphate (HBTU) and DIPEA to afford the Leu-Gln bearing resin. Following the same procedure, three different amino acids (Lys, Ser and Cys) were subsequently incorporated on to the resin by simple coupling reactions. Deprotection of the amine groups, followed with capping with acetic anhydride and cleaving from resin gave the desired PSA peptide sequence. The peptide is characterized by Mass and ¹H NMR. ¹H NMR (500 MHz, CDCl₃) δ ppm: 8.918-8.928 (d, 1H, J=5Hz), 8.062 (s, 1H), 7.402 (s, 2H), 7.259-7.311 (m, 15H), 6.038 (s, 2H), 4.273-4.382 (m, 1H), 3.716-3.925 (m, 3H), 2.667-2.651 (d, 2H, J=8Hz), 1.910 (s, 1H), 1.667 (s, 6H), 1.414 (s, 3H), 0.830-1.251 (m, 21H).

2.5.3.13. Coupling reaction between TPE-In-Boc and PSA peptide sequence

A mixture of Boc deprotected TPE-In (25 mg, 0.044 mmol) and PSA peptide sequence (43.14 mg, 0.05 mmol) was dissolved in dry DCM. To this EDC (17.14 mg, 0.09 mmol) and HOBT (12.08 mg, 0.09 mmol) was added and stirred for 24 hr under

nitrogen atmosphere. The residue was subjected to column chromatography with $\text{CH}_2\text{Cl}_2/\text{MeOH}$ as eluent.



¹HNMR (500 MHz, CDCl_3) δ ppm: 11.001 (s, 6H), 7.817-7.827 (d, 11H, $J=5\text{Hz}$), 7.692 (s, 1H), 7.314-7.394 (m, 11H), 7.244-7.296 (m, 12H), 6.669-6.701 (d, 1H, $J=16\text{Hz}$), 6.097-6.113 (d, 1H, $J=8\text{Hz}$), 3.271 (s, 6H), 3.124-3.116 (m, 12H), 2.838 (s, 3H), 1.948 (s, 1H), 1.395 (s, 6H), 1.258 (s, 6H), 1.045-1.073 (m, 10H), 0.835-0.891 (m, 12H).

2.5.4. Synthesis of gold nanoparticles

For the synthesis 40 nm AuNPs, water was first heated until boiling and adds Chloroauric acid solution in to it and again boiled for 10 min. After 10 min sodium citrate solution was added, resulting in the colour change from pale yellow to dark purple to red. The colour change to red will take around 5 min and heating was stopped to let the solution to cool for 90 min to r.t. The whole reaction was accompanied with constant stirring by a Teflon coated magnetic stir bar at 400 rpm. Formed nanoparticle was characterized by UV visible spectroscopy and TEM.

2.5.5. Western blot analysis

Proteins were extracted from 2×10^6 cells/petridish using Pierce® RIPA buffer (Thermo Scientific, Rockford, USA). Protein concentrations were determined using Coomassie, plus protein assay reagent and bovine serum albumin (BSA) standards (Pierce, Rockford, IL, USA). Approximately 50 µg of proteins were separated on 10% sodium dodecyl sulphate PAGE (SDS-PAGE) and transferred to poly vinylidene- di fluoride membrane (Millipore, Billerica, MA, USA). The membrane was blocked using 5% of BSA (Santa Cruz Biotechnology, Inc. TX, USA) and incubated with the specific primary antibodies (Sigma-Aldrich, St. Louis, MO, USA). Alkaline phosphatase conjugated secondary antibody (Sigma-Aldrich) was used for all the primary antibodies and detected by the colorimetric substrate BCIP®/NBT (Sigma-Aldrich,). The bands were then quantitated using Image J software (NIH, USA) and normalized with β -actin.

2.5.6. Cytotoxicity assay

The growth inhibitory capacity of various constructs was evaluated by MTT assay as previously reported. The absorbance was measured at 570 nm using a micro plate spectrophotometer (BioTek, Power Wave XS) after incubation for 12, 24 and 48 hours with respective compounds. The percentage proliferation and inhibition of the cells were calculated with the following formulas:

$$\text{Percentage Proliferation} = [\text{Abs sample} / \text{Abs control}] \times 100$$

$$\text{Percentage Inhibition} = 100 - \text{percentage Proliferation}$$

2.6 References

- (1) Zhang, X.; Chi, Z.; Li, H.; Xu, B.; Li, X.; Zhou, W.; Liu, S.; Zhang, Y.; Xu, J. Piezofluorochromism of an Aggregation-Induced Emission Compound Derived from Tetraphenylethylene. *Chem. - An Asian J.* **2011**, *6* (3), 808–811. <https://doi.org/10.1002/asia.201000802>.
- (2) Zhang, X.; Zhang, X.; Tao, L.; Chi, Z.; Xu, J.; Wei, Y. Aggregation Induced Emission-Based Fluorescent Nanoparticles: Fabrication Methodologies and Biomedical Applications. *J. Mater. Chem. B* **2014**, *2* (28), 4398–4414. <https://doi.org/10.1039/c4tb00291a>.
- (3) Luo, J.; Xie, Z.; Xie, Z.; Lam, J. W. Y.; Cheng, L.; Chen, H.; Qiu, C.; Kwok, H. S.; Zhan, X.; Liu, Y.; Zhu, D.; Tang, B. Z. Aggregation-Induced Emission of 1-Methyl-1,2,3,4,5-Pentaphenylsilole. *Chem. Commun.* **2001**, *18*, 1740–1741. <https://doi.org/10.1039/b105159h>.
- (4) Tang, B. Z.; Zhan, X.; Yu, G.; Sze Lee, P. P.; Liu, Y.; Zhu, D. Efficient Blue Emission from Siloles. *J. Mater. Chem.* **2001**, *11* (12), 2974–2978. <https://doi.org/10.1039/b102221k>.
- (5) Li, Y.; Xu, L.; Su, B. Aggregation Induced Emission for the Recognition of Latent Fingerprints. *Chem. Commun.* **2012**, *48* (34), 4109–4111. <https://doi.org/10.1039/c2cc30553d>.
- (6) Shi, H.; Kwok, R. T. K.; Liu, J.; Xing, B.; Tang, B. Z.; Liu, B. Real-Time Monitoring of Cell Apoptosis and Drug Screening Using Fluorescent Light-up Probe with Aggregation-Induced Emission Characteristics. *J. Am. Chem. Soc.* **2012**, *134* (43), 17972–17981. <https://doi.org/10.1021/ja3064588>.
- (7) Chen, X.; Shen, X. Y.; Guan, E.; Liu, Y.; Qin, A.; Sun, J. Z.; Tang, B. Z. A Pyridinyl-Functionalized Tetraphenylethylene Fluorogen for Specific Sensing of Trivalent

- Cations. *Chem. Commun.* **2013**, 49 (15), 1503–1505.
<https://doi.org/10.1039/c2cc38246f>.
- (8) Zhu, Z.; Xu, L.; Li, H.; Zhou, X.; Qin, J.; Yang, C. A Tetraphenylethene-Based Zinc Complex as a Sensitive DNA Probe by Coordination Interaction. *Chem. Commun.* **2014**, 50 (53), 7060–7062. <https://doi.org/10.1039/c4cc02172j>.
- (9) Zhang, L.; Hu, W.; Yu, L.; Wang, Y. Click Synthesis of a Novel Triazole Bridged AIE Active Cyclodextrin Probe for Specific Detection of Cd²⁺. *Chem. Commun.* **2015**, 51 (20), 4298–4301. <https://doi.org/10.1039/C4CC09769F>.
- (10) Huang, X.; Gu, X.; Zhang, G.; Zhang, D. A Highly Selective Fluorescence Turn-on Detection of Cyanide Based on the Aggregation of Tetraphenylethylene Molecules Induced by Chemical Reaction. *Chem. Commun.* **2012**, 48 (100), 12195–12197. <https://doi.org/10.1039/c2cc37094h>.
- (11) Liang, G.; Lam, J. W. Y.; Qin, W.; Li, J.; Xie, N.; Tang, B. Z. Molecular Luminogens Based on Restriction of Intramolecular Motions through Host–Guest Inclusion for Cell Imaging. *Chem. Commun.* **2014**, 50 (14), 1725–1727. <https://doi.org/10.1039/c3cc48625g>.
- (12) Jayaram, D. T.; Ramos-Romero, S.; Shankar, B. H.; Garrido, C.; Rubio, N.; Sanchez-Cid, L.; Gómez, S. B.; Blanco, J.; Ramaiah, D. In Vitro and in Vivo Demonstration of Photodynamic Activity and Cytoplasm Imaging through TPE Nanoparticles. *ACS Chem. Biol.* **2016**, 11 (1), 104–112. <https://doi.org/10.1021/acscchembio.5b00537>.
- (13) Qiao, J.; Liu, Z.; Tian, Y.; Wu, M.; Niu, Z. Multifunctional Self-Assembled Polymeric Nanoprobes for FRET-Based Ratiometric Detection of Mitochondrial H₂O₂ in Living Cells. *Chem. Commun.* **2015**, 51 (17), 3641–3644. <https://doi.org/10.1039/c4cc09120e>.

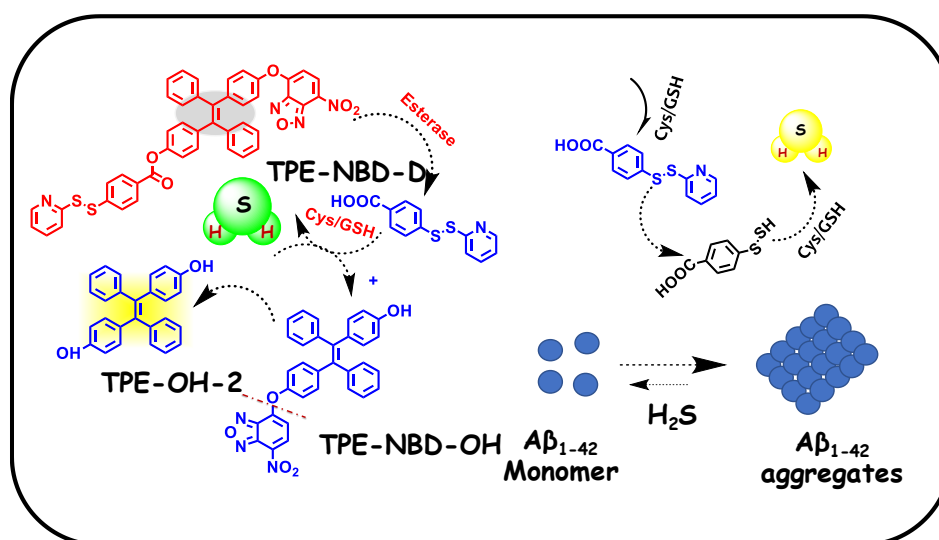
- (14) Yuan, Y.; Kwok, R. T. K.; Feng, G.; Liang, J.; Geng, J.; Tang, B. Z.; Liu, B. Rational Design of Fluorescent Light-up Probes Based on an AIE Luminogen for Targeted Intracellular Thiol Imaging. *Chem. Commun.* **2014**, *50* (3), 295–297. <https://doi.org/10.1039/c3cc47585a>.
- (15) Samanta, A.; Maiti, K. K.; Soh, K. S.; Liao, X.; Vendrell, M.; Dinish, U. S.; Yun, S. W.; Bhuvaneswari, R.; Kim, H.; Rautela, S.; Chung, J.; Olivo, M.; Chang, Y. T. Ultrasensitive Near-Infrared Raman Reporters for SERS-Based in Vivo Cancer Detection. *Angew. Chemie - Int. Ed.* **2011**, *50* (27), 6089–6092. <https://doi.org/10.1002/anie.201007841>.
- (16) Maiti, K. K.; Dinish, U. S.; Samanta, A.; Vendrell, M.; Soh, K. S.; Park, S. J.; Olivo, M.; Chang, Y. T. Multiplex Targeted in Vivo Cancer Detection Using Sensitive Near-Infrared SERS Nanotags. *Nano Today* **2012**, *7* (2), 85–93. <https://doi.org/10.1016/j.nantod.2012.02.008>.
- (17) Joseph, M. M.; Narayanan, N.; Nair, J. B.; Karunakaran, V.; Ramya, A. N.; Sujai, P. T.; Saranya, G.; Arya, J. S.; Vijayan, V. M.; Kumar, K. Exploring the Margins of SERS in Practical Domain : An Emerging Diagnostic Modality for Modern Biomedical Applications. *Biomaterials* **2018**, *181*, 140–181. <https://doi.org/10.1016/j.biomaterials.2018.07.045>.
- (18) Mattley, Y.; Allen, M. W. Innovative Raman Sampling. *Opt. Photonik* **2013**, *8* (4), 44–47. <https://doi.org/10.1002/opph.201300033>.
- (19) Narayanan, N.; Karunakaran, V.; Paul, W.; Venugopal, K.; Sujathan, K.; Kumar Maiti, K. Aggregation Induced Raman Scattering of Squaraine Dye: Implementation in Diagnosis of Cervical Cancer Dysplasia by SERS Imaging. *Biosens. Bioelectron.* **2015**, *70*, 145–152. <https://doi.org/10.1016/j.bios.2015.03.029>.

- (20) Huh, Y. S.; Chung, A. J.; Erickson, D. Surface Enhanced Raman Spectroscopy and Its Application to Molecular and Cellular Analysis. *Microfluid. Nanofluidics* **2009**, *6* (3), 285–297. <https://doi.org/10.1007/s10404-008-0392-3>.
- (21) Ramya, A.; Samanta, A.; Nisha, N.; Chang, Y. T.; Maiti, K. K. New Insight of Squaraine-Based Biocompatible Surface-Enhanced Raman Scattering Nanotag for Cancer-Cell Imaging. *Nanomedicine (Lond)* **2015**, *10* (4), 561–571. <https://doi.org/10.2217/nnm.14.125>.
- (22) Murelli, R. P.; Zhang, A. X.; Michel, J.; Jorgensen, W. L.; Spiegel, D. A. Chemical Control over Immune Recognition: A Class of Antibody-Recruiting Small Molecules That Target Prostate Cancer. *J. Am. Chem. Soc.* **2009**, *131* (47), 17090–17092. <https://doi.org/10.1021/ja906844e>.
- (23) Li, J.; Ma, H.; Wu, D.; Li, X.; Zhao, Y.; Zhang, Y.; Du, B.; Wei, Q. A Label-Free Electrochemiluminescence Immunosensor Based on KNbO_3 - Au Nanoparticles @ Bi_2S_3 for the Detection of Prostate Specific Antigen. *Biosens. Bioelectron.* **2015**, *74*, 104–112. <https://doi.org/10.1016/j.bios.2015.06.027>.
- (24) Liu, D.; Huang, X.; Wang, Z.; Jin, A.; Sun, X.; Zhu, L.; Wang, F.; Ma, Y.; Niu, G.; Hight Walker, A. R.; Chen, X. Gold Nanoparticle-Based Activatable Probe for Sensing Ultralow Levels of Prostate-Specific Antigen. *ACS Nano* **2013**, *7* (6), 5568–5576. <https://doi.org/10.1021/nn401837q>.
- (25) Li, S.; Zhang, Y.; Xu, J.; Li, L.; Zeng, Q.; Lin, L. Noninvasive Prostate Cancer Screening Based on Serum Surface-Enhanced Raman Spectroscopy and Support Vector Machine. *Appl. Phys. Lett.* **2014**, *105*, 0911041–0911044. <https://doi.org/10.1063/1.4892667>.
- (26) Mistro, G. Del; Cervo, S.; Mansutti, E.; Spizzo, R.; Colombatti, A.; Belmonte, P.; Zucconelli, R.; Steffan, A.; Sergio, V.; Bonifacio, A. Surface-Enhanced Raman

- Spectroscopy of Urine for Prostate Cancer Detection: A Preliminary Study. *Anal. Bioanal. Chem.* **2015**, *407* (12), 3271–3275. <https://doi.org/10.1007/s00216-015-8610-9>.
- (27) Kneipp, K.; Kneipp, H.; Itzkan, I.; Dasari, R. R.; Feld, M. S. Surface-Enhanced Raman Scattering and Biophysics. *J. Phys. Condens. Matter* **2002**, *14* (18). <https://doi.org/10.1088/0953-8984/14/18/202>.
- (28) Beierlein, F. R.; Othersen, O. G.; Lanig, H.; Schneider, S.; Clark, T. Simulating FRET from Tryptophan: Is the Rotamer Model Correct? *J. Am. Chem. Soc.* **2006**, *128* (15), 5142–5152. <https://doi.org/10.1021/ja058414l>.
- (29) V. Krishnakumar, V. B. FTIR, FT-Raman Spectral Analysis and Normal Coordinate Calculations of 2-Hydroxy-3-Methoxybenzaldehyde Thiosemicarbozone. *Indian J. Pure Appl. Phys.* **2004**, *42*, 313–318.
- (30) Goun, E. a.; Shinde, R.; Dehnert, K. W.; Adams-Bond, A.; Wender, P. a.; Contag, C. H.; Franc, B. L. Intracellular Cargo Delivery by an Octaarginine Transporter Adapted to Target Prostate Cancer Cells through Cell Surface Protease Activation. *Bioconjug. Chem.* **2006**, *17*, 787–796. <https://doi.org/10.1021/bc0503216>.
- (31) Shelke, A. R. , Roscoe, J. A. , Morrow, G. R. , Colman, L. K. , Banerjee, T. K. , & Kirshner, J. J. Carbon Nanotube Amplification Strategies for Highly Sensitive Immunodetection of Cancer Biomarkers. *J Am Chem Soc* **2006**, *128* (1), 11199–11205.
- (32) Schwartzberg, A. M.; Oshiro, T. Y.; Zhang, J. Z.; Huser, T.; Talley, C. E. Improving Nanoprobe Using Surface-Enhanced Raman Scattering from 30-Nm Hollow Gold Particles. *Anal. Chem.* **2006**, *78* (13), 4732–4736. <https://doi.org/10.1021/ac060220g>.

- (33) Vendrell, M.; Maiti, K. K.; Dhaliwal, K.; Chang, Y. Surface-Enhanced Raman Scattering in Cancer Detection and Imaging. *Trends Biotechnol.* **2013**, *31* (4), 249–257. <https://doi.org/10.1016/j.tibtech.2013.01.013>.

Tetraphenylethylene based Molecular Probe for Endogenous H₂S Detection and its Therapeutic Potential in Alzheimer's Disease



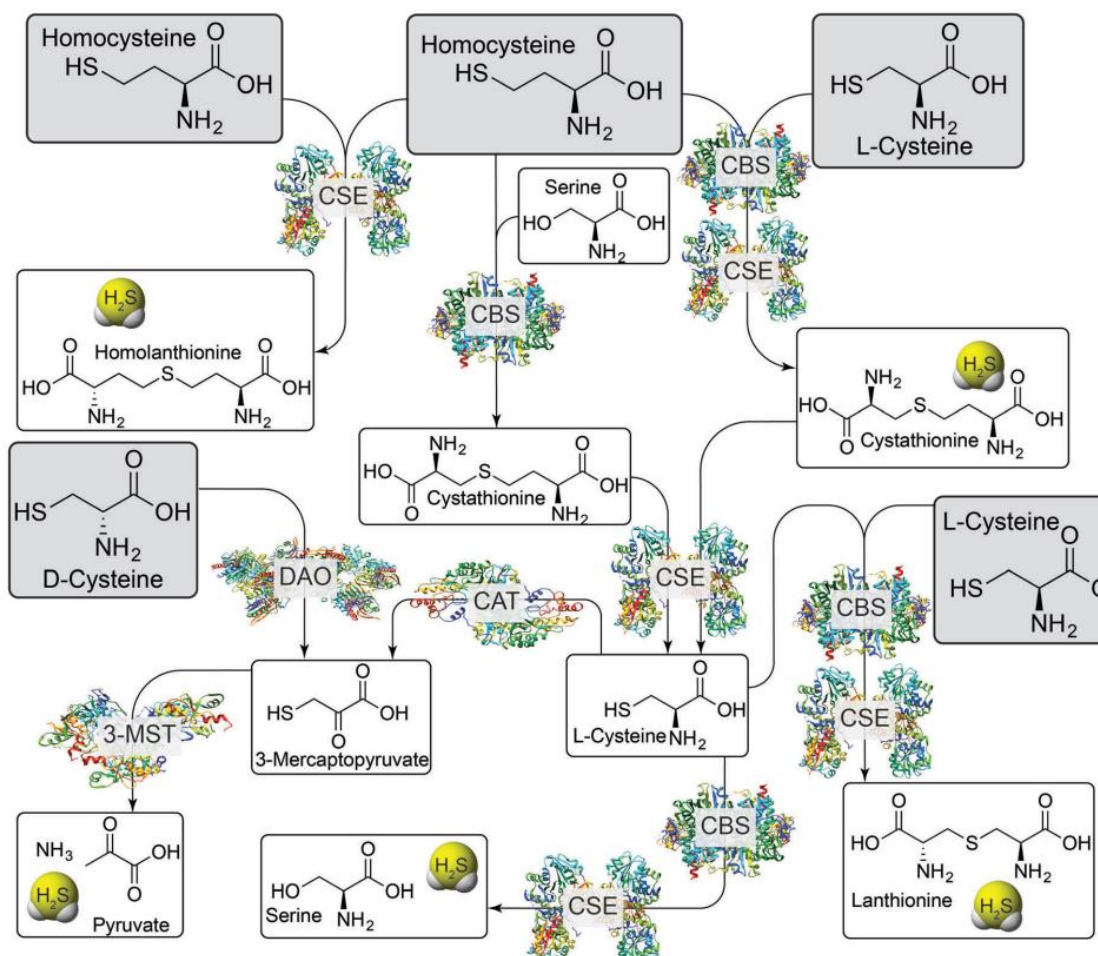
3.1. Abstract:

Beside a gasotransmitter, H₂S act as an important biological mediator for regulating many patho-physiological processes and involved in brain function as a neuromodulator. Lower levels of endogenously produced H₂S may lead to AD, which is a neurodegenerative disorder caused by the aggregation and deposition of amyloid-beta (Aβ) protein in the brain tissue. Development of functional molecules capable of de-agglomerating Aβ aggregates with high specificity has attracted remarkable research attention. Now this challenge can be addressed by the design, synthesis and characterization of an orthogonally substituted TPE dual functional turn on molecular luminophore **TPE-NBD-D**. As-synthesized molecular probe is capable to detect

endogenously produced H₂S in neuroblastoma cell line (SH-SY5Y), and which enable the induction of A β ₁₋₄₂ de-agglomeration to reduce the progression of AD. Furthermore, the AIE of the probe featured its good water solubility, cell membrane permeability, low cytotoxicity and high selectivity towards H₂S. Additionally, the probe generated H₂S in cellular conditions with concomitant detection and imaging of endogenously generated H₂S. This probe was employed for in vivo imaging in mice and enabled to release H₂S in thiol abundant area, which opens up a new insight to understand the involvement of H₂S in the management of AD. Eventually, **TPE-NBD-D** support as a therapeutic entity by sourcing H₂S which experience to the de-agglomeration of A β ₁₋₄₂ sheets and therefore, as a futuristic outcome, this probe can be promoted for clinical utility in the diagnosis and treatment of AD.

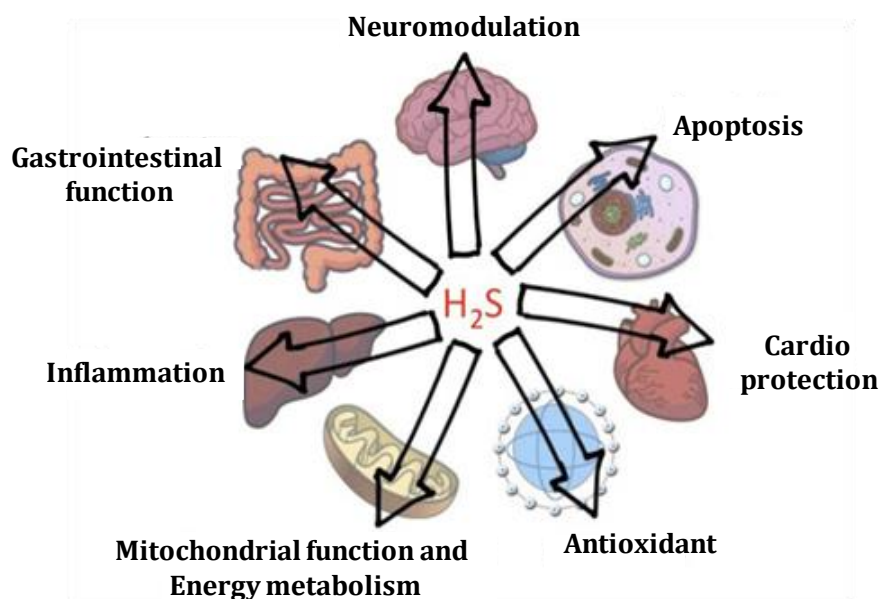
3.2. Introduction

H₂S is an essential gaseous signaling molecule that displays diverse functions different states of patho-physiological processes in mammals. Usually, H₂S was considered as a toxic gas with unpleasant smell but researchers found it as a third member of the gasotransmitter family after NO and CO.^{1,2,3} Endogenously produced sulfide plays critical roles in the cardiovascular, gastrointestinal, immune, and nervous systems. H₂S is generated endogenously from cysteine and homocysteine by several enzymes, such as cystathionine β -synthase (CBS), cystathionine γ -lyase (CSE), cysteine aminotransferase (CAT), and 3-mercaptopyruvate sulphur transferase (3-MST), which are involved either independently or in combination.⁴ **Scheme 3.1.** summarized the detailed pathways involved for the formation of H₂S.



Scheme 3.1. H₂S production through enzymatic pathways. Figure is adapted from ref. 4.

H₂S has demonstrated a variety of biological applications in different fields include neuromodulation, apoptosis, cardio protection, antioxidant and also helps in mitochondrial function and energy metabolism (**Scheme 3.2.**). H₂S appears to have anti-apoptotic actions in cancer cells and is well known to be a neuroprotection agent in AD. The powerful anti-inflammatory, cytoprotective, and mitochondrial functions of H₂S on the biological systems are well explored in modern research.



Scheme 3.2. Significance of H_2S in different fields

Low levels of endogenously produced H_2S may lead to AD,⁵ which is a progressive neurodegenerative disorder characterized by extracellular amyloid plaques and intracellular neurofibrillary tangles of tau protein in the brain tissue.^{6,7} Misfolding of the soluble $A\beta$ protein into larger aggregates acts as the reason behind AD.⁸ Breakdown or preventing the formation of $A\beta$ aggregation is the key challenge to overcome AD. In one of the recent reports, authors demonstrated the de-agglomeration of beta sheet fibrils using H_2S . They have utilized hen egg white lysosome (HEWL) to make the typical beta sheet fibrils and Sodium hydrosulfide (NaHS) for the source of H_2S ⁹. Their results revealed that in presence of H_2S , complete de-agglomeration of the beta fibrils occurring within a short time (**Figure 3.1**). Recent reports indicated that H_2S donor like sodium sulfide reduces the $A\beta$ generation, to provide neuroprotection from $A\beta$ aggregates and decreases the progression of AD.^{10,11}

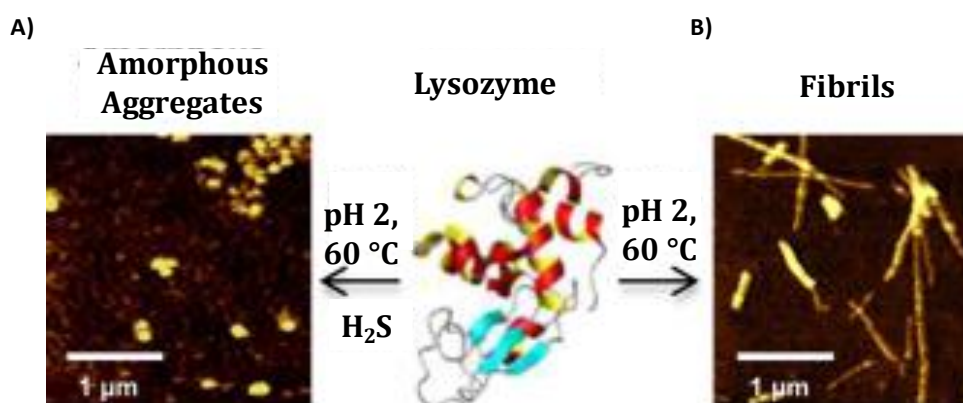
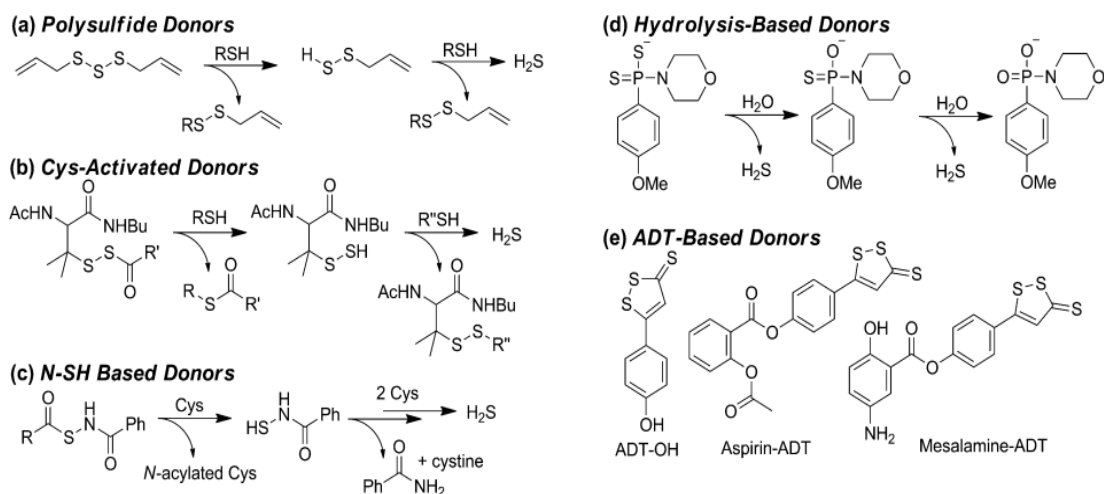


Figure 3.1. Atomic force microscopy (AFM) images of A) HEWL aggregates formed in the presence of H₂S for 48 h, and B) HEWL fibrils formed after incubation of the control solution for 90 min; scale bars are 1 μm.

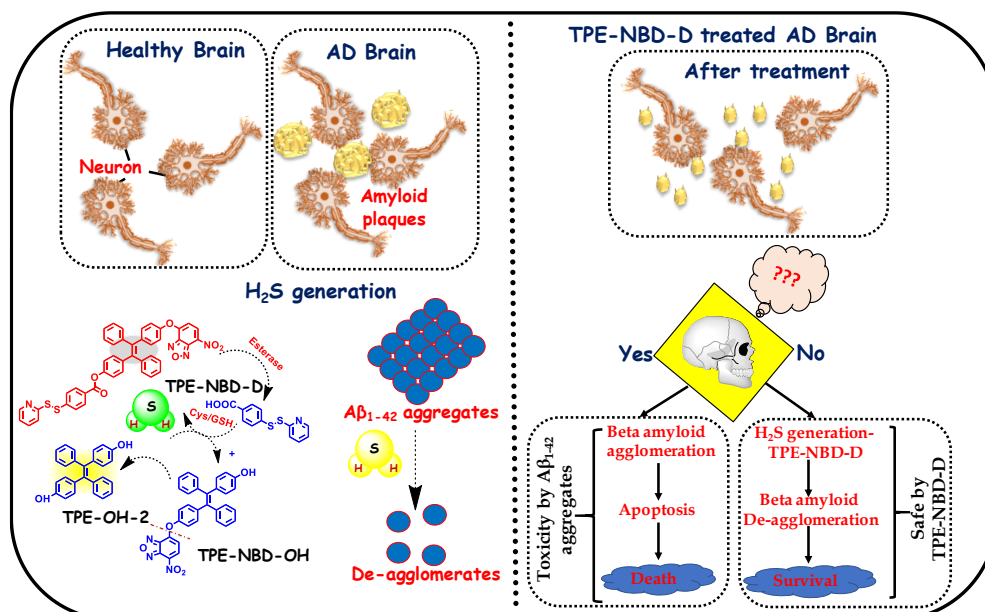
Due to the diverse roles played by H₂S in various patho-physiological processes, H₂S donors like sodium sulfide (Na₂S) and NaHS are widely applied for immediate generation of H₂S in aqueous medium.^{12,13} Complementing these inorganic compounds, small organic molecules can also act as H₂S donors. Some of the simplest sulfide donating motifs are organic polysulfide which are often found in natural products, like diallyltrisulfide (DATS), isolated from garlic and other alliums.^{14,15} Past decades witnessed the development of many novel H₂S releasing agents.^{16,17} More often, H₂S donors based on polysulfide moieties are more likely to attack glutathione (GSH) or other bio-thiols because of their electrophilic nature which in turn generate the intermediate per-sulfide (**Scheme 3.3.**). Subsequently, after a second reaction with GSH it releases H₂S.¹⁸ In the way forward towards establishing the diverse roles played by H₂S in biological system, new chemical methods for H₂S quantification, and reaction-based tools for its imaging were emerged.



Scheme 3.3. Commonly used small-molecule H₂S donors. (a) polysulfides, (b) cysteine-activated H₂S donors, (c) cysteine-activated H₂S donors with N-SH based donors, (d) hydrolysis-based donors, and (e) anethole 1,2-dithiole-3-thione (ADT) type donors.

Quite a large number of fluorescent probes have been constructed based on different strategies for the detection and imaging of H₂S^{19,20,21,22} but most of these suffered poor limit of detection. TPE, an organic AIE luminogen^{23,24} has been used for the construction of various fluorescent sensors^{25,26,27} and successfully applied in the field of biology.^{28,29,30} Compared with conventional small organic molecular probes AIE fluorogens have significant advantages due to its tunable emission, good biocompatibility and excellent photo physical properties.

Herein, a novel molecular probe comprised of TPE core as a fluorescent molecular framework has been synthesised for the detection of endogenous H₂S and synergistic delivery of H₂S in lieu of progressive therapy on AD (**Scheme 3.4**). Disulfide compounds act as H₂S donor, which produces H₂S efficiently by thiol cleavage mechanism. Therefore, a disulfide based molecular probe as effective H₂S donor for specific H₂S therapy on AD has been evaluated in this chapter.



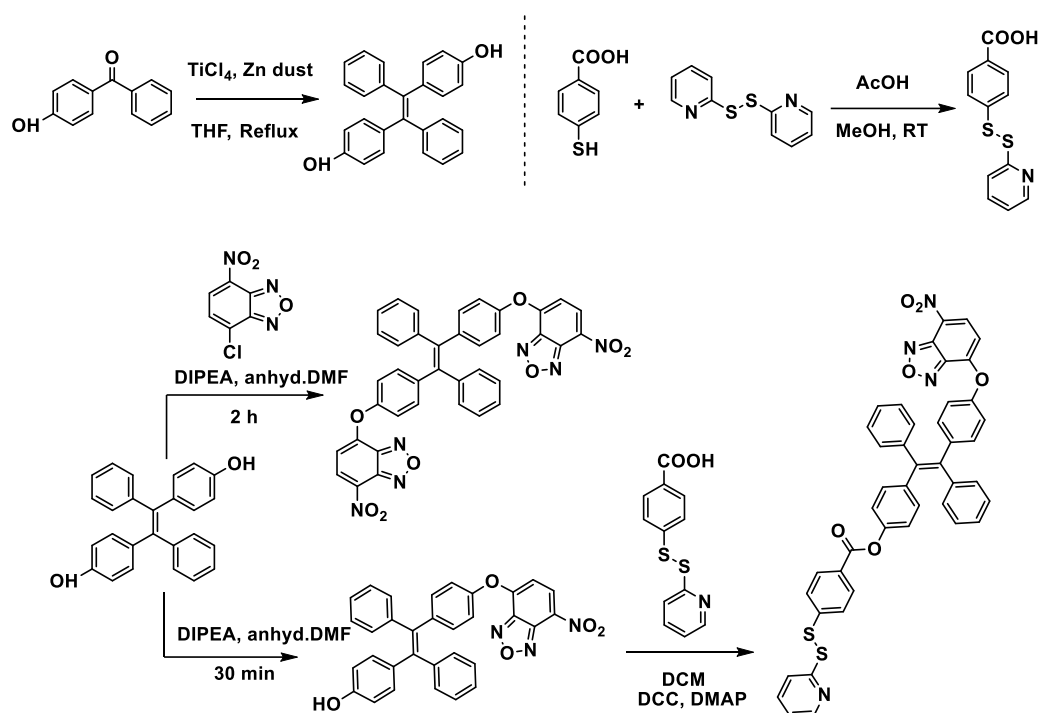
Scheme 3.4. Designing strategy of TPE based molecular probe and their efficiency to generate H₂S in cellular medium.

The strategy is built upon the fact that, disulfide linked donor 4-(pyridin-2-yl)disulfaneyl) benzoate is cleaved off from the TPE anchored molecular probe by the intracellular esterase. Subsequently, disulfide moiety triggered by the intracellular Cys / GSH enabled the generation of H₂S, which will in turn cleaved off the H₂S detection moiety 4-chloro-7-nitrobenzofurazan (NBD) from TPE-core to display a turn-on fluorescence due to the AIE effect. Moreover, the produced H₂S could cause the de-agglomeration of Aβ to reduce the progression of AD. The as-synthesized molecular probe has been programmed (i) for selective detection and generation of H₂S in a condition mimicking the cellular environment (ii) to detect the endogenously produced H₂S from the probe in intracellular milieu *i.e.* in neuronal cell line SH-SY5Y followed by the cellular imaging (iii) to monitor the release profile of H₂S inside the living system by turn-on fluorescence and (iv) finally execute the de-agglomeration of beta amyloid sheets using the released H₂S from the probe considered as a novel therapeutic strategy towards AD.

3.3. Results and Discussion

3.3.1. Synthetic framework for molecular fluorogens

In the current study, AIE active orthogonally substituted TPE based molecular probes **TPE-NBD-D** and **TPE-NBD-2** were designed for endogenous H₂S generation and detection in a synergistic fashion with high sensitivity through “turn-on” fluorescence modality. The molecular probe, **TPE-NBD-D** consists of three components: (i) TPE acts as the core structure of the AIE gen; (ii) NBD plays a role as a fluorescence “on-off” mediator; (iii) a cysteine activated disulfide donor to generate H₂S in presence of thiols.



Scheme 3.5. Synthetic route adopted for the designing of two molecular probes.

On the other hand, molecular probe, **TPE-NBD-2**, contains symmetrically substituted NBD moiety in the AIE core in order to assess the H₂S generation efficiency with **TPE-NBD-D** probe. Both the molecular probes were synthesized using an optimized synthetic route shown in **scheme 3.5**. Initially, the **TPE-OH-2** core was synthesized

using Mc-Murry coupling of 4-Hydroxybenzophenone in presence of zinc (Zn) powder and titanium tetrachloride (TiCl_4) followed by the base mediated ether linked NBD moiety resulted both two side and one side NBD adduct. Molecular probe, **TPE-NBD-D** was obtained by the coupling between orthogonally joined one side NBD intermediate and an in house synthesized disulfide based H_2S donor 4-(pyridin-2-yl)disulfaneyl) benzoate. All the products and intermediates were purified by column chromatographic separation and un-ambiguously characterized by HR-MS and NMR analysis.

3.3.2. Photophysical evaluation and its molecular mechanism

Absorbance and fluorescence properties of both the molecular probes were tested in 4-(2-hydroxyethyl)-1-piperazineethanesulfonic acid (HEPES) buffer / tetrahydrofuran (THF) = 90:10 (v/v) with pH 7.4 (**Figure 3.2.A&B**).

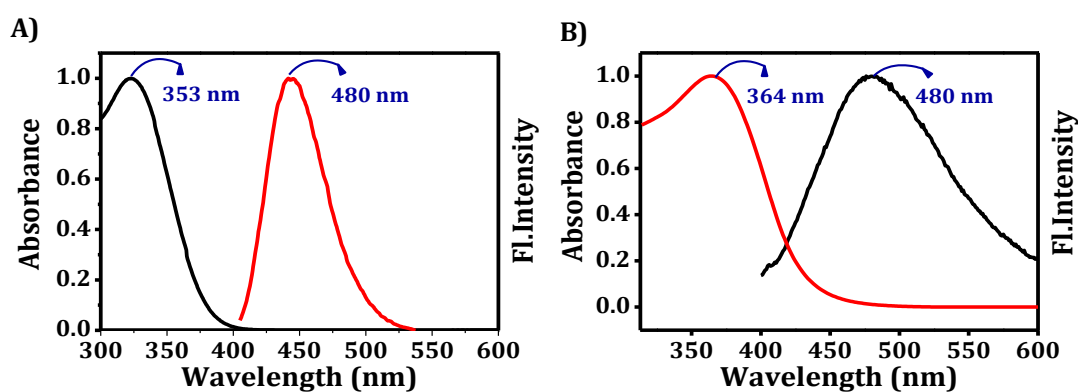


Figure 3.2. UV/Vis absorption and emission spectra of A) **TPE-NBD-2** (30 μM , 9:1 HEPES/THF, 20 μM Na_2S), B) **TPE-NBD-D** (30 μM , 9:1 HEPES/THF, 20 μM Na_2S).

The probe is practically non-emissive in organic solvents like THF and acetonitrile or in aqueous buffer aggregates. It is expected that the quenched fluorescence of TPE-NBD is due to the electron transfer from the NBD moiety to the TPE group. Since after nucleophilic displacement with H_2S , the NBD part is cleaved off

from the TPE core which resulted the recovery of fluorescence from **TPE-OH-2** core as it is known for AIE phenomenon.

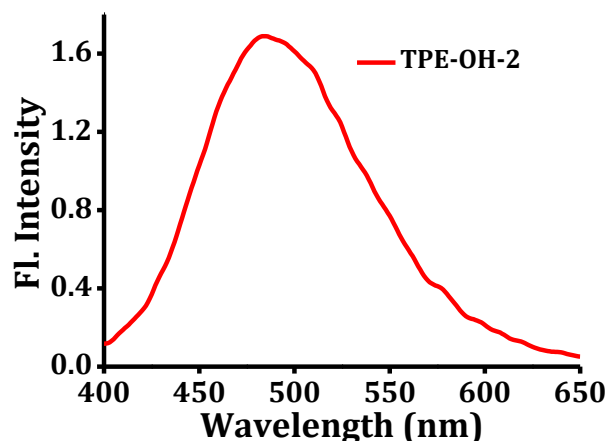


Figure 3.3. Fluorescence spectra of **TPE-OH-2** in 90 % HEPES/THF mixture.

So, the experiments were carried out in HEPES buffer for initial assessment of both the effect *i.e* buffer and pH on fluorogenic TPE core (**TPE-OH-2**). From the **figure 3.3**, it is clear that the TPE core responded well under physiological pH (HEPES, pH 7.4), in 90% HEPES/THF mixture. So, fluorescence properties of synthesized molecular probes were examined under the same condition.

Foremost, the response of **TPE-NBD-2** towards H_2S in HEPES/THF mixture was measured using fluorescence spectroscopy. The free probe was basically non-fluorescent in the buffer, as the NBD moiety quenched its inherent fluorescence. However, remarkable fluorescence enhancement was observed in the presence of H_2S (12-fold change). As predicted, the response of probe towards Na_2S triggered the cleavage of NBD moiety, releasing the most emissive **TPE-OH-2** luminogen. Further investigations were carried out to determine the sensitivity of the probe towards H_2S (**Figure 3.4A**) *i.e.*, change in fluorescence properties with different concentrations of Na_2S (0-50 μM). An enhancement in the fluorescence intensity centred at 480 nm was

apparently observed with increase in concentration of H₂S. A linear calibration curve (**Figure 3.4.B**) ($R = 0.9942$) was acquired between the fluorescence signal at 480 nm and the concentration of H₂S up to 50 μM .

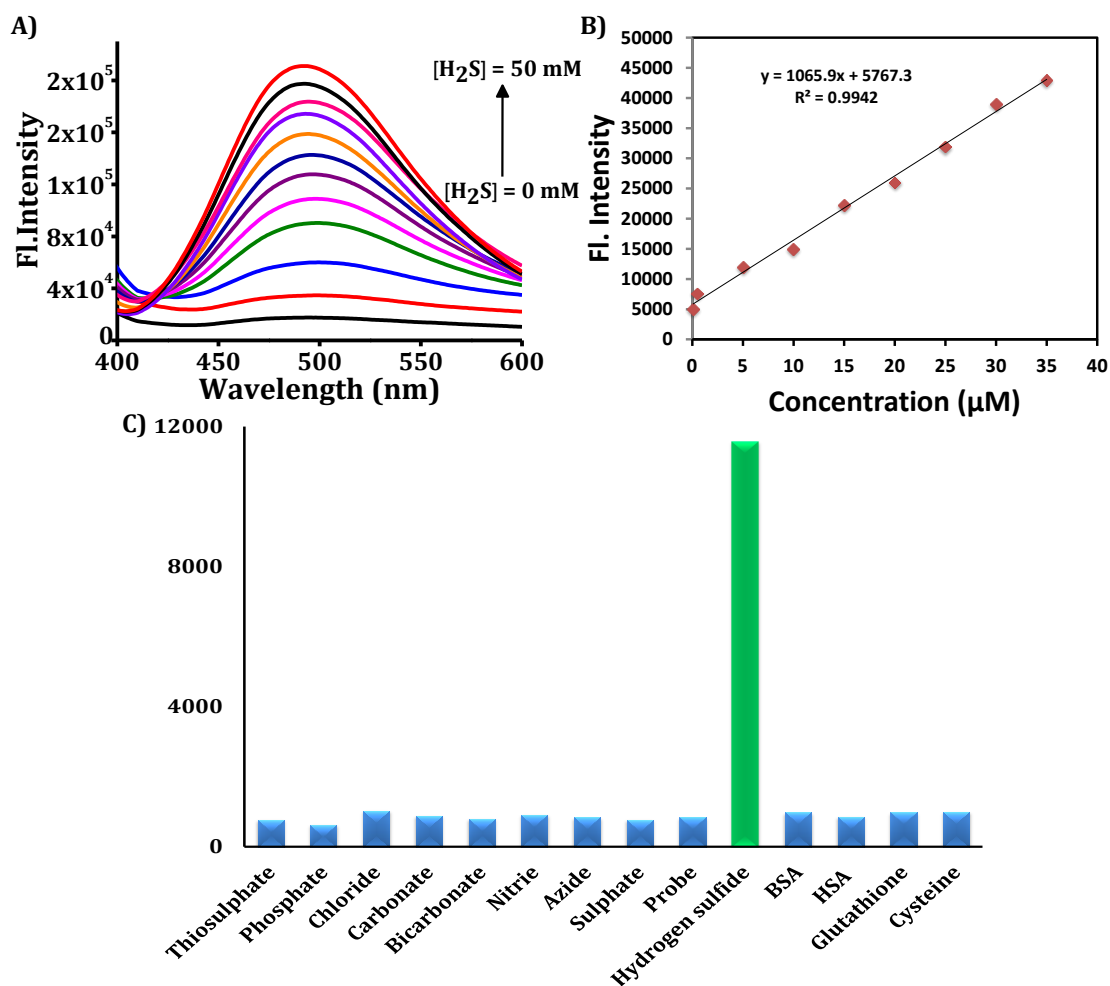
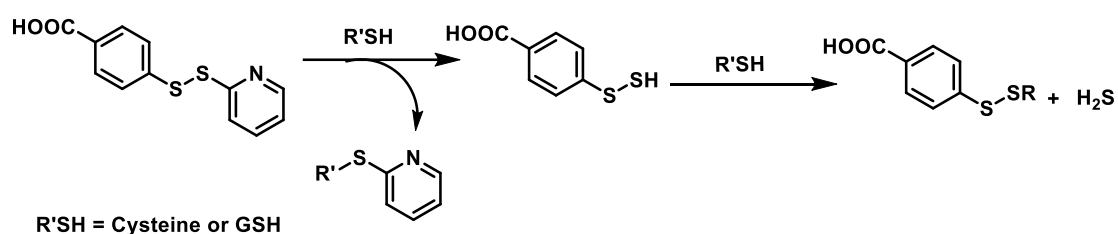


Figure 3.4. A) Fluorescence spectra of TPE-NBD-2 (10 μM) upon titration with different concentration of Na₂S (0-50 μM , 9:1 HEPES/THF), B) corresponding linear plot obtained, C) Relative fluorescence intensity at 480 nm of the probe with various analytes in HEPES/THF mixture.

Next, the selectivity of the probe was assessed with various anions and other sulfur containing species including cysteine, BSA, HSA, glutathione, sulfate, azide, nitrile, bicarbonate, carbonate, chloride, phosphate and thiosulphate (**Figure 3.4.C**). Fluorescence intensity exhibited a significant increase upon reaction with H₂S, whereas the response towards other bio-analytes was found to be negligible.

As **TPE-NBD-2** displayed a very quick response to H_2S , we re-structured the TPE core by introducing a donor moiety as a dual functional motif for sensing as well as production of H_2S within the intracellular milieu. The mechanism behind the generation of H_2S from the donor part is given in **scheme 3.6**. The release mechanism of H_2S is well studied where intracellular bio thiols like cysteine or GSH easily reduce the di-sulfide bond, resulting the formation of an intermediate per-thiol which subsequently release H_2S by a second reaction with another molecule of cysteine or GSH.



Scheme 3.6. Mechanism of generation of H_2S from the donor.

To test the potential of H_2S donor, we first studied their ability to generate H_2S under physiological conditions. The release of H_2S by the donor was monitored by using our selective fluorescent probe **TPE-NBD-2**. The donor was dissolved in HEPES buffer containing 10 % THF with the sensor **TPE-NBD-2**. Indeed, a strong fluorescence of **TPE-OH-2** was detected in presence of donor after incubation with cysteine in HEPES buffer which revealed the donor efficiency for synergistic generation and release of H_2S within the TPE core (**Figure 3.5**).

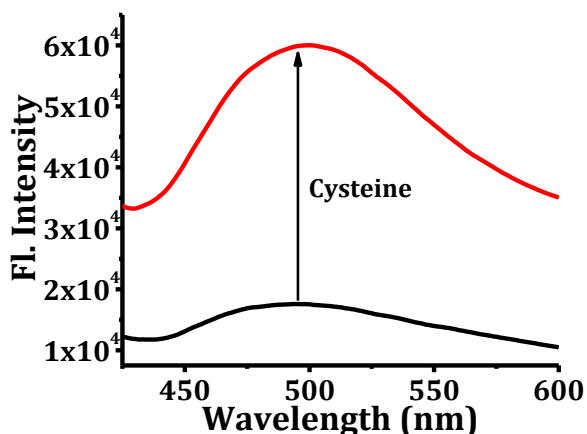


Figure 3.5. Fluorescence spectra of **TPE-NBD-2** in 90 % HEPES/THF mixture incubation with donor [before (black line) and after (red line) donor activation with cysteine].

Next, the dual features of the probe, **TPE-NBD-D** has been evaluated i.e. H_2S releasing as well as detecting ability in solution state. The probe was incubated (10 μM , 90: 10 v/v HEPES/THF) with esterase enzyme (5 mg/ml, 2 μl ,) at 37 $^\circ\text{C}$ for 10 min which is responsible for the cleavage of ester bond bridged between the donor and the probe (**Figure 3.6A**). The cleavage phenomenon of the donor from the TPE core was confirmed from HR-MS analysis before and after the probe incubation with esterase enzyme. From the mass analysis, m/z peak of **TPE-NBD-D** (**Figure 3.6B**) at 773.15 identified initially which is gradually decreased and a new peak at m/z 550.13 appeared after incubation with enzyme which proved the presence of fragment **TPE-NBD-OH** (**Figure 3.6C**). Subsequently, cysteine (10 μM) was added with the reaction mixture in order to generate H_2S from disulfide linked donor part. In the sequential mechanism the generated H_2S is responsible for the cleavage of NBD from the TPE core which was again confirmed by mass analysis. The mass spectrum was obtained for the same solution after 15 min, a peak corresponding to **TPE-OH-2** (m/z 364.14), identified (**Figure 3.6D**) which was in agreement with the cleavage of NBD in the presence of H_2S .

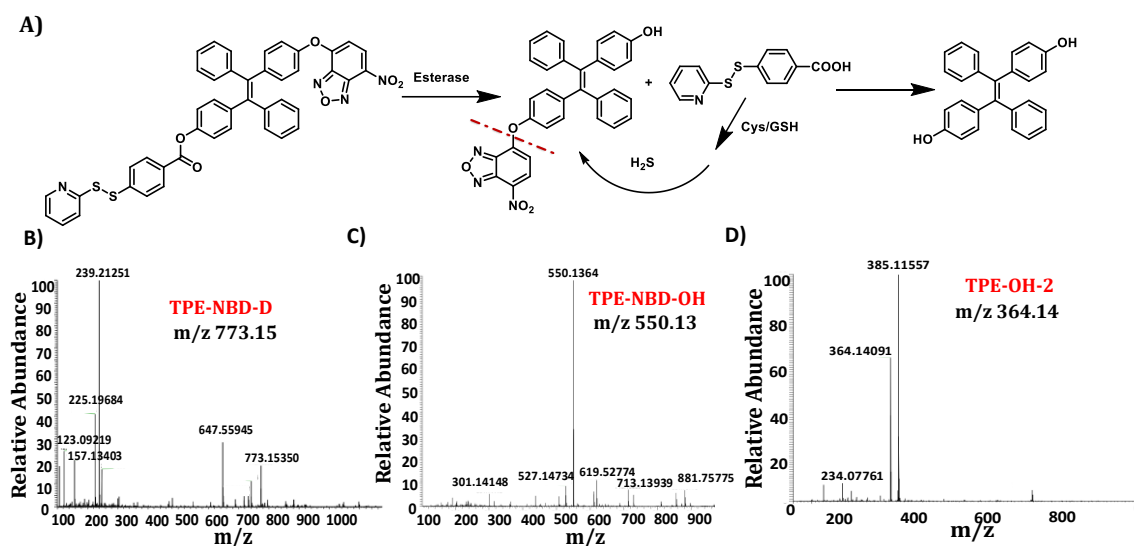


Figure 3.6. A) Fluorescence spectra of **TPE-NBD-2** in 90 % HEPES/THF mixture incubation with donor [before (black line) and after (red line) donor activation with cysteine].

Further, the same phenomenon was confirmed by measuring the fluorescence (**Figure 3.7A**). Initially, the probe was non-fluorescent but after reaction with esterase the donor part became free and was activated by cysteine so that the desired product **TPE-OH-2** was formed as reflected by the well refined fluorescence spectra in aggregated state. Next, the sensitivity of molecular probe **TPE-NBD-D** has been investigated after cleaving with esterase by using Na₂S as the source of H₂S. Fluorescence titration of **TPE-NBD-D** (10 μM, 90: 10 v/v HEPES/THF mixtures) with concentration dependent titration using Na₂S (0 - 50 μM) confirmed its gradual increase in emission intensity with a detection limit of 0.1 μM (**Figure 3.7B**). A linear calibration curve (**Figure 3.7C**) (R= 0.9957) was acquired between the fluorescence signal at 480 nm and the concentration of H₂S up to 50 μM. The selectivity of the probe was assessed with various anions and other sulphur containing species including cysteine, BSA, human serum albumin (HSA), GSH, sulphate, azide, nitrile, bicarbonate, carbonate, chloride, phosphate and thiosulphate (**Figure 3.7D**).

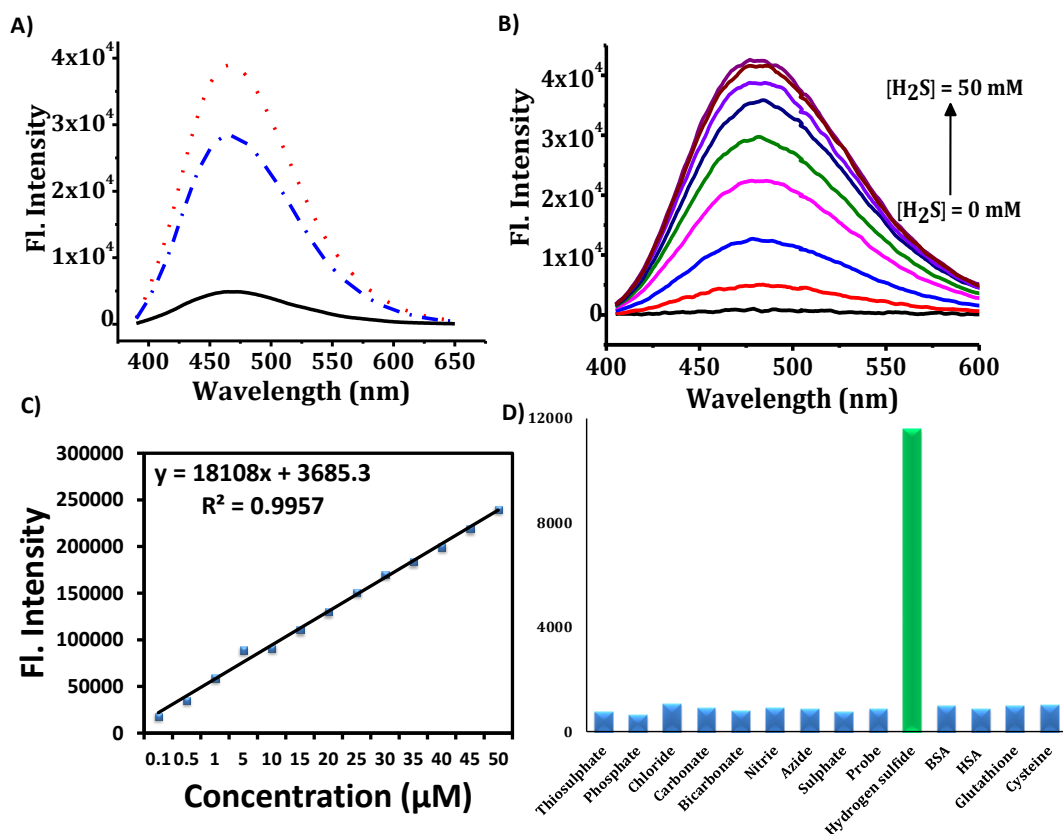


Figure 3.7. A) Fluorescence spectrum showing the intensity enhancement after the generation of H_2S , solid line corresponds to spectra after 10 min with esterase enzyme incubation, dash dotted line represents the spectra after 15 min with cysteine incubation and dotted line after 30 min cysteine incubation, B) fluorescence spectra of **TPE-NBD-D** upon titration with different concentration of Na_2S (0-50 μM), C) linear plot of fluorescence intensity of the probe **TPE-NBD-D**, D) Relative fluorescence intensity at 480 nm of **TPE-NBD-D** with various analytes in HEPES/THF mixture.

Fluorescence intensity exhibited a significant increase upon reaction with H_2S , whereas the response towards other bio-analytes were found to be negligible. Moreover, the molecular probe **TPE-NBD-D** maintained a moderately good fluorescence enhancement in presence of Cys and GSH. The increase in fluorescence intensity is due to the generation of H_2S in presence of these ions by the activation of donor in the probe molecule.

3.3.3. Investigation of TPE-NBD-D towards endogenous detection of H₂S in cellular and mice model level

On the basis of *in vitro* fluorescence studies, the endogenous detection and release of H₂S using both the products with SH-SY5Y has been evaluated. Initially, the biocompatibility was examined by MTT assay (**Figure 3.8.**) which reflected the absence of any noticeable toxicity for the molecular probe **TPE-NBD-D** up to 10 μ M.

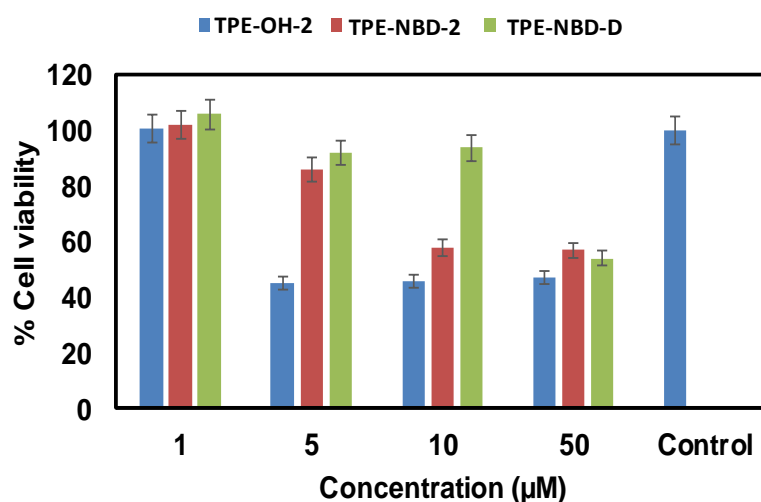


Figure 3.8. A) MTT assay of the compounds **TPE-OH**, **TPE-NBD-2** and **TPE-NBD-D** in SHSY5Y cell lines with a concentration varying from 1 to 50 μ M.

Next, the cellular uptake of the probe was investigated by utilizing the fluorescence of the AIE core **TPE-OH-2**. A distinct intracellular fluorescence evenly in the cytoplasmic area of SH-SY5Y cells (**Figure 3.9A**) revealed the effective internalization of the probe. Next, the intracellular H₂S sensing ability was estimated in SH-SY5Y cells after incubating **TPE-NBD-2** for different time intervals up to 30 min, which reflected very feeble fluorescence turn-on (**Figure 3.9B&C**). In contrast, incubation of the cells with Na₂S for 30 min followed by addition of the probe resulted in a strong fluorescence turn-on which is in good agreement for the visualization of intracellular H₂S levels (**Figure 3.9D**). When cells were treated with an H₂S inhibitor

aminooxyacetic acid (AOAA, 5 μ M), there was a significant reduction in fluorescence. Again, the specificity of **TPE-NBD-2** towards cellular thiols was demonstrated in the presence of a thiol scavenger N-Ethylmaleimide (NEM, 5 μ M) and GSH (5 μ M) (**Figure 3.9D**). The cells displayed no variation in the fluorescence intensity with NEM and GSH, which signified the non-specific nature towards bio-thiols.

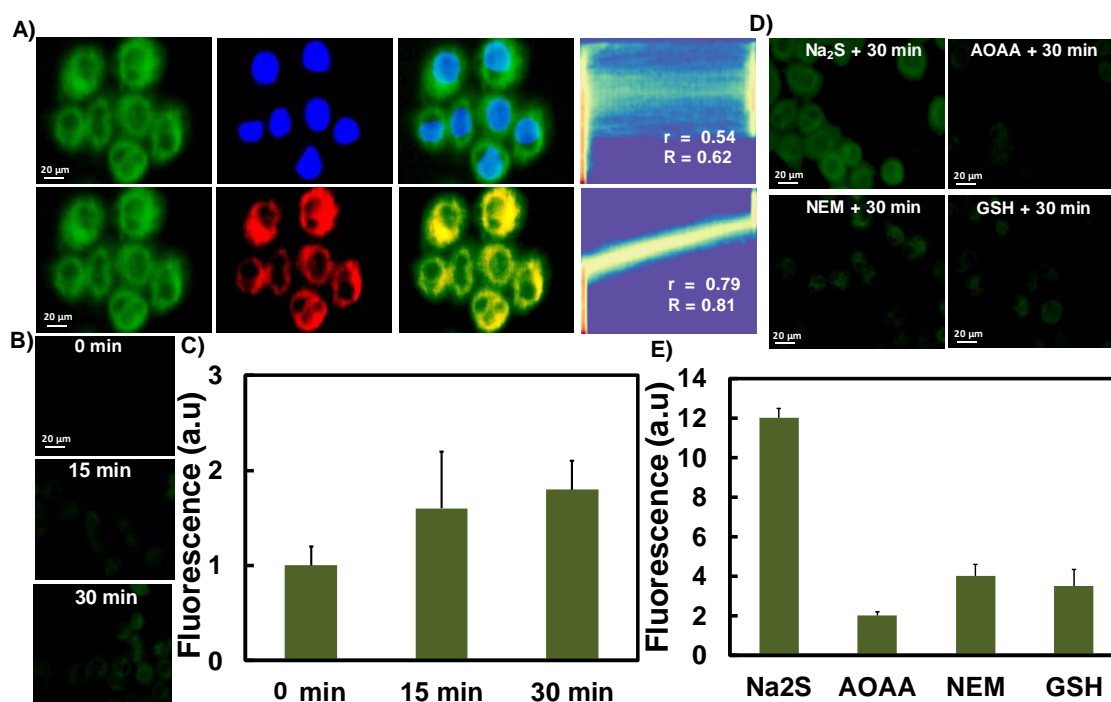


Figure 3.9. A) Evaluation of the intracellular uptake and distribution of **TPE-OH-2** in SH-SY5Y cells using fluorescence microscopy. In the first panel, initial image corresponds to cells treated with **TPE-OH-2**, second image indicated Hoechst treatment, third image represents the merged image and in second panel, second image indicated the treatment with Lyosotracker red, third is the merged image of the probe with Lyostracker red, and r and R represent Pearson's correlation coefficient and Mander's overlap coefficient, respectively, B) Internalization studies with **TPE-NBD-2** in SH-SY5Y cells and quantification C)&D) Fluorescence images of SH-SY5Y cells pre-treated with Na₂S, AOAA, NEM and GSH for 30 min and then incubated with probe, E) represents the fluorescence intensity quantification data of D.

Subsequently, the endogenous generation and visualization of H₂S using **TPE-NBD-D** were assessed. A detectable fluorescence was observed just after 15 min of

incubation which increased after 30 min without the addition of any external H₂S donor (**Figure 3.10A&B**). In order to further validate this assumption, cells were pre-treated with AOAA, which can prevent the production of endogenous H₂S by inhibiting the enzymes CBS and CSE. Here, the H₂S level remained unaltered (**Figure 3.10C&D**) suggesting that the probe is sufficiently sensitive to the production of H₂S as well as its detection in the intercellular milieu.

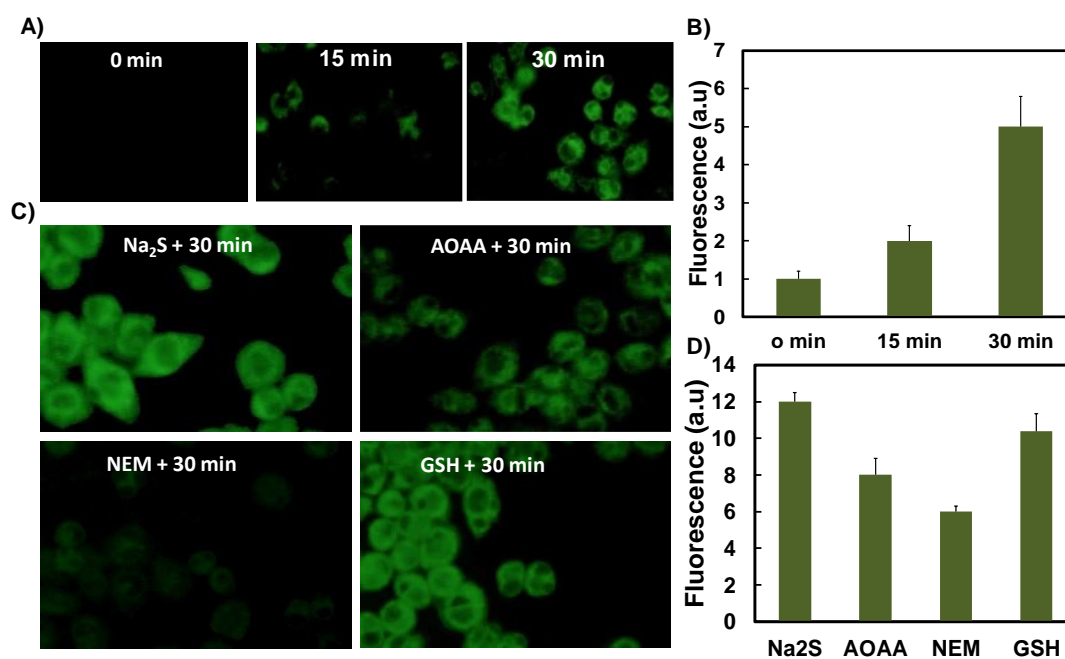


Figure 3.10. A) Internalization studies with TPE-NBD-2 (10 μ M) in SH-SY5Y cells and its B) quantification, C) Fluorescence images of SH-SY5Y cells pre-treated with Na₂S, AOAA, NEM and GSH for 30 min and then incubated with probe, D) represents the fluorescence intensity quantification data of C.

The expected mechanism behind the H₂S production was explained earlier from *in vitro* solution studies wherein it was only occurred by the activation of the probe in presence of thiols in cells. To confirm the thiol specificity in cells, we pre-treated the cells with thiol inhibitor NEM (**Figure 3.10C&D**), wherein the cells displayed a very weak fluorescence after incubation with probe, suggesting the failure to produce endogenous H₂S in the absence of thiols. Enhanced fluorescence at a higher

concentration of GSH clarified the production of H₂S in the cells from the probe **(Figure 3.10C&D)** using cellular thiols. Therefore, **TPE-NBD-D** could act as H₂S donor in the presence of GSH and could simultaneously detect the generated H₂S, which has not been observed in the case of probe **TPE-NBD-2**. Taken together, it is confirmed that the probe **TPE-NBD-D** can be used for the study of endogenous H₂S production and its biological functions.

After establishing the endogenous detection as well as production of H₂S by **TPE-NBD-D** in living cells, the studies for *in vivo* visualization of H₂S in mice was extended. No detectable fluorescence was observed from immuno-deficient NCr Nude female mice administered with **TPE-NBD-2** **(Figure 3.11A)**. It is to be noted that **TPE-NBD-D** treatment could generate sufficient fluorescence with an increased intensity in a time-dependent fashion from 1 to 3 hr **(Figure 3.11B)** and then gradually declined which suggested the clearance of the probe from the body.

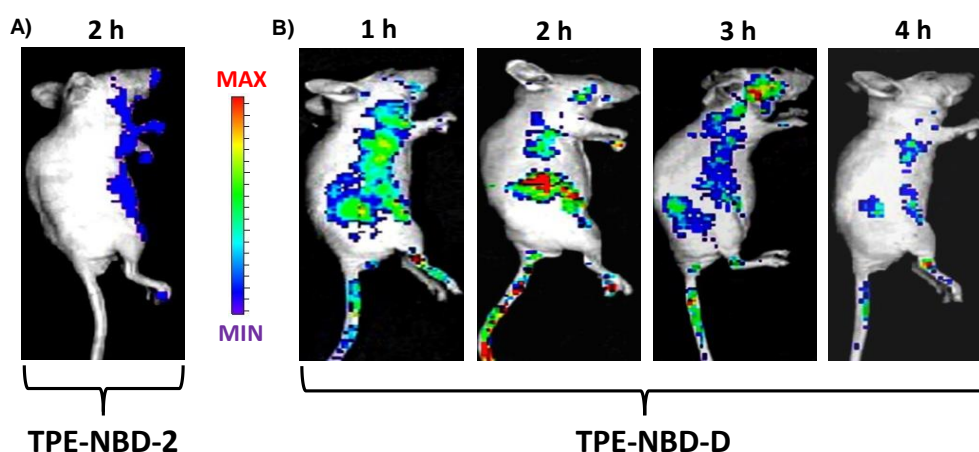


Figure 3.11. Time-dependent whole-body fluorescence imaging for the visualization of endogenous H₂S production as well as detection in living mice with A) **TPE-NBD-2** and B) **TPE-NBD-D**.

Fluorescence was mainly detected from the liver and colorectal areas of the mice. The fluorescence enhancement by **TPE-NBD-D** in the colorectal area is due to the abundance of thiol in that region which could activate the donor part to produce more H_2S and detect simultaneously. Hence, **TPE-NBD-D** can be a potential tool for the *in vivo* monitoring of endogenous hydrogen sulfide in animal models.

3.3.4. Assessment of TPE-NBD-D in AD: H_2S mediated de-agglomeration of $A\beta$ protein

Since the probe is capable of generating H_2S , it has been further utilized for therapeutic application in Alzheimer's disease. In general, H_2S level in the brain of AD patients is significantly reduced in comparison to healthy brain tissues. Also, the rapid aggregation or misfolding of $A\beta$ protein is known to be one of the reasons for AD wherein H_2S can cause the de-agglomeration of $A\beta$ to induce a healing touch. It is well accepted that H_2S has a greater affinity to reduce disulfide bonds and this could be the substantial outcome on the mechanism of protein de-agglomeration.³¹ So in the current study we have investigated whether the produced H_2S from **TPE-NBD-D** can de-agglomerate the $A\beta$ protein. Thus, human beta- amyloid (1 - 42)-HFIP, was chosen as the peptide sequence for making agglomerated form of $A\beta$. There are a number of isoforms of $A\beta$ available, while 42 amino acid form is the focus because of its genetic and pathological connection to AD.

An agglomerated form of $A\beta$ was made and the effect of H_2S liberated from **TPE-NBD-D** was monitored after incubation of $A\beta_{1-42}$ under 37 °C for 12 hr. The morphology was initially confirmed by AFM analysis. The presence of long rod like agglomerated $A\beta_{1-42}$ was evident from **figure 3.12A**. However, incubation of $A\beta_{1-42}$ in presence of probe resulted in the formation of spherical aggregates instead of

agglomerated structures as marked from **figure 3.12B**. This suggested that H₂S prevented the formation of A β ₁₋₄₂ agglomerated sheet and resulted in a significant transition of unaltered protein.

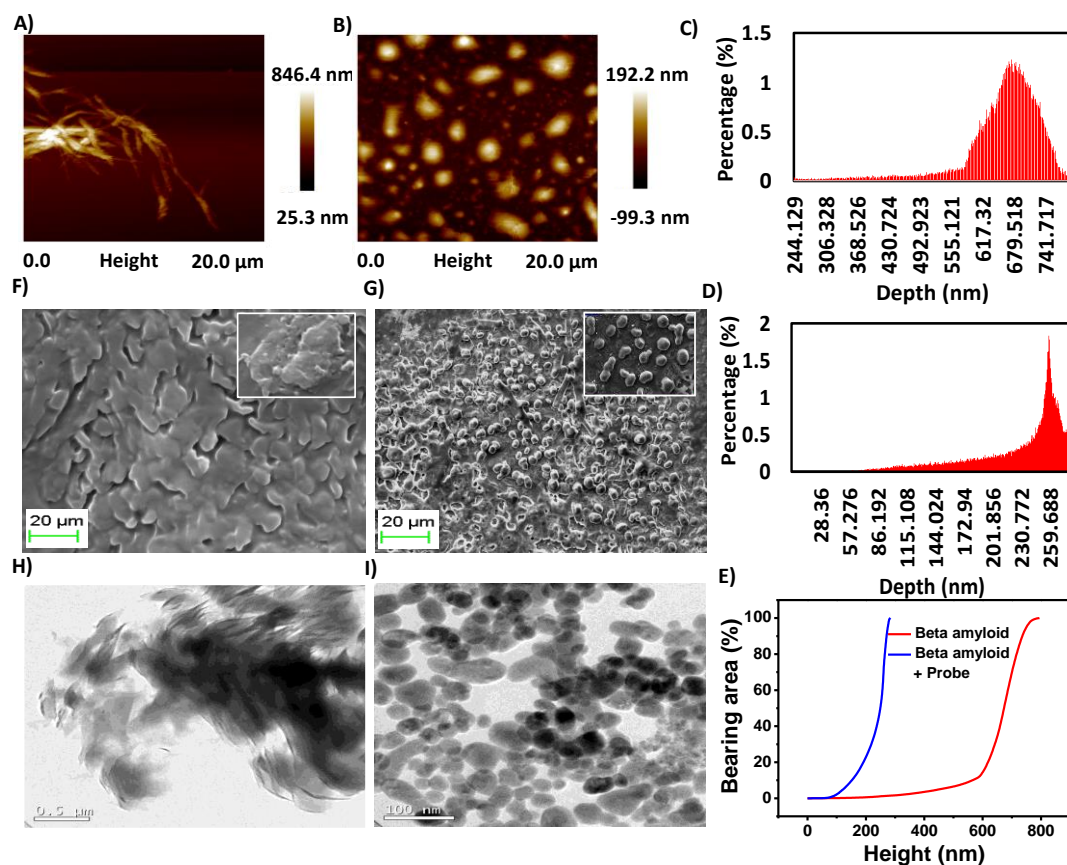


Figure 3.12. AFM images of A) β sheet rich agglomerated form of A β ₁₋₄₂ B) de-agglomerated smaller A β ₁₋₄₂ aggregates formed after incubation with **TPE-NBD-D** (10 μ M) probe for 24 hr. Depth histogram obtained from C) AFM image A and D) AFM image B. E) Bearing area plot accumulated from AFM images A&B. F) SEM and H) TEM images of agglomerated A β ₄₂ and corresponding de-agglomerated aggregates G) SEM and I) TEM after treatment with **TPE-NBD-D**.

A histogram corresponding to depth values for AFM image (**Figure 3.12A &B**) revealed the average depth maximum of agglomerated and de-agglomerated A β ₁₋₄₂. **Figure 3.12C** represents the depth histogram corresponding to A β ₁₋₄₂ agglomerated sheet which have a depth maximum of around 680 nm and **figure 3.12D** corresponding to that of de agglomerated A β ₁₋₄₂ showing a depth maximum around

260 nm. This result is in agreement with the de agglomeration and disassembly of A β proteins determined by AFM morphological study. Bearing area plot (**Figure 3.12E**) showed that in the case of A β_{1-42} agglomerated sheet, ~ 100 % of surface area exists within the height range of 600-750 nm. On contrary, after treating with probe, ~ 100 % of surface area exists within the height range of 200-285 nm which is much lower than the height ranges of A β_{1-42} agglomerated sheet. Thus, bearing area analysis supports the proposed mechanism of preferential de-agglomeration of A β_{1-42} agglomerated sheet after treating with probe. The morphology of agglomerated form of A β_{1-42} was further confirmed by scanning electron microscope (SEM) (**Figure 3.12F**) and TEM (**Figure 3.12H**) which showed a sheet like agglomerated form. Moreover, after treatment the sheet become de-agglomerated in to spherical aggregates which is clear from corresponding SEM (**Figure 3.12G**) and TEM (**Figure 3.12I**) analysis. These morphological results strongly supported that H₂S produced from the probe halted the formation of A β sheet.

Next, the feasibility of the probe has been assessed using SERS technique to detect the two utmost prevalent stages of A β_{1-42} has been evaluated. SERS is a surface sensitive technique used for the detection of protein folding and unfolding with high precision and accuracy. It was believed that the cytotoxic species of A β_{1-42} are in β sheet structure which shows more intense aromatic vibrations, i.e. amide II and amide III of all the amino acids reflected in SERS.³² Raman bright field images were taken from an agglomerated A β_{1-42} before and after addition of **TPE-NBD-D (Figure 3.13A &B)**, which revealed that the probe is capable of de-agglomerating the β sheet structure. Then SERS spectral analysis were carried out to prove the de-agglomeration of β sheet structure through protein degradation. Samples for SERS experiment were

prepared by mixing with 45 nm AuNPs (used as a SERS substrate) solutions (volume ratio 1:9) in water. Spectra were collected using 633 nm laser over the range of 500-2000 cm^{-1} . For $\text{A}\beta_{1-42}$ agglomerated sheet, we observed Raman bands associated with the aromatic side chains at 738, 1002 and 1313 cm^{-1} corresponding to tryptophan, phenylalanine and tyrosine. Apart from this, a strong band at 1262 and 1538 cm^{-1} associated with amide III and amide II vibrations for β sheet structure has been observed (**Figure 3.13C**).

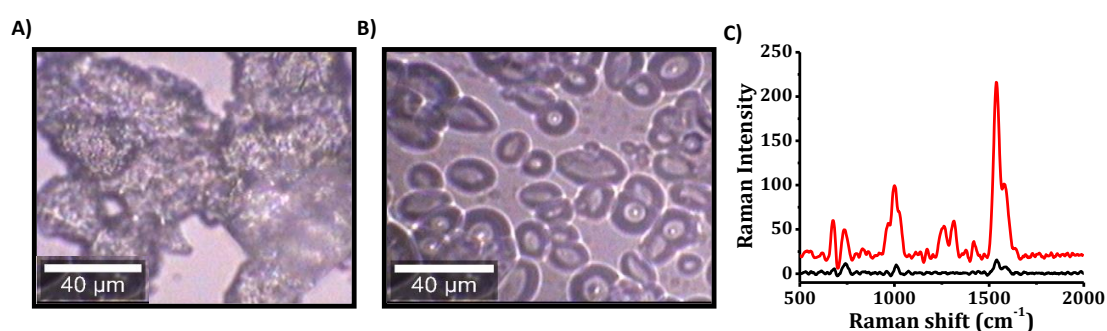


Figure 3.13. Bright field images obtained from Raman microscope, A) β sheet rich agglomerated form of $\text{A}\beta_{1-42}$, B) de-agglomerated $\text{A}\beta$ aggregates formed after incubation of **TPE-NBD-D** for 24 hr. C) SERS spectra obtained for Beta amyloid before and after probe treatment.

As expected, aromatic rings and amide chain vibrations were dominated in the SERS spectrum of $\text{A}\beta_{1-42}$ agglomerated sheets which confirms the β sheet structure. Most importantly the decrease in intensity of the aromatic and amide chain vibrations after treating with probe are most likely due to the unfolding transition of proteins. The Raman spectra were assigned based on amino acids and proteins (**Table 3.1**). The results suggest that **TPE-NBD-D** is a worthy candidate for the de-agglomeration of amyloid beta by generating H_2S .

Table 3.1. SERS spectra obtained from A β_{1-42} agglomerated sheet and its peak assignments.

Peak (cm ⁻¹)	Assignment
738	Aromatic ring chain vibrations in tryptophan
1002	Aromatic ring chain vibrations in phenyl alanine
1262	Amide III
1313	Aromatic ring chain vibrations in tyrosine
1538	Amide II

Biocompatibility studies with **TPE-NBD-D** to check the effect on A β_{1-42} induced toxicity was performed. To determine the protective effects of H₂S, cells were pre-treated with **TPE-NBD-D** (used as the H₂S donor) for 30 min and then incubated with agglomerated A β_{1-42} for 72 hr (**Figure 3.14A**). Samples of **TPE-NBD-D** and A β_{1-42} were prepared using the cell culture medium in order to avoid drastic changes in pH of the cells and other solubility issues.

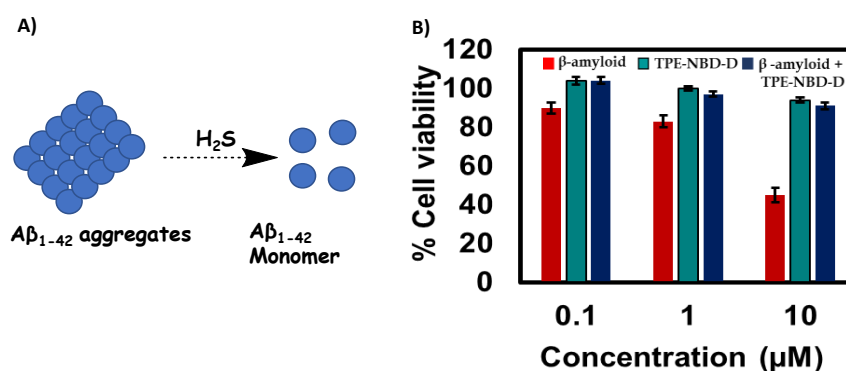


Figure 3.14. A) Schematic representation of beta amyloid deagglomeration in presence of H₂S, B) Cytotoxicity of agglomerated A β_{1-42} (red) and probe treated agglomerated A β_{1-42} (sky-blue).

TPE-NBD-D alone had no toxicity on the cells (**Figure 3.14B**) indicating the biocompatibility. The agglomerated A β_{1-42} inhibited cell growth by 45 %. However,

cells after pre-treatment with **TPE-NBD-D** showed no detectable cytotoxicity. As expected, these results are also confirmed that the **TPE-NBD-D** was effective candidate to produce H₂S and capable of de-agglomerating A β ₁₋₄₂ in to smaller spherical aggregates and subsequently to reduce the cytotoxicity induced by A β ₁₋₄₂.

3.4. Conclusions

In summary, an orthogonally substituted molecular probe **TPE-NBD-D** was developed for endogenous detection of H₂S and H₂S induced A β ₁₋₄₂ de-agglomeration. TPE-NBD part showed selectivity and sensitivity towards H₂S. A disulfide donor was used to generate H₂S in presence of bio thiols. Efficient H₂S sensing was reflected in both neuroblastoma cells lines and in mice. Novel molecular probe enabled to act as H₂S donor and subsequently utilized for amyloid beta de-agglomeration (A β ₁₋₄₂ protein) to reduce the progression of AD. The toxic agglomerated A β ₁₋₄₂ turns to non-toxic de-agglomerated A β ₁₋₄₂ in presence of **TPE-NBD-D**. Therefore, the newly evolved molecular probe opens up an opportunity for simultaneous diagnosis and therapy towards neurodegenerative diseases which requires further clinical interventions.

3.5. Materials and Methods

3.5.1. General techniques

NMR spectra were recorded on Bruker Advance 500 NMR spectrometer, and chemical shifts are expressed in ppm. Mass spectra were recorded under ESI/HRMS at 61800 resolution using Thermo scientific exactive, mass spectrometer. Absorption spectrum of the probe and its derivatives was measured on a Shimadzu, UV-2450 UV-vis-NIR spectrophotometer. The emission and excitation spectrum of TPE compounds

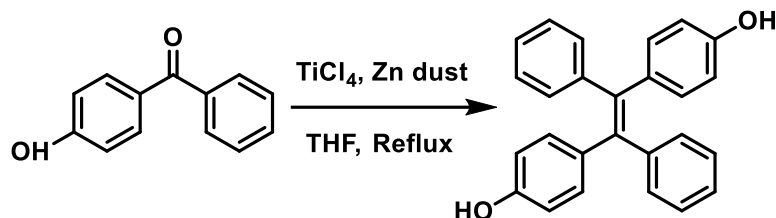
was recorded on a Spex-Fluoromax FL22 spectrofluorimeter equipped with a double grating 0.22 m Spex 1680 monochromator and a 450 W Xe lamp as the excitation source and a Hamamatsu R928P photomultiplier tube detector. SERS analysis were studied in a WI-Tec Raman microscope through 20×objective with a grating of 600 g/mm with peltier cooled CCD detector. 633 nm laser with 7 mW power was used for the sample excitation. Raman spectra were measured in the range of 400–3000 cm^{-1} with a resolution of 1 cm^{-1} and 0.5 integration time for 20 accumulations. A calibration was done using silicon standard. WI-Tec Project plus (v 2.1) software package was used for further analysis.

3.5.2. Materials and methods

All reagents were purchased from Sigma Aldrich, Merck, and Specrochem. Analytical TLC was achieved on a Merck 60 F254 silica gel plate and visualization was done with UV light. Column chromatography was performed on Merck 60 silica gel (60-120 or 100-200 mesh). Human beta- amyloid (1 - 42)-HFIP were purchased from Ana Spec. company, India. SH-SY5Y cell lines has been obtained from National Centre for Cell Science (NCCS) Pune, India. Cells are cultured on 25 cm^2 tissue culture flask and were grown at 37 °C in DMEM medium supplemented with 10 % Fetal Bovine Serum and Antibiotics (100 U mL^{-1} penicillin/100 mg mL^{-1} streptomycin mixture) in a 5 % CO_2 incubator.

3.5.3. Synthesis of molecular probes

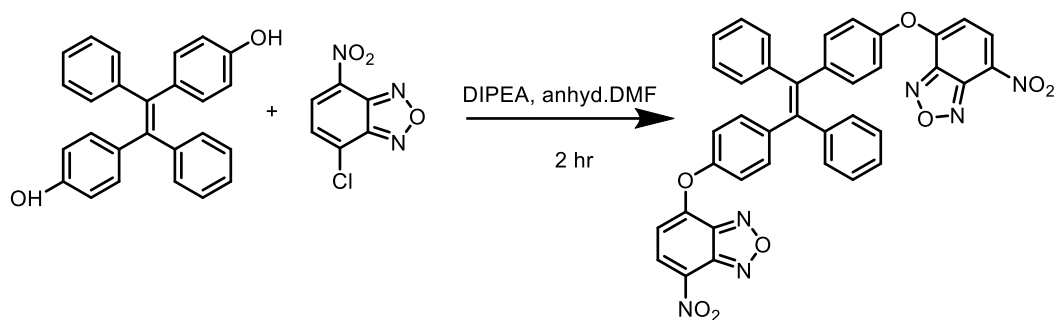
3.5.3.1. Synthesis of TPE-OH-2



4-Hydroxybenzophenone and Zinc dust were dissolved in a 100 ml two necked round bottom flask equipped with a condenser. The flask was evacuated under vacuum and flushed with nitrogen three times. After addition of 50 ml anhydrous THF, the mixture was cooled to 0° C and Titanium tetrachloride was slowly injected. The reaction mixture was slowly warmed to room temperature, stirred for 30 min and then refluxed overnight at 70° C. The reaction was quenched using 10 % K_2CO_3 solution. The mixture was extracted with DCM and the organic layer was washed with brine solution and dried over anhydrous Na_2SO_4 . After removing the solvent, the residue was chromatographed on a silica gel column with *n*-hexane/ CH_2Cl_2 . ^1H NMR (500 Hz, CDCl_3 , δ ppm): 7.002-7.093 (m, 10 H), 6.820-6.872 (m, 4 H), 6.530-6.573 (m, 4H); HRMS, m/z for $\text{C}_{26}\text{H}_{20}\text{O}_2$ calculated: 364.15, found: 364.14.

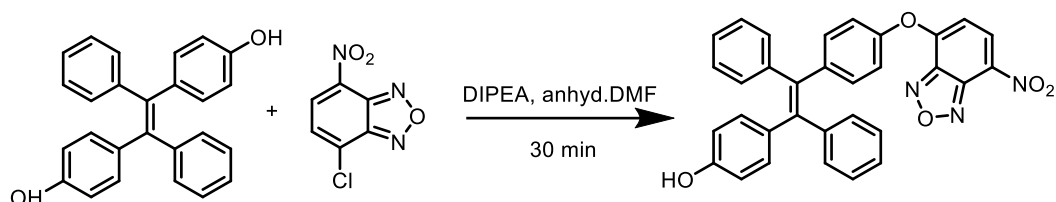
3.5.3.2. Synthesis of the sensor TPE-NBD-2

TPE-OH-2 and 4-chloro-7-nitrobenzofurazan were dissolved in anhydrous DMF (3 ml). 10 μl DIPEA was added in to it and stirred at room temperature for 2 hr under nitrogen atmosphere. The reaction mixture was then purified by column chromatography using DCM/MeOH solvent mixture.



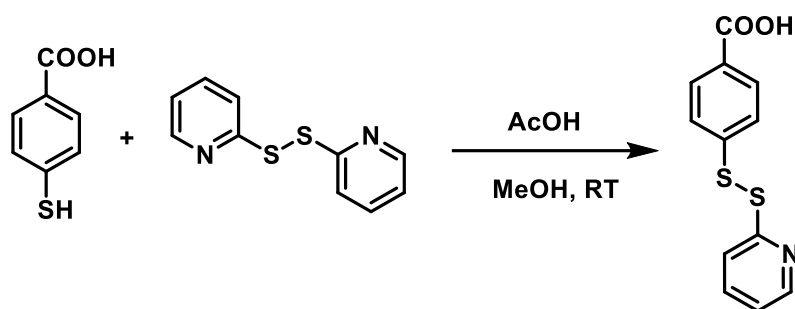
^1H NMR (500 Hz, CDCl_3 , δ ppm): 8.37-8.38 (d, 1 H, $J=10$ Hz), 7.10-7.19 (m, 9 H), 7.02-7.06 (m, 6 H), 6.92-7.01 (m, 3 H), 6.50-6.51 (d, 1 H, $J=10$ Hz); HRMS, m/z for $\text{C}_{38}\text{H}_{22}\text{N}_6\text{O}_8$ calculated: 690.15, found: 713.14 [M+Na].

3.5.3.3. Synthesis of the intermediate TPE-NBD-OH



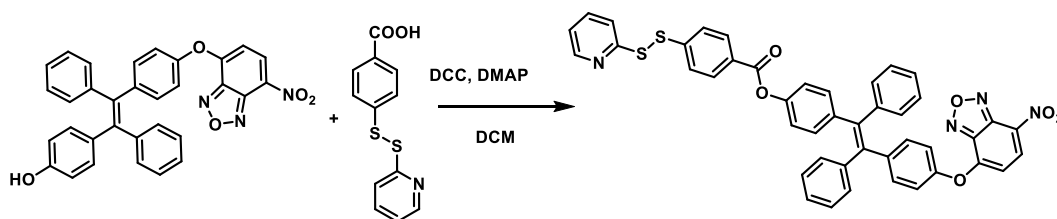
For the preparation of intermediate TPE-NBD-OH, we adopted the same procedure for the synthesis explained earlier for TPE-NBD-2 sensor by monitoring the reaction time. Each 15 minutes we monitor the reaction through TLC and a new spot was started obtaining after first 15 and become more intense after 30 min with the presence of another less intense spot. So, we stopped the reaction and carried out the mass analysis. It showed a major peak corresponding to TPE-NBD-OH. The reaction mixture was purified under column chromatography using DCM/MeOH solvent mixture. HRMS, m/z for $\text{C}_{32}\text{H}_{21}\text{N}_3\text{O}_5$ calculated: 527.15, found: 550.15 [M+Na].

3.5.3.4. Synthesis of donor



2,2' dithiodipyridine and acetic acid were dissolved in methanol and stirred at r.t for 30 min. A solution of 4-Mercaptobenzoic acid in methanol was added drop wise to the reaction mixture and continues stirring for 24 hr. The product was isolated by precipitating the concentrated reaction mixture with diethylether. The washing precipitation was repeated 5 times to lead to a white crystalline product. $^1\text{H NMR}$ (500 Hz, CDCl_3 , δ ppm): 8.381-8.389 (d, 1 H), 7.605-7.734 (m, 3 H), 7.358-7.373 (d, 1 H), 7.139-7.229 (m, 3 H); HRMS, m/z for $\text{C}_{12}\text{H}_9\text{NO}_2\text{S}_2$ calculated: 263.01, found: 264.01 [M+1].

3.5.3.5. Synthesis of the molecular probe TPE-NBD-D



Donor and 4-Dimethylaminopyridine (DMAP) were dissolved in DCM and stirred at room temperature for 30 min. After that, a solution containing TPE-NBD-OH and N,N'-Dicyclohexylcarbodiimide (DCC) was injected in to the reaction mixture and continue stirring for 12 hr. The reaction mixture was then filtered and precipitated with methanol. $^1\text{H NMR}$ (500 Hz, CDCl_3 , δ ppm): 8.46-8.48 (d, 1 H), 8.43-8.45 (d, 1 H),

7.12-7.21 (m, 16 H), 6.64-6.93 (m, 4 H), 6.92-6.93 (d, 2H), 6.60-6.61 (d, 2H); HRMS, m/z for C₄₄H₂₈N₄O₈S₂ calculated: 772.15, found: 773.15 [M+1].

3.6. References

- (1) Hartle, M. D.; Pluth, M. D. A Practical Guide to Working with H₂S at the Interface of Chemistry and Biology. *Chem. Soc. Rev.* **2016**, *45* (22), 6108–6117. <https://doi.org/10.1039/C6CS00212A>.
- (2) Kaushik, R.; Kumar, P.; Ghosh, A.; Gupta, N.; Kaur, D.; Arora, S.; Jose, A. Alizarin Red S –Zinc(II) Fluorescent Ensemble for Selective Detection of Hydrogen Sulphide and Assay with H₂S Donor. *RSC Adv.* **2013**, *1*, 1–3. <https://doi.org/10.1039/C5RA11901D>.
- (3) Steiger, A. K.; Yang, Y.; Royzen, M.; Pluth, M. D. Bio-Orthogonal “Click-and-Release” Donation of Caged Carbonyl Sulfide (COS) and Hydrogen Sulfide (H₂S). *Chem. Commun.* **2017**, *53*, 1378–1380. <https://doi.org/10.1039/C6CC09547J>.
- (4) Zhao, Y.; Biggs, T. D.; Xian, M. Hydrogen Sulfide (H₂S) Releasing Agents: Chemistry and Biological Applications. *Chem. Commun.* **2014**, *50*, 11788–11805. <https://doi.org/10.1039/C4CC00968A>.
- (5) Vandini, E.; Zaffe, D. Mechanisms of Hydrogen Sulfide against the Progression of Severe Alzheimer’s Disease in Transgenic Mice at Different Ages. **2019**, *103*, 50–60. <https://doi.org/10.1159/000494113>.
- (6) Li, Y.; Du, Z.; Liu, X.; Ma, M.; Yu, D.; Lu, Y.; Ren, J. Near-Infrared Activated Black Phosphorus as a Nontoxic Photo-Oxidant for Alzheimer’s Amyloid - β Peptide.

- 2019**, *1901116*, 1–6. <https://doi.org/10.1002/sml.201901116>.
- (7) Zhang, L.; Meng, W.; Lu, L.; Xue, Y.; Li, C.; Zou, F.; Liu, Y.; Zhao, J. Selective Detection of Endogenous H₂S in Living Cells and the Mouse Hippocampus Using a Ratiometric Fluorescent Probe. *Sci. Rep.* **2014**, *4*, 5870. <https://doi.org/10.1038/srep05870>.
- (8) Lin, Y.; Sahoo, B. R.; Ozawa, D.; Kinoshita, M.; Kang, J.; Lim, M. H.; Ryu, K.; Ham, S.; Won, H.; Ryu, K.; Sugiki, T.; Bang, K.-J. K.; Hoe, H.-S.; Fujiwara, T.; Ramamoorthy, A.; Lee, Y.-H. Diverse Structural Conversion and Aggregation Pathways of Alzheimer's Amyloid- β (1–40). *ACS Nano* **2019**, *13* (8), 8766–8783. <https://doi.org/10.1021/acsnano.9b01578>.
- (9) Rosario-Alomar, M. F.; Quiñones-Ruiz, T.; Kurouski, D.; Sereda, V.; Ferreira, E. B.; De Jesús-Kim, L.; Hernández-Rivera, S.; Zagorevski, D. V.; López-Garriga, J.; Lednev, I. K. Hydrogen Sulfide Inhibits Amyloid Formation. *J. Phys. Chem. B* **2015**, *119* (4), 1265–1274. <https://doi.org/10.1021/jp508471v>.
- (10) Wei, H.; Li, X.; Tang, X. Therapeutic Benefits of H₂S in Alzheimer's Disease. *J. Clin. Neurosci. J.* **2014**, *21* (10), 1665–1669. <https://doi.org/10.1016/j.jocn.2014.01.006>.
- (11) Giuliani, D.; Ottani, A.; Zaffe, D.; Galantucci, M.; Strinati, F.; Lodi, R.; Guarini, S. Neurobiology of Learning and Memory Hydrogen Sulfide Slows down Progression of Experimental Alzheimer's Disease by Targeting Multiple Pathophysiological Mechanisms. *Neurobiol. Learn. Mem.* **2013**, *104*, 82–91. <https://doi.org/10.1016/j.nlm.2013.05.006>.
- (12) Kang, J.; Li, Z.; Organ, C. L.; Park, C.; Yang, C.; Pacheco, A.; Wang, D.; Lefer, D. J.;

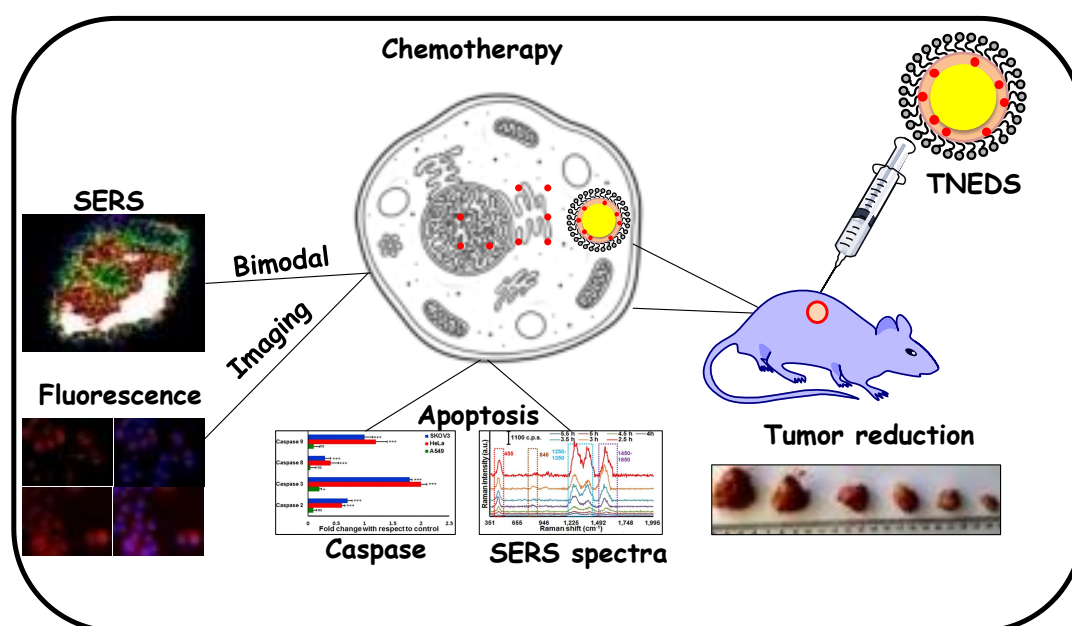
- Xian, M. PH-Controlled Hydrogen Sul Fi de Release for Myocardial Ischemia-Reperfusion Injury. *J. Am. Chem. Soc.* **2016**, *138*, 6336–6339. <https://doi.org/10.1021/jacs.6b01373>.
- (13) Zhao, Y.; Henthorn, H. A.; Pluth, M. D. Kinetic Insights into Hydrogen Sul Fi de Delivery from Caged-Carbonyl Sul Fi de Isomeric Donor Platforms. *J. Am. Chem. Soc.* **2017**, *139*, 16365–16376. <https://doi.org/10.1021/jacs.7b09527>.
- (14) Zheng, Y.; Ji, X.; Ji, K.; Wang, B. Hydrogen Sulfide Prodrugs-a Review. *Acta Pharm. Sin. B* **2015**, *5* (5), 367–377. <https://doi.org/10.1016/j.apsb.2015.06.004>.
- (15) Park, C.; Zhao, Y.; Zhu, Z.; Pacheco, A.; Peng, B.; Devarie-Baez, O. N.; Bagdon, P.; Zhang, H.; Xian, M. Synthesis and Evaluation of Phosphorodithioate-Based Hydrogen Sulfide Donors. *Mol. Biosyst.* **2013**, *9*, 2430–2434. <https://doi.org/10.1039/c3mb70145j>.
- (16) Zhao, Y.; Bolton, S. G.; Pluth, M. D. Light-Activated COS/H 2 S Donation from Photocaged Thiocarbamates. *Org. Lett.* **2017**, *19*, 2278–2281. <https://doi.org/10.1021/acs.orglett.7b00808>.
- (17) Steiger, A. K.; Marcatti, M.; Szabo, C.; Szczesny, B.; Pluth, M. D. Inhibition of Mitochondrial Bioenergetics by Esterase-Triggered COS/H 2 S Donors. *ACS Chem. Biol.* **2017**, *12*, 2117–2123. <https://doi.org/10.1021/acscchembio.7b00279>.
- (18) Cerda, M. M.; Hammers, M. D.; Earp, M. S.; Zakharov, L. N.; Pluth, M. D. Applications of Synthetic Organic Tetrasulfides as H 2 S Donors. *Org. Lett.* **2017**, *19*, 2314–2317. <https://doi.org/10.1021/acs.orglett.7b00858>.

- (19) Gupta, N.; Reja, S. I.; Bhalla, V.; Gupta, M.; Kaur, G.; Kumar, M. A Bodipy Based Dual Functional Probe for the Detection of Hydrogen Sulfide and H₂S Induced Apoptosis in Cellular Systems. *Chem. Commun.* **2015**, *51* (54), 10875–10878. <https://doi.org/10.1039/C5CC02984H>.
- (20) Wang, X.; Sun, J.; Zhang, W.; Ma, X.; Lv, J.; Tang, B. A Near-Infrared Ratiometric Fluorescent Probe for Rapid and Highly Sensitive Imaging of Endogenous Hydrogen Sulfide in Living Cells. *Chem. Commun.* **2013**, *4*, 2551–2556. <https://doi.org/10.1039/c3sc50369k>.
- (21) Zhang, K.; Zhang, J.; Xi, Z.; Li, L.; Gu, X.; Zhang, Q.; Yi, L. A New H₂S-Specific near-Infrared Fluorescence-Enhanced Probe Can Visualize H₂S Level in Colorectal Cancer Cells in Mice. *Chem. Sci.* **2017**, *8*, 2776–2781. <https://doi.org/10.1039/C6SC05646F>.
- (22) Chen, Y.; Zhu, C.; Yang, Z.; Chen, J.; He, Y.; Jiao, Y.; He, W.; Qiu, L.; Cen, J.; Guo, Z. A Ratiometric Fluorescent Probe for Rapid Detection of Hydrogen Sulfide in Mitochondria. *Angew. Chemie - Int. Ed.* **2013**, *52*, 1688–1691. <https://doi.org/10.1002/anie.201207701>.
- (23) Hong, Y.; Lam, J. W. Y.; Tang, B. Z. Aggregation-Induced Emission. *Chem. Soc. Rev.* **2011**, *40* (11), 5361–5388. <https://doi.org/10.1039/c1cs15113d>.
- (24) Ramya, A. N.; Joseph, M. M.; Nair, J. B.; Karunakaran, V.; Narayanan, N.; Maiti, K. K. New Insight of Tetraphenylethylene-Based Raman Signatures for Targeted SERS Nanoprobe Construction Toward Prostate Cancer Cell Detection. *ACS Appl. Mater. Interfaces* **2016**, *8* (16), 10220–10225. <https://doi.org/10.1021/acsami.6b01908>.

- (25) Zhang, W.; Kang, J.; Li, P.; Wang, H.; Tang, B. A Dual Signaling Molecule Sensor for Rapid Detection of Hydrogen Sulfide Based on Modified Tetraphenylethylene. *Anal. Chem.* **2015**, *87*, 8964–8969.
- (26) Liang, J.; Kwok, R. T. K.; Shi, H.; Tang, B. Z.; Liu, B. Fluorescent Light-up Probe with Aggregation-Induced Emission Characteristics for Alkaline Phosphatase Sensing and Activity Study. *ACS Appl. Mater. Interfaces* **2013**, *5* (17), 8784–8789. <https://doi.org/10.1021/am4026517>.
- (27) Huang, X.; Gu, X.; Zhang, G.; Zhang, D. A Highly Selective Fluorescence Turn-on Detection of Cyanide Based on the Aggregation of Tetraphenylethylene Molecules Induced by Chemical Reaction. *Chem. Commun.* **2012**, *48* (100), 12195–12197. <https://doi.org/10.1039/c2cc37094h>.
- (28) Leung, C. W. T.; Hong, Y.; Chen, S.; Zhao, E.; Lam, J. W. Y.; Tang, B. Z. A Photostable AIE Luminogen for Specific Mitochondrial Imaging and Tracking. *J. Am. Chem. Soc.* **2013**, *135* (1), 62–65. <https://doi.org/10.1021/ja310324q>.
- (29) Wang, Z.; Chen, S.; Lam, J. W. Y.; Qin, W.; Kwok, R. T. K.; Xie, N.; Hu, Q.; Tang, B. Z. Long-Term Fluorescent Cellular Tracing by the Aggregates of AIE Bioconjugates. *J. Am. Chem. Soc.* **2013**, *135* (22), 8238–8245. <https://doi.org/10.1021/ja312581r>.
- (30) Chen, S.; Hong, Y.; Liu, Y.; Liu, J.; Leung, C. W. T.; Li, M.; Kwok, R. T. K.; Zhao, E.; Lam, J. W. Y.; Yu, Y.; Tang, B. Z. Full-Range Intracellular PH Sensing by an Aggregation-Induced Emission-Active Two-Channel Ratiometric Fluorogen. *J. Am. Chem. Soc.* **2013**, *135* (13), 4926–4929. <https://doi.org/10.1021/ja400337p>.

- (31) Rosario-Alomar, M. F.; Quiñones-Ruiz, T.; Kurouski, D.; Sereda, V.; Ferreira, E. B.; De Jesus-Kim, L.; Hernández-Rivera, S.; Zagorevski, D. V.; López-Garriga, J.; Lednev, I. K. Hydrogen Sulfide Inhibits Amyloid Formation. *J. Phys. Chem. B* **2015**, *119* (4), 1265–1274. <https://doi.org/10.1021/jp508471v>.
- (32) Yu, X.; Hayden, E. Y.; Xia, M.; Liang, O.; Cheah, L.; Teplow, D. B.; Xie, Y. Surface Enhanced Raman Spectroscopy Distinguishes Amyloid B-Protein Isoforms and Conformational States. *PROTEIN Soc.* **2018**, *27*, 1427–1438. <https://doi.org/10.1002/pro.3434>.

Gold-Mesoporous Silica Nanotheranostic Platform for Targeted Chemotherapy with the Aid of Fluorescence and SERS Dual Detection Modality



4.1. Abstract:

A theranostic nano-carrier delivery system is an unmet need in personalized medicine. Herein, a multipurpose folate receptor targeted nano-envelop delivery system (TNEDS) has been fabricated with gold core silica shell followed by surface functionalization with chitosan-folic acid (CS-FA) covalent conjugate for precise loading of Dox, resembled as Au@SiO₂-Dox-CS-FA. TNEDS possessed up to 90% Dox loading efficiency and internalized through endocytosis pathway leading to pH and redox sensitive release kinetics. The superior folate receptor (FR)-targeted cytotoxicity has been evaluated by the nanocarrier in comparison with FDA approved liposomal

*Dox conjugate, Lipodox™. Moreover, **TNEDS** exhibited theranostic features through caspase mediated apoptosis and envisaged high surface plasmon resonance enabling the nano-construct as a promising SERS nanotag. Distinct changes in the biochemical components inside cells exerted by the **TNEDS** along with the Dox release was evaluated explicitly in a time-dependent fashion using bimodal SERS / Fluorescence nanoprobe. In therapeutic senerio, **TNEDS** displayed superior anti-tumor response in FR-positive ascites as well as solid tumor syngraft mouse models with specific tumor-targeting biodistribution pattern. Therefore, this futuristic **TNEDS** is expected to be a potential alternative as a clinically relevant theranostic nano-medicine to effectively combat neoplasia.*

4.2. Introduction

Advancement in nano-drug delivery system have scrutinized for the controlled delivery of therapeutic payloads against cancer¹. Systemic delivery of anticancer agents often results in the damage of healthy organs which significantly impedes the survival rates. Ongoing research on nanomedicine aims to enhance the therapeutic index of anti-neoplastic drugs by adjusting their pharmacokinetics and bio-distribution. The idea that nanomedicine aims to enhance the therapeutic index of anti-neoplastic drugs by adjusting their pharmacokinetics and bio-distribution to enhance conveyance to the site of action is clinically demonstrated. The enhanced permeation and retention (EPR) effect of the tumor microenvironment provides easier access of chemotherapeutic drugs to tumor tissues. Dox is a widely used anti-neoplastic agent, but its severe side effects² especially noticeable cardiotoxicity limits clinical efficacy. Designed to exploit the advantages of NPs, liposomal Dox formulations were approved by FDA³ but has a whimsical disadvantage of being

non-targeted towards cancer cells⁴. Among different nanocarriers, AuNPs and MSNs based carriers are widely employed towards cancer diagnosis and imaging, either alone or in conjugation with therapeutic motifs.

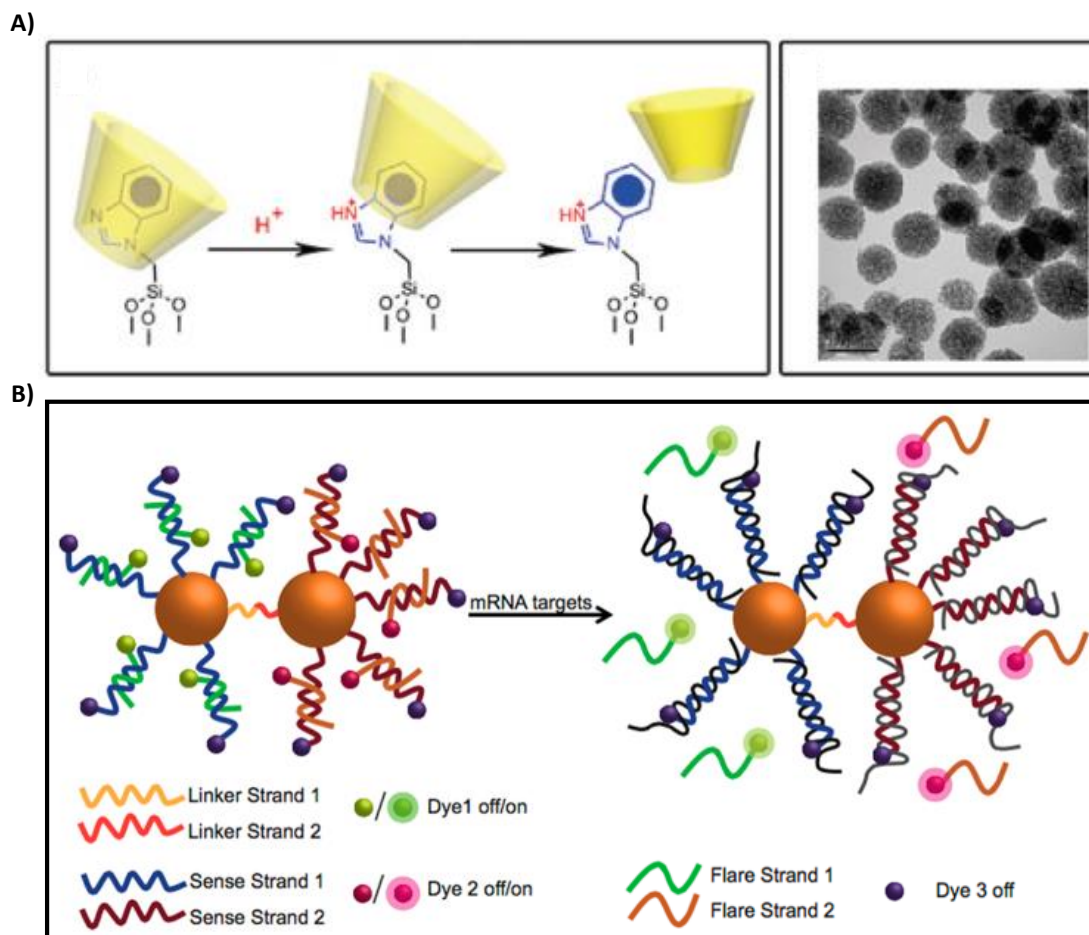


Figure 4.1. A) A graphical representation of the pH responsive MSN nanovalve, and its protonation caused release of beta-cyclodextrin and corresponding TEM image of capped MSN, B) schematic representation of DNA-AuNPs self-assembly, Figure A is adapted from ref. 5 and B is adapted from ref. 6.

Andre and co-workers reported MSNs based carrier system for the effective delivery of anticancer agent Dox in the nuclei of KB-31 cells⁵. In this study, they have used a β -cyclodextrin modified Dox loaded MSNs for pH-triggered drug release (**Figure 4.1A**). In another report, the authors utilized a DNA-AuNPs self-assembly for multiple synergistic applications in cellular environment (**Figure 4.1B**). This carrier

is responsible for the delivery of two anticancer drugs like Dox and mitoxantrone in living cells and displayed therapeutic advantages⁶.

High localized surface plasmon resonance (LSPR) of AuNPs facilitates in diagnostic modality as a SERS substrate to provide structural information of many biomolecules based on their unique vibrational Raman fingerprints. The LSPR spectral shifts induced by interparticle plasmonic coupling have attracted considerable interest in the fabrication of assembled plasmonic nanoparticles⁷. Duan and co-workers demonstrated a SERS encoded gold nanoparticle vesicle for targeted cancer diagnosis and therapy. SERS nanotags contains a 14 nm AuNPs, Raman reporter molecule and a pH sensitive polymer brushes contains poly ethylene glycol (PEG) and hydrophobic copolymer, PMMAVP of methyl methacrylate (MMA) and 4-vinylpyridine (**Figure 4.2.**). This multifunctional drug carrier system allows efficient loading and releasing of cargo in to cancer cells and the process was monitored with the aid of SERS technique⁸.

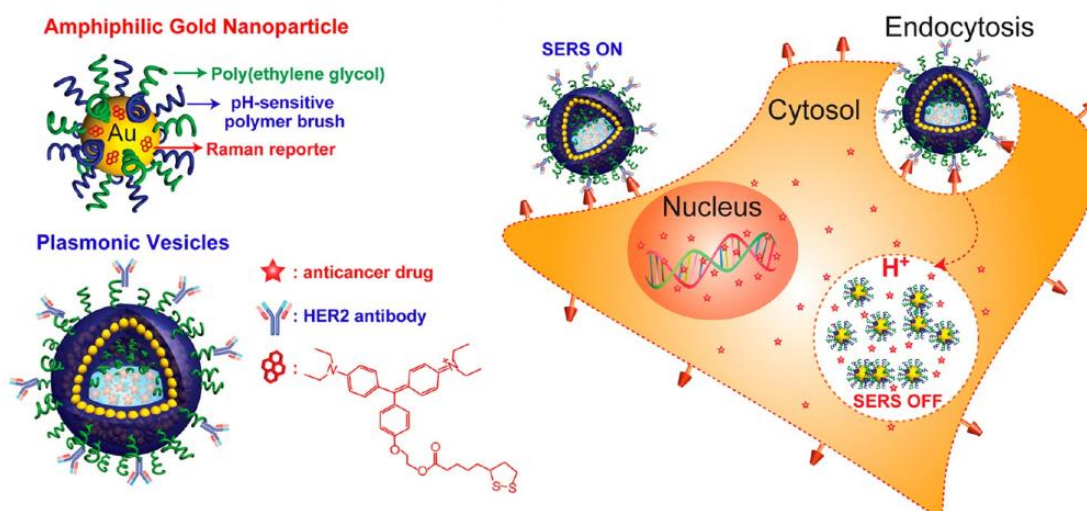
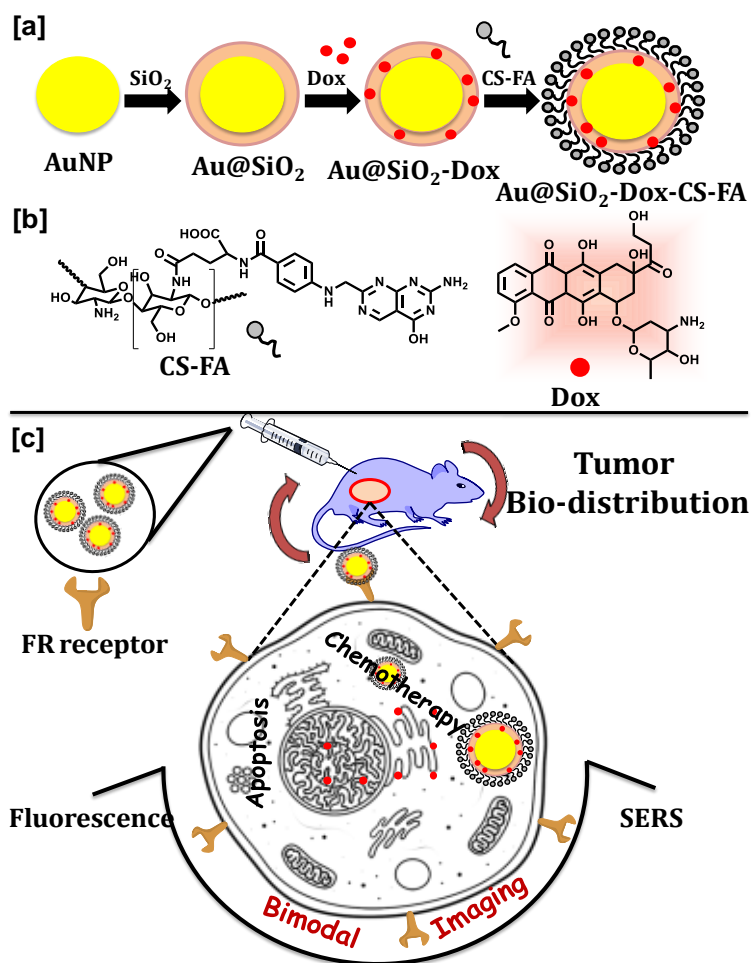


Figure 4.2. Schematic illustration of the SERS nanotags for diagnosis and therapy. Figure is adapted from ref. 8.

In SERS, hot spots created in the gaps between NPs or at the edges and tips of anisotropic NPs provide sufficiently intense electromagnetic fields to promote a tremendous increase in the Raman intensity of molecules located in these regions, making it possible to detect even molecular level changes. AuNPs with tunable size and shape acts as excellent SERS substrates was used in label-free immunoassays, bio-sensing, imaging of living cells and microbes in ultralow level of LOD. Engineering plasmonic nanostructures confined within a defined architecture and surface caged with bio-materials with defined optical and structural properties have captivated biological applications. Moreover, SERS-encoded plasmonic NPs capable of generating stable and reproducible Raman signals have made Raman imaging and spectral analysis into clinical milieu⁹. Construction of nano-carrier's based on MSNs have attracted biomedical applications owing to their many unique features such as high surface area, tunable pore morphologies, large pore volume, facile functionalization of exterior surfaces and bio-compatibility. MSNs provided a high drug loading capability, therefore encapsulation of AuNPs with silica layer (Au@SiO₂) not only enable facile surface modification and stimuli responsive release but also enhances the LSPR of the construct to be an effective SERS substrate¹⁰. Even though the clinically used NPs formulations of Dox demonstrated effectiveness, the lack of cancer cell targeting moieties makes them amiable to normal cells. Capping of drug loaded Au@SiO₂ NPs with bio-degradable natural polymer chitosan will avert premature drug release and promotes the bio-compatibility. FR is known to be over-expressed in several human malignancies and the exploration of FR-mediated drug delivery has been referred to a molecular "Trojan horse" approach¹¹. Non-targeted chemotherapeutic strategies often caused greater side effects whereas targeted nano-carrier system prevents random drug exposure to normal tissues. Again,

targeted nano-carrier system often allows the delivery of drugs at lesser quantities, due to a combination of molecular targeting and increased circulation time preventing random exposure to normal tissues^{12,13}.

Considering all this in mind, a clinically viable smart **TNEDS** has been aimed to build Au@SiO₂ NPs loaded with Dox which is enveloped by a layer of CS-FA covalent conjugate **Au@SiO₂-Dox-CS-FA (Scheme 4.1)**. The major emphasize on theranostic efficiency of **TNEDS** has been exploited by (i) impressing bio-compatibility with efficient Dox loading and tumor niche-specific release enabled targeted cytotoxicity by FR-mediated endocytosis; (ii) the significant Raman spectral enhancement of the **TNEDS** utilized as a SERS nanotag for quantifying Dox loading and tracing of intracellular Dox release by Raman imaging; (iii) evaluation of apoptotic cell death by **TNEDS** using SERS/Fluorescence bimodality; (iv) detailed investigation with tumor challenged mouse models deciphered excellent targeted bio-distribution pattern with a highlighted therapeutic potential of **Au@SiO₂-Dox-CS-FA** than clinically used Dox and Lipodox. Although further investigations are warranted to establish the current **TNEDS** in clinical milieu, the contemporary studies presented here emphasized the superiority of **Au@SiO₂-Dox-CS-FA** as a futuristic multi-model theranostic nanomedicine towards efficient cancer management.



Scheme 4.1. Schematic illustration (a) of various steps involved in the fabrication of **Au@SiO₂-Dox-CS-FA** starting from AuNPs. (b) Chemical structure of CS-FA and Dox. (c) Biological evaluation after Intraperitoneal (*ip*) administration of **TNEDS** on tumor-bearing mice.

4.3. Results and Discussion

4.3.1. Preparation and Characterization of TNEDS

The targeted nano envelop system was synthesised using gold nanoparticle as core which upon coating with a layer of silica by tetraethylorthosilicate (TEOS). Anti-cancer drug Dox was incorporated on to the pores of silica layer to get therapeutic effect. A layer of CS-FA further encapsulated over the silica layer to target the system towards folate receptor specific cancer cells. The successful preparation of **Au@SiO₂-Dox-CS-FA** in a stepwise manner was effectively

monitored by UV-Vis spectroscopy, TEM, DLS and confocal Raman spectroscopy. The presence of silica layer on AuNPs core was indicated by the red shifted (531 to 534 nm) plasmon maxima of the nano-construct. Presence of drug loading was confirmed by the blue shift of the absorption maxima of 521 nm as a broad peak. Dox loaded on Au@SiO₂ further shielded by CS-FA has been well studied by UV-Vis spectroscopy in which absorbance maxima showed a slight blue shift with peak broadening (**Figure 4.3A**). TEM analysis further confirmed the step wise formation of the nano-construct where average size of AuNPs (40-45 nm) increased to 105 nm upon silica coating (**Figure 4.3B**). Additional surface functionalization with CS-FA increased the size to 125 nm of the final nano-construct. Morphological analysis revealed the presence of AuNPs as core confined within the silica shell along with single AuNPs. The average hydrodynamic size (**Figure 4.3C**) around 125 nm was in agreement with TEM analysis. A non-targeted construct, Au@SiO₂-Dox-CS was also constructed by the same method by using CS instead of CS-FA. Dox impregnation into the SiO₂ pores was evaluated by the drug loading efficiency (DLE), drug loading content (DLC) and actual amount of drug within the nano envelop. **Au@SiO₂-Dox-CS-FA** showed a high DLE of 90% with around 93.75 mg Dox per gram of the construct and 9.3 % DLC whereas **Au@SiO₂-Dox-CS** demonstrated 81 % DLE, 8.5 % DLC and 85 mg Dox per gram of the construct respectively.

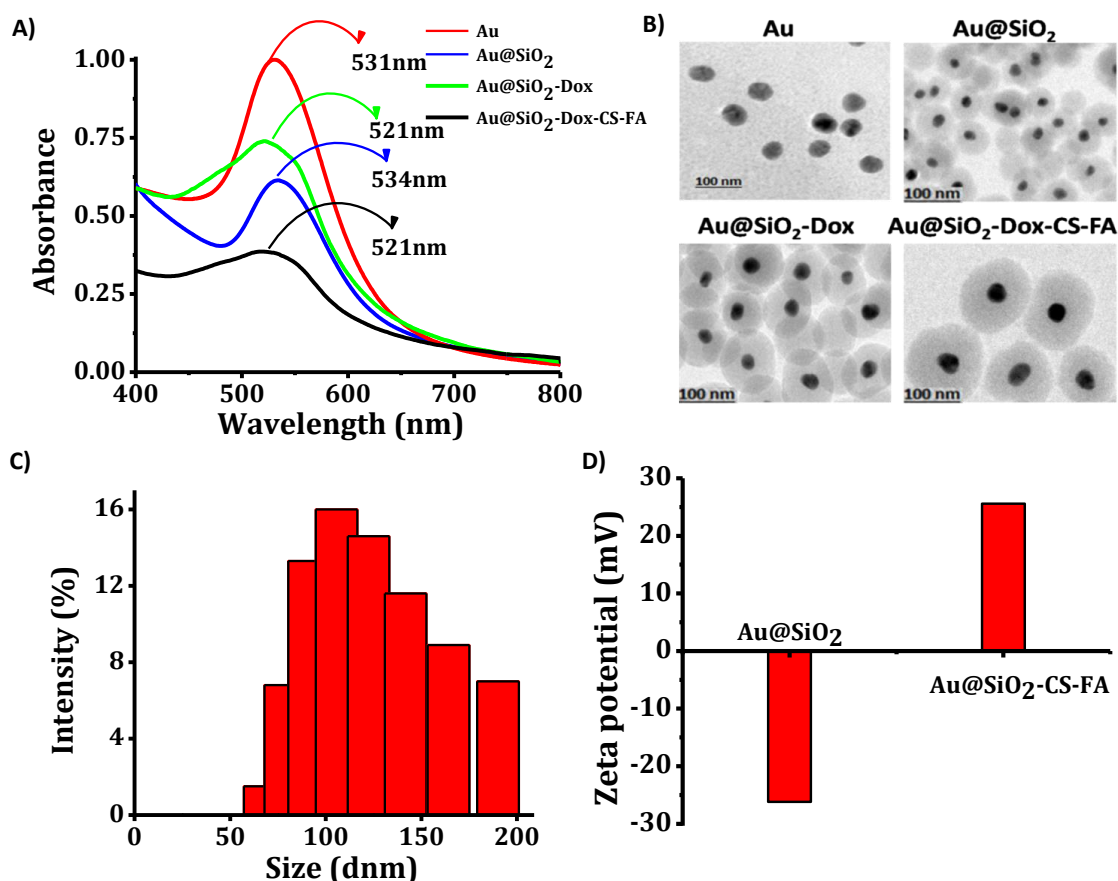


Figure 4.3. A) UV-Visible spectra obtained from each step for the construction of TNEDS B) corresponding TEM images C) Hydrodynamic size distribution of Au@SiO₂-Dox-CS-FA determined by DLS D) Zeta potential changes from each step.

The successful functionalization of CS-FA with Dox loaded silica nanoparticle was initially confirmed by UV-Vis spectroscopy and later with Fourier-transform infrared spectroscopy (FT-IR) analysis. FT-IR spectrum of CS (**Figure 4.4A**) was characterized with the bands around 3396 cm⁻¹, 1655 cm⁻¹, 1378 cm⁻¹, 1075 cm⁻¹ and at 611 cm⁻¹ whereas CS-FA spectrum (**Figure 4.4B&C**) showed the appearance of -CONH amide band at 1645 cm⁻¹ and the N-H bending in the second amine at 1590 cm⁻¹ which indicated the amide coupling between FA and CS. Further, the peak at 3300 cm⁻¹ of CS-FA becomes wider; indicating the extended hydrogen bonding between the FA and CS¹⁴.

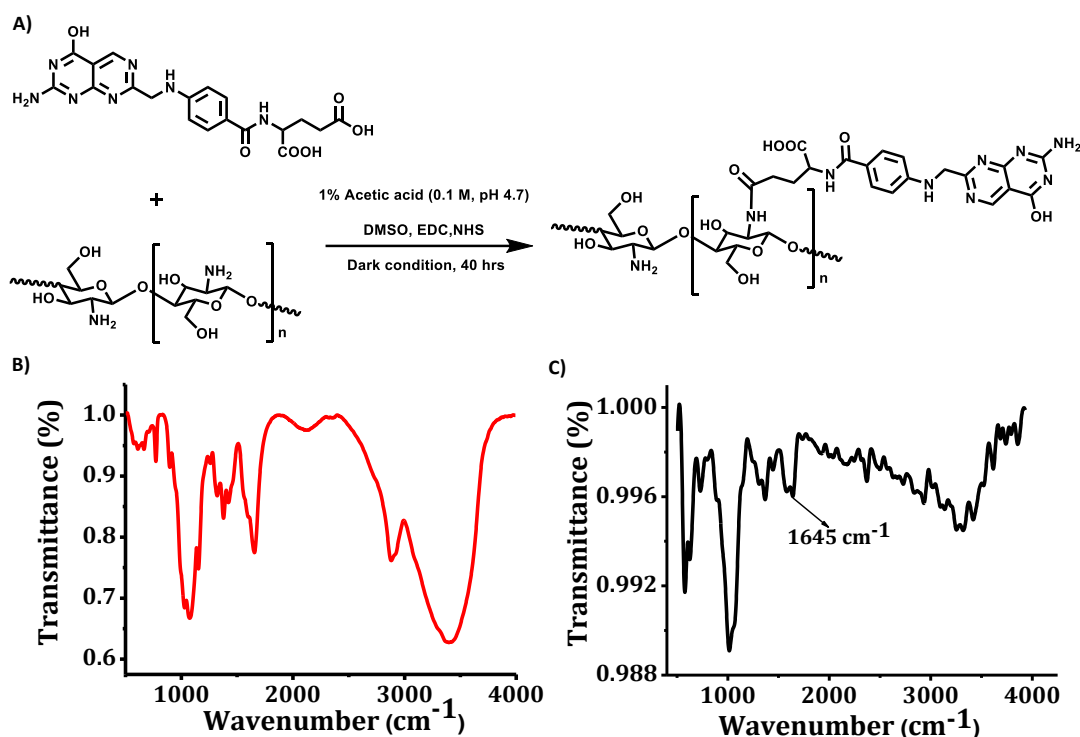


Figure 4.4. A) Synthetic scheme for the conjugation of CS-FA, FT-IR spectrum of B) chitosan and C) chitosan-folic acid derivative.

Due to the existence of silica coating on the exterior surface of AuNPs, a zeta potential value of -26.2 was observed but it has been changed to +25.6 upon CS-FA coating indicating the presence of amino group on the surface of NPs¹⁵ (**Figure 4.3D**). Finally, loading of Dox was confirmed by SERS spectral analysis, where signature Raman peaks of Dox appeared from the nano-construct (**Figure 4.5**). The presence of silica envelop and surface modifications will not affect the robust SERS intensity of the analyte¹⁶. More precisely, the presence of Dox within **Au@SiO₂-Dox-CS-FA** was established by SERS single spectral analysis which was in agreement with the SERS spectra of bare Dox incubated with AuNPs. Dox showed characteristic Raman signature peaks at 455 cm^{-1} assigned to the C=O in plane deformation, peaks between 1247 - 1318 cm^{-1} corresponds to the in-plane bending motions from C-O, C-O-H and C-H, respectively and peak at 1438 cm^{-1} attributed to the presence of skeletal ring vibrations of Dox¹⁷. The SERS signal of Dox is originated from the hot

spot generated by the cluster of NPs surrounding the silica shell. The silica layer in the close vicinity of AuNPs leads to excellent interparticle plasmonic coupling, as demonstrated by the significant red-shift of plasmon resonance of AuNPs.

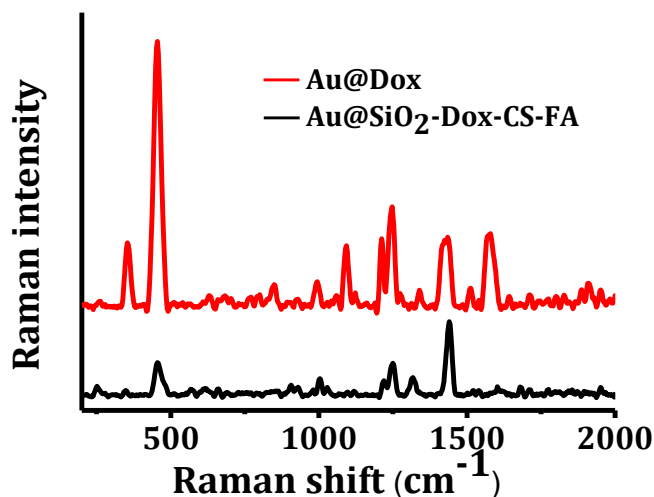


Figure 4.5. SERS spectral pattern analysis of Au@SiO₂-Dox-CS-FA compared with pure Dox spectra (Au@Dox).

4.3.2. Stimuli Responsive Drug Releases

Initially, the release kinetics of Dox from **Au@SiO₂-Dox-CS-FA** was evaluated under parameters of pH and reducing atmosphere at ambient temperature by UV-Vis spectroscopy. It was found that **Au@SiO₂-Dox-CS-FA** exhibited an optimal Dox release kinetics (**Figure 4.6A**) which is largely dependent on pH and to a lesser extent towards redox balance. A cumulative Dox release kinetics was observed with a pH of 5 wherein almost 96% and 89% was released within 9 hr in the presence and absence of reducing agents. The Dox release was further evaluated in SERS modality (**Figure 4.6B**) where the appearance of characteristic peak of Dox at 455 cm⁻¹ demonstrated the release under varying pH. The signal intensity of Dox signature showed a steep decline from pH 7.4 to 5 indicating pH dependent release from **Au@SiO₂-Dox-CS-FA**. The released Dox from the nano-construct in acidic pH

exits through the dialysis membrane and was monitored by gradual decrease in SERS spectra.

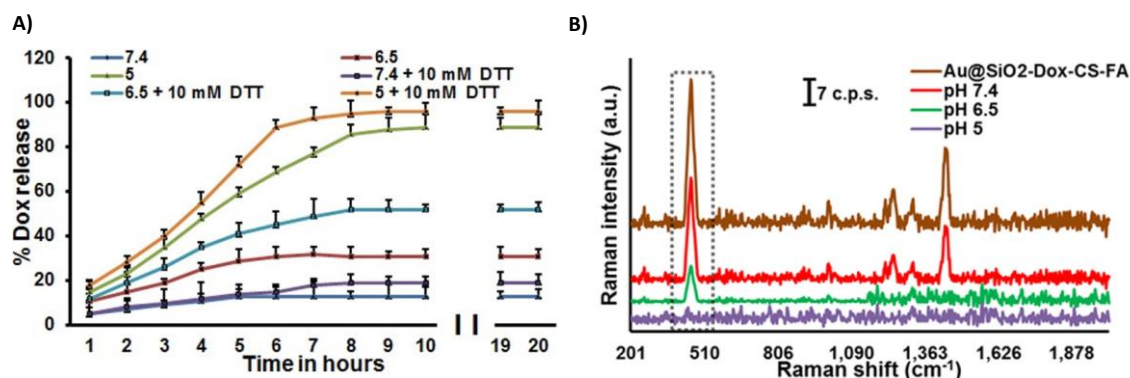


Figure 4.6. Evaluation of Dox release kinetics from **Au@SiO₂-Dox-CS-FA** with A) UV and B) confocal Raman microscopy.

Normally, tumor tissue is accompanied with acidosis by high metabolic activity and the microenvironment has a lower pH with high redox potential than the surrounding normal tissue. The cumulative redox and pH dual responsive Dox release from **Au@SiO₂-Dox-CS-FA** enforce targeted cytotoxicity specifically at the tumor area, sparing the normal tissue, which has a pH of 7.4 and less redox environment¹⁸. The precise entrapment of Dox within the SiO₂ layer and further caged with chitosan could be the potential factor regulating the controlled release. At higher pH, the primary amino groups of chitosan undergo a sort of shrinking mode leading to a slow drug release whereas lower pH promotes protonation of primary amines, leading to swelling of polymeric matrix to allow drug molecules to move more freely through normal diffusion. Furthermore, chitosan acts as gatekeeper to retain Dox in the pores and prevent undesired leaching from the pores in the absence of acidic environment¹⁹.

4.3.3. Western blot analysis and Hemolysis Assay

Next, the FR expression status of human, murine cancer cells and normal fibroblast cells were assessed by Western blot analysis using antibodies directed against the FR. Quantitative evaluation of the resulting bands was performed after normalizing with those of β -actin. Out of the eight cell lines examined, HeLa and ovarian cancer (SKOV3) cells showed significantly higher FR expression, whereas A549 and 3T3L1 exhibited minimum FR expression (**Figure 4.7A**).

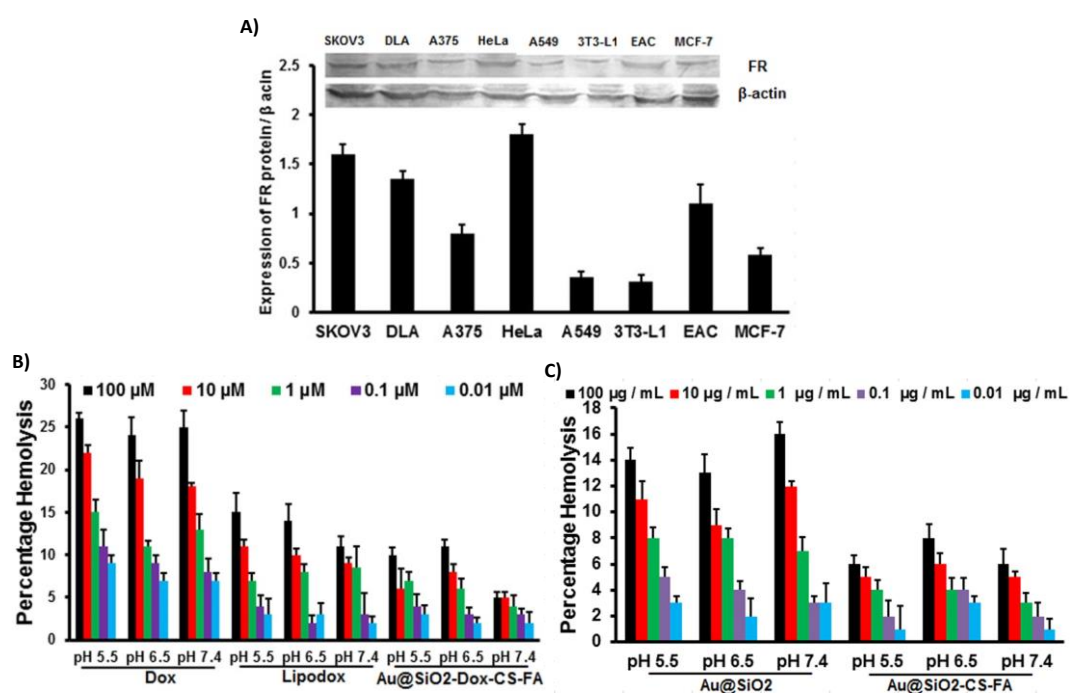


Figure 4.7. A) Western blot showing the expression levels of FR in cells and quantification of protein bands normalized to β -actin using Image J software, B&C) Hemolysis experiment performed under various pH conditions; data are the mean \pm SD of three independent experiments.

Again, hemolysis assay was performed to determine the toxicity towards red blood cells (RBCs) under three different pH conditions. The highest hemolytic activity was observed for free Dox, which demonstrates concentration-dependent pH-independent lysis wherein as high as 26% hemolysis was observed for 100 μ M Dox

at pH 5.5, and even at 0.01 μM causes 7% hemolysis at pH 7.4. Lipodox demonstrated reasonably reduced toxicity towards RBCs in comparison with Dox. **Au@SiO₂-Dox-CS-FA** displayed concentration and pH dependent hemolytic behavior; even at the highest concentration of 100 μM , 10% lysis was observed at pH 5.5, whereas only 5% was recorded at pH 7.4 under same conditions. Lower concentrations are largely safer to RBCs especially at physiological pH (**Figure 4.7B**). The uncoated Au@SiO₂ displayed severe hemolytic behavior independent of a change in pH. However, coating with CS-FA makes **Au@SiO₂-CS-FA** more biocompatible and safer towards RBCs (**Figure 4.7C**). Among the different strategies for receptor mediated drug delivery, FRs are used as a promising target because of their over-expression in many human cancer cells. FR expression varies significantly between cancer cell lines which urges to evaluate the receptor status prior to cell-based experiments²⁰. The results obtained correlated well with similar studies and enabled us to select HeLa and SKOV3 as FR-positive and A549 as FR-negative cells for *in vitro* assays. Again, Ehrlich ascites carcinoma (EAC) and Daltons lymphoma ascites (DLA) cells showed moderate levels of FR expression which has been chosen for *in vivo* assays with FR-targeting systems. Even though silica-based NPs are reported to execute hemolytic features, it is significantly reduced by surface coating with any bio-polymers or proteins. Moreover MSNs based NPs of size in between 100-200 nm are reported to execute bio-compatibility to RBCs²¹ in comparison with smaller particles. The moderate hemolytic nature of naked Au@SiO₂ NPs and the major reduction upon coating with CS-FA could be well explained with the above-mentioned facts. Again, the isoelectric pH of blood prevents the Dox release from **Au@SiO₂-Dox-CS-FA** making it as an efficient delivery system having bio-compatibility to RBCs.

4.3.4. SERS imaging of live cells using Au@SiO₂-CS-FA

As a new insight, the efficiency of Au@SiO₂-CS-FA as SERS-nanotag was explored on HeLa cells with the aid of a confocal Raman microscope. HeLa cells upon treatment with Au@SiO₂-CS-FA for 1hr revealed a well-defined Raman image (Figure 4.8A&B) with a proper clustering pattern (Figure 4.8C). Figure 4.8D represents the condor image which clears the internalization.

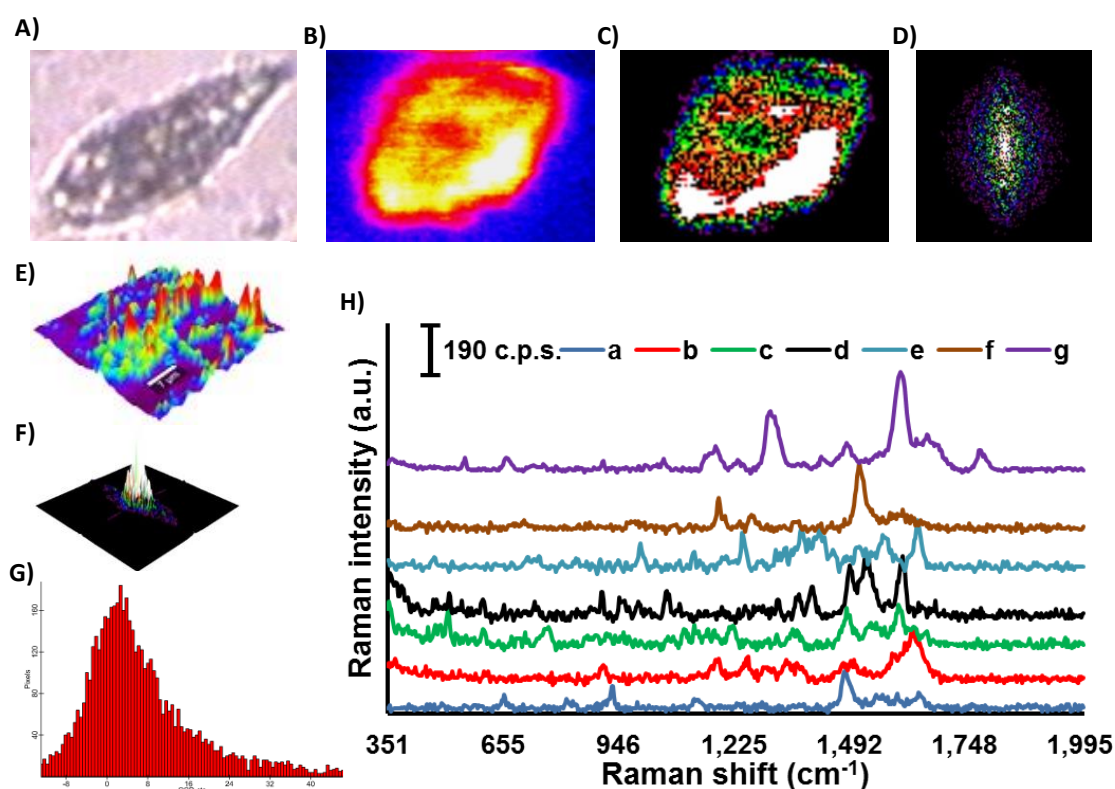


Figure 4.8. A) Bright field, B) Raman, C) cluster and corresponding D) condor images of Au@SiO₂-CS-FA treated HeLa cells, three dimensional Raman intensities of E) images B and F) image C, G) Histogram of the two most intense peaks from HeLa cells, H) Raman spectra abstracted from various regions of the Raman image.

Three dimensional representations of the images clearly indicated the enhanced cellular information in contrast with the surroundings (Figure 4.8E&F). Condor images and histogram of the relative intensity of the two most intense peaks from the NP-treated cells deciphered the significant signal enhancement (Figure 2.8G).

Raman spectra (**Figure 4.8H**) abstracted at various regions of the Raman image exhibited characteristic fingerprint SERS peaks from sub-cellular locations such as cell membrane, cytoplasm, nucleus and other cellular organelles (**Table 4.1**).

Table 4.1. Tentative peak assignment of SERS spectra abstracted from various regions of the Raman image of HeLa cells treated with **Au@SiO₂-CS-FA**. Legends a-g represents the corresponding spectra of **Figure 4.8**.

Raman Shift (cm ⁻¹)	Tentative Assignment
Spectra- [a]	
658 cm ⁻¹	C-C twist Phe
923 cm ⁻¹	C-C str. α -helix
1118 cm ⁻¹	C-N str. of proteins
1476 cm ⁻¹	C-H def
1647 cm ⁻¹	Amide I α -helix
1552 cm ⁻¹	nucleic acid (adenine, guanine)
Spectra- [b]	
918 cm ⁻¹	C-C str. α -helix
1189 cm ⁻¹	C-H bend Tyr
1249 cm ⁻¹	Amide III
1357 cm ⁻¹	C-H def
1476 cm ⁻¹	C-H def
1650 cm ⁻¹	Amide I α -helix
Spectra- [c]	
602 cm ⁻¹	C-C twist Phe
759 cm ⁻¹	Ring breath Trp
1217 cm ⁻¹	Amide III
1357 cm ⁻¹	CH def of protein
1487 cm ⁻¹	nucleic acid (adenine, guanine)
Spectra- [d]	
903 cm ⁻¹	C-O-C ring of carbohydrate
1062 cm ⁻¹	Chain C-C str of lipids
1325-1375 cm ⁻¹	C-H str. of proteins
1405-1492 cm ⁻¹	G, A, CH def of nucleic acids
1534 cm ⁻¹	nucleic acid (adenine, guanine)
1614 cm ⁻¹	C=C Tyr, Trp of proteins
Spectra- [e]	
1000 cm ⁻¹	Sym. Ring brPhe
1123 cm ⁻¹	C-N str. of protein
1244 cm ⁻¹	Amide III of proteins
1384-1568 cm ⁻¹	CH def of proteins
1619 cm ⁻¹	C=C Tyr, Trp
Spectra- [f]	
1189 cm ⁻¹	C-H bend Tyr

1260 cm ⁻¹	Amide III of proteins
1510 cm ⁻¹	nucleic acid (adenine, guanine)
1610 cm ⁻¹	C=C Phe, Tyr
Spectra- [g]	
550 cm ⁻¹	Tryptophan; cytosine; nucleic acid (guanine)
646 cm ⁻¹	C-C twist Tyr
903 cm ⁻¹	C-O-C ring of carbohydrate
1051 cm ⁻¹	C-H in-plane Phe
1170 cm ⁻¹	C-H bend Tyr
1222 cm ⁻¹	Amide III of protein
1484 cm ⁻¹	CH def
1039 cm ⁻¹	CH ₂ twist
1660 cm ⁻¹	C=C Phe, Tyr
1779 cm ⁻¹	C=O ester of lipids

SERS imaging is a new arena involving intensive study utilizing the high SPR of NPs and among which silica coated AuNPs are reported to be excellent SERS substrates with uniform hot spot generation²². The hyper cluster analysis (HCA) from the strongest Raman bands of the HeLa cells clearly provided label-free methods for the visualization of intracellular components and processes based on strong Raman signals²³. SERS spectra obtained from the nuclear regions are mainly characterized with sharp peaks at 1487 cm⁻¹, 1510 cm⁻¹ and 1534 cm⁻¹ which corresponds to nucleic acids whereas the spectra obtained from the cytoplasmic region bears signatures from ribose vibration of ribo nucleic acid (RNA) (917 cm⁻¹), carotenoids (1006 cm⁻¹), C-C stretching of lipids and carbohydrates (1060 cm⁻¹), C=C stretching of proteins (1615 cm⁻¹) and many more²⁴. The distinct three-dimensional spectra and cluster analysis obtained using **Au@SiO₂-CS-FA** could be a promising step to understand the physicochemical processes in the local cellular environment in real time, in order to benefit for specific intracellular targeting.

4.3.5. Evaluation of cytotoxicity

Cytotoxicity of the prepared nano-envelop along with free Dox and Lipodox was evaluated on FR-positive and negative cell lines.

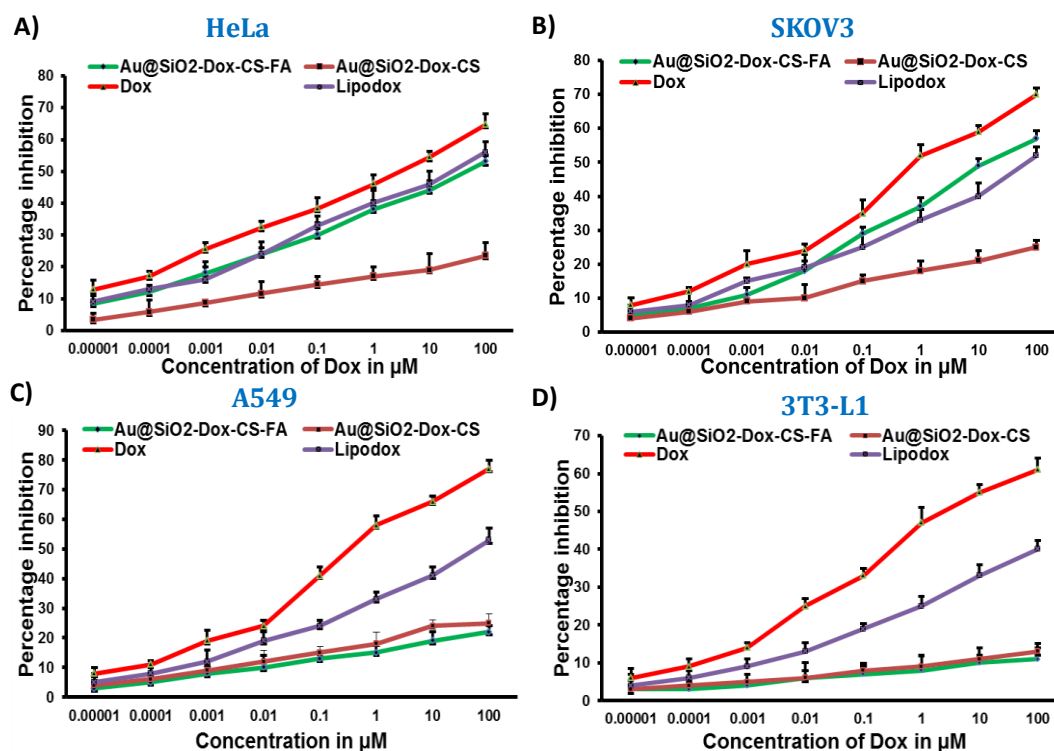


Figure 4.9. Evaluation of cytotoxicity of Dox, Lipodox, Au@SiO₂-CS-FA and Au@SiO₂-Dox-CS-FA after 24 h by MTT assays on A) HeLa, B) SKOV3, C) A549 and D) 3T3-L1 cells.

Au@SiO₂-Dox-CS-FA displayed cytotoxicity selectively toward HeLa (**Figure 4.9A**) and SKOV3 (**Figure 4.9B**) cell that over-express FR, but was less toxic towards Adenocarcinomic human alveolar basal epithelial cells (A549) (**Figure 4.9C**) and murine fibroblasts (3T3L1) (**Figure 4.9D**) with minimal FR expression. Cytotoxicity of Au@SiO₂-Dox-CS-FA towards FR positive cells were less pronounced than Dox and Lipodox but was efficient than Au@SiO₂-Dox-CS.

4.3.6. Investigation of cellular uptake pathways and intracellular dox release by fluorescence modality

Cellular uptake and intracellular release of Dox from **Au@SiO₂-Dox-CS-FA** was compared with naked Dox, Lipodox and **Au@SiO₂-Dox-CS** on HeLa and A549 cells by fluorescence measurements. Among them Dox uptake was maximum in **Au@SiO₂-Dox-CS-FA** and minimum in Au@SiO₂-Dox-CS on HeLa cells (**Figure 4.10A&B**). However, in case of FR-negative A549 cells **TNEDS** displayed minimal Dox uptake wherein naked Dox displayed the maximal effect (**Figure 4.10B**). Since positively charged nano-constructs are reported to follow receptor mediated uptake pathways, the cellular uptake mechanism of **Au@SiO₂-Dox-CS-FA** was investigated fluorometrically after pre-incubation of cells with specific inhibitors and folic acid (**Figure 4.10C**). Cellular endocytosis is used to uptake nutrients, growth factors and plays as a master regulator of the signaling pathway. In order to examine the mode of cellular uptake mechanism of **TNEDS**, dox concentration was estimated in FR over expressed cells after pre-incubated with specific endocytosis inhibitors. Estimation of Dox uptake displayed a significant ($p < 0.001$) reduction upon treatment with genistein (100 $\mu\text{g}/\text{mL}$), chlorpromazine (20 $\mu\text{g}/\text{mL}$) and folic acid (2 mM) but was not affected by 5-(N-ethyl-N-isopropyl)-amiloride (10 $\mu\text{g}/\text{mL}$) upon comparison with the respective controls.

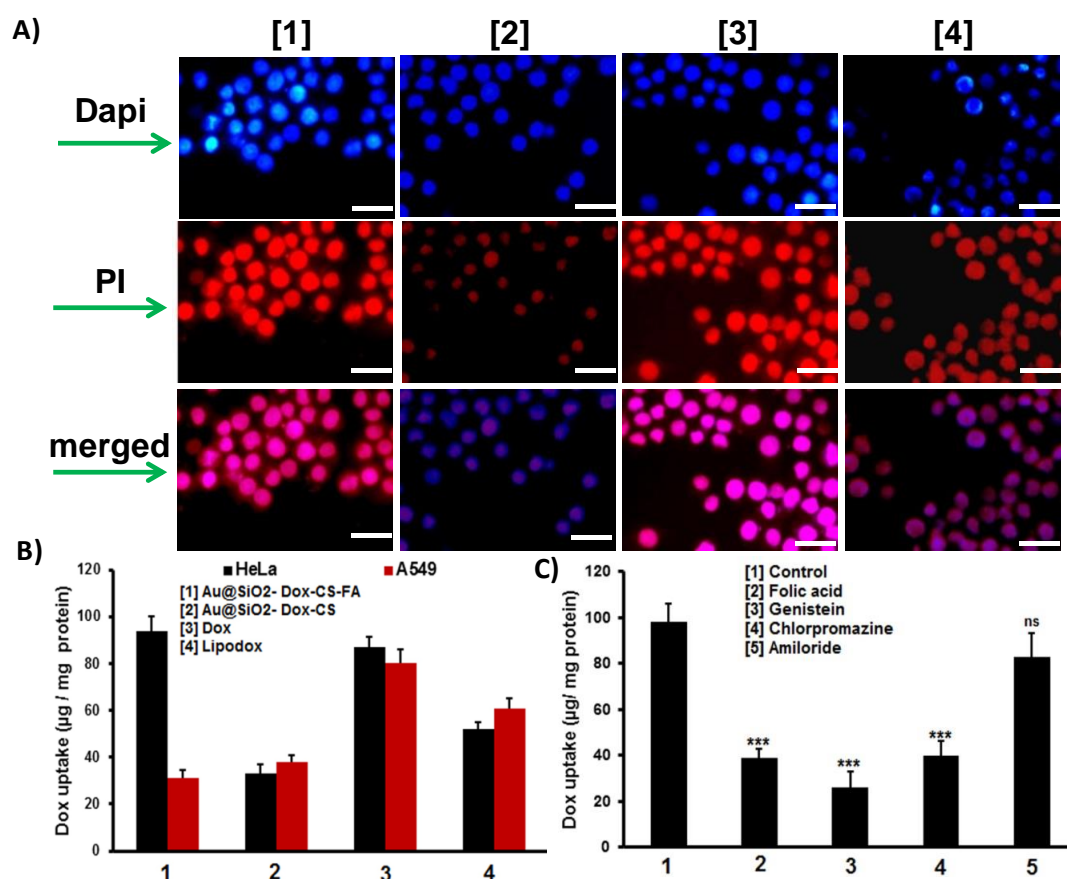


Figure 4.10. Evaluation of the intracellular uptake and distribution of Dox in HeLa cells after 4 h administration ($1 \mu\text{M}$) using A) fluorescence microscopy, the legends [1] represents **Au@SiO₂-Dox-CS-FA**; [2] **Au@SiO₂-Dox-CS**; [3] Dox and [4] Lipodox. B) Quantitation of Dox uptake fluorometrically. C) Estimation of the effect of inhibitors on the uptake of **Au@SiO₂-Dox-CS-FA** on HeLa cells by fluorimetry.

Moreover, cellular uptake was visualized using fluorescent microscope which again confirmed the highly FR-selective and efficient cellular Dox uptake by **Au@SiO₂-Dox-CS-FA** (Figure 4.11.). The released Dox was localized in the nuclear region for effective therapeutic utility within 4 h of administration. Functional biomolecules on the surface, size and morphology of nano-construct play a predominant role in determining the probable mechanism of internalization which are namely, clathrin, caveolae, macropinocytosis and phagocytosis²⁵. Endocytosis pathway determination using specific inhibitors revealed that FR mediated caveolae and clathrin dependent pathway plays a prominent role in the cellular uptake of **Au@SiO₂-Dox-CS-FA**

whereas micropinocytosis has little effect. Cationic AuNPs around 100 nm are reported to follow receptor-mediated endocytosis mainly through caveolae, which are flask-shaped invaginations of the plasma membrane coated by caveolin-1 and to a lesser extent by clathrin dependent pathways²⁶.

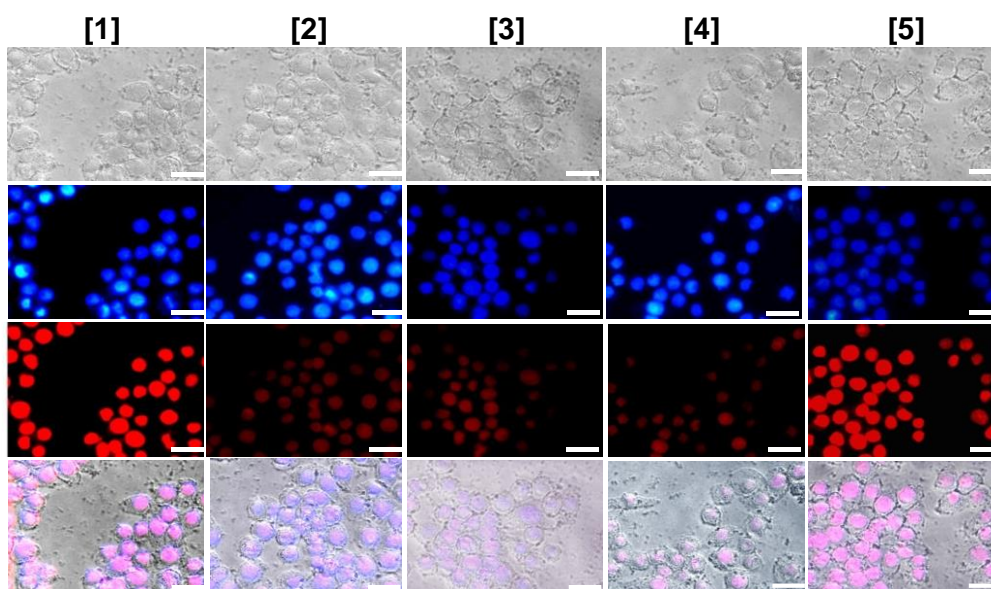


Figure 4.11. Fluorescence images of **Au@SiO₂-Dox-CS-FA** uptake on HeLa cells with inhibitors represented by the legends [1] vehicle control; [2] folic acid; [3] genistein; [4] chlorpromazine and [5] amiloride. The first panel represents bright field; second panel Dapi; third panel PI and fourth panel indicates the merged images. Scale bar: 50 μ m. Data are the mean \pm SD of three independent experiments; *** p <0.001, ns: not significant relative to control.

4.3.7. Cellular internalization and dox release by SERS imaging

Again, the cellular internalization and Dox release kinetics from **TNEDS** were explored by Raman spectral and imaging analysis. Bright field (**Figure 4.12A**) and Raman mapping for Dox localization was observed within 1 hr (**Figure 4.12B**) and 3 hr (**Figure 4.12C**) of incubation of **Au@SiO₂-Dox-CS-FA** in HeLa cells. Confocal images and histogram from HeLa cells showed the enhanced Raman signal. Raman spectra (**Figure 4.12D**) abstracted from nucleus and cytoplasmic regions after 1 hr

of treatment clearly demonstrated the signature Dox peak around 455 cm^{-1} only from the cytoplasmic area.

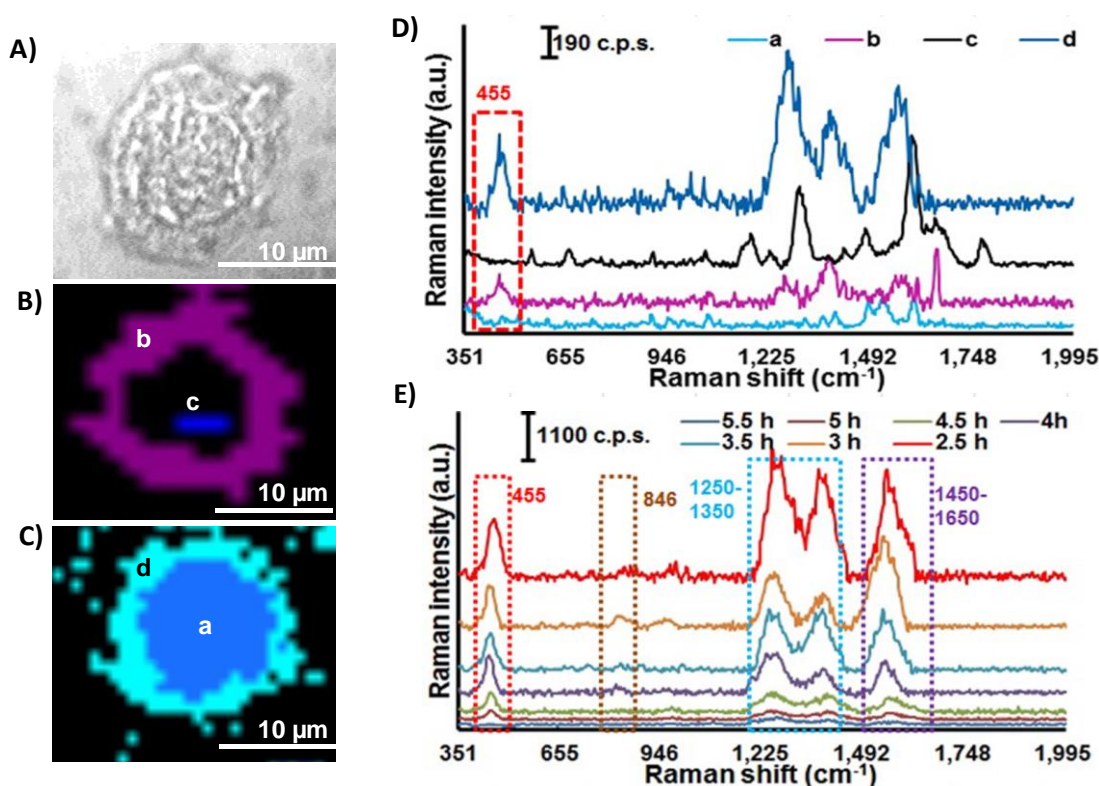


Figure 4.12. A) Bright field and Raman images after B) 1 and C) 3 h incubation of **Au@SiO₂-Dox-CS-FA** on HeLa cells, D) Raman spectra abstracted from the Raman images (b) and (c) wherein the legends represent the labelled area of the corresponding images according to the color code. E) Raman spectra abstracted from the nuclear area.

However, after 3 hr the integrated Dox peak from the nucleus and an absence from the cytoplasmic region were noticed. The ability of **TNEDS** to retain and enhance Dox signature enabled real-time monitoring for intracellular Dox release kinetics. SERS technique has recently been used for label-free *in situ* monitoring of drug release from a variety of carrier constructs. The Dox Raman peaks from the cells enabled tracking the intracellular drug distribution pathway²⁷ in a non-invasive manner. Raman imaging and corresponding spectral analysis of Dox demonstrated a time-dependent localization with an early distribution in the cytoplasm and later

migration towards the nucleus. Disappearance of Dox peak at 455 cm^{-1} from the cytoplasm and appearance of the same in the nuclear region over time clearly defined Dox distribution (**Figure 4.12E**).

4.3.8. Evaluation of apoptotic events by SERS fingerprinting

Raman spectral analysis from HeLa cells in a time resolved manner after treatment of **Au@SiO₂-Dox-CS-FA** revealed characteristic biochemical changes (**Figure 4.12E**). The sub-cellular SERS spectral patterns are well characterized with the dominant Dox signatures with unique Raman peaks corresponding to the nuclear damage due to apoptosis (**Table 4.2**).

Table 4.2. Tentative peak assignment of SERS spectra abstracted from nuclear regions of HeLa cells treated with **Au@SiO₂-Dox-CS-FA**.

Raman Shift (cm^{-1})	Tentative Assignment
450 cm^{-1}	C=O in-plane deformation
817 cm^{-1}	O-P-O str. RNA
938 cm^{-1}	C-C str. α -helix
1260 cm^{-1}	Amide III
1384 cm^{-1}	nucleic acid (adenine, guanine, tyrosine)
1562 cm^{-1}	nucleic acid (adenine, guanine)

Further, monitoring of SERS spectra from the cytoplasmic region over a time period of 1-4 hr displayed the disappearance of Dox peak over time highlighting the nuclear migration of Dox and subsequent initiation of apoptosis through the induction of nuclear damage. Interestingly Dox was distributed in cytoplasmic area within 2 h and slowly migrated into nucleus after 3 hr. Accumulation in the nucleus was observed after 4 h with no cytoplasmic fluorescence which rationalizes the SERS

studies. In addition to the monitoring of drug release, time-resolved SERS spectra has been well explored to monitor cellular changes in response to chemotherapeutic agents demonstrating a more sensitive and faster detection modality than conventional assays²⁸. The disappearance of cellular peaks at 846 cm^{-1} and decrease in the intensity of peaks at 1250-1350 cm^{-1} and 1450-1650 cm^{-1} were assigned to the nucleic acids, O-P-O backbone of DNA, and protein degradation²⁹ upon treatment of **Au@SiO₂-Dox-CS-FA** which are consistent with the expected Dox induced biochemical changes in nucleus. Thus, it is evident that apoptotic DNA fragmentation induced by **Au@SiO₂-Dox-CS-FA** can be monitored through SERS which enabled label-free monitoring and could further potentiates the therapeutic utility.

4.3.9. Investigation of cell death mechanism

To validate the apoptosis mediated growth inhibition by **TNEDS** reflected by molecular changes in SERS fingerprinting, various apoptosis assays were conducted in HeLa and A549 cells. Morphological observation revealed salient features of apoptosis such as distorted shape, membrane blebbing and decreased cell number relative to control groups for HeLa (**Figure 4.13A upper panel**). Acridine orange-ethidium bromide dual staining in FR-positive cells revealed a change in color from green to yellow/red, which is associated with other apoptotic features (**Figure 4.13A middle panel**). Cells undergoing apoptosis demonstrated nuclear condensation and DNA fragmentation, which was clearly detected by Hoechst 33342 nuclear staining. The percentage of chromatin condensation after **Au@SiO₂-Dox-CS-FA** treatment was significantly higher in HeLa (**Figure 4.13A lower panel**). The mechanism of cell death induced by **Au@SiO₂-Dox-CS-FA** was further confirmed by

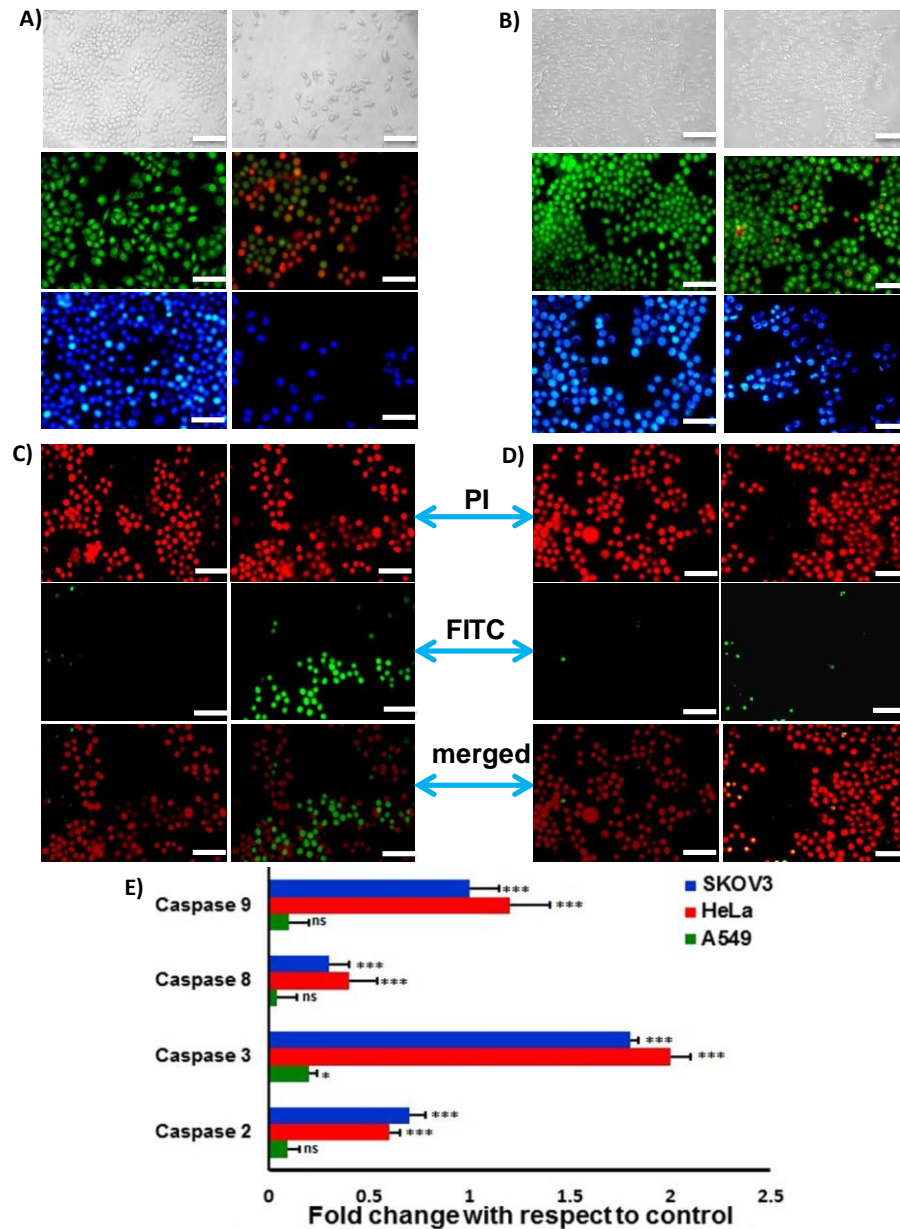


Figure 4.13. Induction of apoptosis in A) HeLa and B) A549 cells by **Au@SiO₂-Dox-CS-FA** (1 μ M) for 24 h and were evaluated using phase contrast microscopy (upper panel), acridine orange-ethidium bromide (middle panel) and Hoechst staining (lower panel). Left panel represents the control and right panel indicates the treatment groups, evaluation of apoptosis by TUNEL staining assay in C) HeLa and A) A549 cells; left row represents the control and right row indicates the treatment groups. Scale bar: 50 μ m, A) Caspase profiling of cell lines treated with **Au@SiO₂-Dox-CS-FA**. Data are the mean \pm SD of three independent experiments; ***p<0.001, **p<0.01, ns: not significant relative to control.

terminal deoxynucleotidyltransferase (TdT) dUTP nick-end labeling (TUNEL) assay which provides simple, accurate and rapid detection of apoptotic cells *in situ* at the single-cell level. However, morphological evaluation for apoptosis with **Au@SiO₂-Dox-CS-FA** treatment revealed no significant changes in FR-negative cell A549 (**Figure 4.13B**). FR-positive cells displayed a green color, indicating TUNEL positivity (**Figure 4.13C**), whereas FR-negative cells were found to be largely TUNEL negative (**Figure 4.13D**). Many chemotherapeutic drugs including Dox, triggered apoptosis through the activation of caspases dependent pathways⁵ and hence the expression of caspases 3, 8, 9, and 2 has been gauged by fluorimetry to thoroughly substantiate the mechanism of cell death. Upon treatment of **Au@SiO₂-Dox-CS-FA**, HeLa and SKOV3 cells presented a significant ($p < 0.001$) increase in the expression of caspases 9, 8, 3 and 2, (**Figure 4.13E**) but the change was insignificant for A549 cells except for caspase 3 ($p < 0.05$).

4.3.10. Therapeutic efficacy in murine models

The excellent *in vitro* targeted cytotoxicity urged us to investigate the *in vivo* antitumor therapeutic potential of the **TNEDS**. Evaluation of various parameters on DLA ascites tumor-bearing mice on the 16th and 23rd day of administration revealed a significant reduction in the tumor volume ($P < 0.001$) in both groups administered with **Au@SiO₂-Dox-CS-FA**, **Au@SiO₂-Dox-CS**, Dox and Lipodox (**Figure 4.14A**), except **Au@SiO₂-CS-FA** which did not elicit any response. Among the various treatment options **Au@SiO₂-Dox-CS-FA** generated the best overall response. Detailed investigation with tumor cell count, percentage of viable cells, body weight change and mean survival at the end of the experimental period revealed the superior therapeutic efficacy of **Au@SiO₂-Dox-CS-FA** over other treatment options.

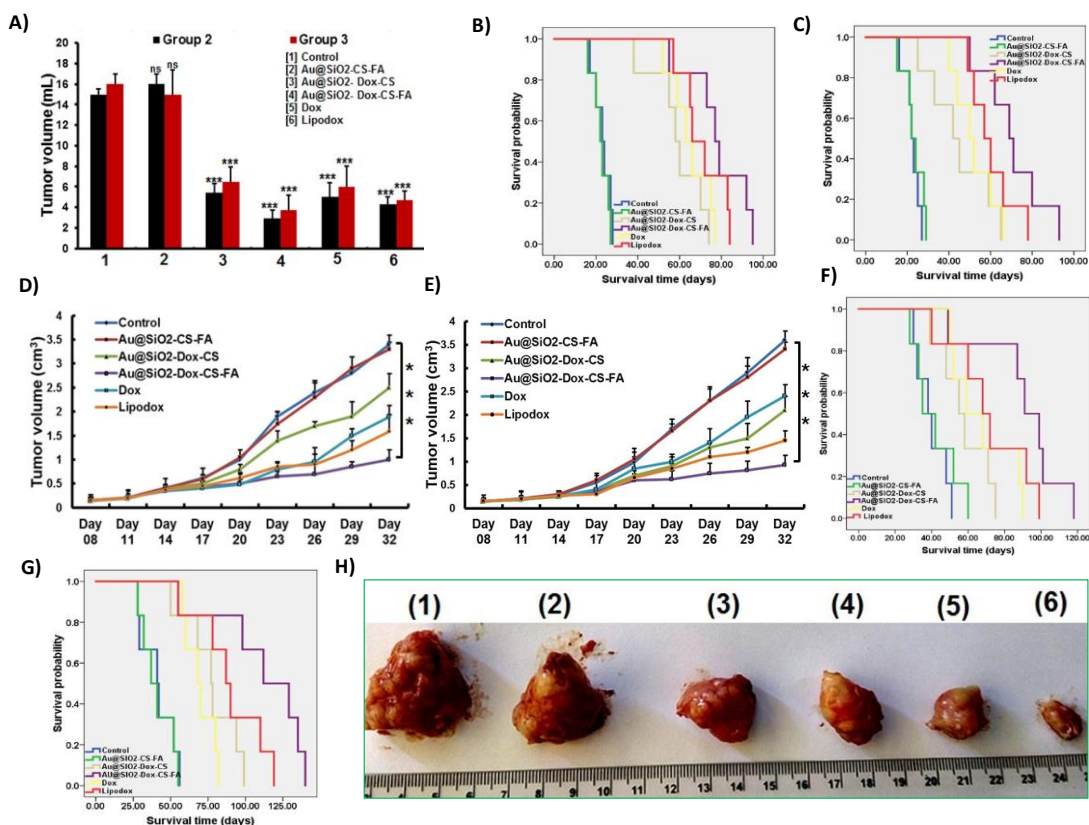


Figure 4.14. DLA ascites tumor volume measurements (A) and Kaplan-Meier survival curve of (B) group 2 and group 3 (C). EAC-induced solid-tumor measurements were taken after *i.p.*(D) or *i.t.* (E) administration and its corresponding Kaplan-Meier survival curves (F, G); Log rank p value <0.0001. Representative images of resected tumours after *i.t.* administration (H). The legends (1) represent vehicle control, (2) Au@SiO₂-CS-FA, (3) Dox, (4) Au@SiO₂-Dox-CS, (5) Lipodox and (6) Au@SiO₂-Dox-CS-FA treated animals. Statistically significant differences at *** P < 0.001 and ns, non-significant, compared with the control group.

The Kaplan-Meier survival analysis (**Figure 4.14B&C**) revealed that Au@SiO₂-Dox-CS-FA treatment prolonged the survival probability. There was a significant reduction in the tumor burden by both *i.p.* and intratumoral (*i.t.*) administration of Au@SiO₂-Dox-CS-FA in EAC-induced solid-tumor mice syngraft where *i.p.* (**Figure 4.14D**) mode was observed to be less effective than *i.t.* mode (**Figure 4.14E**). Although Lipodox was observed to be more effective than naked Dox, the non-targeted construct Au@SiO₂-Dox-CS produced better therapeutic efficacy than Dox with *i.t.* administration. The nano-constructs demonstrated maximum reduction in

tumor volume and a significant ($P < 0.001$) increase in life span. Furthermore, the Kaplan-Meier analysis (**Figure 4.14F&G**) exposed the prolonged survival of tumor bearing mice with **Au@SiO₂-Dox-CS-FA** administration up to a level for making it a therapeutically viable construct. Representative images of expunged tumors with different treatments (**Figure 4.14H**) revealed the greater tumor volume reduction upon **Au@SiO₂-Dox-CS-FA** treatment. This superior therapeutic effect could be due to the optimal drug loading and targeting efficiency of the **TNEDS** for more intensive localized applications without causing any non-specific toxicity, especially in the case of easily accessible solid malignancies and potentiates the future pre-clinical investigations. The efficiency of tumor targeting by **Au@SiO₂-FL-CS-FA** was notable, particularly considering that the mice used in this study were fed a regular diet rather than a folate-free diet, which is usually necessary to increase the detection sensitivity of the FR-targeted delivery systems³⁰.

4.4. Conclusions

In summary, **TNEDS** not only demonstrated the excellent *in vitro* FR- targeted cytotoxicity but also presented to be an appalling biocompatible cancer targeted nano-carrier. High Dox loading with tumor niche specific release kinetics enabled the **TNEDS** to execute superior salutary therapeutic effects. In diagnostic modality, **Au@SiO₂** core transformed **TNEDS** to be an effective SERS nanoprobe for Raman imaging to monitor the cellular uptake, release of the impregnated Dox and dynamic visualization of biochemical changes at molecular level during apoptosis. Finally, **TNEDS** was experimented in murine models which explicitly presented therapeutic efficiency superior to the clinically used Dox and Lipodox. Albeit further

investigations are envisaged, the outcome exhibited by the **TNEDS** definitely holds an aspiration for future pre-clinical and clinical applications in oncology.

3.5. Experimental Section

3.5.1. Materials

Gold (III) chloride hydrate, trisodium citrate dehydrate, TEOS, aqueous ammonia (NH₄OH, 25-28%), HCl (36-38%), fluorescein isothiocyanate (FITC), (3-Aminopropyl) triethoxysilane (APTES), MTT and Dox hydrochloride were purchased from Sigma Aldrich. Acetic acid (99.5% purity) and chitosan, 85% deacylated power was purchased from Alfa aesar. Ethyl alcohol (99.9% purity), was purchased from Changshu Yangyuan Chemical, China. Lipodox™ was generously gifted by Sun Pharma Advanced Research Company Ltd., India.

3.5.2. Culture and maintenance of cell lines

HeLa, MCF-7 (breast cancer), and A549 were obtained from ATCC (Manassas, USA). SKOV3 cells was generously provided by the Rajiv Gandhi Centre for Biotechnology (Thiruvananthapuram, India). The fibroblast-like murine pre-adipocyte cell line 3T3L1 was gifted from the Inter-University Centre for Genomics and Gene Technology, University of Kerala (Thiruvananthapuram, India). A375 (malignant melanoma) cells were obtained from NCCS (Pune, India). Cells were maintained in DMEM with 10% FBS and 5% CO₂ at 37°C.

3.5.3. TEOS mediated synthesis of Au@SiO₂ nanoparticles

Synthesis of spherical citrate stabilized gold nanoparticles of 40 nm was done using citrate reduction method³¹. Mono-dispersed Au@SiO₂ nanoparticles with 40 nm gold cores and uniform thicknesses of silica shell was synthesized via modified stober method³² using vigorous shaking in alcohol solutions. Briefly, 50 ml of citrate stabilized AuNPs was centrifuged using 8000 rpm for 30 min and the pellets were dissolved in 5 ml milli-Q water. The solution was diluted with 15 ml of ethanol solution and adjusted the pH ~ 10 using ammonia solutions. To this solution, 48 µl of 1: 45 NCO-TEOS: TEOS was added and shake for 24 hr. After 24 hr the solution was centrifuged two or three times with 10000 rpm for 30 min to remove uncoated silica on AuNPs.

3.5.4. Conjugation of folic acid with chitosan

A solution of folic acid and EDC in 20 ml anhydrous DMSO was prepared and stirred at room temperature until EDC and folic acid were well-dissolved³³. The mixture was then added slowly to 0.5% (w/v) chitosan in acetic acid aqueous solution and stirred at room temperature in the dark for 16 h to let folic acid conjugate onto chitosan molecules. The solution adjusted to pH 9.0 by adding NaOH aqueous solution (1.0 M) and centrifuged at 2500 rpm. The precipitate was dialyzed first against PBS (pH 7.4) for 3 days and then against water for 4 days. NMR spectra were recorded on Bruker Advance 500 NMR spectrometer, and chemical shifts are expressed in ppm.

3.5.5. Synthesis of CS-FA coated Au@SiO₂ nanoparticle

CS-FA conjugate (25 mg) was dissolved in 5 ml 3% acetic acid and the suspension was stirred at 600 rpm for 24 hr to form CS-FA solution (0.5% w/v). 5 ml of Au@SiO₂ NPs were centrifuged and made a solution in 5 ml ethyl alcohol and the dispersion was adjusted to pH 3.5 - 4.5 by adding acetic acid. Subsequently, 200 μ l APTES was added to modify Au@SiO₂ nanoparticle and was reacted with silanol groups on the SiO₂ surface to form Si-O-Si bonds. Then CS-FA solution was added to accomplish cross-linking of nanoparticle and allowed to stir at room temperature for 24 hr. The CS-FA coated Au@SiO₂ (**Au@SiO₂-CS-FA**) was collected by centrifugation at 10,000 rpm, following washing with excessive distilled water and ethyl alcohol solution.

3.5.6. Dox loading and redox and pH-responsive dox release kinetics of Au@SiO₂-Dox-CS-FA NPs

Dox was loaded into the pores of the silica coated gold nanoparticles. 5 ml of Au@SiO₂ nanoparticle in milli – Q water was sonicated for 10 min; afterward 500 μ L of 2 mM Dox solution in water was added in to it and was stirred at 600 rpm for 24 hr. The Dox-loaded Au@SiO₂ nanoparticles were collected by centrifugation at 10,000 rpm. The DLE, DLC and actual amount of drug in nanoparticle was calculated using the following formula³⁴.

Drug loading efficiency = (Total Dox-Free Dox/ Total Dox) x 100%

Drug loading content = (Weight of drug in NPs/Weight of prepared NPs) x 100%

Actual amount of drug in NPs = Dox per gram of NPs

3.5.7. Cytotoxicity assays

The growth inhibitory capacity was initially evaluated on cancer and normal cell lines by MTT assay as previously reported¹⁸. The absorbance was recorded at 570 nm after incubation for 12, 24 and 48 hr with test compounds. The cytotoxicity was further confirmed with BrdU assay kit (colorimetric - 11647229001, Roche Diagnostics, IN, USA) and the experiments were carried out with the instructions given in the kit and the measurements were made at 450/690 nm. Evaluation of the effect of folic acid on the growth inhibitory capacity of the constructs was also carried out by MTT assay after the addition of 2 mM folic acid to the medium for 2 h as reported³⁰.

3.5.8. Western blot analysis and Hemolysis assay

Proteins were extracted from 2×10^6 cells per petridish using RIPA buffer (Thermo Scientific, Rockford, IL, USA). Protein concentrations were determined using Coomassie Plus protein assay reagent and BSA standards (Pierce, Rockford, IL, USA). Proteins (~50 mg) were separated by 10% SDS-PAGE and transferred to polyvinylidenedifluoride membranes (Millipore, Billerica, MA, USA). Membranes were blocked with 5% BSA (Santa Cruz Biotechnology Inc., TX, USA) and incubated with the specific primary antibodies. The primary antibodies FOLR2 (folate receptor b) and β -actin were purchased from Sigma-Aldrich (St. Louis, MO, USA). Alkaline phosphatase conjugated secondary antibody (Sigma-Aldrich) was used for all primary antibodies and detected by the colorimetric substrate BCIP®/NBT (Sigma-Aldrich). The resulting bands were then quantitated using Image J software (version 1.48, NIH, USA) and normalized with β -actin.

EDTA-stabilized human blood samples were centrifuged at 700 g for 5 min, and blood plasma and the surface layer were diluted in 25 mL PBS. Test compounds

at various concentrations in PBS (0.8 mL) were then added to RBC suspension (0.2 mL). Positive and negative control samples were also prepared by adding 0.8 mL 2% Triton X-100 and PBS, respectively, to 0.2 mL RBC solution. Samples were then incubated at room temperature for 2 hr, centrifuged at 700 g, and supernatants (100 μ l) were transferred to a 96-well plate and absorbance was measured with a microplate reader at 570 nm. Percent RBC lysis was calculated with the following formula

$$\text{Hemolysis [\%]} = [(A_{\text{sample}} - A_{\text{Negative control}}) / (A_{\text{positive control}} - A_{\text{Negative control}})] \times 100$$

3.5.9. Apoptotic assays

Morphological assessment of apoptosis was conducted in HeLa, SKOV3 and A549 cells treated with **Au@SiO₂-Dox-CS-FA** (1 mM) for 24 h. Initially cells were observed for any visible gross morphological changes under phase contrast objective (Olympus 1X51, Singapore) to view the apoptotic or non-apoptotic cells. Acridine orange-ethidium bromide dual staining was performed as described earlier³⁵ and the cells were observed under a FITC filter (Olympus 1X51, Singapore). Observation of nuclei for any apoptosis related changes was done with Hoechst 33342 staining using a DAPI filter (Olympus 1X51, Singapore) as described before. TUNEL assay (DeadEnd™ fluorometric TUNEL system, Promega, Madison, USA) was used to detect the incorporation of the fluorescein-12-DUTP in the fragmented DNA of apoptotic cells, using the terminal-deoxynucleotidyl-transferase recombinant (rTdT) enzyme as per the manufacturer's instructions using propidium iodide as counter-stain. Caspase profiling was determined by using Apo Alert™ Caspase Profiling kit (Clontech, CA, USA) as per the manufacturer's protocol. Cells were treated with **Au@SiO₂-Dox-CS-FA** (1 mM) for 24 h, and samples were transferred to

96-well plates for fluorimetric reading (λ_{ex} 380 nm, λ_{em} 460 nm), and signals were recorded by spectro fluorimetry (FLx800, BioTek).

3.5.10. Live cell Raman imaging

Evaluating the efficacy of Au@SiO₂-CS-FA as a Raman substrate was done with confocal Raman microscope with a laser beam of 633 nm directed to the sample through 20 X objective. For cellular imaging 20 μ l (1mM) of Au@SiO₂-CS-FA was added to HeLa cells and was incubated at 37°C for 1 hr. SERS mapping was recorded by focusing the laser beam on the cell surface selected at a position $z = 0$ μ m using 0.5 as integration time, 150 x 150 as points per line and 50 x 50 μ m mapping area along X and Y directions. The Raman and SERS cell maps were acquired over a motorized scan stage. The chemical images were computed from the two dimensional collection of Raman/SERS spectra by integrating the intensity of a specific band over a defined wave number range after baseline subtraction. Raman images were subsequently subjected to cluster mapping and later three dimensional plots were made out of it. A minimum of three independent measurements were made for each sample.

3.5.11. Cellular internalization study

Cellular uptake and release of Dox or FITC was tested with various constructs with fluorescent microscopy, Raman microscopy, fluorimeter, and flow cytometer. HeLa and A549 cells were treated with (1 μ M) Dox, Lipodox, Au@SiO₂-Dox-CS and **Au@SiO₂-Dox-CS-FA** for 4 hr. Cells were then washed with PBS and stained with Hoechst 33342 for nuclei and incubated for 5–10 min and the cellular Dox uptake was visualized under a PI filter and Hoechst under Dapi filter (Olympus 1X51,

Singapore). Evaluation of the internalization of Au@SiO₂-FL-CS-FA (1 mM) by HeLa cells after 2 h incubation was also performed in the FITC filter using fluorescent microscopy. Time dependent cellular Dox release from **Au@SiO₂-Dox-CS-FA** was also evaluated on HeLa cells from 1-4 hr over PI filter of a fluorescent microscope (Olympus 1X51, Singapore) after counter staining with Hoechst 33342. Quantification cellular uptake of Dox was performed as described previously³⁵ with slight modifications. Briefly, cells were plated onto 12-well plates at 10⁵ cells/well and were treated with the agents for 4 hr, trypsinized and washed with ice-cold phosphate buffered saline (PBS, pH 7.4). Pellets were lysed again with PBS containing 1% Triton-X accompanied with vigorous vortexing and Dox in the supernatant was measured in a fluorometer (FLx800, BioTek) at an excitation wavelength of 485 nm and an emission wavelength of 590 nm. Results are expressed as micrograms of Dox per milligrams of cellular protein. Protein concentration of the cell lysates was determined using Coomassie plus protein assay reagent and BSA as standards (Pierce, Rockford, IL, USA).

3.3.12. Evaluation of dox uptake and apoptosis using SERS

Since **Au@SiO₂-Dox-CS-FA** could generate sufficiently higher intensity Dox finger prints and enabled cellular imaging in SERS platform, it was used for tracing Dox release using a confocal Raman microscope and the cellular imaging was performed as explained above. The specific Raman band area of Dox was selected to create an SERS maps after 1 hr and 3 hr of **Au@SiO₂-Dox-CS-FA** treatment. The intensity of the SERS spectra was measured at different spots belonging to the nuclear and cytoplasmic region and the spectra were averaged to create every single curve³⁶. The cells were maintained for up to 6 hr and SERS spectra were extracted

from the nuclear area for every 30 min for identification of change in spectral pattern over time with Dox exposure.

3.5.13. Tumor reduction studies on ascites and solid tumor mice

3.5.13.1. Tumor reduction on ascites tumor mice

For the inoculation of ascites tumors in the mice, DLA cells collected from the donor mouse were suspended briefly in sterile isotonic saline. Viable cells were counted (Trypan blue assay) and adjusted to a concentration ensuring that each animal receives an i.p. injection of 1×10^6 cells/100 μ L. Briefly; animals were divided into two groups. All groups had mice inoculated with DLA on Day 1. In group 2, compounds were administered on days 2 to 15. Group 3 had compounds administered on days 9 to 22. After the administration of agents in the respective groups, six animals from each group were sacrificed by cervical dislocation to determine the tumor volume^{37,38}. Briefly, mice were euthanized and then the abdomen of each mouse was incised over a clean vessel and the volume of the ascites fluid obtained (V1) was calculated. The peritoneal cavity was washed thoroughly with isotonic saline until the return was clear, and the volume of the added saline (V2) was then noted. The volume of ascites tumor (V3) was calculated using the formula: $V3 = (V1 + V2) - V2$. The mean survival time (MST) and percentage of increase in life span (% ILS) was calculated as previously reported³⁹. $MST = (A + B)/2$, where A is the day of the first death and B is the day of last death. The percentage of increase in life span was calculated using the following formula: $\% ILS = (T - C)/C \times 100$, where T and C are the MST of treated and control animals, respectively.

3.5.13.2. Tumor reduction on solid tumor mice syngraft

Viable EAC cells (1×10^6 cells) were injected sub-cutaneously into the hind limb of mice with a very fine needle (31G). Experimental agents were administered via two different routes, intraperitoneal (i.p.) and i.t. injections, daily for 14 consecutive days, starting on day 9 after tumor inoculation. Tumor volume was calculated every 3rd day starting on the 8th day up to the 32nd day. Unlike in the previous set of experiments, all the mice were used to determine tumor volume and overall survival. Tumor volume was calculated as previously described and the mean survival time and percent-age of increase in life span (%ILS) was calculated as described above.

3.6. References

- (1) Sun, T.; Zhang, Y. S.; Pang, B.; Hyun, D. C.; Yang, M.; Xia, Y. Engineered Nanoparticles for Drug Delivery in Cancer Therapy. *Angew. Chemie - Int. Ed.* **2014**, *53* (46), 12320–12364. <https://doi.org/10.1002/anie.201403036>.
- (2) Wang, F.; Wang, Y.; Dou, S.; Xiong, M.; Sun, T.; Wang, J.; Al, W. E. T. Doxorubicin-Tethered Responsive Gold Nanoparticles Facilitate Intracellular Drug Delivery for Overcoming Multidrug Resistance in Cancer Cells. *ACS Nano* **2011**, *5* (5), 3679–3692.
- (3) Barenholz, Y. Doxil - The First FDA-Approved Nano-Drug: Lessons Learned. *J. Control. Release* **2012**, *160* (2), 117–134. <https://doi.org/10.1016/j.jconrel.2012.03.020>.
- (4) Popp, J.; Krafft, C.; Schmitt, M.; Schie, I.; Cialla-May, D.; Mattheaus, C.; Bocklitz, T. Label-Free Molecular Imaging of Biological Cells and Tissues by Linear and Non-Linear Raman Spectroscopic Approaches. *Angew. Chemie Int. Ed.* **2016**. <https://doi.org/10.1002/anie.201607604>.
- (5) Meng, H.; Xue, M.; Xia, T.; Zhao, Y. L.; Tamanoi, F.; Stoddart, J. F.; Zink, J. I.; Nel,

- A. E. Autonomous in Vitro Anticancer Drug Release from Mesoporous Silica Nanoparticles by PH-Sensitive Nanovalves. *J. Am. Chem. Soc.* **2010**, *132* (36), 12690–12697. <https://doi.org/10.1021/ja104501a>.
- (6) Dimers, D. N.; Kyriazi, M.; Giust, D.; El-sagheer, A. H.; Lackie, P. M.; Muskens, O. L.; Brown, T.; Kanaras, A. G. Multiplexed mRNA Sensing and Combinatorial-Targeted Drug Delivery Using DNA-Gold Nanoparticle Dimers. **2018**. <https://doi.org/10.1021/acsnano.7b08620>.
- (7) Chen, Y.; Yoon, Y. J.; Pang, X.; He, Y.; Jung, J.; Feng, C.; Zhang, G.; Lin, Z. Precisely Size-Tunable Monodisperse Hairy Plasmonic Nanoparticles via Amphiphilic Star-Like Block Copolymers. *Small* **2016**, *12* (48), 6714–6723. <https://doi.org/10.1002/sml.201602820>.
- (8) Song, J.; Zhou, J.; Duan, H. Self-Assembled Plasmonic Vesicles of Sers-Encoded Amphiphilic Gold Nanoparticles for Cancer Cell Targeting and Traceable Intracellular Drug Delivery. *J. Am. Chem. Soc.* **2012**, *134*, 13458. <https://doi.org/10.1021/ja305154a>.
- (9) Song, J.; Pu, L.; Zhou, J.; Duan, B.; Duan, H. Biodegradable Theranostic Plasmonic Vesicles of Amphiphilic Gold Nanorods. *ACS Nano* **2013**, *7* (11), 9947–9960. <https://doi.org/10.1021/nn403846v>.
- (10) Bosslet, K.; Straub, R.; Blumrich, M.; Czech, J.; Gerken, M.; Sperker, B.; Kroemer, H. K.; Gesson, J. P.; Koch, M.; Monneret, C. Elucidation of the Mechanism Enabling Tumor Selective Prodrug Monotherapy. *Cancer Res.* **1998**, *58* (6), 1195–1201.
- (11) Fales, A. M.; Crawford, B. M.; Vo-Dinh, T. Folate Receptor-Targeted Theranostic Nanoconstruct for Surface-Enhanced Raman Scattering Imaging and Photodynamic Therapy. *ACS Omega* **2016**, *1* (4), 730–735.

- <https://doi.org/10.1021/acsomega.6b00176>.
- (12) Conde, J.; Bao, C.; Cui, D.; Baptista, P. V.; Tian, F. Antibody-Drug Gold Nanoantennas with Raman Spectroscopic Fingerprints for in Vivo Tumour Theranostics. *J. Control. Release* **2014**, *183* (1), 87–93. <https://doi.org/10.1016/j.jconrel.2014.03.045>.
- (13) Barbosa, S.; Topete, A.; Alatorre-Meda, M.; Villar-Alvarez, E. M.; Pardo, A.; Alvarez-Lorenzo, C.; Concheiro, A.; Taboada, P.; Mosquera, V. Targeted Combinatorial Therapy Using Gold Nanostars as Theranostic Platforms. *J. Phys. Chem. C* **2014**, *118* (45), 26313–26323. <https://doi.org/10.1021/jp505979e>.
- (14) Shi, Z.; Guo, R.; Li, W.; Zhang, Y.; Xue, W.; Tang, Y.; Zhang, Y. Nanoparticles of Deoxycholic Acid, Polyethylene Glycol and Folic Acid-Modified Chitosan for Targeted Delivery of Doxorubicin. *J. Mater. Sci. Mater. Med.* **2014**, *25* (3), 723–731. <https://doi.org/10.1007/s10856-013-5113-0>.
- (15) Dick, K.; Dhanasekaran, T.; Zhang, Z.; Meisel, D. Size-Dependent Melting of Silica-Encapsulated Gold Nanoparticles. *J Am Chem Soc* **2002**, *124* (10), 2312–2317. <https://doi.org/10.1021/ja017281a>.
- (16) Zong, S.; Wang, Z.; Yang, J.; Wang, C.; Xu, S.; Cui, Y. A SERS and Fluorescence Dual Mode Cancer Cell Targeting Probe Based on Silica Coated Au@Ag Core-Shell Nanorods. *Talanta* **2012**, *97*, 368–375. <https://doi.org/10.1016/j.talanta.2012.04.047>.
- (17) Eliasson, C.; Lorén, A.; Murty, K. V. G. K.; Josefson, M.; Käll, M.; Abrahamsson, J.; Abrahamsson, K. Multivariate Evaluation of Doxorubicin Surface-Enhanced Raman Spectra. *Spectrochim. Acta - Part A* **2001**, *57* (9), 1907–1915. [https://doi.org/10.1016/S1386-1425\(01\)00453-X](https://doi.org/10.1016/S1386-1425(01)00453-X).

- (18) Joseph, M. M.; Aravind, S. R.; George, S. K.; Raveendran Pillai, K.; Mini, S.; Sreelekha, T. T. Galactoxyloglucan-Modified Nanocarriers of Doxorubicin for Improved Tumor-Targeted Drug Delivery with Minimal Toxicity. *J. Biomed. Nanotechnol.* **2014**, *10* (11), 3253–3268. <https://doi.org/10.1166/jbn.2014.1957>.
- (19) Cui, Y.; Dong, H.; Cai, X.; Wang, D.; Li, Y. Mesoporous Silica Nanoparticles Capped with Disulfide-Linked PEG Gatekeepers for Glutathione-Mediated Controlled Release. *ACS Appl. Mater. Interfaces* **2012**, *4* (6), 3177–3183. <https://doi.org/10.1021/am3005225>.
- (20) Bhattacharya, D.; Das, M.; Mishra, D.; Banerjee, I.; Sahu, S. K.; Maiti, T. K.; Pramanik, P. Folate Receptor Targeted, Carboxymethyl Chitosan Functionalized Iron Oxide Nanoparticles: A Novel Ultradispersed Nanoconjugates for Bimodal Imaging. *Nanoscale* **2011**, *3* (4), 1653–1662. <https://doi.org/10.1039/c0nr00821d>.
- (21) Shinto, H.; Fukasawa, T.; Yoshisue, K.; Tezuka, M.; Orita, M. Cell Membrane Disruption Induced by Amorphous Silica Nanoparticles in Erythrocytes, Lymphocytes, Malignant Melanocytes, and Macrophages. *Adv. Powder Technol.* **2014**, *25* (6), 1872–1881. <https://doi.org/10.1016/j.apt.2014.09.002>.
- (22) Zhang, Z.; Wang, J.; Chen, C. Near-Infrared Light-Mediated Nanoplatfoms for Cancer Thermo-Chemotherapy and Optical Imaging. *Adv. Mater.* **2013**, *25* (28), 3869–3880. <https://doi.org/10.1002/adma.201301890>.
- (23) Radziuk, D.; Moehwald, H. Prospects for Plasmonic Hot Spots in Single Molecule SERS towards the Chemical Imaging of Live Cells. *Phys. Chem. Chem. Phys.* **2015**, *17* (33), 21072–21093. <https://doi.org/10.1039/c4cp04946b>.
- (24) Movasaghi, Z.; Rehman, S.; Rehman, I. Raman Spectroscopy of Biological

- Tissues. *Appl. Spectrosc. Rev.* **2007**, *42* (5), 493–541.
<https://doi.org/10.1080/05704920701551530>.
- (25) Perrault SD, Walkey C, Jennings T, Fischer HC, C. W. Mediating Tumor Targeting Efficiency of Nanoparticles through Design. *Nano Lett* **2009**, *9* (5), 1909–1915. <https://doi.org/10.1021/nl900031y>.
- (26) Iversen, T. G.; Skotland, T.; Sandvig, K. Endocytosis and Intracellular Transport of Nanoparticles: Present Knowledge and Need for Future Studies. *Nano Today* **2011**, *6* (2), 176–185. <https://doi.org/10.1016/j.nantod.2011.02.003>.
- (27) Tipping, W. J.; Lee, M.; Serrels, A.; Brunton, V. G.; Hulme, A. N. Stimulated Raman Scattering Microscopy: An Emerging Tool for Drug Discovery. *Chem. Soc. Rev.* **2016**, *45* (8), 2075–2089. <https://doi.org/10.1039/c5cs00693g>.
- (28) Panikkanvalappil, S. R.; James, M.; Hira, S. M.; Mobley, J.; Jilling, T.; Ambalavanan, N.; El-Sayed, M. A. Hyperoxia Induces Intracellular Acidification in Neonatal Mouse Lung Fibroblasts: Real-Time Investigation Using Plasmonically Enhanced Raman Spectroscopy. *J. Am. Chem. Soc.* **2016**, *138* (11), 3779–3788. <https://doi.org/10.1021/jacs.5b13177>.
- (29) Silveira, L.; Silveira, F. L.; Bodanese, B.; Za^ngaro, R. A.; Pacheco, M. T. T. Discriminating Model for Diagnosis of Basal Cell Carcinoma and Melanoma in Vitro Based on the Raman Spectra of Selected Biochemicals. *J. Biomed. Opt.* **2012**, *17* (7), 077003. <https://doi.org/10.1117/1.JBO.17.7.077003>.
- (30) Nair, J. B.; Joseph, M. M.; Mohapatra, S.; Safeera, M.; Ghosh, S.; Sreelekha, T. T.; Maiti, K. K. A Dual-Targeting Octaguanidine-Doxorubicin Conjugate Transporter for Inducing Caspase-Mediated Apoptosis on Folate-Expressing Cancer Cells. *ChemMedChem* **2016**, *11* (7), 702–712. <https://doi.org/10.1002/cmdc.201600029>.

- (31) Ahner, T. T.; Delissen, F.; Sokolov, S. Mechanism of Gold Nanoparticle Formation in the Classical Citrate Synthesis Method Derived from Coupled In Situ XANES and SAXS Evaluation. *J. Am. Chem. society* **2010**, *132* (9), 1296–1301.
- (32) Liu, S.; Han, M. Y. Silica-Coated Metal Nanoparticles. *Chem. - An Asian J.* **2010**, *5* (1), 36–45. <https://doi.org/10.1002/asia.200900228>.
- (33) Gulfam, M.; Chung, B. G. Development of PH-Responsive Chitosan-Coated Mesoporous Silica Nanoparticles. *Macromol. Res.* **2014**, *22* (4), 412–417. <https://doi.org/10.1007/s13233-014-2063-4>.
- (34) Sahu, S. K.; Maiti, S.; Maiti, T. K.; Ghosh, S. K.; Pramanik, P. Folate-Decorated Succinylchitosan Nanoparticles Conjugated with Doxorubicin for Targeted Drug Delivery. *Macromol. Biosci.* **2011**, *11* (2), 285–295. <https://doi.org/10.1002/mabi.201000353>.
- (35) Joseph, M. M.; Aravind, S. R.; George, S. K.; Pillai, R. K.; Mini, S.; Sreelekha, T. T. Co-Encapsulation of Doxorubicin with Galactoxyloglucan Nanoparticles for Intracellular Tumor-Targeted Delivery in Murine Ascites and Solid Tumors. *Transl. Oncol.* **2014**, *7* (5), 525–536. <https://doi.org/10.1016/j.tranon.2014.07.003>.
- (36) El-Said, W. A.; Kim, T. H.; Kim, H.; Choi, J. W. Detection of Effect of Chemotherapeutic Agents to Cancer Cells on Gold Nanoflower Patterned Substrate Using Surface-Enhanced Raman Scattering and Cyclic Voltammetry. *Biosens. Bioelectron.* **2010**, *26* (4), 1486–1492. <https://doi.org/10.1016/j.bios.2010.07.089>.
- (37) Aravind, S. R.; Joseph, M. M.; Varghese, S.; Balaram, P.; Sreelekha, T. T. Antitumor and Immunopotentiating Activity of Polysaccharide PST001

- Isolated from the Seed Kernel of Tamarindus Indica: An In Vivo Study in Mice. *Sci. World J.* **2012**, 2012, 1–14. <https://doi.org/10.1100/2012/361382>.
- (38) Joseph, M. M.; Aravind, S. R.; George, S. K.; Varghese, S.; Sreelekha, T. T. A Galactomannan Polysaccharide from Punica Granatum Imparts in Vitro and in Vivo Anticancer Activity. *Carbohydr. Polym.* **2013**, 98 (2), 1466–1475. <https://doi.org/10.1016/j.carbpol.2013.07.023>.
- (39) Attia, M. A.; Weiss, D. W. Immunology of Spontaneous Mammary Carcinomas in Mice. V. Acquired Tumor Resistance and Enhancement in Strain A Mice Infected with Mammary Tumor Virus. *Cancer Res.* **1966**, 26 (8), 1787–1800.

ABSTRACT

Name of the Student: **Ms. Ramya A.N.**

Faculty of Study: Chemical Sciences

AcSIR academic centre/CSIR Lab: CSIR-National

Institute for Interdisciplinary Science

and Technology (CSIR-NIIST)

Title of the thesis: **Development of Molecular Probes and Nano-carrier Delivery System for Intracellular Sensing and Theranostic Applications**

Registration No.: 10CC16A39008

Year of Submission: 2021

Name of the Supervisor: Dr. Kaustabh Kumar Maiti

Development of molecular probes and functional nanomaterials with improved sensing capabilities together with high therapeutic potential is one among the thrust areas of current science. In the **First Chapter**, we summarize the recent developments in the field of fluorescent probes and SERS nanotags for diagnostic and therapeutic applications in biomedical research.

Surface enhanced Raman scattering (SERS) modality has been successfully utilized on cancer diagnosis as an alternative early detection tool which has great potential over conventional cytopathology. In the **Second chapter**, a series of novel tetraphenylethylene appended fluorogens has been developed and unfold their aggregation induced emission and aggregation caused quenching properties and consequently revealed their SERS fingerprint. An efficient SERS nanoprobe has been constructed using gold nanoparticles as SERS substrate where TPE-In incorporated as the Raman reporter, which was further conjugated with a specific peptide substrate, Cys-Ser-Lys-Leu-Gln-OH, well-known for the recognition motif of prostate specific antigen (PSA). This nanoprobe distinctly recognizes PSA expression with a limit of detection of 0.5 ng in SERS platform.

Hydrogen sulfide, is evolved as a biological mediator for regulating many patho-physiological processes and involved in brain function as a neuromodulator along with neuroprotectant. In fact, lower levels of endogenously produced H₂S may lead to Alzheimer's disease, which is a progressive neurodegenerative disorder characterized by the deposition of amyloid-beta in the brain tissue. In the **Third Chapter**, design and synthesis of an orthogonally substituted tetraphenylethylene based dual functional turn on molecular luminophore has been demonstrated for selective detection of endogenously produced H₂S in neuroblastoma cell line, SH-SY5Y and its induction on A β de-agglomeration to reduce the progression of AD. Further, the probe generated H₂S in cellular conditions with concomitant detection and imaging of endogenously generated H₂S and the probe was employed for in vivo imaging in mice and enabled to release H₂S in thiol abundant area. Finally, the probe acted as a H₂S donor and enabled de-agglomeration of A β agglomerated sheets.

Chapter 4 deals with the exploration of theranostic nano-envelop, Au@SiO₂-Dox-CS-FA, which possesses an excellent Dox loading efficiency and proved to be biocompatible targeted nano-envelop delivery system, internalized through folate receptor-mediated endocytosis with a dual pH and redox sensitive Dox release kinetics. The carrier, Au@SiO₂ NPs provided high surface plasmon resonance thereby enabling the nanosystem to be a promising SERS nanotag for the label-free Raman imaging in order to monitor the intracellular Dox release. Minute changes in the biochemical components of organelles inside cells during Dox mediated apoptosis by the nanosystem has been effectively evaluated in a time-dependent fashion using dual responsive SERS /Fluorescence modality. Finally, the nanoenvelop displayed superior anti-tumor response than clinically used Dox and Lipodox in FR-positive tumor syngraft mouse models.

List of Publications

Related to Thesis

1. **A. N. Ramya**, M. M. Joseph, S. Maniganda, V. Karunakaran, T. T. Sreelekha, K. K. Maiti, Emergence of Gold-Mesoporous Silica Hybrid Nano-Theranostic: Dox-Encoded, Folate Targeted Chemotherapy with Modulation of SERS Fingerprinting for Apoptosis Toward Tumor Eradication. **Small**, 2017, 13, 1700819.
2. **A. N. Ramya**, M. M. Joseph, J. B. Nair, V. Karunakaran, N. Narayanan, K. K. Maiti, New insight of tetraphenylethylene-based Raman signatures for targeted SERS nanoprobe construction toward prostate cancer cell detection, **ACS Appl. Mater. Interfaces** 2016, 8, 10220–10225.
3. **A. N. Ramya**, Manu M. Joseph, Varsha Karunakaran, Shihash Ahammed, Vishnu Priya Murali and Kaustabh K. Maiti, Molecular Luminophore Structured with Orthogonally Substituted Tetraphenylethylene (TPE) Enabling Endogenous Detection and Signaling Role of Hydrogen Sulfide in Alzheimer's disease, 2021, **(Manuscript to be communicated)**.

Not related to Thesis

4. **A. N. Ramya**, A. Samanta, N. Nisha, Y. T. Chang, K. K. Maiti, New Insight of Squaraine-Based Biocompatible Surface-Enhanced Raman Scattering Nanotag for Cancer-Cell Imaging. **Nanomedicine**, 2015, 10, 561-571.
5. **A. N. Ramya**, P. S. Ambily, B. S. Sujitha, M. Arumugam, K. K. Maiti, Single cell lipid profiling of *Scenedesmus quadricauda* CASA-CC202 under nitrogen starved condition by surface enhanced Raman scattering (SERS) fingerprinting. **Algal Research** 2017, 25, 200–206.
6. N. Narayanan, L.V. Nair, V. Karunakaran, M.M. Joseph, J.B. Nair, **A N. Ramya**, R. S. Jayasree, K. K. Maiti, Investigation of apoptotic events at molecular level induced by SERS guided targeted theranostic nanoprobe, **Nanoscale** 2016, 8, 11392–11397.
7. M. M. Joseph, J. B. Nair, **A. N. Ramya**, N. Hari, R. K. Pillai, A. J. Nair, K. K. Maiti, T. Sreelekha, Exploration of Biogenic Nano-chemobiotics Fabricated by Silver Nanoparticle and Galactoxyloglucan with an Efficient Biodistribution in Solid

- Tumor Investigated by SERS Fingerprinting, **ACS Appl. Mater. Interfaces** 2017, 9, 19578-19590.
8. N. Adarsh, **A. N. Ramya**, K. K. Maiti, D. Ramaiah, SERS-Guided Detection and Imaging of Human Cancer Cells through NIR Absorbing Aza-BODIPY Dyes, **Chem.Eur. J**, 2017, 23, 14286-14291.
9. Palasseri T. Sujai, Manu M. Joseph, Varsha Karunakaran, Giridharan Saranya, **A. N. Ramya**, Shanmughan Shamjith, Reshmi Thomas, Jyothi B. Nair, Rotti Srinivasamurthy, Swathi, and Kaustabh Kumar Maiti, Biogenic Cluster-Encased Gold Nanorods as a Targeted Three-inOne Theranostic Nanoenvelope for SERS-Guided Photochemotherapy against Metastatic Melanoma, **ACS Appl. Bio Mater.** 2019, 2, 588-600.
10. Manu M. Joseph, **A. N. Ramya**, Vineeth M. Vijayan, Jyothi B. Nair, Blossom Treesa Bastian, Raveendran K. Pillai, Sreelekha Therakathinal T, Kaustabh Kumar Maiti, Targeted Theranostic Nano Vehicle Endorsed with Self-Destruction and Immunostimulatory Features to Circumvent Drug Resistance and Wipe-out Tumor Reinitiating Cancer Stem Cells, **Small** 2020, 16, 2003309.

Review Article

11. **A.N Ramya**, Jayadev S Arya, Murali Madhukrishnan, Shanmughan Shamjith, Murukan S Vidyalakshmi and Kaustabh K. Maiti, Raman Imaging: An Impending approach towards cancer diagnosis, **Chem. Asian J** 2021, 16, 409-422.
12. Manu. M. Joseph, Nisha. Narayanan, Jyothi. B. Nair, Varsha Karunakaran, **A. N. Ramya**, P. T. Sujai, G. Saranya , Jayadev. S. Arya, Vineeth. M. Vijayan, Kaustabh. Kumar Maiti; Exploring the margins of SERS in practical domain: An emerging diagnostic modality for modern biomedical applications **Biomaterials** 2018, 181, 140-181.

List of Conferences attended

1. "Investigation of Tetra Phenyl Ethylene (TPE) Based Raman Reporters for Construction of SERS Nanoprobe in Prostate Cancer Detection", **A. N. Ramya**, M. M. Joseph, J. B. Nair, and K. K. Maiti, **Poster presented** at the international symposium on photonics applications and nano materials, (ISPAN-2015), Trivandrum, Kerala, India, 2015, October 28-30.
2. "Stimuli Responsive Nanocarrier Drug Delivery System (DDS) For Targeted Delivery of Doxorubicin towards Folate Expressing Cancer Cells", **A. N. Ramya**, M. M. Joseph, P.T. Sujai and K. K. Maiti, **poster presented** at the 18th National Symposium in Chemistry (NSC-18), Panjab University, Chandigarh, India, 2016, February 5-7.
3. "Emergence of Gold-Mesoporous Silica Hybrid Nano-Theranostic: Dox-Encoded, Folate Targeted Chemotherapy with Modulation of SERS Finger printing for Apoptosis towards Tumor Eradication", **A. N. Ramya**, M. M. Joseph, J. S. Arya and K. K. Maiti, **poster presented** at the 8th East Asia Symposium on Functional Dyes and Advanced Materials (EAS8), Trivandrum, Kerala, India, 2017, September 20-22.
4. "Emergence of Gold-Mesoporous Silica Hybrid Nano-Theranostic: Dox-Encoded, Folate Targeted Chemotherapy with Modulation of SERS Finger printing for Apoptosis towards Tumor Eradication", **A. N. Ramya**, M. M. Joseph, J. S. Arya and K. K. Maiti, **poster presented** at the 6th Asian Biomaterials Congress (ABMC6), Trivandrum, Kerala, India, 2017, October 25-27.
5. "Molecular Probe Based on Tetraphenylethylene (TPE) Utilized for Detection and Signaling Role of Hydrogen Sulfide in Alzheimer's Disease", **A. N. Ramya**, Shihas Ahammed and Kaustabh Kumar Maiti, **poster presented** at 8th Annual Conference of Indian Academy of Biomedical Sciences (IABS) Thiruvananthapuram, Kerala, India, 2019, February 25-27.
6. "Emergence of Gold-Mesoporous Silica Hybrid Nano-Theranostic: Dox-Encoded, Folate Targeted Chemotherapy with Modulation of SERS Finger printing for Apoptosis towards Tumor Eradication", **A. N. Ramya**, M. M. Joseph, and K. K. Maiti, **Oral presentation** at the CSIR- Inter Institutional Students Conference (SU-CHEM Yuva,), CSIR-IICT, Hyderabad, India, 2019, July 24-26.

Emergence of Gold-Mesoporous Silica Hybrid Nanotheranostics: Dox-Encoded, Folate Targeted Chemotherapy with Modulation of SERS Fingerprinting for Apoptosis Toward Tumor Eradication

Adukkadan N. Ramya, Manu M. Joseph, Santhi Maniganda, Varsha Karunakaran, Sreelekha T. T.,* and Kaustabh Kumar Maiti**

Small 2017, 13, 1700819

DOI: 10.1002/sml.201700819

The address information of the Academy of Scientific and Innovative Research (AcSIR) affiliation needs to be updated. Please find the correct presentation below:

A. N. Ramya, S. Maniganda, V. Karunakaran, Dr. K. K. Maiti
Academy of Scientific and Innovative Research (AcSIR)
Ghaziabad 201002, India

DOI: 10.1002/sml.202007852

Emergence of Gold-Mesoporous Silica Hybrid Nanotheranostics: Dox-Encoded, Folate Targeted Chemotherapy with Modulation of SERS Fingerprinting for Apoptosis Toward Tumor Eradication

Adukkadan N. Ramya, Manu M. Joseph,* Santhi Maniganda, Varsha Karunakaran, Sreelekha T. T.,* and Kaustabh Kumar Maiti*

Strategically fabricated theranostic nanocarrier delivery system is an unmet need in personalized medicine. Herein, this study reports a versatile folate receptor (FR) targeted nanoenvelope delivery system (TNEDS) fabricated with gold core silica shell followed by chitosan–folic acid conjugate surface functionalization by for precise loading of doxorubicin (Dox), resembled as Au@SiO₂-Dox-CS-FA. TNEDS possesses up to 90% Dox loading efficiency and internalized through endocytosis pathway leading to pH and redox-sensitive release kinetics. The superior FR-targeted cytotoxicity is evaluated by the nanocarrier in comparison with US Food and Drug Administration (FDA)-approved liposomal Dox conjugate, Lipodox. Moreover, TNEDS exhibits theranostic features through caspase-mediated apoptosis and envisages high surface plasmon resonance enabling the nanoconstruct as a promising surface enhanced Raman scattering (SERS) nanotag. Minuscule changes in the biochemical components inside cells exerted by the TNEDS along with the Dox release are evaluated explicitly in a time-dependent fashion using bimodal SERS/fluorescence nanoprobe. Finally, TNEDS displays superior antitumor response in FR-positive ascites as well as solid tumor syngraft mouse models. Therefore, this futuristic TNEDS is expected to be a potential alternative as a clinically relevant theranostic nanomedicine to effectively combat neoplasia.

A. N. Ramya, Dr. M. M. Joseph, S. Maniganda,
V. Karunakaran, Dr. K. K. Maiti
Chemical Sciences and Technology Division (CSTD)
CSIR-National Institute for Interdisciplinary Science
and Technology (CSIR-NIIST)
Industrial Estate, Pappanamcode
Thiruvananthapuram, Kerala 695019, India
E-mail: manumjoseph2000@gmail.com;
kkmaiti@niist.res.in, kkmaiti29@gmail.com

A. N. Ramya, S. Maniganda, V. Karunakaran, Dr. K. K. Maiti
Academy of Scientific and Innovative Research (AcSIR)
New Delhi 110020, India

Dr. M. M. Joseph, Dr. S. T. T.
Laboratory of Biopharmaceutics and Nanomedicine
Division of Cancer Research
Regional Cancer Centre (RCC)
Thiruvananthapuram, Kerala 695011, India
E-mail: ttsreelekha@gmail.com

DOI: 10.1002/sml.201700819



1. Introduction

Advances in nanotechnology have scrutinized an assortment of carriers for controlled delivery of therapeutic payloads against cancer^[1] which still holds the second leading cause of modality worldwide. Nonspecific delivery of anticancer agents often results in damage of healthy organs, which significantly impedes cancer survival rates. Ongoing research on nanomedicine aims to enhance the therapeutic index of antineoplastic drugs by adjusting their pharmacokinetics and biodistribution. The idea that nanomedicine aims to enhance the therapeutic index of antineoplastic drugs by adjusting their pharmacokinetics and biodistribution to enhance conveyance to the site of action is clinically demonstrated. The enhanced permeation and retention effect of the tumor microenvironment provides easier access of chemotherapeutic drugs to tumor tissues. Doxorubicin (Dox) is a widely used antineoplastic agent, but its severe side effects^[2] limit its clinical efficacy. Designed to

exploit the advantages of nanoparticles (NPs), liposomal Dox formulations were approved by the FDA^[3] but has a whimsical disadvantage of being nontargeted toward cancer cells.^[4] Among different nanocarriers, gold nanoparticle (AuNP)-based carriers are widely employed for cancer diagnosis and imaging, either alone or in conjugation with therapeutic motifs.^[5] Moreover, high localized surface plasmon resonance (LSPR) of AuNPs facilitates in diagnostic modality as a surface enhanced Raman scattering (SERS) substrate to provide structural information of many biomolecules within subcellular components without altering the biology of cells based on their unique vibrational Raman fingerprint. The LSPR spectral shifts induced by interparticle plasmonic coupling have attracted considerable interest in the fabrication of assembled plasmonic nanoparticles.^[6,7]

In SERS, hot spots created in the gaps between NPs or at the edges and tips of anisotropic NPs provide sufficiently intense electromagnetic fields to promote a tremendous increase in the Raman intensity of molecules located in these regions, making it possible to detect even minute changes. AuNPs with tunable size and shape act as excellent SERS substrates and were used in label-free immunoassays, biosensing, imaging of living cells, and microbes in ultralow level of limit of detection. Engineering plasmonic nanostructures confined within a defined architecture and surface caged with biomaterials often execute optical and structural properties enabling them for captivated biological applications. Moreover, SERS-encoded plasmonic NPs are capable of generating a stable and reproducible Raman spectral pattern and imaging in a particular clinical milieu.^[8] In the construction of nanocarriers, mesoporous silica nanoparticles (MSNs) have attracted much attention owing to their many unique features such as tunable pore morphologies, high surface area, large pore volume, facile functionalization of exterior surfaces, and biocompatibility. MSNs provided a high drug loading capability; therefore, encapsulation of AuNPs with silica layer (Au@SiO₂) not only enables facile surface modification and stimuli responsive release but also enhances the LSPR of the construct to be an effective SERS substrate.^[9] Even though the clinically used NP formulations of Dox demonstrated effectiveness, the lack of cancer cell targeting moieties makes them amiable to normal cells. Capping of drug-loaded Au@SiO₂ NPs with biodegradable natural polymer chitosan will avert premature drug release and promote the biocompatibility. Folate receptor (FR) is known to be overexpressed in several human tumors, and the exploration of FR-mediated drug delivery has been referred to a molecular “Trojan horse” approach.^[10] Nontargeted chemotherapeutic strategies often caused greater side effects. On the other hand, a targeted nanocarrier system often allows the delivery of drugs at much lower doses, due to a combination of molecular targeting and increased circulation time preventing random exposure to normal tissues.^[11,12]

Considering the present necessity for the development of a clinically viable smart targeted nanoenvelope delivery system (TNEDS), we aimed to build Au@SiO₂ NPs loaded with Dox that is enveloped by a layer of chitosan–folic acid covalent conjugate (CS-FA) Au@SiO₂-Dox-CS-FA (**Scheme 1**).

The major emphasis on theranostic efficiency of TNEDS has been exploited by (i) impressing biocompatibility with efficient Dox loading and tumor niche-specific release enabled targeted cytotoxicity by FR-mediated endocytosis; (ii) the significant Raman spectral enhancement of the TNEDS utilized as an SERS nanotag for quantifying Dox loading and tracing of intracellular Dox release by Raman imaging; (iii) evaluation of apoptotic cell death by TNEDS using SERS/fluorescence bimodality; (iv) detailed investigation with tumor challenged mouse models has been highlighted in terms of therapeutic potential of Au@SiO₂-Dox-CS-FA and compared clinically used Dox and Lipodox. Even though further investigations are warranted to establish the current TNEDS in clinical milieu, the contemporary studies presented here emphasized the superiority of Au@SiO₂-Dox-CS-FA as a futuristic multimodel theranostic nanoprobe toward efficient cancer management.

2. Results and Discussion

2.1. Preparation and Characterization of TNEDS

The successful preparation of Au@SiO₂-Dox-CS-FA in a stepwise manner (**Scheme 1**; **Figure S1**, Supporting Information) was effectively monitored by the evaluation of physicochemical parameters by UV–vis spectrophotometry, high-resolution transmission electron microscopy (HRTEM), dynamic light scattering, and confocal Raman spectroscopy. The presence of a silica layer on the AuNP core was indicated by the redshifted (531–534 nm) plasmon maxima of the nanoconstruct. Dox loaded on Au@SiO₂, further shielded by CS-FA, has been well studied by UV–vis in which absorbance maxima showed a slight blueshift with peak broadening (**Figure 1a**; **Figure S2a**, Supporting Information). HR-TEM analysis further confirmed the stepwise formation of the nanoconstruct where the average size of AuNPs (40–45 nm) increased to 105 nm upon silica coating. Additional surface functionalization with CS-FA increased the size to 125 nm of the nanoconstruct (**Figure 1b**; **Figure S2b**, Supporting Information). Morphological analysis revealed the presence of clusters of AuNPs confined within the silica shell along with single AuNPs. A nontargeted construct, Au@SiO₂-Dox-CS, was also prepared by using CS instead of CS-FA (**Section SI-1**, Supporting Information). Dox impregnation into the SiO₂ pores was evaluated by the drug-loading efficiency (DLE), drug-loading content (DLC), and actual amount of drug in NPs. Au@SiO₂-Dox-CS-FA showed a high DLE of 90% with around 93.75 mg Dox per gram of the construct and 9.3% DLC whereas Au@SiO₂-Dox-CS demonstrated 81% DLE, 8.5% DLC, and 85 mg Dox per gram of the construct, respectively. The successful functionalization of CS-FA with Dox-loaded silica nanoparticle was initially confirmed by UV–vis and later with Fourier transform infrared (FTIR) analysis (**Section SI-2** and **Figure S3** of the Supporting Information). The FT-IR spectrum of CS was characterized with the bands around 3396, 1655, 1378, 1075, and at 611 cm⁻¹ whereas the CS-FA spectrum shows the appearance of –CONH amide band at 1645 cm⁻¹ and the N–H bending in the second amine

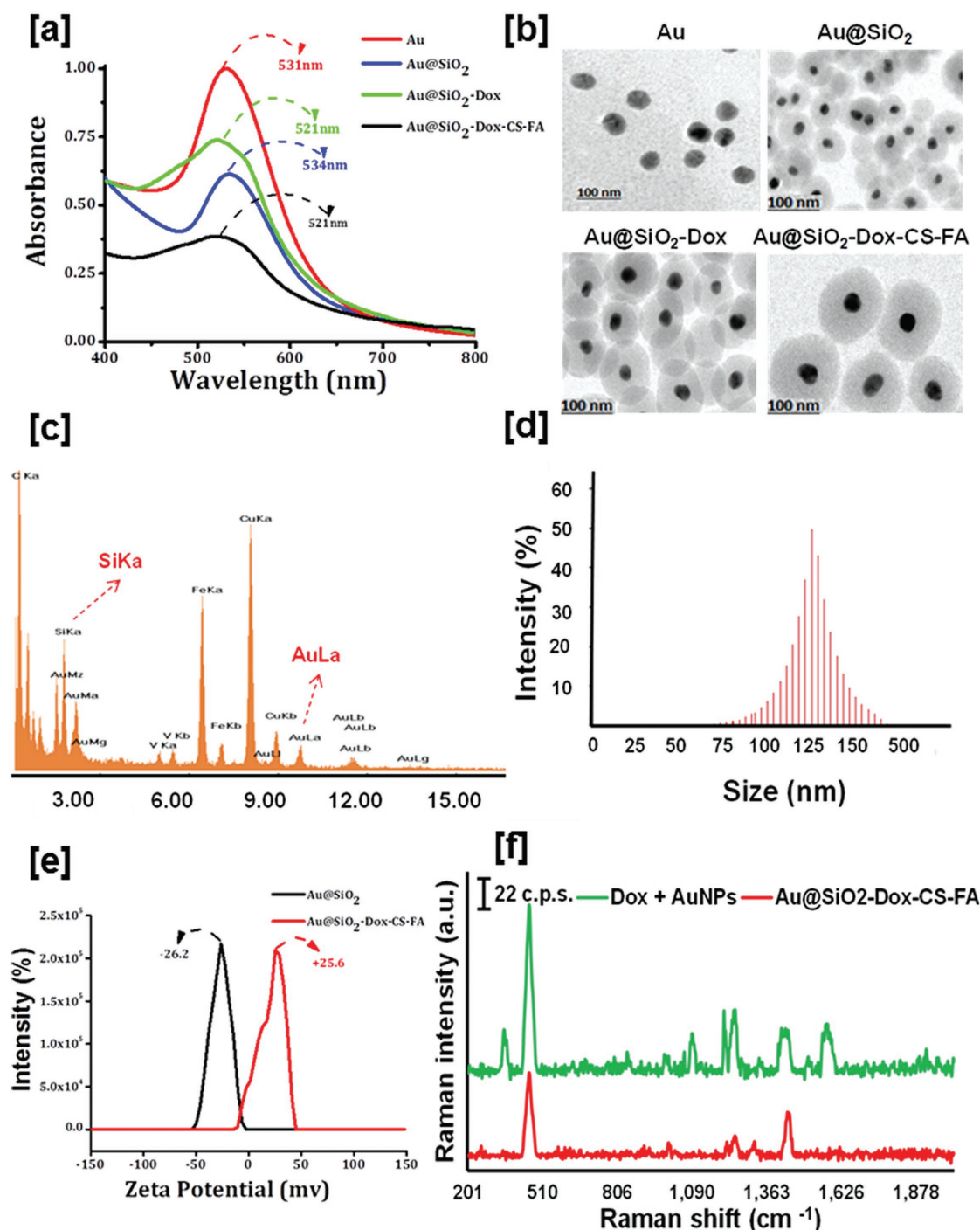


Figure 1. a) UV-vis spectra, b) TEM images and c) Energy dispersive X-ray spectroscopy (EDAX) spectrum of TNEDS from different stages. d) Hydrodynamic size distribution of Au@SiO₂-Dox-CS-FA determined by dynamic light scattering (DLS), e) ζ potential changes, and f) SERS spectral pattern analysis of Au@SiO₂-Dox-CS-FA compared with pure Dox spectra (Au@Dox). Results are plotted as the mean \pm standard deviation (SD), $n = 4$.

the silica layer leads to strong interparticle plasmonic coupling, as evidenced by the noticeable redshift of plasmon resonance of the nanoparticles.

2.2. Stimuli Responsive Drug Releases

The release kinetics of Dox from Au@SiO₂-Dox-CS-FA, Lipodox, and doxorubicin hydrochloride was evaluated

under parameters of pH and reducing atmosphere at ambient temperature initially by UV-vis spectroscopy. It was found that doxorubicin hydrochloride showed a burst release within 2–4 h regardless of the change in pH and reducing agents (Figure S4a, Supporting Information). Lipodox displayed minimal response toward stimuli in which an acidic pH with a reducing atmosphere caused a rapid Dox release whereas at neutral pH the release was prolonged up to 7–8 h (Figure S4b, Supporting Information). Au@SiO₂-Dox-CS-FA

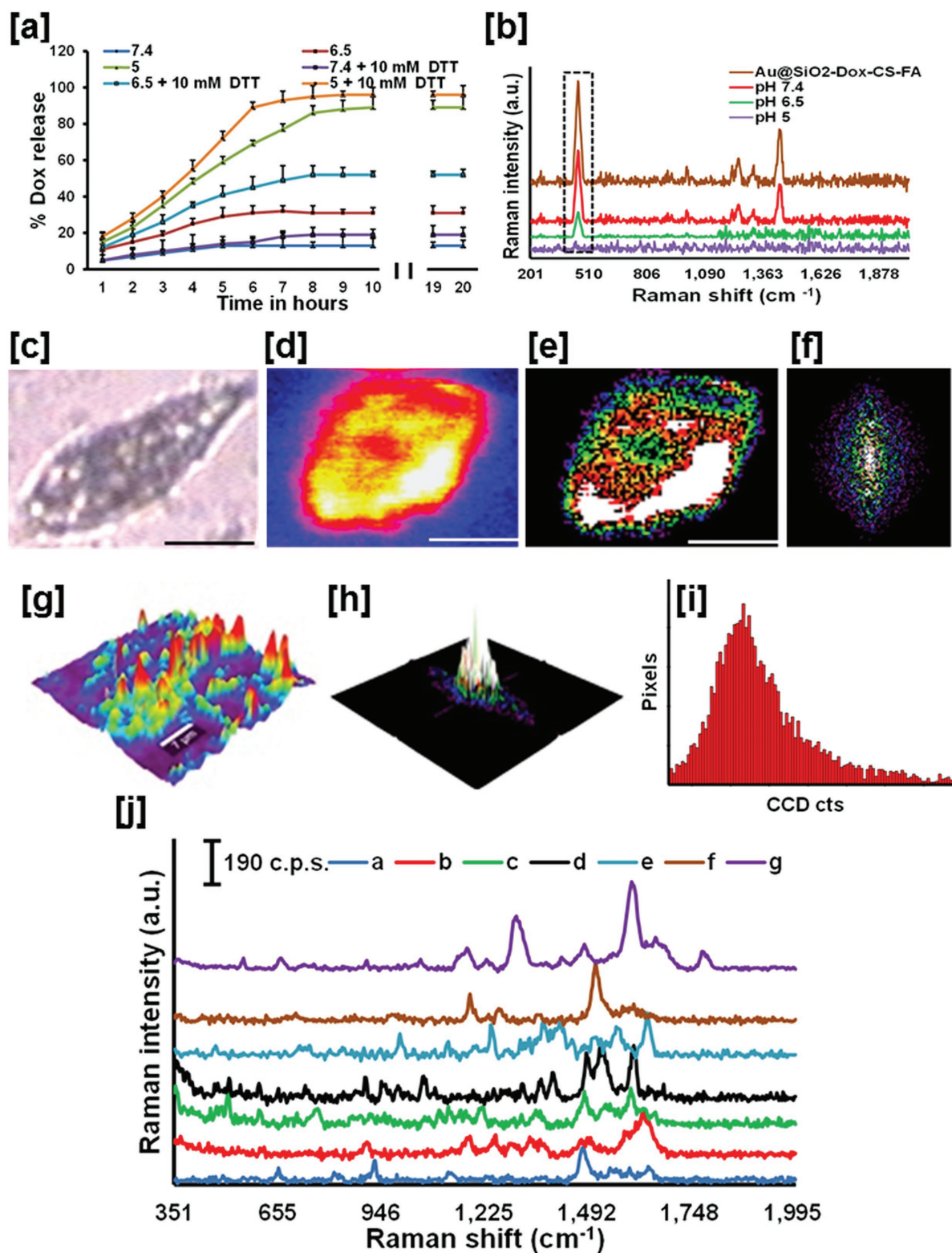


Figure 2. a) Evaluation of Dox release kinetics from Au@SiO₂-Dox-CS-FA with UV and b) confocal Raman microscopy. c–f) Bright field, Raman, cluster, and corresponding condor images of Au@SiO₂-CS-FA treated HeLa cells. g,h) 3D Raman intensities. i) Histogram of the two most intense peaks from HeLa cells. j) The Raman spectra abstracted from various regions of the Raman image. Scale bar corresponds to 10 μm unless and otherwise indicated. Data are the mean ± SD of four independent experiments.

exhibited an optimal Dox release kinetics (**Figure 2a**) which is largely dependent on pH and, to a lesser extent, toward reducing atmosphere. A cumulative Dox release kinetics was

observed with a pH of 5 wherein almost 96% and 89% was released within 9 h in the presence and absence of reducing agents. The Dox release was further evaluated in the SERS

platform (Figure 2b) wherein the appearance of the characteristic peak of Dox at 455 cm^{-1} demonstrated the release under varying pH. The signal intensity of Dox signature showed a steep decline of pH from 7.4 to 5 indicating pH-dependent release from Au@SiO₂-Dox-CS-FA. The released Dox from the nanoconstruct in acidic pH exits through the dialysis membrane and was monitored by gradual decrease in SERS spectra. Normally, tumor tissue is accompanied with acidosis by high metabolic activity, and the microenvironment has a lower pH with high redox potential than the surrounding normal tissue. The cumulative redox and pH dual responsive Dox release from Au@SiO₂-Dox-CS-FA enforce targeted cytotoxicity, specifically, at the tumor area, sparing the normal tissue, which has a pH of 7.4 and less redox environment.^[17] The unique entrapment of Dox within the SiO₂ layer and further caged with chitosan could be the potential factor regulating the controlled release. At higher pH, the primary amino groups of chitosan undergo a sort of shrinking mode leading to a slow drug release whereas a lower pH promotes protonation of primary amines, leading to swelling of polymeric matrix that will allow drug molecules to move more freely through normal diffusion. Furthermore, chitosan acts as a gatekeeper to retain Dox in the pores and prevent undesired leaching from the mesopores in the absence of acidic environment.^[18]

2.3. Western Blot Analysis and Hemolysis

Later, we evaluated the FR expression status of human, murine cancer cells, and normal fibroblast cells by western blot analysis using antibodies directed against the FR. Quantitative evaluation of the resulting bands was performed after normalizing with those of β -actin. Out of the eight cell lines examined, HeLa and SKOV3 cells showed significantly higher FR expression, whereas A549 and 3T3L1 exhibited minimum FR expression (Figure S5a, Supporting Information). Next, hemolysis assays were performed to determine the toxicity toward red blood cells (RBCs) under three different pH conditions. The highest hemolytic activity was observed for free Dox, which demonstrates concentration-dependent pH-independent lysis wherein as high as 26% hemolysis was observed for $100 \times 10^{-6}\text{ M}$ Dox at pH 5.5, and even at $0.01 \times 10^{-6}\text{ M}$ causes 7% hemolysis at pH 7.4. Lipodox demonstrated reasonably reduced toxicity toward RBC in comparison with Dox. Au@SiO₂-Dox-CS-FA displayed concentration and pH-dependent hemolytic behavior; even at the highest concentration of $100 \times 10^{-6}\text{ M}$, 10% lysis was observed at pH 5.5, whereas only 5% was recorded at pH 7.4 under the same conditions. Lower concentrations are largely safer to RBCs especially at physiological pH (Figure S5b, Supporting Information). The uncoated Au@SiO₂ displayed severe hemolytic behavior independent of a change in pH. However, coating with CS-FA makes Au@SiO₂-CS-FA more biocompatible and safer toward RBCs (Figure S5c, Supporting Information). Among the different strategies for receptor-mediated drug delivery, FRs are used as a promising target because of their overexpression in many human cancer cells. Folate receptor expression varies significantly between

cancer cell lines, which urges to evaluate the receptor status prior to cell-based experiments.^[19] The results so obtained correlated well with similar studies and enabled us to select HeLa and SKOV3 as FR-positive and A549 as FR-negative cells for in vitro assays. Again, Ehrlich ascites carcinoma (EAC) and Dalton lymphoma ascites (DLA) cells showed moderate levels of FR expression that has been chosen for in vivo assays with FR-targeting systems. Even though silica-based NPs are reported to execute hemolytic features, it is significantly reduced by surface coating with any biopolymers or proteins. Moreover, MSN-based NPs of size in between 100 and 200 nm are reported to execute biocompatibility to RBCs^[20] in comparison with smaller particles. The moderate hemolytic nature of naked Au@SiO₂ NPs and the major reduction upon coating with CS-FA could be well explained with the above-mentioned facts. Again the isoelectric pH of blood prevents the Dox release from Au@SiO₂-Dox-CS-FA making it as an efficient delivery system having biocompatibility to RBCs.

2.4. SERS Imaging of Live Cells Using Au@SiO₂-CS-FA

As a new insight, we explored the efficiency of Au@SiO₂-CS-FA as an SERS nanotag on HeLa cells (Figure 2c–f) with the aid of a confocal Raman microscope (WI-Tec, Inc., Germany). HeLa cells upon treatment with Au@SiO₂-CS-FA for 1 h revealed a well-defined Raman image (Figure 2d) with a proper clustering pattern (Figure 2e). 3D representations of the images clearly indicated the enhanced cellular information in contrast with the surroundings (Figure 2f,g). Condor images and histogram of the relative intensity of the two most intense peaks from the NP-treated cells deciphered the significant signal enhancement (Figure 2 h,i). Raman spectra (Figure 2j; Figure S6a–g, Supporting Information) abstracted at various regions of the Raman image exhibited characteristic fingerprint SERS peaks from subcellular locations such as cell membrane, cytoplasm, nucleus, and other cellular organelles (Table S2, Supporting Information). SERS imaging of live cells is a new arena involving intensive study utilizing the high SPR of NPs and among which silica-coated AuNPs are reported to be excellent SERS substrates with uniform hot spot generation.^[21] The hypercluster analysis from the strongest Raman bands of the HeLa cells clearly provided label-free methods for the visualization of intracellular components and processes based on strong Raman signals.^[22] SERS spectra obtained from the nuclear regions are mainly characterized with regions including 1487, 1510, and 1534 cm^{-1} which corresponds to nucleic acids whereas the spectra obtained from the cytoplasmic region bears signatures from ribose vibration of RNA (917 cm^{-1}), carotenoids (1006 cm^{-1}), C–C stretching of lipids, and carbohydrates (1060 cm^{-1}), C=C stretching of proteins (1615 cm^{-1}), and many more.^[23] The distinct between 3D spectra and cluster analysis obtained using Au@SiO₂-CS-FA could be a promising step to understand the physicochemical processes in the local cellular environment in real time, in order to benefit for specific intracellular targeting.

2.5. Evaluation of Cytotoxicity and FR Inhibition

Cytotoxicity of the prepared nanoconstructs along with free Dox and Lipodox was evaluated on FR-positive and negative cell lines. Au@SiO₂-Dox-CS-FA displayed preferential cytotoxicity toward human cervical (HeLa) and ovarian cancer (SKOV3) cells that overexpress FR, but was less toxic toward human lung adenocarcinoma (A549) and murine fibroblasts (3T3L1) with minimal FR expression (Table S3, Supporting Information). Cytotoxicity of Au@SiO₂-Dox-CS-FA toward HeLa cells was less pronounced than Dox and Lipodox but was efficient than Au@SiO₂-Dox-CS (Figures S7a and S8a,b of the Supporting Information). In the case of SKOV3 cells, Au@SiO₂-Dox-CS-FA demonstrated an enhanced cytotoxic potential than Lipodox and Au@SiO₂-Dox-CS, but less efficient than Dox (Figures S7b and S8c,d of the Supporting Information). The TNEDS demonstrated least toxicity on A549 (Figures S7c and S8e,f of the Supporting Information) and 3T3L1 (Figures S7d and S8g,h of the Supporting Information) cells. Furthermore, both the carriers Au@SiO₂ (Table S4, Supporting Information) and Au@SiO₂-CS-FA (Table S5, Supporting Information) were observed to be devoid of any significant toxicity toward either FR-positive or FR-negative cells. The FR-targeted cytotoxicity demonstrated by Au@SiO₂-Dox-CS-FA was further confirmed after preincubation with folic acid wherein a dramatic decrease in the cytotoxicity toward HeLa and SKOV3 cells (Figure S7e,f, Supporting Information) and no significant alteration in FR-negative cell lines A549 and 3T3L1 (Figure S7g,h, Supporting Information) were observed, validating the FR-targeting capacity of Au@SiO₂-Dox-CS-FA. As an alternative, the targeted cytotoxic behavior displayed by Au@SiO₂-Dox-CS-FA was confirmed by 5-bromo-2'-deoxyuridine (BrdU) assay, wherein all the agents demonstrated a similar cytotoxicity profile as observed with 4,5-dimethylthiazol-2-yl)-2,5-diphenyltetrazoliumbromide (MTT) assay (Figure S9a–d, Supporting Information). The indiscriminate toxicity exhibited by Dox toward normal cells is well documented whereas the liposomal Dox–NP formulations such as Doxil and Lipodox are relatively safer toward normal cells^[24] and are more effective than Dox for in vivo applications, yet they are still not effective toward targeted delivery approaches.

2.6. Investigation of Cellular Uptake Pathways and Intracellular Dox Release by Fluorescence Modality

Cellular uptake and intracellular release of Dox from Au@SiO₂-Dox-CS-FA were compared with naked Dox, Lipodox, and Au@SiO₂-Dox-CS on HeLa and A549 cells by fluorescence measurements. Among them, Dox uptake was maximum in Au@SiO₂-Dox-CS-FA and minimum in Au@SiO₂-Dox-CS on HeLa cells (Figure 3a,b). However, in the case of FR-negative A549 cells, TNEDS displayed minimal Dox uptake wherein the naked Dox displayed the maximal effect (Figure 3b; Figure S10, Supporting Information). Dox was found co-localized with Hoechst indicating the nuclear transport. The FR-mediated cellular uptake of Au@SiO₂-Dox-CS-FA was further confirmed by flow cytometry

wherein HeLa cells displayed an enhanced Dox internalization but A549 cells were minimally responsive. Further, preincubation of cells with external supply of folic acid has no effect on A549 cells whereas HeLa cells were severely affected (Figure S11a,b, Supporting Information) with significantly ($p < 0.01$) reduced Dox uptake. Since positively charged nanoconstructs are reported to follow receptor-mediated uptake pathways, the cellular uptake mechanism of Au@SiO₂-Dox-CS-FA was investigated fluorimetrically after preincubation of cells with specific inhibitors and folic acid (Figure 3c). Cellular endocytosis is used for uptake nutrients and growth factors, and plays as a master regulator of the signaling circuitry. In order to examine the mode of cellular uptake mechanism of our TNEDS, the Dox concentration was estimated in FR over expressed cells preincubated with specific endocytosis inhibitors. Estimation of Dox uptake displayed a significant ($p < 0.001$) reduction upon treatment with genistein (100 $\mu\text{g mL}^{-1}$), chlorpromazine (20 $\mu\text{g mL}^{-1}$), and folic acid (2×10^{-3} M) but was not affected with 5-(*N*-ethyl-*N*-isopropyl)-amiloride (10 $\mu\text{g mL}^{-1}$) upon comparison with the respective controls. Moreover, cellular uptake was visualized using a fluorescent microscope which again confirmed the highly FR-selective and efficient cellular Dox uptake by Au@SiO₂-Dox-CS-FA (Figure 3d). The released Dox was perfectly localized in the nuclear region for effective therapeutic utility within 4 h of administration. Functional biomolecules on the surface, size, and morphology of nanoconstruct play a predominant role in determining the probable mechanism of internalization, which are, namely, clathrin, caveolae, micropinocytosis, and phagocytosis.^[25] Endocytosis pathway determination using specific inhibitors revealed that FR-mediated caveolae- and clathrin-dependent pathways play a prominent role in the cellular uptake of Au@SiO₂-Dox-CS-FA whereas micropinocytosis has a little effect. Cationic AuNPs around 100 nm are reported to follow receptor-mediated endocytosis mainly through caveolae, which are flask shaped invaginations of the plasma membrane coated by caveolin-1 and, to a lesser extent, by clathrin-dependent pathways.^[26]

2.7. Cellular Internalization and Dox Release by SERS Imaging

Again, we have explored the cellular internalization and Dox release kinetics from TNEDS by Raman spectral and imaging analysis. Bright field (Figure 4a) and Raman mapping for Dox localization were observed within 1 h (Figure 4b) and 3 h (Figure 4c) of incubation of Au@SiO₂-Dox-CS-FA in HeLa cells. Confocal images and histogram (Figure S12a–c, Supporting Information) from HeLa cells showed the enhanced Raman signal. Raman spectra (Figure 4d; Figure S13a–d, Supporting Information) abstracted from nucleus and cytoplasmic regions after 1 h of treatment clearly demonstrated the signature Dox peak around 455 cm^{-1} only from the cytoplasmic area. However, after 3 h, the integrated Dox peak from the nucleus and the absence from the cytoplasmic region were detected (Table S6, Supporting Information). The ability of TNEDS to retain and enhance Dox signature enabled real-time monitoring for intracellular Dox release kinetics. SERS technique has recently been used for

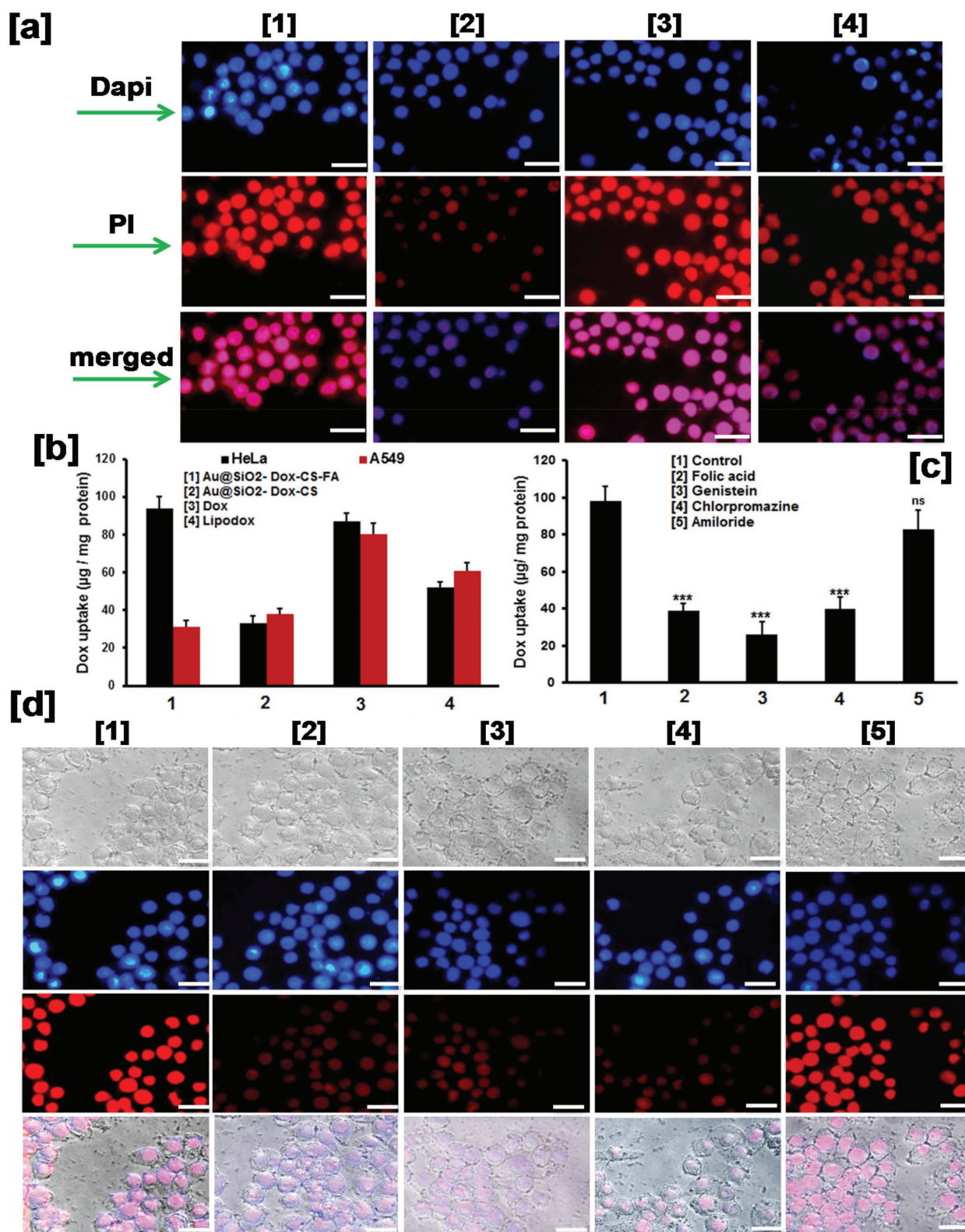


Figure 3. a) Evaluation of the intracellular uptake and distribution of Dox in HeLa cells after 4 h of administration (1×10^{-6} M) using fluorescence microscopy. The legend [1] represents Au@SiO₂-Dox-CS-FA; [2] Au@SiO₂-Dox-CS, [3] Dox, and [4] Lipodox. b) Quantitation of Dox uptake fluorimetrically. c) Estimation of the effect of inhibitors on the uptake of Au@SiO₂-Dox-CS-FA on HeLa cells by fluorimetry. d) Fluorescence images of Au@SiO₂-Dox-CS-FA uptake on HeLa cells with inhibitors represented by the following legends: [1], vehicle control; [2], folic acid; [3], genistein; [4], chlorpromazine; and [5], amiloride. The first panel represents bright field; the second panel DAPI; the third panel propidium iodide (PI), and the fourth panel indicates the merged images. Scale bar: 50 µm. Data are the mean ± SD of three independent experiments; *** $p < 0.001$; ns: not significant relative to control.

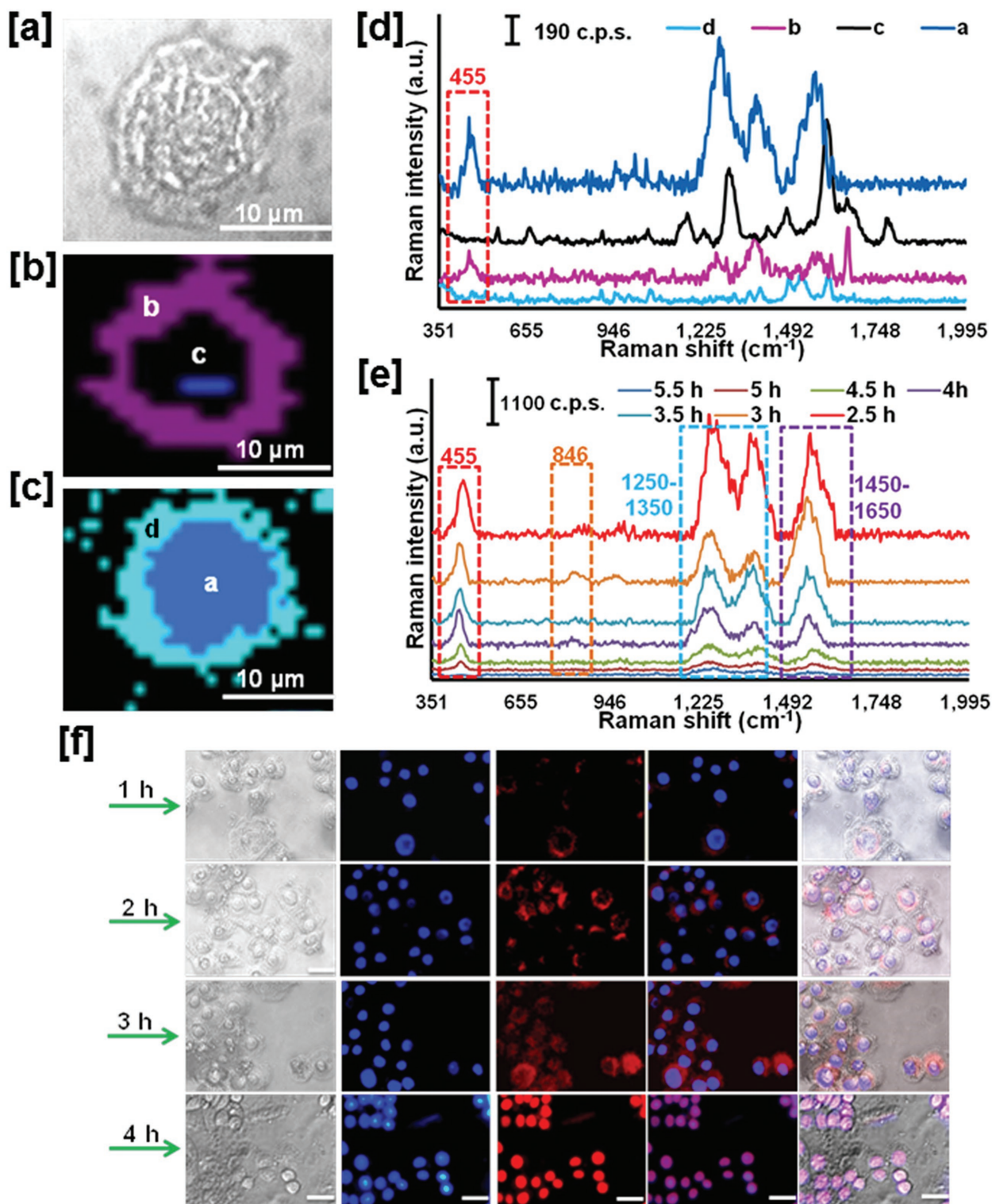


Figure 4. a) Bright field and Raman images after b) 1 and c) 3 h incubation of Au@SiO₂-Dox-CS-FA on HeLa cells. d) The Raman spectra abstracted from the Raman images (b) and (c) wherein the legends represent the labeled area of the corresponding images according to the color code. e) Raman spectra abstracted from the nuclear area. f) Fluorescence microscopy images of Dox distribution from Au@SiO₂-Dox-CS-FA. Starting from left, the first lane represents the bright field; second, DAPI; third, PI; fourth, the merged image of DAPI and PI; and fifth, the composite image. Scale bar corresponds to 50 μm unless and otherwise indicated. Data are the mean ± SD of three independent experiments.

label-free in situ monitoring of drug release from a variety of carrier constructs. The Dox Raman peaks from the cells effectively enabled tracking of the intracellular drug distribution

pathway^[27] in a noninvasive manner. Raman imaging and corresponding spectral analysis of Dox demonstrated a time-dependent localization with an early distribution in the

cytoplasm and later migration toward the nucleus. Disappearance of the Dox peak at 455 cm^{-1} from the cytoplasm and appearance of the same in the nuclear region over time clearly defined the Dox distribution (Figure 4e).

2.8. Evaluation of Apoptotic Events by SERS Fingerprinting

Raman spectral analysis from HeLa cells in a time-resolved manner after the treatment of Au@SiO₂-Dox-CS-FA revealed characteristic biochemical changes (Figure 4e). The subcellular SERS spectral patterns are well characterized with the dominant Dox signatures with unique Raman peaks corresponding to the nuclear damage due to apoptosis (Table S7, Supporting Information). Furthermore, monitoring of SERS spectra from the cytoplasmic region over a time period of 1–4 h showed the disappearance of Dox peak over time (Figure S14, Supporting Information) highlighting the nuclear migration of Dox and subsequent initiation of apoptosis through the induction of nuclear damage (Table S8, Supporting Information). Although the initiation of apoptosis by Dox from Au@SiO₂-Dox-CS-FA has been established with SERS spectral analysis, a time-dependent uptake study was performed by fluorescence imaging (Figure 4f) in order to confirm the apoptotic event by the TNEDS. Interestingly, Dox was distributed in the cytoplasmic area within 2 h and slowly migrated into nucleus after 3 h. Nuclear accumulation was observed after 4 h with no cytoplasmic fluorescence that rationalizes the SERS studies. In addition to the effective monitoring of drug release, time-resolved SERS spectra have been well explored to monitor cellular changes in response to chemotherapeutic agents demonstrating a more sensitive and faster detection modality than conventional assays.^[28] The disappearance of cellular peaks at 846 cm^{-1} and decrease in the intensity of peaks at $1250\text{--}1350$ and $1450\text{--}1650\text{ cm}^{-1}$ were assigned to the nucleic acids, O–P–O backbone of DNA, and protein degradation^[29] upon treatment of Au@SiO₂-Dox-CS-FA which are consistent with the expected Dox-induced biochemical changes in the nucleus. We have previously reported the effective real-time monitoring of DNA backbone breakage and the corresponding nuclear degradation upon treatment with a Dox-loaded nanoprobe using differential SERS spectral analysis.^[30] Thus, it is evident that apoptotic DNA fragmentation induced by Au@SiO₂-Dox-CS-FA can be effectively monitored through SERS, which enabled label-free monitoring and could further potentiates the therapeutic utility.

2.9. Investigation of Cell Death Mechanism

In order to validate the apoptosis-mediated growth inhibition by TNEDS reflected by molecular changes in SERS fingerprinting, various apoptosis assays were conducted with HeLa, SKOV3, and A549 cells. Morphological observation revealed salient features of apoptosis such as distorted shape, membrane blebbing, and decreased cell number relative to control groups for HeLa (Figure 5a, upper panel) and SKOV3 cells (Figure S15a (upper panel), Supporting Information).

Acridine orange–ethidium bromide dual staining in FR-positive cells revealed a change in color from green to yellow/red, which is associated with other apoptotic features (Figure 5b (middle panel); Figure S15a (middle panel), Supporting Information). Cells undergoing apoptosis demonstrated nuclear condensation and DNA fragmentation, which was clearly detected by Hoechst 33342 nuclear staining. The percentage of chromatin condensation after Au@SiO₂-Dox-CS-FA treatment was significantly higher in HeLa (Figure 5a, lower panel) and SKOV3 cells (Figure S15a (lower panel), Supporting Information) as compared with respective controls. However, morphological evaluation of apoptosis with Au@SiO₂-Dox-CS-FA treatment revealed no significant changes in FR-negative cell A549 (Figure 5b). The mechanism of cell death induced by Au@SiO₂-Dox-CS-FA was further confirmed by terminal deoxynucleotidyl transferase 2'-deoxyuridine 5'-triphosphate (dUTP) nick-end labeling (TUNEL) assay which provides simple, accurate, and rapid detection of apoptotic cells in situ at the single-cell level. FR-positive cells displayed a green color, indicating TUNEL positivity (Figure 5c; Figure S15b, Supporting Information), whereas FR-negative cells were found to be largely TUNEL negative (Figure 5d). Many chemotherapeutic drugs, including Dox, triggered apoptosis through the activation of caspase-dependent pathways^[5] and hence the expression of caspases 3, 8, 9, and 2 has been gauged by fluorimetry to thoroughly substantiate the mechanism of cell death. Upon treatment of Au@SiO₂-Dox-CS-FA, both HeLa and SKOV3 cells presented a significant ($p < 0.001$) increase in the expression of caspases 9, 8, 3, and 2, (Figure 5e) but the change was insignificant for A549 cells except for caspase 3 ($p < 0.05$).

2.10. Therapeutic Efficacy on Murine Models

The excellent in vitro targeted cytotoxicity urged us to investigate the in vivo antitumor therapeutic potential of the TNEDS. Evaluation of various parameters on DLA ascites tumor-bearing mice on days 16 and 23 of administration revealed a significant reduction in the tumor volume ($p < 0.001$) in both groups administered with Au@SiO₂-Dox-CS-FA, Au@SiO₂-Dox-CS, Dox, and Lipodox (Figure 6a), except Au@SiO₂-CS-FA, which did not elicit any response. Among the various treatment options, Au@SiO₂-Dox-CS-FA generated the best overall response (Figure S16a, Supporting Information). Detailed investigation with tumor cell count, percentage of viable cells, body weight change, and mean survival at the end of the experimental period (Tables S9 and S10, Supporting Information) revealed the superior therapeutic efficacy of Au@SiO₂-Dox-CS-FA over other treatment options. The Kaplan–Meier survival analysis (Figure 6b,c) revealed that Au@SiO₂-Dox-CS-FA treatment prolonged the survival probability significantly ($p < 0.001$). There was a significant reduction in the tumor burden by both intraperitoneal (i.p.) and intratumoral (i.t.) administration of Au@SiO₂-Dox-CS-FA in EAC-induced solid-tumor mice syngraft where i.p. (Figure 6d; Table S11, Supporting Information) mode was observed to be less effective than i.t. mode (Figure 6e; Table S12, Supporting Information). Although

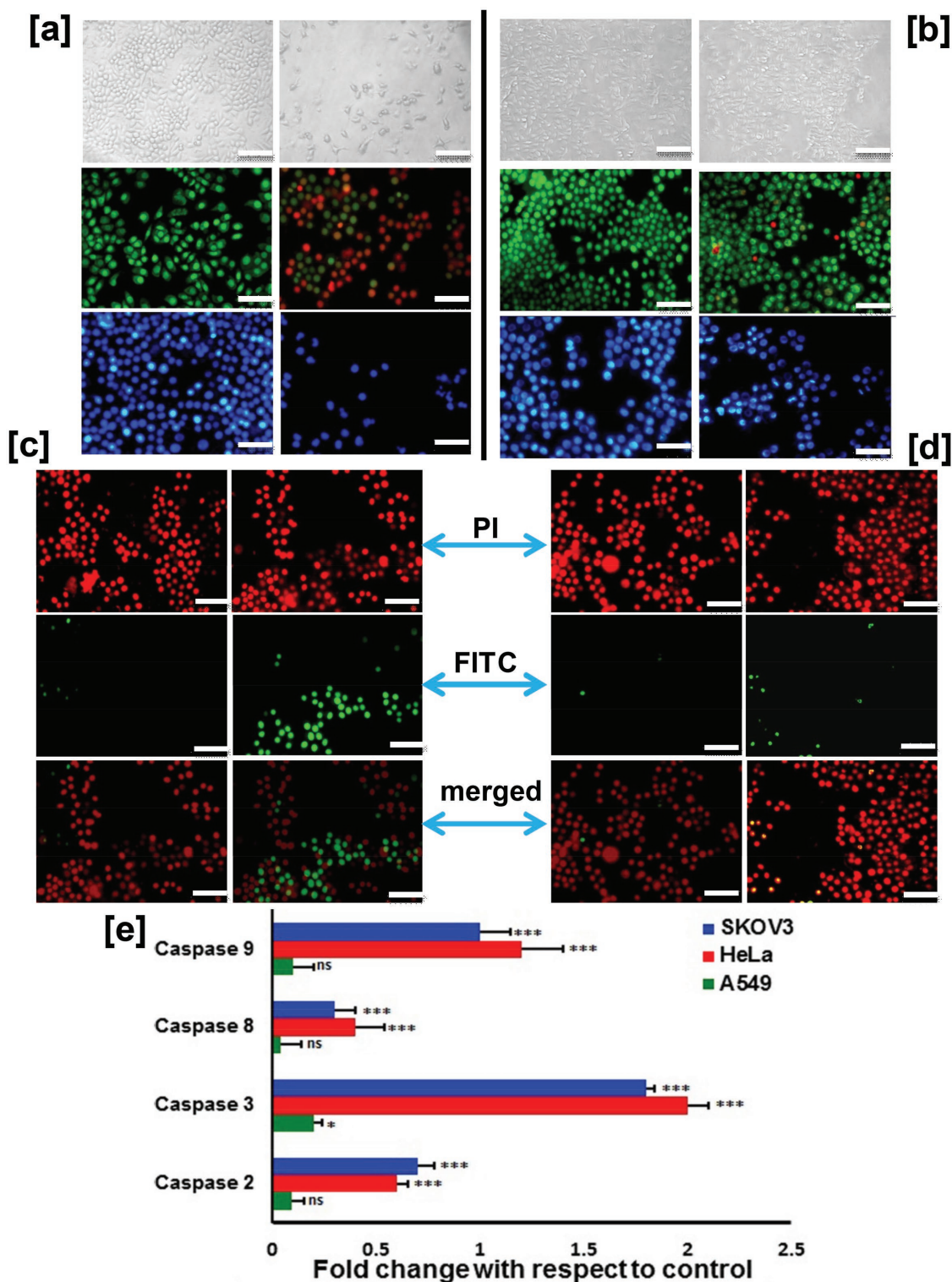


Figure 5. Induction of apoptosis in a) HeLa and b) A549 cells by Au@SiO₂-Dox-CS-FA (1×10^{-6} M) for 24 h, and the cells were evaluated using phase contrast microscopy (upper panel), acridine orange-ethidium bromide (middle panel), and Hoechst staining (lower panel). The left panel represents the control and the right panel indicates the treatment groups. Evaluation of apoptosis by TUNEL staining assay in c) HeLa and d) A549 cells; the left row represents the control and the right row indicates the treatment groups. Scale bar: 50 μ m. e) Caspase profiling of cell lines treated with Au@SiO₂-Dox-CS-FA. Data are the mean \pm SD of three independent experiments; **** p < 0.001, ** p < 0.01; ns: not significant relative to control.

Lipodox was observed to be more effective than naked Dox, the nontargeted construct Au@SiO₂-Dox-CS produced better therapeutic efficacy than Dox with i.t. administration. The

nanoconstructs demonstrated a maximum reduction in tumor volume and a significant (p < 0.001) increase in life span (Figure S16b, Supporting Information). Furthermore, the

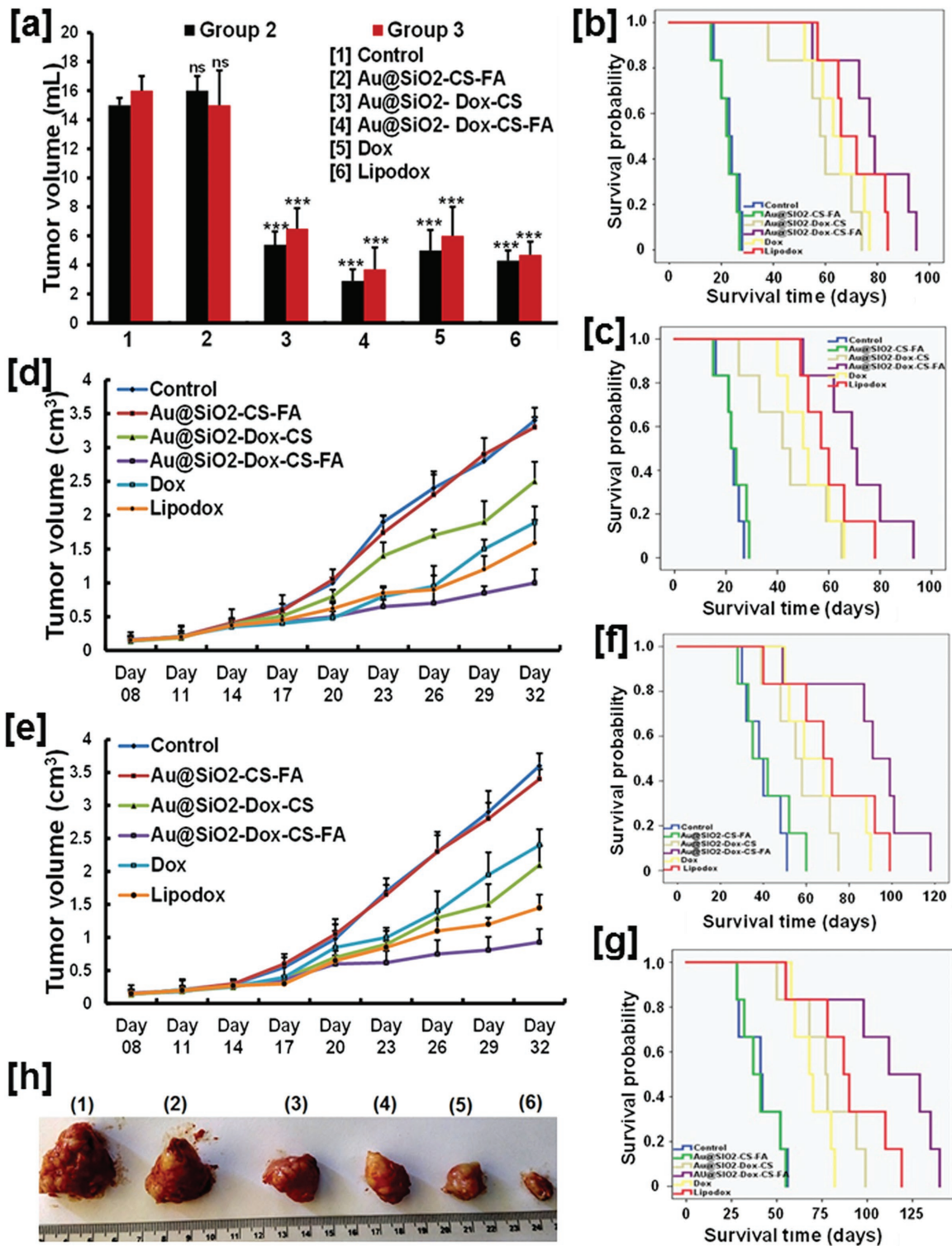


Figure 6. a) DLA ascites tumor volume measurements and Kaplan–Meier survival curve of b) group 2 and c) group 3. EAC-induced solid-tumor measurements were taken after d) i.p. or e) i.t. administration, and f,g) their corresponding Kaplan–Meier survival curves; log rank value $p < 0.0001$. h) Representative images of resected tumors after i.t. administration. The legend (1) represents vehicle control, (2) Au@SiO₂-CS-FA, (3) Dox, (4) Au@SiO₂-Dox-CS, (5) Lipodox, and (6) Au@SiO₂-Dox-CS-FA-treated animals. Statistically significant differences at *** $p < 0.001$; ns, not significant compared with the control group.

Kaplan–Meier analysis (Figure 6f,g) exposed the prolonged survival of tumor-bearing mice with Au@SiO₂-Dox-CS-FA administration up to a level for making it a therapeutically

viable construct. Representative images of expunged tumors with different treatments (Figure 6h) revealed the greater tumor volume reduction upon Au@SiO₂-Dox-CS-FA

treatment. This superior therapeutic effect could be due to the optimal drug loading and targeting efficiency of the TNEDS for more intensive localized applications without causing any nonspecific toxicity, especially in the case of easily accessible solid malignancies and potentiates the future preclinical investigations. The efficiency of tumor targeting by Au@SiO₂-FL-CS-FA was notable, particularly considering that the mice used in this study were fed with a regular diet rather than a folate-free diet, which is usually necessary to increase the detection sensitivity of the FR-targeted delivery systems.^[31]

3. Conclusions

In summary, the novel TNEDS explored in this study not only demonstrated excellent in vitro FR-targeted cytotoxicity but also presented to be an appalling biocompatible targeted nanocarrier delivery construct. High Dox loading with tumor niche specific release kinetics enabled the TNEDS to execute superior salutary therapeutic effects. In diagnostic modality Au@SiO₂, core transformed TNEDS to be an effective SERS nanoprobe for Raman imaging to monitor the cellular uptake, release of the impregnated Dox, and dynamic visualization of biochemical changes at molecular level during apoptosis. Finally, the TNEDS was explored in mouse models that explicitly showed greater therapeutic efficiency superior to the clinically used Dox and Lipodox. Albeit further investigations are justified, the outcome exhibited by the TNEDS definitely holds an aspiration for future preclinical and clinical applications in oncology.

4. Experimental Section

Materials: Gold (III) chloride hydrate, trisodium citrate dehydrate, tetraethyl orthosilicate (TEOS), aqueous ammonia (NH₄OH, 25%–28%), hydrochloric acid (HCl, 36%–38%), fluorescein isothiocyanate (FITC), (3-aminopropyl) triethoxysilane (APTES), MTT, and doxorubicin hydrochloride were purchased from Sigma Aldrich. Acetic acid (CH₃COOH, 99.5% purity), chitosan, and 85% deacylated power were purchased from Alfa aesar. Ethyl alcohol (99.9% purity) was purchased from Changshu Yangyuan Chemical, China. Lipodox was generously gifted by Sun Pharma Advanced Research Company Ltd, India.

TEOS-Mediated Synthesis of Au@SiO₂ Nanoparticles: The synthesis of spherical citrate-stabilized gold nanoparticles of 40 nm was done using the citrate reduction method.^[32] Mono-dispersed Au@SiO₂ nanoparticles with 40 nm gold cores and uniform thicknesses of silica shell were successfully synthesized via the modified Stober method^[33] using vigorous shaking in alcohol solutions. Briefly, 50 mL of citrate stabilized gold nanoparticle was centrifuged using 8000 rpm for 30 min, and the pellets were dissolved in 5 mL of Milli-Q water. The solution was diluted with 15 mL of ethanol solution and adjusted the pH ≈10 using ammonia solutions. To this solution, 48 μL of 1:45 3-isocyanato propyl trimethoxy silane (NCO)-TEOS:TEOS was added and shaken for 24 h. After 24 h, the solution was centrifuged two or three times with 10 000 rpm for 30 min to remove uncoated silica on AuNPs.

Conjugation of Folic Acid with Chitosan: A solution of folic acid and 1-ethyl-3-(3-dimethylaminopropyl) carbodiimide (EDC) in 20 mL of anhydrous dimethyl sulfoxide (DMSO) was prepared and stirred at room temperature until EDC and folic acid were well dissolved.^[34] The mixture was then added slowly to 0.5% (w/v) chitosan in the aqueous solution of acetic acid and stirred at room temperature in the dark for 16 h to let folic acid conjugate onto chitosan molecules (Figure S1, Supporting Information). The solution was adjusted to pH 9.0 by adding NaOH aqueous solution (1.0 M) and centrifuged at 2500 rpm. The precipitate was dialyzed first against phosphate buffered saline (PBS, pH 7.4) for 3 d and then against water for 4 d. NMR spectra were recorded on the Bruker Advance 500 NMR spectrometer, and chemical shifts are expressed in parts per million.

Synthesis of Chitosan–Folic Acid (CS-FA)-Coated Au@SiO₂ Nanoparticle: Chitosan–folic acid conjugate (25 mg) was dissolved in 5 mL of 3% acetic acid, and the suspension was stirred at 600 rpm for 24 h to form CS-FA solution (0.5% w/v). About 5 mL of Au@SiO₂ nanoparticles was centrifuged and made a solution in 5 mL of ethyl alcohol, and the dispersion was adjusted to pH 3.5–4.5 by adding acetic acid. Subsequently, 200 μL of APTES was added to modify Au@SiO₂ nanoparticle and was reacted with silanol groups on the SiO₂ surface to form Si–O–Si bonds. Then CS-FA solution was added to accomplish cross-linking of nanoparticle and allowed to stir at room temperature for 24 h. The CS-FA-coated Au@SiO₂ (Au@SiO₂-CS-FA) was collected by centrifugation at 10 000 rpm, followed by washing with excessive distilled water and ethyl alcohol solution.

Doxorubicin Loading and Redox and pH-Responsive Dox Release Kinetics of Au@SiO₂-Dox-CS-FA NPs: The detailed procedure and the DLE, DLC,^[35] and actual amount of drug in nanoparticle calculated are shown in Section SI-2 of the Supporting Information). The release of Dox from Au@SiO₂-Dox-CS-FA, Lipodox, and doxorubicin hydrochloride under various pH and redox conditions was evaluated as reported elsewhere^[36] and detailed in Section SI-3 of the Supporting Information.

Culture and Maintenance of Cell lines: Human cancer cell lines HeLa (cervical cancer), MCF-7 (breast cancer), and A549 (lung adenocarcinoma) were obtained from American Type Culture Collection (Manassas, USA). SKOV3 (ovarian cancer) cells were generously provided by the Rajiv Gandhi Centre for Biotechnology (Thiruvananthapuram, India). The fibroblast-like murine preadipocyte cell line 3T3L1 was gifted from the Inter-University Centre for Genomics and Gene Technology, University of Kerala (Thiruvananthapuram, India). A375 (malignant melanoma) cells were obtained from NCCS (Pune, India). Cells were maintained in Dulbecco's modified Eagle medium (DMEM) with 10% fetal bovine serum (FBS) and 5% CO₂ at 37 °C. Source and maintenance of murine cancer cell lines are described in Section SI-4 of the Supporting Information. Animal experiments were performed according to the CPCSEA (Committee for the Purpose of Control and Supervision of Experiments on Animals) guidelines and was approved by the Institutional Animal Ethics Committee (IAEC) of the Regional Cancer Centre (Accreditation number: 657/Go/Re/02/CPCSEA), Trivandrum, India.

Cytotoxicity Assays: The growth inhibitory capacity was initially evaluated on cancer and normal cell lines by MTT assay as previously reported.^[17] The absorbance was measured at 570 nm using a microplate spectrophotometer (BioTek, Power Wave XS) after incubation for 12, 24, and 48 h with test compounds. The cytotoxicity

was further confirmed with BrdU assay kit (colorimetric – 11647229001, Roche Diagnostics, IN, USA), and the experiments were carried out with the instructions given in the kit and the measurements were made at 450/690 nm. Evaluation of the effect of folic acid on the growth inhibitory capacity of the constructs was also carried out by MTT assay after the addition of 2×10^{-3} M folic acid to the medium for 2 h as reported.^[31]

Western Blot Analysis and Hemolysis assay: The expression status of folate receptors in the cell lines was evaluated using western blot analysis using FOLR2 (folate receptor b) primary antibodies and β -actin as the reference control. The resulting bands were then quantitated using Image J software (version 1.48, NIH, USA), normalized with β -actin and the experimental procedure was detailed in Section SI-5 of the Supporting Information). Furthermore, the biocompatibility of the constructs against red blood cells was evaluated using hemolysis assay using 2% Triton X-100 and PBS as positive and negative controls, respectively, and was detailed in Section SI-6 of the Supporting Information.

Apoptotic Assays: Morphological assessment of apoptosis was conducted in HeLa, SKOV3, and A549 cells treated with Au@SiO₂-Dox-CS-FA (1×10^{-3} M) for 24 h. Initially, cells were observed for any visible gross morphological changes under phase contrast objective (Olympus 1×51 , Singapore) to view the apoptotic or nonapoptotic cells. Acridine orange–ethidium bromide dual staining was performed as described earlier,^[37] and the cells were observed under an FITC filter (Olympus 1×51 , Singapore). Observation of nuclei for any apoptosis related changes was done with Hoechst 33342 staining using a 4',6-diaminido-2-phenylindole (DAPI) filter (Olympus 1×51 , Singapore) as described before. TUNEL assay (DeadEnd Fluorometric TUNEL system, Promega, Madison, WI, USA) was used to detect the incorporation of the fluorescein-12-dUTP in the fragmented DNA of apoptotic cells, using the terminal-deoxynucleotidyl-transferase recombinant enzyme as per the manufacturer's instructions using propidium iodide as counterstain. Caspase profiling was determined by using Apo Alert Caspase Profiling kit (Clontech, CA, USA) as per the manufacturer's protocol. Cells were treated with Au@SiO₂-Dox-CS-FA (1×10^{-3} M) for 24 h, and samples were transferred to 96-well plates for fluorimetric reading ($\lambda_{\text{ex}} = 380$ nm; $\lambda_{\text{em}} = 460$ nm), and signals were recorded by spectrofluorimetry (FLx800, BioTek).

Live Cell Raman Imaging: Evaluating the efficacy of Au@SiO₂-CS-FA as a Raman substrate was done with the aid of a confocal Raman microscope (WI-Tec, Inc., Germany) with a laser beam directed to the sample through 20 \times objective with a Peltier cooled CCD detector. For cellular imaging, 20 μ L (1×10^{-3} M) of Au@SiO₂-CS-FA was added to HeLa cells and was incubated at 37 °C for 1 h. SERS mapping was recorded by focusing the laser beam on the cell surface selected at a position $z = 0$ μ m using 0.5 as the integration time, 150 \times 150 as points per line, and 50 \times 50 μ m mapping area along the X and Y directions. The Raman and SERS cell maps were acquired over a motorized scan stage. The chemical images were computed from the 2D collection of Raman/SERS spectra by integrating the intensity of a specific band over a defined wave number range after baseline subtraction. Raman images were subsequently subjected to cluster mapping and later 3D plots were made out of it. A minimum of three independent measurements were made for each sample.

Cellular Internalization Study: Cellular uptake and release of Dox or FITC were tested with various constructs with fluorescent

microscopy, Raman microscopy, fluorimeter, and flow cytometer. HeLa and A549 cells were treated with (1×10^{-6} M) Dox, Lipodox, Au@SiO₂-Dox-CS, and Au@SiO₂-Dox-CS-FA for 4 h (Section SI-7, Supporting Information).

Nanoparticle Uptake Pathway Determination: Pharmacological inhibitors were employed to determine the cellular uptake pathways responsible for cellular uptake and transport of positively charged Au@SiO₂-Dox-CS-FA nanoparticles, and the experiments were performed as previously described.^[37] HeLa cell monolayers were incubated with previously optimized doses of endocytosis inhibitors, and the detailed procedures are given in Section SI-8 of the Supporting Information.

Evaluation of Dox Uptake and Apoptosis Using SERS: Since Au@SiO₂-Dox-CS-FA could generate sufficiently higher intensity Dox fingerprints and enabled cellular imaging in the SERS platform, it was used for tracing Dox release using a confocal Raman microscope, and the cellular imaging was performed as explained above. The specific Raman band area of Dox was selected to create an SERS maps after 1 and 3 h of Au@SiO₂-Dox-CS-FA treatment. The intensity of the SERS spectra was measured at different spots belonging to the nuclear and cytoplasmic regions, and the spectra were averaged to create every single curve.^[38] The cells were maintained for up to 6 h, and SERS spectra were extracted from the nuclear area for every 30 min for identification of change in spectral pattern over time with Dox exposure.

Tumor Reduction Studies on Ascites and Solid-Tumor Mice: Female BALB/c mice were maintained in well-ventilated cages with free access to normal mouse food and water. Temperature (25 ± 2 °C) and humidity ($50\% \pm 5\%$) were regulated and the illumination cycle was set to 12 h light/dark. Experimental design with DLA ascites tumor was illustrated (Figure S17, Supporting Information). Tumor volume, mean survival time, and percentage of increment in life span were calculated as previously reported (Section SI-9a, Supporting Information). Experiments with EAC–solid-tumor mice syngraft were performed by two different routes: i.p. and i.t. injections, daily for 14 consecutive days, starting on day 9 after tumor inoculation (days 9–22 as shown in Figure S17 (Group 3), Supporting Information). Animals were sacrificed on day 23 to determine tumor volume and overall survival ($n = 6$ per subgroup). The radii of the developing tumors were measured every third day from day 7 to day 31 using Vernier calipers, and the tumor volume was estimated using the following formula: $V = 4/3\pi r_1 r_2$, where r_1 and r_2 represent the radii from two^[37,39] and was described in Section SI-9b of the Supporting Information.

Supporting Information

Supporting Information is available from the Wiley Online Library or from the author.

Acknowledgements

A.N.R. and M.M.J. contributed equally to this work. K.K.M. wish to thank SERB, Department of Science and Technology (SR/S1/OC-67/2012), Department of Biotechnology (BT/PR14698/

NNT/28/832/2015), and Council of Scientific and Industrial Research (CSIR), network project CSC-0134, BSC-0112, Govt. of India for research funding. M.M.J. thanks the Kerala Biotechnology Commission, Government of Kerala (KBC-KSCSTE) for the postdoctoral research fellowship. AcSIR student R.A.N. acknowledges CSIR network project (NanoSHE) for the research fellowship.

Conflict of Interest

The authors declare no conflict of interest.

-
- [1] T. Sun, Y. S. Zhang, B. Pang, D. C. Hyun, M. Yang, Y. Xia, *Angew. Chem., Int. Ed.* **2014**, *53*, 12320.
- [2] F. Wang, Y. Wang, S. Dou, M. Xiong, T. Sun, J. Wang, *ACS Nano* **2011**, *5*, 3679.
- [3] Y. Barenholz, *J. Controlled Release* **2012**, *160*, 117.
- [4] J. Popp, C. Krafft, M. Schmitt, I. Schie, D. Cialla-May, C. Matthaues, T. Bocklitz, *Angew. Chem., Int. Ed.* **2017**, *56*, 4392.
- [5] H. Meng, M. Xue, T. Xia, Y. L. Zhao, F. Tamanoi, J. F. Stoddart, J. I. Zink, A. E. Nel, *J. Am. Chem. Soc.* **2010**, *132*, 12690.
- [6] J. Song, J. Zhou, H. Duan, *J. Am. Chem. Soc.* **2012**, *134*, 13458.
- [7] Y. Chen, Y. J. Yoon, X. Pang, Y. He, J. Jung, C. Feng, G. Zhang, Z. Lin, *Small* **2016**, *12*, 6714.
- [8] J. Song, L. Pu, J. Zhou, B. Duan, H. Duan, *ACS Nano* **2013**, *7*, 9947.
- [9] K. Bosslet, R. Straub, M. Blumrich, J. Czech, M. Gerken, B. Sperker, H. K. Kroemer, J. P. Gesson, M. Koch, C. Monneret, *Cancer Res.* **1998**, *58*, 1195.
- [10] A. M. Fales, B. M. Crawford, T. Vo-Dinh, *ACS Omega* **2016**, *1*, 730.
- [11] J. Conde, C. Bao, D. Cui, P. V. Baptista, F. Tian, *J. Controlled Release* **2014**, *183*, 87.
- [12] S. Barbosa, A. Topete, M. Alatorre-Meda, E. M. Villar-Alvarez, A. Pardo, C. Alvarez-Lorenzo, A. Concheiro, P. Taboada, V. Mosquera, *J. Phys. Chem. C* **2014**, *118*, 26313.
- [13] Z. Shi, R. Guo, W. Li, Y. Zhang, W. Xue, Y. Tang, Y. Zhang, *J. Mater. Sci.: Mater. Med.* **2014**, *25*, 723.
- [14] K. Dick, T. Dhanasekaran, Z. Zhang, D. Meisel, *J. Am. Chem. Soc.* **2002**, *124*, 2312.
- [15] S. Zong, Z. Wang, J. Yang, C. Wang, S. Xu, Y. Cui, *Talanta* **2012**, *97*, 368.
- [16] C. Eliasson, A. Lorén, K. V. G. K. Murty, M. Josefson, M. Käll, J. Abrahamsson, K. Abrahamsson, *Spectrochim. Acta, Part A* **2001**, *57*, 1907.
- [17] M. M. Joseph, S. R. Aravind, S. K. George, K. Raveendran Pillai, S. Mini, T. T. Sreelekha, *J. Biomed. Nanotechnol.* **2014**, *10*, 3253.
- [18] Y. Cui, H. Dong, X. Cai, D. Wang, Y. Li, *ACS Appl. Mater. Interfaces* **2012**, *4*, 3177.
- [19] D. Bhattacharya, M. Das, D. Mishra, I. Banerjee, S. K. Sahu, T. K. Maiti, P. Pramanik, *Nanoscale* **2011**, *3*, 1653.
- [20] H. Shinto, T. Fukasawa, K. Yoshisue, M. Tezuka, M. Orita, *Adv. Powder Technol.* **2014**, *25*, 1872.
- [21] Z. Zhang, J. Wang, C. Chen, *Adv. Mater.* **2013**, *25*, 3869.
- [22] D. Radziuk, H. Moehwald, *Phys. Chem. Chem. Phys.* **2015**, *17*, 21072.
- [23] Z. Movasaghi, S. Rehman, I. Rehman, *Appl. Spectrosc. Rev.* **2007**, *42*, 493.
- [24] M. Kamimura, J. O. Kim, A. V. Kabanov, T. K. Bronich, Y. Nagasaki, *J. Controlled Release* **2012**, *160*, 486.
- [25] S. D. Perrault, C. Walkey, T. Jennings, H. C. Fischer, W. C. Chan, *Nano Lett.* **2009**, *9*, 1909.
- [26] T. G. Iversen, T. Skotland, K. Sandvig, *Nano Today* **2011**, *6*, 176.
- [27] W. J. Tipping, M. Lee, A. Serrels, V. G. Brunton, A. N. Hulme, *Chem. Soc. Rev.* **2016**, *45*, 2075.
- [28] S. R. Panikkanvalappil, M. James, S. M. Hira, J. Mobley, T. Jilling, N. Ambalavanan, M. A. El-Sayed, *J. Am. Chem. Soc.* **2016**, *138*, 3779.
- [29] L. Silveira, F. L. Silveira, B. Bodanese, R. A. Zângaro, M. T. T. Pacheco, *J. Biomed. Opt.* **2012**, *17*, 77003.
- [30] N. Narayanan, L. V. Nair, V. Karunakaran, M. M. Joseph, J. B. Nair, A. N. Ramya, R. S. Jayasree, K. K. Maiti, *Nanoscale* **2016**, *8*, 11392.
- [31] J. B. Nair, M. M. Joseph, S. Mohapatra, M. Safeera, S. Ghosh, T. T. Sreelekha, K. K. Maiti, *ChemMedChem* **2016**, *11*, 702.
- [32] T. T. Ahner, F. Delissen, S. Sokolov, *J. Am. Chem. Soc.* **2010**, *132*, 1296.
- [33] S. Liu, M. Y. Han, *Chem. – Asian J.* **2010**, *5*, 36.
- [34] M. Gulfam, B. G. Chung, *Macromol. Res.* **2014**, *22*, 412.
- [35] H. Yi, P. Liu, N. Sheng, P. Gong, Y. Ma, L. Cai, *Nanoscale* **2016**, *8*, 5985.
- [36] A. M. Bannunah, D. Vllasaliu, J. Lord, S. Stolnik, *Mol. Pharmacol.* **2014**, *11*, 4363.
- [37] M. M. Joseph, S. R. Aravind, S. K. George, R. K. Pillai, S. Mini, T. T. Sreelekha, *Clin. Transl. Oncol.* **2014**, *7*, 525.
- [38] W. A. El-Said, T. H. Kim, H. Kim, J. W. Choi, *Biosens. Bioelectron.* **2010**, *26*, 1486.
- [39] M. M. Joseph, S. R. Aravind, S. K. George, K. R. Pillai, S. Mini, T. T. Sreelekha, *Colloids Surf., B* **2014**, *116*, 219.

Received: March 13, 2017
Revised: May 3, 2017
Published online: July 3, 2017

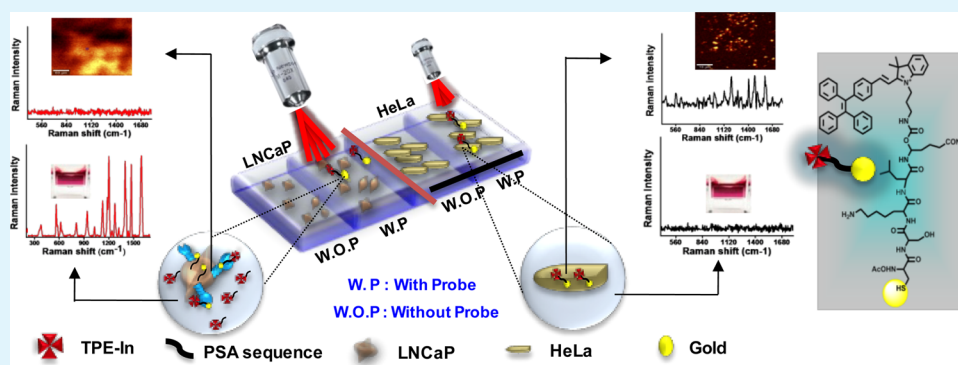
New Insight of Tetraphenylethylene-based Raman Signatures for Targeted SERS Nanoprobe Construction Toward Prostate Cancer Cell Detection

Adukkadan N. Ramya,[†] Manu M. Joseph,[†] Jyothi B. Nair,^{†,‡} Varsha Karunakaran,^{†,‡} Nisha Narayanan,^{†,‡} and Kaustabh Kumar Maiti^{*,†,‡}

[†]Chemical Sciences & Technology Division, CSIR-National Institute for Interdisciplinary Science & Technology (CSIR-NIIST), Industrial Estate, Pappanamcode, Thiruvananthapuram 695019, Kerala, India

[‡]Academy of Scientific and Innovative Research, AcSIR, CSIR-NIIST, Thiruvananthapuram 695019, Kerala, India

S Supporting Information



ABSTRACT: We have designed and synthesized novel tetraphenylethylene (TPE) appended organic fluorogens and unfold their unique Raman fingerprinting reflected by surface-enhanced Raman scattering (SERS) upon adsorption on nanoroughened gold surface as a new insight in addition to their prevalent aggregation-induced emission (AIE) and aggregation-caused quenching (ACQ) phenomena. A series of five TPE analogues has been synthesized consisting of different electron donors such as (1) indoline with propyl (TPE-In), (2) indoline with lipoic acid (TPE-In-L), (3) indoline with Boc-protected propyl amine (TPE-In-Boc), (4) benzothiazole (TPE-B), and (5) quinaldine (TPE-Q). Interestingly, all five TPE analogues produced multiplexing Raman signal pattern, out of which TPE-In-Boc showed a significant increase in signal intensity in the fingerprint region. An efficient SERS nanoprobe has been constructed using gold nanoparticles as SERS substrate, and the TPE-In as the Raman reporter, which conjugated with a specific peptide substrate, Cys-Ser-Lys-Leu-Gln-OH, well-known for the recognition of prostate-specific antigen (PSA). The designated nanoprobe TPE-In-PSA@Au acted as SERS “ON/OFF” probe in peace with the vicinity of PSA protease, which distinctly recognizes PSA expression with a limit of detection of 0.5 ng in SERS platform. Furthermore, TPE-In-PSA@Au nanoprobe was efficiently recognized the overexpressed PSA in human LNCaP cells, which can be visualized through SERS spectral analysis and SERS mapping.

KEYWORDS: tetraphenylethylene, PSA peptide sequence, gold nanoparticle, SERS, cancer detection

INTRODUCTION

The diversified chemical structure of organic fluorescent molecules modulating fundamental photophysical properties have continuously evolved over the past several years, imparting a huge impact on biomedical research with special emphasis on bioimaging.^{1,2} One such unique photophysical phenomenon of organic fluorogens is known as aggregation-induced emission (AIE), which was first reported in 2001 by Su et al.³ On the contrary, an opposite mechanism called aggregation-caused quenching, occurred due to the formation of excimers and exciplexes upon collision between the aromatic molecules in the excited and ground states, which is mainly through fluorescence resonance energy transfer (FRET), internal charge transfer

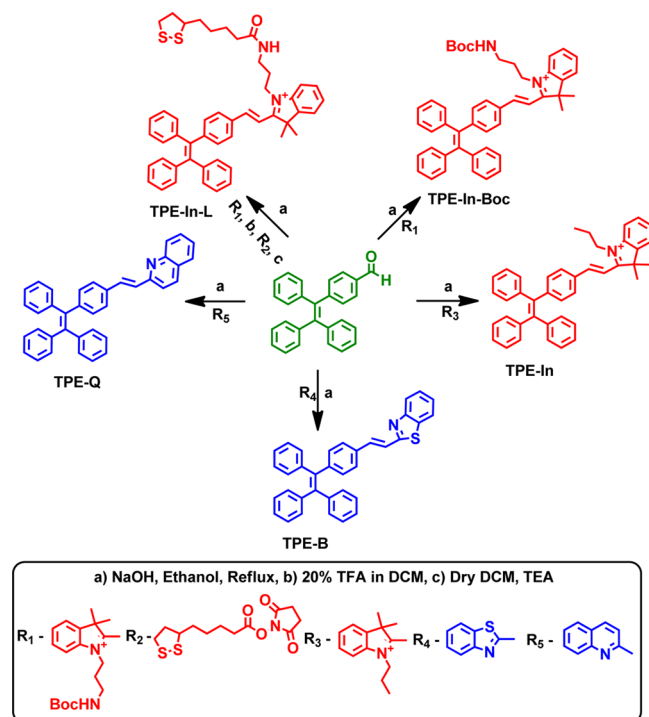
(ICT), or both. A well-known example for an AIE fluorogen is tetraphenylethylene (TPE), in which the olefin stator is surrounded by phenyl rotors that are nonemissive in a molecularly dissolved state and are emissive by aggregate formation⁴ and also exhibit ACQ effect by modifying the molecular structure. Due to AIE and ACQ effects, TPE analogues found surplus applications in sensing and detection of various metal cations^{5–7} and anions,⁸ biological applications

Received: February 17, 2016

Accepted: April 6, 2016

Published: April 6, 2016

Scheme 2. Synthetic Route to TPE Derivatives



TPE-In, TPE-In-L, and TPE-In-Boc showed absorption at 445, 449, and 446 nm and were red in color (Figure S20). Because TPE molecules are well-known for aggregation studies we have evaluated their aggregation properties in DMSO–water system. Upon increasing the water (f_w) proportion, TPE-B and TPE-Q showed AIE effect, whereas the fluorescent quenching (ACQ) was observed in TPE-In, TPE-In-L, and TPE-In-Boc under similar conditions, which is probably due to the intermolecular FRET.²⁵ Figures 1 and 2 represent the fluorescence spectra of TPE analogues showing the AIE and ACQ effects in varying percentages of DMSO/water system, respectively.

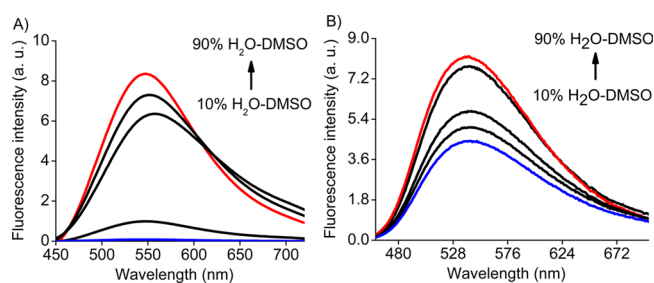


Figure 1. Fluorescence spectra of (A) TPE-B (0.50 mM, $\lambda_{\text{ex}} = 371$ nm) and (B) TPE-Q (0.50 mM, $\lambda_{\text{ex}} = 376$ nm), in DMSO/water mixture with different water percentages (f_w).

Surface-Enhanced Raman Scattering (SERS) Phenomenon. Further, we have investigated the SERS fingerprint pattern of all five TPE derivatives under a particular solvent concentration other than their AIE and ACQ properties. SERS experiments have been carried out by incubating the TPE-analogues as Raman reporter with citrate stabilized spherical gold nanoparticle (Au NP; 40 nm) (Figure S21) as a SERS substrate and SERS spectra was measured under a WI-Tec Raman microscope with a wavelength of 633 nm laser excitation and 20 \times objective. All the TPE derivatives exhibit

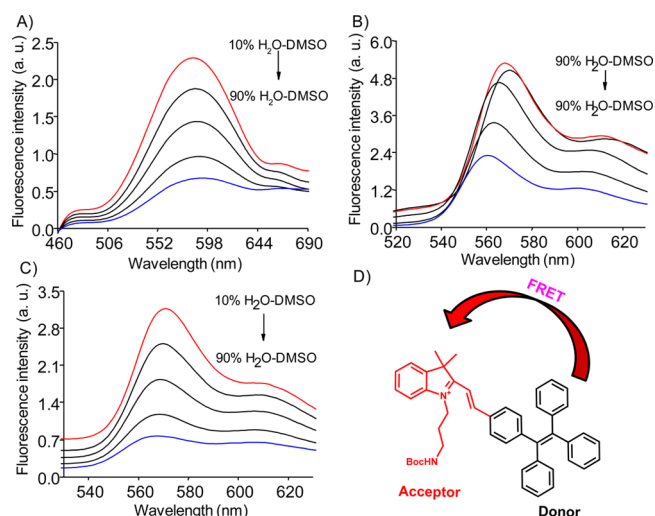


Figure 2. Fluorescence spectra of (A) TPE-In (0.50 mM, $\lambda_{\text{ex}} = 445$ nm), (B) TPE-In-L (0.50 mM, $\lambda_{\text{ex}} = 449$ nm), and (C) TPE-In-Boc (0.50 mM, $\lambda_{\text{ex}} = 446$ nm) in DMSO/water mixture with different water percentages (f_w). (D) Representation of FRET between the donor and the acceptor.

signature Raman peaks at 687, 800–930, and 1000–2000 cm^{-1} corresponding to C–C in plane bending, aliphatic chain vibrations and aromatic ring vibrations, respectively (Figure 3).²⁶ Significant Raman fingerprints are obtained corresponding to the derivative, TPE-In-Boc. This noticeable enhancement of Raman signal in SERS platform depends on variable factors, for example, particular molecular orientation on nanoparticle

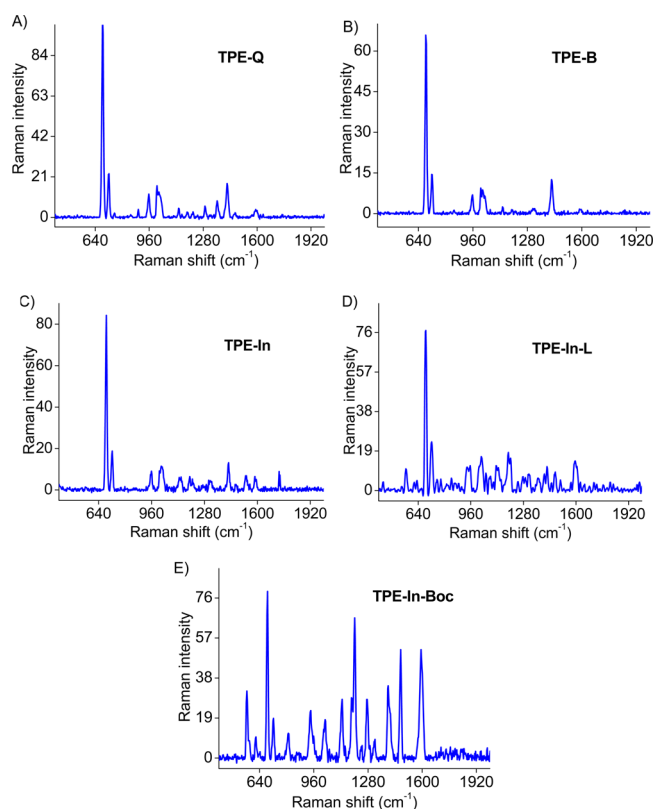


Figure 3. SERS spectral pattern of TPE derivatives after incubating with citrate stabilized gold nanoparticles as substrate by 9:1 ratio; (A) TPE-Q, (B) TPE-B, (C) TPE-In, (D) TPE-In-L, and (E) TPE-In-Boc.

surface, which can generate a good number of hotspots and produce enhanced electromagnetic field, leading to signal enhancement.²⁴

Construction of TPE-In-PSA SERS Nanoprobe. We have selected the best Raman signature TPE-In-Boc for further construction of SERS nanoprobe aiming to detect prostate specific antigen, cancer protein by SERS spectral analysis. For the construction of designated synthetic counterpart TPE-In-PSA, the corresponding Boc protected analogue (TPE-In-Boc) was conjugated to PSA recognizing peptide substrate, Cys-Ser-Lys-Leu-Gln-OH. The peptide sequence was synthesized by adopting the well-known solid phase peptide synthesis (SPPS; Scheme S7). Subsequently, the synthesized peptide sequence was coupled with Boc deprotected free amino terminal of TPE-In in the presence of EDC using HOBt as coupling agent (Scheme S8) and characterized by ¹H NMR and mass spectral analysis. Trityl group of Cys residue from TPE-In-PSA counterpart underwent deprotection by 20% TFA in DCM which resulted free thiol functionality. The free thiol moiety undergoes chemisorption on AuNP surface resulted in the formation of the targeted nanoprobe, TPE-In-PSA@Au.

The fluorescent property of TPE-In-PSA has been monitored upon incubation with different percentage of colloidal AuNP which exhibited ACQ effect similar to TPE-In-Boc, but the strong quenching efficiency was observed because of internal charge transfer between the AuNP and the TPE moiety. We have correlated these two reversal effects between fluorescence quenching and SERS signal enhancement at 90% of colloidal AuNP solution. The maximum SERS signal enhancement occurred at 90% of colloidal AuNP which is further reflected in a visible color change from red to blue attributed to the formation of TPE-In-PSA and AuNP aggregates (Figure 4A). Subsequently, more hotspots are generated which significantly enhances the SERS intensity (Figure 4B).

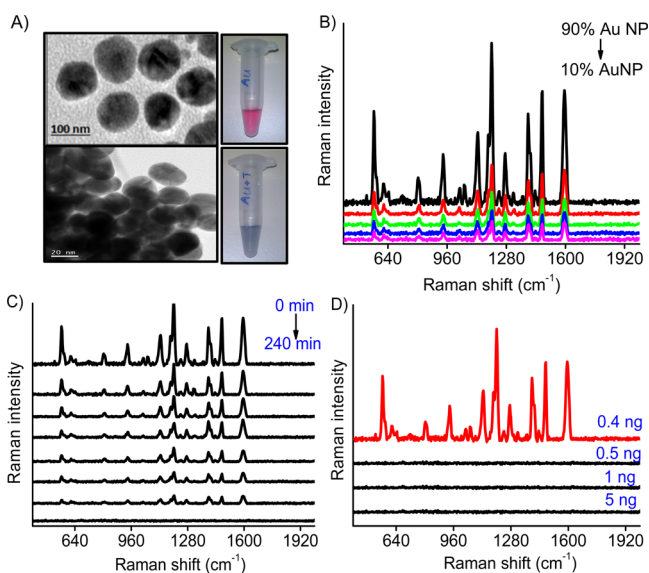


Figure 4. (A) TEM images of (top) gold nanoparticle alone and (bottom) TPE-In-PSA@Au nanoprobe and corresponding visual color changes. (B) SERS spectra of TPE-In-PSA@Au nanoprobe by varying the percentage of gold concentration. (C) Time-dependent changes in SERS spectra of TPE-In-PSA@Au nanoprobe after the incubation of 0.5 ng of the PSA protease in PSA buffer solution at 37 °C recorded at each 30 min. (D) SERS spectra showing the limit of detection by varying the concentration of PSA protease.

PSA Protease Detection and LOD Calculation through SERS.

For the detection of PSA protein, the initial study was performed by incubating PSA protease in PSA buffer within TPE-In-PSA@Au nanoprobe at 37 °C.²⁷ During incubation with PSA protease the target specific peptide sequence from TPE-In-PSA was cleaved and TPE-In detached from AuNP, and subsequently, gradual decrease in SERS signal intensity was observed. Interestingly, with time the SERS intensity of the nanoprobe was minimized and completely lost after 210 min (Figure 4C). We have evaluated the limit of detection (LOD) of the probe through SERS spectra by changing the concentration of the PSA protease (5, 1, 0.5, and 0.4 ng). Figure 4D represents the SERS spectra showing the limit of detection by varying the concentration of PSA enzyme which is responsible for the effective cleavage of the peptide sequence at 210 min. The LOD of our probe was found to be 0.5 ng of PSA protease, which could effectively cleave the peptide sequence.

Recognition of Human Prostate Cancer Cells Using SERS Nanoprobe.

PSA expression varies between cancer types and hence we evaluated PSA expression on a human prostate cancer (LNCaP) and cervical cancer (HeLa) cells by Western blot analysis using PSA antibodies. Quantitative evaluation of the bands was performed after normalizing with that of β -actin which indicated significantly high expression of PSA on LNCaP than HeLa cells (Figure 5A). In this context,

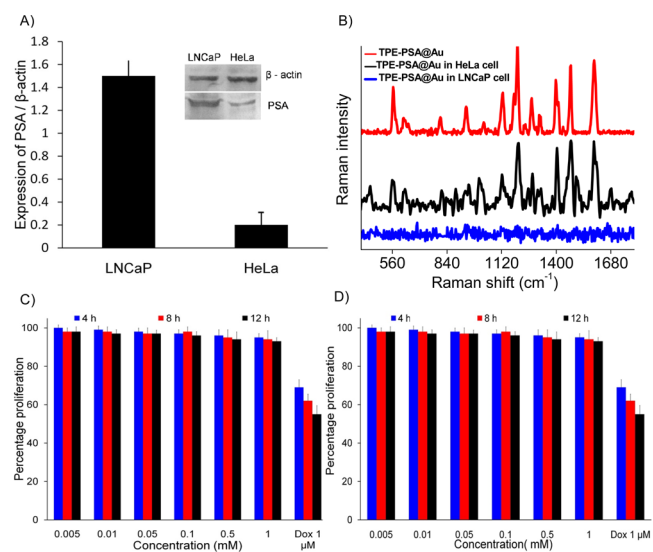


Figure 5. (A) Protein level expression analysis of PSA on LNCaP and HeLa cell lines by Western blot, the bands normalized to β -actin and quantified using ImageJ software, (B) SERS spectra analysis of probes on HeLa and LNCaP cells after washing with PBS solution. Cytotoxicity profiles of TPE-PSA@Au using MTT assay on (C) LNCaP and (D) HeLa cell line.

LNCaP could be used as positive and HeLa as negative control for the PSA expression studies. The results obtained was correlated with other similar studies reported in the literature.²⁸ Evaluation of the cytotoxicity of TPE-In-PSA@Au nanoprobe was performed on both the cell lines by MTT assay against a wide dose range (0.005 mM to 1 mM) for 4, 8, and 12 h including doxorubicin (1 μ M) as positive control. It was observed that the nanoprobe was largely nontoxic to both the cell lines for all doses and time periods (Figure 5C,D), whereas the positive control doxorubicin demonstrated its cytotoxicity. The nontoxic behavior of nanoprobe will enable detailed

biological assays in all contexts. Further we have carried out the SERS based assay for the detection of PSA expression on LNCaP and HeLa cells.

LNCaP cells were cultured in four-well chamber slide and 200 μL (9:1, Au/TPE-In-PSA) of TPE-In-PSA@Au nanoprobe were added to the wells separately and was incubated at 37 $^{\circ}\text{C}$. SERS spectra were recorded after 30 min onward and continued up to 4 h. Due to the overexpression of PSA on LNCaP cell surfaces, PSA peptide bearing AuNP was cleaved from TPE-In-PSA@Au and AuNP was internalized without TPE analogue, so that TPE-In part is remained in the culture medium. Therefore, the SERS intensity of the culture medium was decreased with time and completely lost at around 4 h which resembled to the screening study performed using PSA protease. To confirm the above-mentioned facts, we monitored the SERS spectra inside the cells after 4 h but no characteristic spectra were obtained (Figure 5B). Complete absence of SERS spectra inside the cell confirmed the fact that highly expressed PSA enzyme effectively cleaved off the Raman reporter bearing PSA peptide sequence from the nanoprobe. A similar study has been carried out using PSA negative HeLa cells and monitored the SERS intensity from both culture medium and within the cells. In contrary to LNCaP cells, a complete absence of SERS spectra in the culture medium even after 4 h accompanied by significant SERS intensity was observed inside the cells (Figure 5B). The absence of PSA enzyme in HeLa cell enabled the entry of the nanoprobe inside the cell.

SERS Mapping. After checking the SERS spectra inside the cells, we performed the SERS mapping of the two cells by confocal Raman microscopy using 0.5 s as integration time, 150 \times 150 as points per line and 50 \times 50 μm mapping area along X and Y directions. In Figure 6, panels A and B show the bright field images, panels C and D show the corresponding 2D Raman images, and panels E and F show the 3D Raman images of LNCaP and HeLa cells, respectively. The histogram images^{29,30} in Figure 3G,H shows the statistical representation of the most intense peak coming from the Raman reporter (I_{1600}/I_{1100}) chemisorbed on AuNPs. From the Raman images and histogram images it is clear that TPE-In-PSA@Au nanoprobe is entered only into HeLa cells but not in to LNCaP cells, in which effective cleavage is occurred from the cell surface and TPE-In-PSA part failed to enter in to the cells.

CONCLUSIONS

In conclusion, we have synthesized a series of five diversified tetraphenylethylene (TPE) analogues, exhibiting predominantly AIE ACQ phenomenon with excellent SERS fingerprint and multiplex signal pattern. The unique SERS nanoprobe TPE-In-PSA@Au has been developed in conjugation with target-specific PSA peptide substrate aiming for the detection of PSA protein. The nanoprobe successfully recognizes PSA enzyme in SERS-based detection platform with a LOD of 0.5 ng which unfold a new avenue in prostate cancer diagnosis. Furthermore, TPE-In-PSA@Au nanoprobe was nicely recognized by PSA overexpressed LNCaP cells, which was visualized through SERS spectral analysis and SERS mapping. For the first time, we explored a SERS nanoprobe that recognizes PSA overexpression on cancer cells using a novel TPE analogue as Raman reporter.

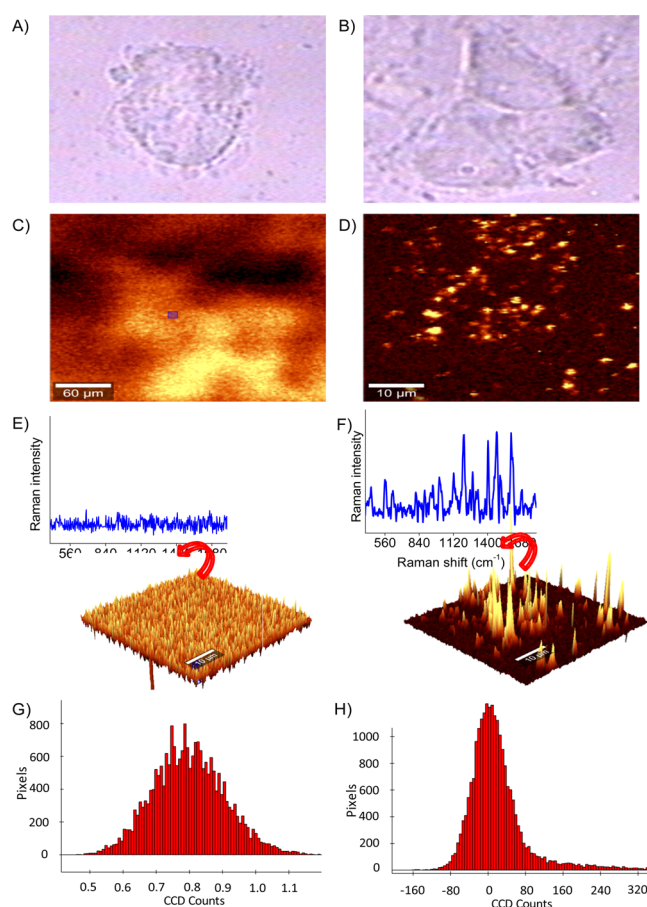


Figure 6. Raman imaging of cells with nanoprobe. Bright field images of (A) LNCaP and (B) HeLa cells and the corresponding (C, D) 2D and (E, F) 3D images of LNCaP cells and HeLa cells. Histogram representation of the most intense peak coming from the Raman reporter (I_{1600}/I_{1100}) with the gold nanoparticles in (G) LNCaP cells and (H) HeLa cells.

ASSOCIATED CONTENT

Supporting Information

The Supporting Information is available free of charge on the ACS Publications website at DOI: 10.1021/acsami.6b01908.

Synthetic details, additional figures of photophysical experiments, and characterization data such as ^1H NMR, ^{13}C NMR, and HRMS spectra. (PDF)

AUTHOR INFORMATION

Corresponding Author

* Tel: +91-471-2515475. E-mail: kkmaiti@niist.res.in, kkmaiti29@gmail.com.

Notes

The authors declare no competing financial interest.

ACKNOWLEDGMENTS

K.K.M. thanks the Council of Scientific and Industrial Research (CSIR), Govt. of India, BSC-0112, CSC-0134 (CSIR Network project) and SERB (DST No. SR/S1/OC-67/2012) for research funding. R.A.N. acknowledges the CSIR network project for the research fellowship. M.M.J. thanks Kerala Biotechnology Commission, Govt. of Kerala (KBC-KSCSTE) for the Post-Doctoral Research Fellowship. The authors also thank CSIR-NIIST, for the instrumental facilities and Division

of Cancer Research, Regional Cancer Centre (RCC), Thiruvananthapuram.

REFERENCES

- (1) Zhang, X.; Chi, Z.; Li, H.; Xu, B.; Li, X.; Zhou, W.; Liu, S.; Zhang, Y.; Xu, J. Piezofluorochromism of an Aggregation-Induced Emission Compound Derived from Tetraphenylethylene. *Chem. - Asian J.* **2011**, *6*, 808–811.
- (2) Zhang, X.; Zhang, X.; Tao, L.; Chi, Z.; Xu, J.; Wei, Y. Aggregation Induced Emission-Based Fluorescent Nanoparticles: Fabrication Methodologies and Biomedical Applications. *J. Mater. Chem. B* **2014**, *2*, 4398–4414.
- (3) Li, Y.; Xu, L.; Su, B. Aggregation Induced Emission for the Recognition of Latent Fingerprints. *Chem. Commun.* **2012**, *48*, 4109–4111.
- (4) Shi, H.; Kwok, R. T. K.; Liu, J.; Xing, B.; Tang, B. Z.; Liu, B. Real-Time Monitoring of Cell Apoptosis and Drug Screening Using Fluorescent Light-up Probe with Aggregation-Induced Emission Characteristics. *J. Am. Chem. Soc.* **2012**, *134*, 17972–17981.
- (5) Chen, X.; Shen, X. Y.; Guan, E.; Liu, Y.; Qin, A.; Sun, J. Z.; Tang, B. Z. A Pyridinyl-Functionalized Tetraphenylethylene Fluorogen for Specific Sensing of Trivalent Cations. *Chem. Commun.* **2013**, *49*, 1503–1505.
- (6) Zhu, Z.; Xu, L.; Li, H.; Zhou, X.; Qin, J.; Yang, C. A Tetraphenylethylene-Based Zinc Complex as a Sensitive DNA Probe by Coordination Interaction. *Chem. Commun.* **2014**, *50*, 7060–7062.
- (7) Zhang, L.; Hu, W.; Yu, L.; Wang, Y. Click Synthesis of a Novel Triazole Bridged AIE Active Cyclodextrin Probe for Specific Detection of Cd²⁺. *Chem. Commun.* **2015**, *51*, 4298–4301.
- (8) Huang, X.; Gu, X.; Zhang, G.; Zhang, D. A Highly Selective Fluorescence Turn-on Detection of Cyanide Based on the Aggregation of Tetraphenylethylene Molecules Induced by Chemical Reaction. *Chem. Commun.* **2012**, *48*, 12195–12197.
- (9) Liang, G.; Lam, J. W. Y.; Qin, W.; Li, J.; Xie, N.; Tang, B. Z. Molecular Luminogens Based on Restriction of Intramolecular Motions through Host–guest Inclusion for Cell Imaging. *Chem. Commun.* **2014**, *50*, 1725–1727.
- (10) Jayaram, D. T.; Ramos-Romero, S.; Shankar, B. H.; Garrido, C.; Rubio, N.; Sanchez-Cid, L.; Gómez, S. B.; Blanco, J.; Ramaiah, D. In Vitro and in Vivo Demonstration of Photodynamic Activity and Cytoplasm Imaging through TPE Nanoparticles. *ACS Chem. Biol.* **2016**, *11*, 104–112.
- (11) Qiao, J.; Liu, Z.; Tian, Y.; Wu, M.; Niu, Z. Multifunctional Self-Assembled Polymeric Nanoprobes for FRET-Based Ratiometric Detection of Mitochondrial H₂O₂ in Living Cells. *Chem. Commun.* **2015**, *51*, 3641–3644.
- (12) Yuan, Y.; Kwok, R. T. K.; Feng, G.; Liang, J.; Geng, J.; Tang, B. Z.; Liu, B. Rational Design of Fluorescent Light-up Probes Based on an AIE Luminogen for Targeted Intracellular Thiol Imaging. *Chem. Commun.* **2014**, *50*, 295–297.
- (13) Samanta, A.; Maiti, K. K.; Soh, K. S.; Liao, X.; Vendrell, M.; Dinish, U. S.; Yun, S. W.; Bhuvaneshwari, R.; Kim, H.; Rautela, S.; Chung, J.; Olivo, M.; Chang, Y. T. Ultrasensitive near-Infrared Raman Reporters for SERS-Based in Vivo Cancer Detection. *Angew. Chem., Int. Ed.* **2011**, *50*, 6089–6092.
- (14) Maiti, K. K.; Dinish, U. S.; Samanta, A.; Vendrell, M.; Soh, K. S.; Park, S. J.; Olivo, M.; Chang, Y. T. Multiplex Targeted in Vivo Cancer Detection Using Sensitive near-Infrared SERS Nanotags. *Nano Today* **2012**, *7*, 85–93.
- (15) Mattley, Y.; Allen, M. W. Innovative Raman Sampling. *Opt. Photonik* **2013**, *8*, 44–47.
- (16) Narayanan, N.; Karunakaran, V.; Paul, W.; Venugopal, K.; Sujathan, K.; Kumar Maiti, K. Aggregation Induced Raman Scattering of Squaraine Dye: Implementation in Diagnosis of Cervical Cancer Dysplasia by SERS Imaging. *Biosens. Bioelectron.* **2015**, *70*, 145–152.
- (17) Huh, Y. S.; Chung, A. J.; Erickson, D. Surface Enhanced Raman Spectroscopy and Its Application to Molecular and Cellular Analysis. *Microfluid. Nanofluid.* **2009**, *6*, 285–297.
- (18) Ramya, A.; Samanta, A.; Nisha, N.; Chang, Y. T.; Maiti, K. K. New Insight of Squaraine-Based Biocompatible Surface-Enhanced Raman Scattering Nanotag for Cancer-Cell Imaging. *Nanomedicine (London, U. K.)* **2015**, *10*, 561–571.
- (19) Murelli, R. P.; Zhang, A. X.; Michel, J.; Jorgensen, W. L.; Spiegel, D. A. Chemical Control over Immune Recognition: A Class of Antibody-Recruiting Small Molecules that Target Prostate Cancer. *J. Am. Chem. Soc.* **2009**, *131*, 17090–17092.
- (20) Li, J.; Ma, H.; Wu, D.; Li, X.; Zhao, Y.; Zhang, Y.; Du, B.; Wei, Q. Biosensors and Bioelectronics A Label-Free Electrochemiluminescence Immunosensor Based on KNbO₃ – Au Nanoparticles @ Bi₂S₃ for the Detection of Prostate Specific Antigen. *Biosens. Bioelectron.* **2015**, *74*, 104–112.
- (21) Liu, D.; Huang, X.; Wang, Z.; Jin, A.; Sun, X.; Zhu, L.; Wang, F.; Ma, Y.; Niu, G.; Hight Walker, A. R.; Chen, X. Gold Nanoparticle-Based Activatable Probe for Sensing Ultralow Levels of Prostate-Specific Antigen. *ACS Nano* **2013**, *7*, 5568–5576.
- (22) Li, S.; Zhang, Y.; Xu, J.; Li, L.; Zeng, Q.; Lin, L.; Guo, Z.; Liu, Z.; Xiong, H.; Liu, S. Noninvasive Prostate Cancer Screening Based on Serum Surface-Enhanced Raman Spectroscopy and Support Vector Machine. *Appl. Phys. Lett.* **2014**, *105*, 091104.
- (23) Del Mistro, G.; Cervo, S.; Mansutti, E.; Spizzo, R.; Colombatti, A.; Belmonte, P.; Zucconelli, R.; Steffan, A.; Sergio, V.; Bonifacio, A. Surface-Enhanced Raman Spectroscopy of Urine for Prostate Cancer Detection: A Preliminary Study. *Anal. Bioanal. Chem.* **2015**, *407*, 3271–3275.
- (24) Kneipp, K.; Kneipp, H.; Itzkan, I.; Dasari, R. R.; Feld, M. S. Surface-Enhanced Raman Scattering and Biophysics. *J. Phys.: Condens. Matter* **2002**, *14*, 597–624.
- (25) Beierlein, F. R.; Othersen, O. G.; Lanig, H.; Schneider, S.; Clark, T. Simulating FRET from Tryptophan: Is the Rotamer Model Correct? *J. Am. Chem. Soc.* **2006**, *128*, 5142–5152.
- (26) Krishnakumar, V.; Balachandran, V. FTIR, FT-Raman Spectral Analysis and Normal Coordinate Calculations of 2-Hydroxy-3-Methoxybenzaldehyde Thiosemicarbozone. *Indian J. Pure Appl. Phys.* **2004**, *42*, 313–318.
- (27) Goun, E. a.; Shinde, R.; Dehnert, K. W.; Adams-Bond, A.; Wender, P. a.; Contag, C. H.; Franc, B. L. Intracellular Cargo Delivery by an Octaarginine Transporter Adapted to Target Prostate Cancer Cells through Cell Surface Protease Activation. *Bioconjugate Chem.* **2006**, *17*, 787–796.
- (28) Yu, X.; Munge, B.; Patel, V.; Jensen, G.; Bhirde, A.; Gong, J. D.; Kim, S. N.; Gillespie, J.; Gutkind, J. S.; Papadimitrakopoulos, F.; Rusling, J. F. Carbon Nanotube Amplification Strategies for Highly Sensitive Immunodetection of Cancer Biomarkers. *J. Am. Chem. Soc.* **2006**, *128*, 11199–11205.
- (29) Schwartzberg, A. M.; Oshiro, T. Y.; Zhang, J. Z.; Huser, T.; Talley, C. E. Small Correspondence Improving Nanoprobes Using Surface-Enhanced Raman Scattering from 30-Nm Hollow Gold Particles Improving Nanoprobes Using Surface-Enhanced Raman Scattering from 30-Nm Hollow Gold Particles. *Anal. Chem.* **2006**, *78*, 4732–4736.
- (30) Vendrell, M.; Maiti, K. K.; Dhaliwal, K.; Chang, Y.-T. Surface-Enhanced Raman Scattering in Cancer Detection and Imaging. *Trends Biotechnol.* **2013**, *31*, 249–257.